Photokatalytische Eigenschaften oxidischer und sulfidischer Materialien

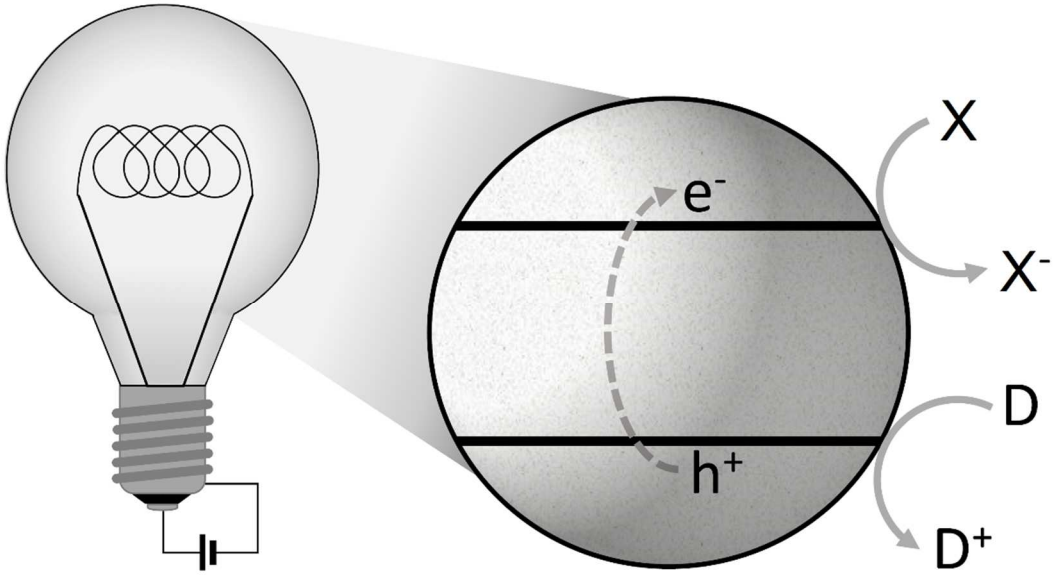

Dissertation

zur Erlangung des Doktorgrades

der Mathematisch-Naturwissenschaftlichen Fakultät

der Christian-Albrechts-Universität zu Kiel

vorgelegt von

Michael Alexander Thomas Poschmann

Kiel, 2019

Erster Gutacher:	Prof. Dr. Wolfgang Bensch
Zweite/r Gutachter/in:	Prof. Dr. Norbert Stock
Tag der mündlichen Prüfung:	16.07.2019
Zum Druck genehmigt:	17.07.2019

Die vorliegende Dissertation wurde unter Anleitung von

Prof. Dr. Wolfgang Bensch

in der Zeit von

2014 bis 2019

am Institut für Anorganische Chemie

der Christian-Albrechts-Universität zu Kiel

angefertigt.

Kurzzusammenfassung

Diese Arbeit widmet sich der Untersuchung der photokatalytischen Eigenschaften von oxidischen und sulfidischen Materialien. Im Detail geht es um die photokatalytische Gewinnung von Energieträgern und die Reinigung wässriger Lösungen von organischen Schadstoffen.

Im ersten Teil dieser Arbeit werden die photokatalytischen Eigenschaften von $ZnCr_2O_4$ vorgestellt und diskutiert. Der Einfluss der Synthesetemperatur auf die photokatalytische Zersetzung von y-Eosin in wässrigen Lösungen wurde systematisch untersucht. Die Ergebnisse belegen, dass bei niedrigen Temperaturen wenige Nanometer große Kristallite mit einer großen spezifischen Oberfläche und einer hohen Defektdichte erhalten werden, welche äußerst aktive Katalysatoren darstellen. Eine detaillierte Analyse der Reaktionen während der Bestrahlung der Reaktionsmischungen mit sichtbarem Licht ergab, dass Chromatanionen durch einen Photokorrosionsprozess gebildet werden. Experimente mit CrO_4^{2-} belegten, dass diesen Anionen die katalytische Aktivität zugeschrieben werden kann. Aufgrund der krebserzeugenden Wirkung dieser Ionen ist von einem Einsatz von $ZnCr_2O_4$ im Rahmen einer photokatalytischen Abwasserklärung abzusehen.

Im zweiten Teil der Arbeit werden die Ergebnisse zur lichtgetriebenen Wasserstoffgenerierung mit der Verbindung $\{[Ni(1,4,7,10\text{-Tetraazacyclododecan})]_6[Sn_6S_{12}O_2(OH)_6]\} \cdot 2(ClO_4) \cdot 19H_2O$ präsentiert. Oxothiostannate sind eine nur wenig erforschte Klasse an Verbindungen, welche die Eigenschaften von Zinnoxid und –sulfid vereinigen. Zusätzlich sind Ni^{2+}-zentrierte Komplexe vorhanden, welche teilweise als homogene Katalysatoren für die photokatalytische Wasserstoffgenerierung eingesetzt werden können. Da sowohl Zinnsulfide als auch Zinnoxide Anwendung in photokatalytischen Prozessen finden, sollte das Oxothiostannat eine katalytische Wirkung zeigen. Tatsächlich wird eine deutliche Aktivität in der photokatalytischen Wasserstoffgenerierung beobachtet. Allerdings scheint nach längerer Reaktionszeit Photokorrosion einzutreten und es konnten mit dem Tyndall-Effekt kolloidale Teilchen nachgewiesen werden. Durch die Komplexität des Reaktionssystems konnte der Beitrag der einzelnen Komponenten zum katalytischen Prozess nicht aufgeklärt werden.

Der dritte Teil dieser Arbeit befasst sich mit dem zuvor unbekannten Oxothiostannat [Ni(1,4,7,10-Tetraazacyclododecan)(H_2O)$_2$]$_4$[$Sn_{10}S_{20}O_4$]·∼13H_2O. Analog zu der in Abschnitt zwei diskutierten Verbindung weist auch dieses Material im Reaktionsmedium aus Triethylamin, Acetonitril und Wasser in Gegenwart des Photosensibilisators tris-Bipyridin-Ruthenium(II) eine katalytische Wasserstoffgenerierung auf. Da die Verbindung durch Photokorrosion langsam zerstört wird, nimmt die Wasserstoffgenerierung mit fortschreitender Belichtungszeit ab. Im letzten Teil dieser Arbeit wird über die photokatalytischen Eigenschaften des Spinells $CuCo_2S_4$ berichtet. Da dieses Material ein elektrischer Leiter ist und daher nicht photoaktiv ist, wurden verschiedene Mengen $CuCo_2S_4$ auf TiO_2 abgeschieden und die photokatalytische Aktivität in einer basischen Triethanolaminlösung untersucht. Bei Bestrahlung mit ultraviolettem Licht wurde eine hohe Entwicklungsrate von Wasserstoffgas beobachtet. Bei längerer Bestrahlung ist jedoch eine kontinuierliche Abnahme der Aktivität zu beobachten, was auf einen Lösungsprozess von $CuCo_2S_4$ in der basischen Lösung zurückgeführt werden kann.

Abstract

This thesis deals with the investigation of the photocatalytic properties of oxidic and sulphidic materials. In detail, the focus of the investigations was on the photocatalytic production of solar fuels and wastewater purification.

In the first part of the thesis the photocatalytic properties of $ZnCr_2O_4$ are presented and discussed. The influence of the synthesis temperature of the spinel on the photocatalytic decomposition of y-Eosin in aqueous solutions was systematically investigated. The results show that, using low temperatures, nanometer-sized crystallites are obtained with a high specific surface area and high defect density, which are highly active catalysts. A detailed analysis of the reactions during irradiation of the reaction mixtures with visible light revealed that chromate anions are formed by a photo-corrosion process. Experiments with CrO_4^{2-} demonstrated that the catalytic activity can be attributed to these anions. Due to the carcinogenic effects of these ions, the use of $ZnCr_2O_4$ in the context of a photocatalytic wastewater treatment can be foreseen.

In the second part of the work the results for light-driven hydrogen generation with the compound $\{[Ni(1,4,7,10\text{-Tetraazacyclododecane})]_6[Sn_6S_{12}O_2(OH)_6]\}\cdot 2(ClO_4)\cdot 19H_2O$ are presented. Oxothiostannates are a poorly understood class of compounds that combine the properties of tin oxide and sulfide. In addition, Ni^{2+}-centrated complexes are present, some of which can be used as homogeneous catalysts for the photocatalytic hydrogen generation. Since both tin sulfides and tin oxides find application in photocatalytic processes, the oxothiostannate should show a catalytic effect. In fact, a marked activity is observed in photocatalytic hydrogen generation. However, after a prolonged reaction time, photocorrosion appears to occur and colloidal particles could be detected by the Tyndall effect. Due to the complexity of the reaction system, the contribution of the individual components to the catalytic process could not be clarified.

The third part of this thesis deals with a previously unknown oxothiostannate with the formula $[Ni(1,4,7,10\text{-Tetraazacyclododecane})(H_2O)_2]_4[Sn_{10}S_{20}O_4]\cdot\sim 13H_2O$. Like the above-mentioned $\{[Ni(1,4,7,10\text{-tetraazacyclododecane})]_6[Sn_6S_{12}O_2(OH)_6]\}\cdot 2(ClO_4)\cdot 19H_2O$, this compound has the ability to react in a reaction medium of triethylamine, acetonitrile and

water by photosensitization with tris-bipyridine-ruthenium (II) to catalytically produce hydrogen. As in the second part, photocorrosion is observed, which limits the continuity of hydrogen generation.

In the last part of this work the photocatalytic effect of the spinel $CuCo_2S_4$ was investigated. Since this material is an electrical conductor and thus is not photoactive itself, the $CuCo_2S_4$ was deposited in different quantities on TiO_2. The photocatalytic activity was investigated in a basic triethanolamine solution. When irradiated with ultraviolet light, there is a high rate of hydrogen evolution. With continuous irradiation, however, a decrease in catalytic activity can be observed. This is attributable to a solution process of $CuCo_2S_4$ in the basic solution. The composite therefore continuously loses $CuCo_2S_4$ and the Material exhibits no long-term stability under these conditions.

Abkürzungen und Bezeichnungen

ATP	Adenosintriphosphat
$NADP^+$	oxidiertes Nicotinamidadenindinukleotidphosphat
NADPH	reduziertes Nicotinamidadenindinukleotidphosphat
GTP	Guanosintriphosphat
HOMO	höchstes besetztes Molekülorbital (engl.: highest occupied molecular Orbital)
LUMO	tiefstes nicht besetztes Molekülorbital (engl.: lowest unoccupied molecular Orbital)
NHE	Normal-Wasserstoff-Elektrode (engl.: RHE, regular Hydrogen electrode)
POP	Persistenter organischer Schadstoff (engl.: persistent organic pollutant)
ROS	Reaktive Sauerstoffspezies (engl.: reactive oxygen species)
HPLC/MS	Hochleistungsflüssigkeitschromatographie gekoppelte Massenspektrometrie (engl.: high performance liquid chromatography coupled mass spectrometry)
Cat	Katalysator
RCP	Repräsentativer Konzentrationspfad (engl.: representative concentration pathway, Bezeichnung spezieller Klimamodelle des IPCC)
IPCC	Internationales Gremium zum Klimawandel (engl.: international panel on climate change)
$\Delta pH_{Oberfläche}$	Änderung des pH-Wertes des Ozean-Oberflächenwassers
OEC	Sauerstoffentwickelnder Komplex (engl.: oxygen evolving complex) des Photosystem II
LEAG	Marke der *Lausitz Energie Verwaltungs GmbH*, *Lausitz Energie Bergbau AG* und der *Lausitz Energie Kraftwerke AG*
E_g	Energetische Bandlücke in Halbleitern
UPS	Ultraviolettphotoelektronenspektroskopie
XPS	Röntgenphotoelektronenspektroskopie
UV	Ultraviolettes Licht
Vis	Sichtbares Licht
IUPAC	Internationale Vereinigung für reine und angewandte Chemie (engl.: international union of pure and applied chemistry)
LB	Leitungsband
VB	Valenzband

Abbildungsverzeichnis

Tabellenverzeichnis

Inhalt

1. Wissenschaftlicher Hintergrund

1.1. Motivation

Zu den vielen Herausforderungen, mit denen die heutige Gesellschaft konfrontiert wird, gehören die zunehmende Umweltverschmutzung und die Verknappung der fossilen Energieträger. Beide Faktoren können zu gesellschaftlichen und politischen Spannungen führen. Eine wichtige Aufgabe der Naturwissenschaften ist, die chemisch-physikalischen bzw. technischen Voraussetzungen zu schaffen, dass diese Probleme in geeigneter Weise gelöst werden können. Zwar lassen sich die genannten Probleme leicht in sich zusammenfassen, wobei sie sich auch zu einem beachtlichen Teil überschneiden, jedoch besitzen sie viele Teilaspekte die separat voneinander zu lösen sind. In den folgenden Kapiteln soll ein kleiner Überblick über die beiden Problemfelder gegeben werden.

1.1.1. Fossile Energieträger

Zu den fossilen Energieträgern werden in der Regel Kohlen (Braunkohle, Steinkohle), Erdgas und Erdöl sowie dessen zur Energiegewinnung genutzte Bestandteile gezählt. Je nach Auffassung wird auch Uran als fossiler Energieträger angesehen, da es ähnlich wie Kohle, Erdöl und –gas gewonnen wird und ebenfalls nur in limitierten Mengen förderbar bzw. vorhanden ist. Abhängig von prognostizierten Effizienzsteigerungen der Energiegewinnung, Weltbevölkerungswachstum und Wirtschaftswachstum kommen Studien zu dem Schluss, dass die förderbaren Energieträgerreserven in den Jahren 2070-2110 aufgebraucht sein werden (siehe Abb. 1).[1] Durch erschwerte Förderbedingungen wird es vermutlich schon deutlich vorher zur Verknappung der Rohstoffe und daher zu deutlichen Preissteigerungen kommen.

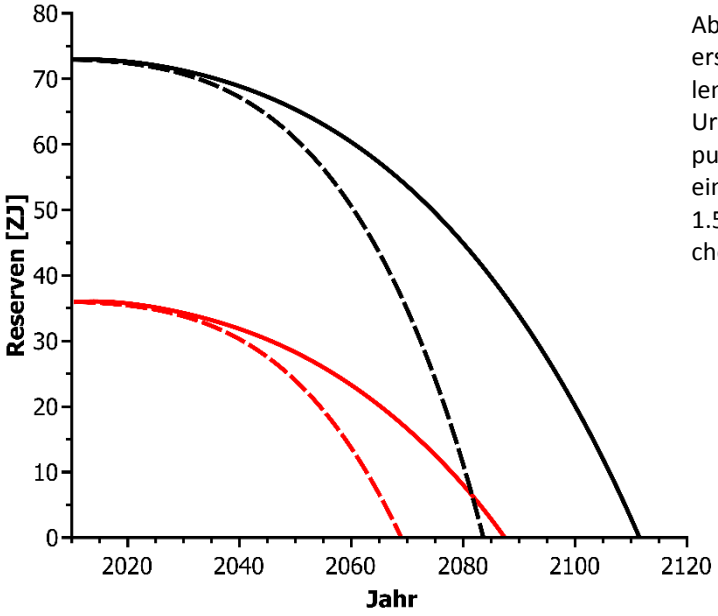

Abb. 1: Zugängliche (schwarz) und derzeit erschlossene (rot) Lagerstätten der fossilen Energieträger Erdöl, Kohle, Erdgas und Uran und deren prognostizierte Verknappung in den kommenden 100 Jahren bei einem Weltwirtschaftswachstum von 1.5 % (durchgezogen) und 3 % (unterbrochen).[1]

Ein besonderes Problem der fossilen Energieträger Erdöl, Kohle und Erdgas stellen die durch die Verbrennung resultierenden CO_2-Emissionen dar. Seit 1950 hat sich die über das Jahr und global gemittelte CO_2 Konzentration in der Atmosphäre von 310 auf ca. 390 ppm im Jahr 2010 erhöht (siehe Abb. 2).[1] Je nach Prognosemodell wird die CO_2-Konzentration bis 2035 auf 410-500 ppm steigen und damit als hauptsächlich anthropogenes Treibhausgas einen großen Beitrag zur global gemittelten Erderwärmung um 0.4-2.6 °C bis zum Zeitraum 2046-2065 im Verglich zum Zeitraum 1986-2005 liefern, oder 0.3-4.8 °C bis zum Zeitraum 2081-2100.[1] Neben den komplizierten klimatischen Veränderungen wird durch die bodennahe atmosphärische Temperaturerhöhung ein Meeresspiegelanstieg von 17-38 cm für 2046 bis 2065 im Vergleich zum Zeitraum 1986-2005 erwartet (siehe Abb. 2).[1] Dies wird besonders in Küstenregionen durch Überschwemmungen zu gesellschaftlichen Problemen und wirtschaftlichen Konsequenzen führen. Zusätzlich kommt es durch den Eintrag von CO_2 zu einer Versauerung der Ozeane, $\Delta pH_{Oberfläche}$ = -0.065 bis -0.31 bis 2100 im Vergleich zum Jahr 2005, sodass es zu einer drastischen Beeinflussung der Meeresökologie kommt (siehe Abb. 2).[1]

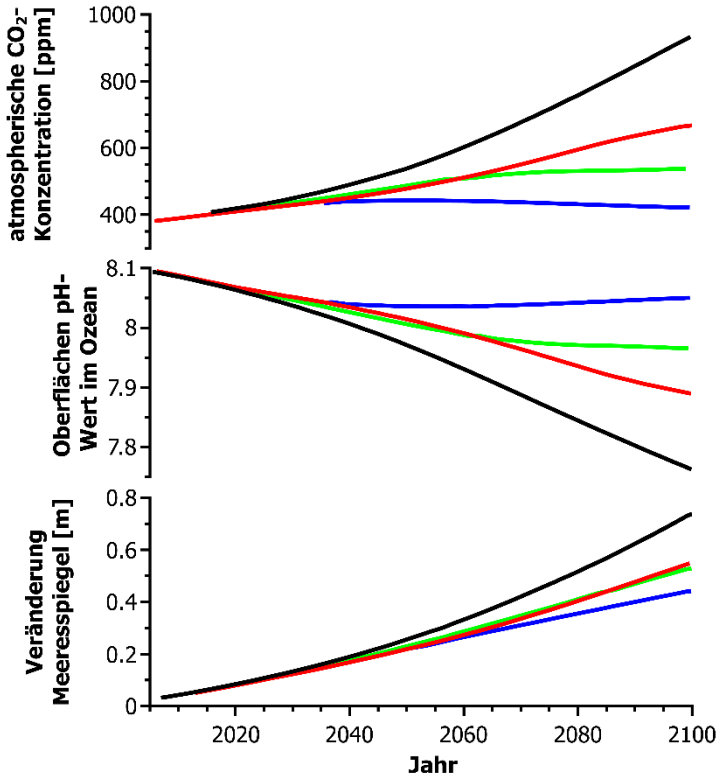

Abb. 2: Erhöhung der atmosphärischen CO_2-Konzentration im 21. Jahrhundert (Oben) prognostiziert durch vier verschiedene Modelle des International Panel on Climate Change (IPCC).[1] Die Modelle sind bezeichnet durch RCP 8.5 (schwarz), RCP 6.0 (rot), RCP 4.5 (grün) und RCP 2.6 (blau). RCP bedeutet hier Representative Concentration Pathway und die angehängte Zahl den im Jahr 2100 zu erwartenden Strahlungsantrieb (Einheit: W/m^2) auf der Erdoberfläche, hauptsächlich verursacht durch CO_2 in der Atmosphäre. Durch die Erhöhung der atmosphärischen CO_2-Konzentration wird eine Verringerung des pH-Werts des Oberflächenwassers der Ozeane erwartet (Mitte).[1] Und durch die globale Erwärmung und Abschmelzen der Polkappen eine Erhöhung des Meeresspiegels (Unten).[1]

Neben dem Ausstoß von CO_2 kommt es bei der Verbrennung von fossilen Energieträgern zusätzlich zu Emissionen an feinpartikulären Kohlenstoffen, persistenten Organika, NO_x, SO_x und Schwermetallen wie z.B. Blei.[2–4] Trotz Verwendung geeigneter Filtersysteme, wie sie in fortschrittlichen Kraftwerken üblich sind, kommt es trotzdem regional zur Kontamination der Umwelt. Durch ein fortschrittliches Kraftwerk (Schwarze Pumpe in Spremberg betrieben durch LEAG), so angegeben in einem Bericht des Umweltbundesamtes, kam es im Jahr 2015 für die Energiegewinnung von 1500 MW aus Braunkohle unter anderem zur Emission von 12.2 Mrd. kg CO_2, 5.81 Mio. kg NO_x, 9.24 Mio. kg SO_x, 58700 kg Feinstaub (Teilchendurchmesser $d < 10\ \mu m$), 339 kg Quecksilberverbindungen, 26.2 kg Arsenverbindungen und 18.1 kg Cadmiumverbindungen.[4] Ein Maß für die Umweltbelastung durch die jeweiligen Energieträger wurde in Deutschland durch die Methodenkonvention 2.0 des Umweltbundesamtes festgelegt.[5] Nach dieser Konvention berechnen sich die Umweltkosten von Braunkohleverstromung zu 19.19 €-Cent/kWh und bei Steinkohleverstromung zu 16.13 €-Cent/kWh. Die umweltfreundlicheren erneuerbaren Energieträger weisen jedoch weit geringere Umweltkosten auf, 0.38 €-Cent/kWh für Windkraft und 1.82 €-Cent/kWh für Photovoltaik.[4]

Eine Möglichkeit zur Energieträgergewinnung, bei gleichzeitig geringer Gefahr der Umweltverschmutzung, bietet die Wasserspaltung zur Produktion von Wasserstoff (mögliche

Wege der nachhaltigen Herstellung in Kap. 1.4). Wasserstoff als Energieträger oder auch Energiespeicher bietet neben der Stromerzeugung durch Brennstoffzellen oder die Verbrennung in Gaskraftwerken den Vorteil, dass dieser auch für viele industrielle Prozesse benötigt wird, für die er derzeit noch aus der Wassergas-Shift-Reaktion gewonnen wird. Daher führt eine nachhaltige umweltfreundliche Gewinnung von Wasserstoff zu einem Energieträger mit äußerst vielfältigem Nutzen. Jedoch bereitet neben der einfachen Herstellung auch die Speicherung derzeit noch einige Probleme. Durch den kleinen Wechselwirkungsquerschnitt weist Wasserstoff eine relativ hohe Diffusionsgeschwindigkeit in Metallen auf, welche üblicherweise für Gasspeicher benutzt werden.[6–9]

1.1.2. Gewässerverschmutzung

Durch die Verwendung vieler chemischer und pharmazeutischer Substanzen in der Industrie, den privaten Haushalten und in der Agrarwirtschaft wird eine zunehmende Belastung der natürlichen Gewässer mit Rückständen dieser Substanzen beobachtet.[10–12] Teilweise lassen sich diese Substanzen auch nicht durch die derzeit übliche Abwasserklärung in Kläranlagen, wie sie in Deutschland üblich sind, beseitigen. So werden z.B. Pharmazeutika wie Cabamazepin (Median: 752 ng/L), Tramadol (Median: 218 ng/L), Trimethoprim (Median: 178 ng/L), etc. im Kläranlagenablauf, das heißt nach einer umfangreichen Klärung bevor sie in natürliche Gewässer entlassen werden, gefunden (siehe Abb. 3 und Abb. 4).[12] In den natürlichen Gewässern akkumulieren sich diese Substanzen und werden von hier auch in das Grundwasser und in die Trinkwasserbrunnen eingetragen.[13] Am gefährlichsten sind die persistenten organischen Schadstoffe (POPs, engl.: persistent organic pollutants). Diese weisen eine große Verweilzeit in der Umwelt auf, da sie nicht durch Lebewesen wie z.B. Bakterien effizient abgebaut werden können. Zu dieser Substanzklasse gehören unter anderem polycyclische Aromaten, Dioxine, Organochlorverbindungen (z.B. Pestizide), Organobromverbindungen (Flammschutzmittel) oder polyfluorierte Verbindungen (z.B. Perfluoroctansulfonsäure).[2,3,10,12,14]

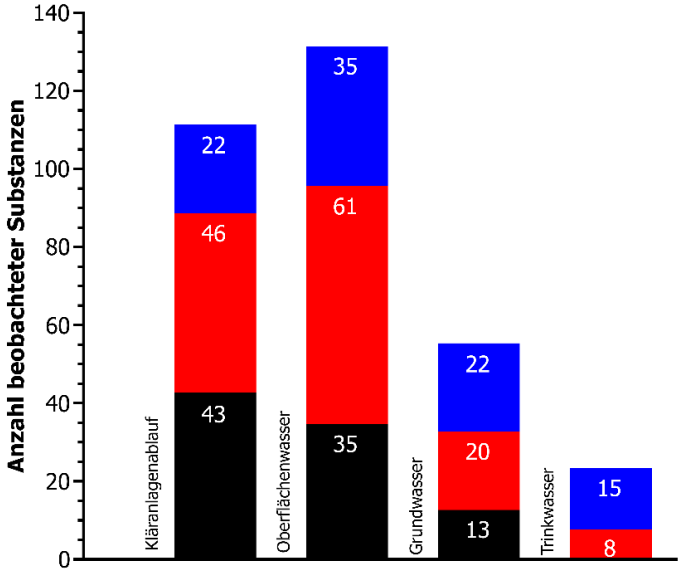

Abb. 3: Im Kläranlagenablauf, Oberflächenwasser, Grundwasser und Trinkwasser beobachtete Arzneimittelwirkstoffe mit Maximalkonzentrationen von >1.0 µg/L (schwarz), 0.1-1.0 µg/L (rot) und < 0.1 µg/L (blau).[13]

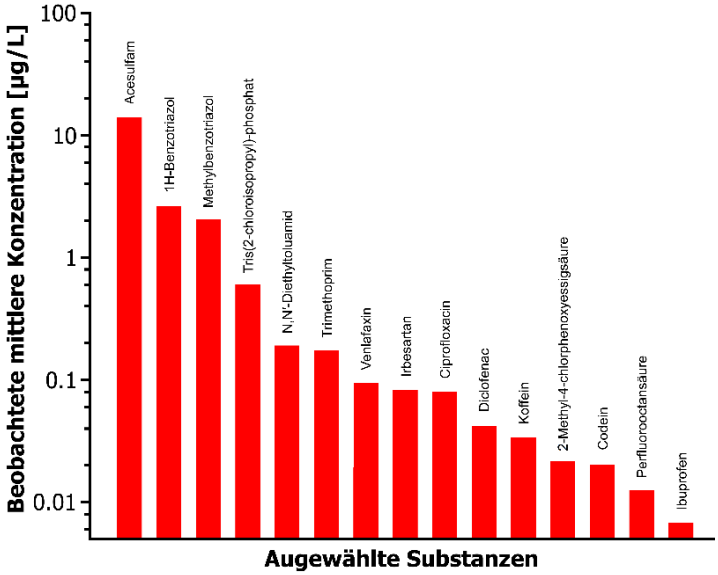

Abb. 4: Im Kläranlagenablauf beobachtete mittlere Konzentrationen (Median) ausgewählter Substanzen mit teilweise pharmazeutischer Wirkung.[12]

Da bei Pharmazeutika und krebserzeugenden Substanzen schon bei geringen Konzentrationen ein Einfluss auf den Menschen bzw. auch auf andere Lebewesen vorstellbar ist, stellen die kontaminierten Gewässer ein gewisses Gefahrenpotential dar.[15] Aus Industrie und Landwirtschaft kommt es zusätzlich zu einem Eintrag von Gefahrstoffen wie Insektiziden, Bioziden, Reinigungsmitteln, etc.[16] Diese haben direkte Auswirkungen auf die Gewässerökosysteme und indirekt damit auch auf Landökosysteme und den Menschen. Weiteres Gefahrenpotential tritt durch die immer häufiger beobachteten Mikroplastikpartikel auf. Neben ihrem eigenen Gefahrenpotential, welches noch wenig untersucht ist, akkumulieren diese Partikel die zuvor genannten meist organischen und fettlöslichen Gefahrstoffe, sodass

diese ein gesteigertes Gefahrenpotential aufweisen.[17–19] Neben der Vermeidung des Eintrags in die Gewässer ist daher auch eine Ergänzung der üblichen Abwasserklärung notwendig, um diese Substanzen effektiv aus Gewässern zu entfernen. Eine Möglichkeit stellt die katalytische Zersetzung der Gefahrstoffe durch reaktive Sauerstoffspezies dar (siehe Kap. 1.5).[20,21]

1.2. Katalyse

Bei katalytischen Prozessen wird die Kinetik einer chemischen Reaktion durch Einsatz eines Stoffes (Katalysator) beschleunigt indem die Aktivierungsenergie herabgesetzt wird. Die Thermodynamik einer chemischen Reaktion wird dabei nicht beeinflusst. Der Katalysator wird während der chemischen Reaktion nicht verbraucht und liegt nach der Reaktion im Idealfall im Ausgangszustand vor. Neben der Beschleunigung der Reaktion sollen Katalysatoren oft die Selektivität eines Prozesses hin zu dem gewünschten Produkt erhöhen bzw steuern. Bei katalytischen Reaktionen kann grob zwischen homogener, enzymatischer und heterogener Katalyse unterschieden werden, je nachdem ob sich der Katalysator und die Reaktanden in der gleichen (homogen) oder unterschiedlichen (heterogen) Phasen befinden. In der homogenen Katalyse kommen Katalysatoren in Form von Ionen, Molekülen oder auch Metallkomplexen zum Einsatz, während in der enzymatischen Katalyse ausschließlich Enzyme verwendet werden. Da der Fokus dieser Arbeit im Bereich der heterogenen Katalyse liegt, soll diese etwas genauer dargestellt werden.[22–24]

Bei der heterogenen Katalyse tritt der Katalysator stets in einer anderen Phase als die Reaktanden auf, wobei die Reaktion stets an der Grenzfläche zwischen Katalysator und Reaktionsgemisch stattfindet.[24] Typische Beispiele sind Reaktionen in einer flüssigen oder gasförmigen Reaktionsmischung in Gegenwart eines Katalysators. Aber es würde auch als heterogene Katalyse gelten, wenn Flüssigkeitstropfen eine Festkörperreaktion oder eine Reaktion in der Gasphase beschleunigen. Auch wenn Gasteilchen eine Reaktion an der Grenzfläche zu einer Flüssigkeit oder eines Feststoffes beschleunigen, kann von heterogener Katalyse gesprochen werden. Ein Beispiel stellt die korrosionsfördernde Wirkung von Gasmolekülen und Flüssigkeiten bei Metalloxidationen dar.[25]

Die katalytische Wirkung eines Festkörpers in einer flüssigen oder gasförmigen Phase wird durch seine Oberflächenchemie und –struktur bestimmt. Der Mechanismus einer katalytischen Reaktion lässt sich verallgemeinert in mehrere Schritte aufteilen. Zunächst ist eine Diffusion des oder der Edukte zur Oberfläche nötig, welche durch die Oberflächenmorphologie beeinflusst wird. Anschließend findet eine Adsorption statt und es wird ein Katalysator-Substrat-Addukt gebildet (siehe Abb. 5).[24] Es folgt eine Oberflächendiffusion, -reorganisation und Aktivierung des Edukts, sodass anschließend eine Reaktion mit einem Reaktanden stattfinden kann, welcher ebenfalls am Katalysator gebunden ist oder aus der umgebenden Reaktionsmischung stammt (siehe Abb. 5). Die letzten Schritte des Mechanismus bestehen aus der Dissoziation des Katalysator-Produkt-Addukts und der Diffusion des Produktmoleküls von der Oberfläche (siehe Abb. 5).[24] Jeder Reaktionsschritt weist dabei seine eigenen kinetischen Besonderheiten auf. Typische Mechanismen an idealen Katalysatoren sind der Eley-Rideal-[26,27], Langmuir-Hinshelwood-[28,29] und der Mars-von-Krevelen-Mechanismus[30]. Die komplizierten Kinetiken haben jedoch zur Folge, dass die detaillierten Mechanismen von heterogenen Katalyseprozessen im Detail an den Grenzflächen von Realkatalysatoren nur selten verstanden und beschrieben werden können. Bei Idealkatalysatoren, das heißt bei Katalysatoren mit einer definierten und spektroskopisch leicht zugänglichen Oberfläche, gestaltet sich die Aufklärung der Mechanismen einfacher, sodass z.B. der

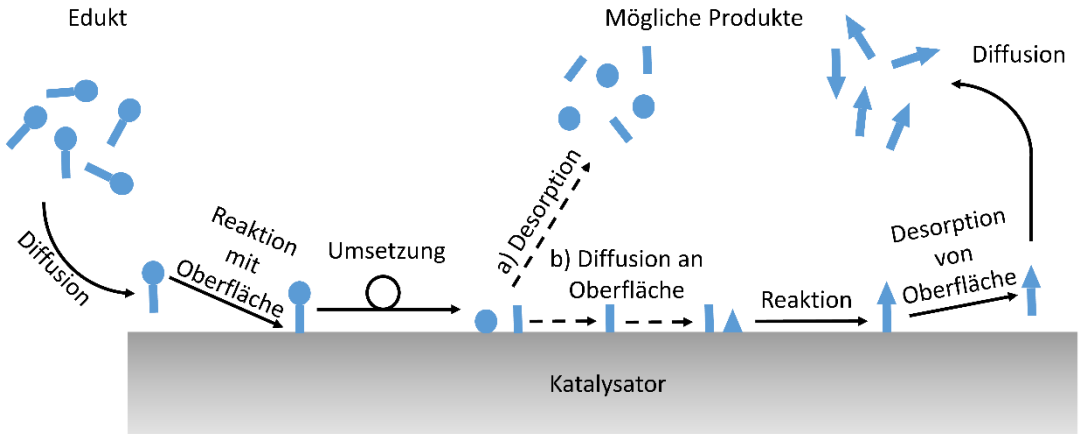

Mechanismus der Ammoniak-Synthese auf einer Eisen-{100}-Einkristalloberfläche aufgeklärt werden konnte.[24]

Abb. 5: Verallgemeinerte Prozesse einer Reaktion auf einer Oberfläche eines heterogenen Katalysators unterteilt in mögliche Schritte des Mechanismus. Der Pfad a) könnte z. B. ein Teil eines Mars-von-Krevelen-Mechanismus[31] sein und der Pfad b) ein Teil des Langmuir-Hinshelwood-Mechanismus[28,29].

1.3. Photokatalyse

Bei der Photokatalyse wird Licht als Energielieferant für katalysierte Reaktionen benutzt.[31] Der wohl prominenteste Vertreter photokatalytischer Prozesse ist die Photosynthese, bei der Pflanzen mit Hilfe von Lichtenergie energiereiche Polyphosphate ($NADPH+H^+$, ATP, GTP) bilden, welche anschließend z.B. zur Synthese von Kohlenhydraten dienen können.[32–35] Die tatsächliche fundamentale Reaktion basiert jedoch auf der Spaltung von Wasser in Sauerstoff, Protonen und Elektronen. Diese Reaktion wird durch den OEC (engl.: Oxygen Evolving Complex) im Photosystem II ermöglicht, ein Membranprotein in den Mitochondrien von Pflanzenzellen. Durch die Einwirkung von Licht auf Antennenkomplexe (Porphyrine) im Photosystem II werden Elektronen angeregt und über ein Redox-Shuttle-System auf das Photosystem I übertragen, an dem die Elektronen und zusätzlich Protonen für die Reaktion $NADP^+ + 2H^+ + e^- \rightarrow NADPH + H^+$ verwendet werden.[32–35] Die angeregten Elektronen in den Antennenkomplexen des Photosystems II hinterlassen positive Ladungen, sogenannte Löcher, welche anschließend durch Elektronen aus dem OEC aufgefüllt werden.[34] Der OEC enthält, stabilisiert von einem Proteingerüst, einen $CaMn_4O_4$-Cluster, welcher durch die flexiblen Oxidationsstufen des Mangans bei der Photosynthese bis zu 4 Elektronen auf die Porphyrine des Photosystems II übertragen kann.[34,35] Dabei werden die Manganionen von +II, +III, +IV und +IV zwischenzeitlich zu +V, +IV, +IV und +IV oxidiert.[34] Dieser hochgeladene Cluster ist dann fähig 2 O^{2-} zu O_2 zu oxidieren, wobei er selbst in seinen Ausgangszustand zurückkehrt.[34,35]

In künstlichen Photokatalysatoren wird die Arbeit des Porphyrins durch Moleküle (z. B. Farbstoffe wie y-Eosin)[36], Metallkomplexe (z. B. $[(Bipyridin)_3Ru]^{2+}$)[9,37] oder Halbleitermaterialien (z. B. TiO_2)[9,38,39] übernommen. In Molekülen wird dabei durch die Absorption eines Photons ein Elektron vom höchsten besetzten Molekülorbital (engl.: HOMO) ins niedrigste unbesetzte Molekülorbital (engl.: LUMO) angeregt.[9] In Metallkomplexen müssen für katalytische Prozesse Elektronen durch die Absorption eines Photons vom Metallzentrum auf die Liganden oder von den Liganden auf das Metallzentrum übertragen werden (Charge-Transfer-Prozesse).[40,41] Übergänge zwischen den d-Orbitalen eines Übergangsmetalls können wegen ihrer Metallzentrierung nicht für katalytische Zwecke genutzt werden, denn dafür ist immer eine Ladungsseparation nötig. In Halbleitermaterialien werden durch die Absorption von Photonen Elektronen aus dem Valenzband ins Leitungsband übertragen, sodass

zwei Ladungsträger gebildet werden die sich in der Regel getrennt voneinander durch den Festkörper bewegen können (genauer in Kap. 1.4).[9,42]

Für die Nutzung in katalytischen Reaktionen müssen die angeregten Elektronen für eine ausreichende Zeit stabilisiert sein, um auf oxidative Moleküle/Substrate, unter Umständen unter Verwendung eines Katalysatormaterials, übertragen zu werden. Den Elektronenmangel füllt der Photokatalysator durch Elektronenaufnahme von oxidierbaren Molekülen/Substraten wieder auf. So können Photokatalysatoren für Oxidations- oder Reduktionsreaktionen des Substrates zum Zielmolekül genutzt werden.[31,42,43]

1.4. Photohalbleiter

Die elektrochemischen Potentiale eines Photohalbleiters werden durch Absorption von Photonen erzeugt. Im einfachsten Fall kann hierbei jeweils ein absorbiertes Photon ein Elektron aus dem Valenzband in das Leitungsband anheben. Ausgehend von einzelnen Atomen mit ihren Atomorbitalen kommt es bei der Bildung eines Moleküls zur Überlappung der Atomorbitale zu Molekülorbitalen mit ihren eigenen Besetzungsenergien und -wahrscheinlichkeiten (siehe Abb. 6). Durch die periodische Anordnung der Atome im Festkörper und die symmetrische Form der Orbitale bezogen auf die Atomkerne, bilden sich in einem Festkörper energetische Bänder aus elektronisch erlaubten Zuständen aus (siehe Abb. 6). Das Valenzband wird durch Überlagerung der besetzten Atomorbitale in einer Verbindung erzeugt, während das Leitungsband aus unbesetzten Atomorbitalen gebildet wird.[23,44–46]

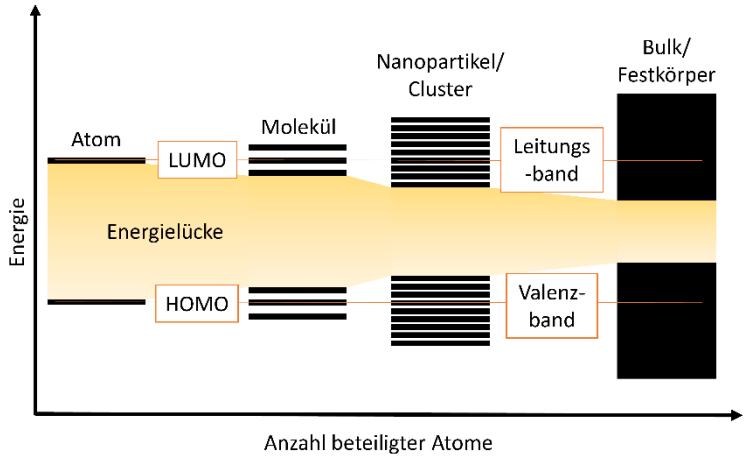

Abb. 6: Schematische Darstellung der Bandbildung durch Überlagerung vieler Atomorbitale bei der Bildung eines Moleküls, zum Molekülverbund, Nanopartikel bis hin zum Festkörpermaterial. Ausgehend von den höchsten besetzten Molekülorbitalen (HOMO) bildet sich das Valenzband, aus den niedrigsten unbesetzten Molekülorbitalen (LUMO) das Leitungsband. Das Leitungs- und Valenzband im Halbleiter trennt eine energetische Lücke aus verbotenen Zuständen.[23,44]

Der energetische Abstand der besetzten, teilbesetzten und unbesetzten Bänder ist entscheidend für die physikalischen und elektronischen Eigenschaften eines Materials. Bei Metallen

überlappen Valenz- und Leitungsband und je nach räumlicher Orientierung und energetischer Lage werden unterschiedliche Leitfähigkeiten beobachtet.[23,47] Isolatoren sind durch eine große energetische Lücke zwischen Valenz- und Leitungsband charakterisiert, welche von Elektronen nicht durch Anregung mit Wärme oder sichtbarem Licht überwunden werden kann. Halbleitermaterialien weisen nur eine kleine Energielücke/Bandlücke zwischen dem Valenz- und Leitungsband auf. Durch thermische oder optische Anregung können Elektronen vom Valenzband in das Leitungsband angeregt werden, wodurch ein sogenanntes Loch im Valenzband, gleichbedeutend mit einer positiven Ladung, gebildet wird.[23,47] Die angeregten Elektronen und resultierenden Löcher werden als Elektron-Loch-Paare (Exzitonen) bezeichnet. Die angeregten Elektronen, aber auch die Löcher im Valenzband sind nicht ortsfest und können sich durch den Kristall bewegen, so dass eine eingeschränkte elektrische Leitfähigkeit auftreten kann. Diese Leitfähigkeit ist dabei abhängig von der räumlichen und energetischen Ausdehnung der Bänder und davon, ob die Löcher oder die Elektronen beweglicher im Festkörper sind. Die Ausdehnung der Bänder beeinflusst außerdem die Stabilität des angeregten Zustandes. Zu unterscheiden sind hier direkte und indirekte Halbleiter. Bei direkten Halbleitern erfolgt die Anregung ohne Impulsübertrag durch das Photon: der Wellenvektor k, welcher die Bewegung des Elektrons beschreibt, bleibt unverändert. Daher ist die Rekombination der Elektron-Loch-Paare ohne zusätzlichem Impuls möglich. Als Folge weisen Anregungen und Rekombinationen in direkten Halbleitern eine sehr hohe Wahrscheinlichkeit und die Ladungsträger eine kurze Halbwertszeit auf. In indirekten Halbleitern sind die Anregung und Rekombination mit einem Impulsübertrag, in der Regel durch Phononen, verbunden. Daher sind Elektronenübergänge in indirekten Halbleitern weniger wahrscheinlich, temperaturabhängig und die angeregten Ladungsträger weisen eine vergleichsweise lange Halbwertszeit auf.[23,47,48]

Die Lebenszeit der Elektron-Loch-Paare ist zusätzlich abhängig von der Defektkonzentration, da jegliche Art von Defekt eine Möglichkeit der Rekombination bietet. Im Umkehrschluss sollten daher hochkristalline Halbleiter gut für eine photokatalytische Anwendung sein. Jedoch sind auch eine große Oberfläche und eine kurze Diffusionsstrecke zur Oberfläche von Vorteil, um die Kontaktfläche zum Substrat groß und die Verweilzeit im Halbleiter gering zu halten. Daher ist stets ein Kompromiss aus großer Oberfläche, kleiner Kristallite, jedoch hoher Kristallinität zu wählen. Eine Möglichkeit, um die Halbwertszeit „künstlich“ zu verlängern, stellen Z-Schema-Halbleiter dar. Hierbei handelt es sich um Komposite oder

eine Wirtstruktur mit unterschiedlich dotierten Bereichen. Die Materialien werden so ausgewählt, dass deren Bandstruktur einen kleinen energetischen Versatz des Leitungs- und Valenzbandes aufweist. Um ihr Potential zu verringern fließen die angeregten Elektronen nun zu Orten im Material mit geringerer Leitungsbandenergie und die Löcher zu Orten mit hoher Valenzbandenergie. Da die Ladungsträger nun lokalisiert und voneinander räumlich getrennt sind, ist eine Rekombination dieser unterdrückt. Die photochemischen Prozesse in einem Halbleiter sind in Abb. 7 schematisch dargestellt.[23,48,49]

Die chemischen Potentiale der Elektron-Loch-Paare sind durch die Potentiale des Valenz- und Leitungsbandes vorgegeben. Diese ändern sich jedoch in der Nähe der Oberfläche durch die geänderten Bedingungen an der Grenzfläche zum umgebenden Medium und dadurch, dass diese Bereiche nicht mehr als kristallin angesehen werden können.[42,48]

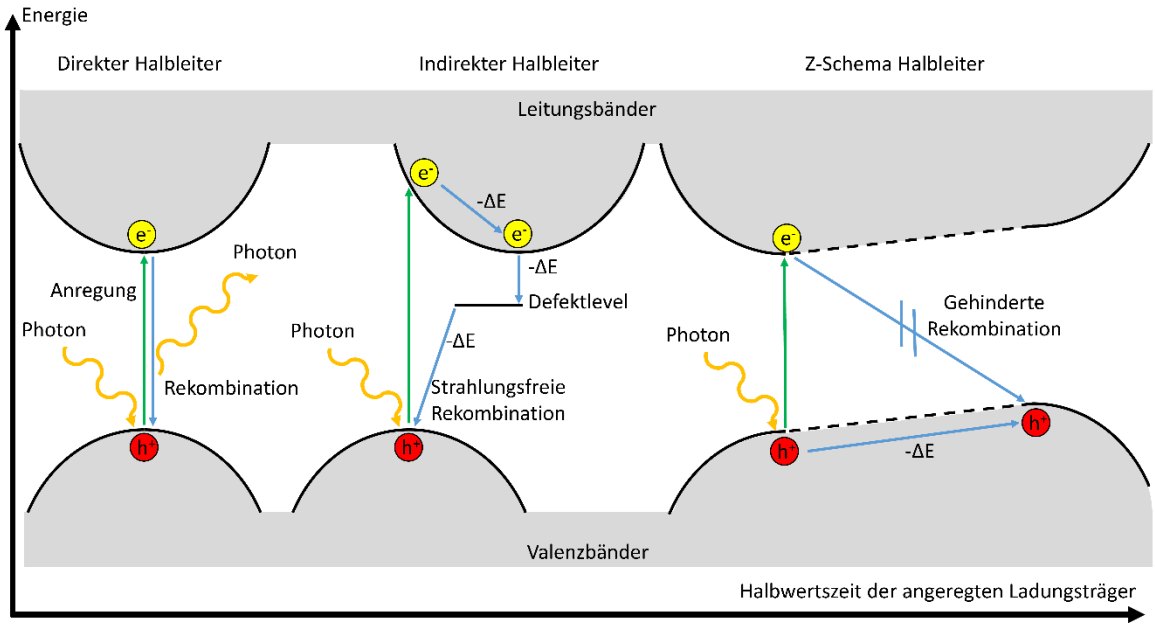

Abb. 7: Schematische Darstellung der photochemischen Prozesse in den Halbleitertypen: Direkter Halbleiter (links), indirekter Halbleiter (mitte) und Z-Schema-Halbleiterverbund (rechts).

Die Potentiale dichter Materialien lassen sich über die Elektronegativität nach Mulliken χ eines Halbleiters M_aX_b abschätzen:

$$\chi(M_aX_b) = (\chi(M)^a\chi(X)^b)^{1/(a+b)} \qquad \text{(Gl.1)}$$

wobei sich die Elektronegativitäten nach Mulliken für die jeweiligen Elemente M und X aus:

$$\chi(M \text{ oder } X) = \frac{A_f + I_1}{2} \qquad \text{(Gl.2)}$$

ergeben, mit der jeweiligen Elektronenaffinität A_f und der ersten Ionisierungsenergie I_1 des Elementes.[50,51]

Die Elektronegativität nach Mulliken χ eines Festkörpers lässt sich gleichsetzen mit der Fermienergie der Verbindung, welche sich bei einem nichtdotierten Halbleiter per Definition in der Mitte zwischen Valenz- und Leitungsband befindet. So ergibt sich die Energie des Leitungsbandes durch:

$$E_{CB} = \chi - \frac{E_g}{2} \qquad \text{(Gl.3)}$$

Und des Valenzbandes:

$$E_{VB} = \chi + \frac{E_g}{2} \qquad \text{(Gl.4)}$$

Mit Kenntnissen über die Größe der Bandlücke lassen sich so z. B. die Potentiale von TiO_2 in der Rutilphase (E_g = 3.0 eV) zu 4.24 V vs. Vakuum (-0.26 V vs. NHE) für das Leitungsband und für das Valenzband 7.24 V vs. Vakuum (2.74 V vs. NHE) abschätzen. Daher ist Rutil prinzipiell gut geeignet für eine photokatalytische Wasserstoffgenerierung oder die Oxidation von Wasser zu O_2 oder reaktiven Sauerstoffspezies.[50,51]

1.5. Photokatalytische Wasserstoffentwicklung

Um die genannten Nachteile der fossilen Energieträger (Kap. 1.1.1.) zu umgehen und einen nachhaltigen und umweltfreundlichen Energieträger zu erhalten, ist das Interesse an der katalytischen Wasserstoffgenerierung in den letzten Jahrzehnten stetig angestiegen.

Drei verschiedene Methoden zur Synthese von Wasserstoff haben sich als zielführend herausgestellt: die Elektrokatalyse, die Photoelektrokatalyse und die Photokatalyse. Die einfachste dieser Methoden ist die Elektrokatalyse. Unter optimalen Bedingungen ist für die Wasserspaltung eine Spannung von 1.23 V vs. NHE nötig, wobei an der Kathode ein Potential von 0 V vs. NHE und an der Anode ein Potential von 1.23 V vs. NHE anliegen muss. Selbst bei der Wahl der besten bekannten Katalysatoren (platiniertes Platin für die Kathode und RuO_2 oder IrO_2 für die Anode) ist aufgrund von Reaktionen an den Grenzflächen zum Elektrolyt und der Limitierung der Ionendiffusion stets mit einem Überpotential von einigen Millivolt zu rechnen.[6,9,52]

Alternativ zur Wasseroxidation kann zur Senkung der benötigten Gesamtenergie auch eine oxidative Synthese an der Anode erfolgen. Bei dieser Oxidation kann es sich um organische Substanzen wie z.B. Alkohole oder Amine handeln, die im Prozess zu wertvolleren oxidierten Substanzen umgesetzt werden. Da katalytisch entwickelter Sauerstoff keinen kommerziellen Nutzen hat, wäre durch eine derartig gekoppelte Elektrosynthese eine simultane Wertschöpfung (Wasserstoff und organische Produkte) möglich.[53,54]

In der Photoelektrokatalyse werden zusätzlich zum Anlegen einer Spannung die Elektroden, welche teilweise aus einem Photohalbleiter bestehen, mit Licht wie z. B. Sonnenlicht bestrahlt. Dadurch sinkt die für die Wasserspaltung benötigte elektrische Spannung, weil das Halbleitermaterial durch Photonenabsorption eine zusätzliche Spannung generiert. Bei der Photokatalyse wird die elektrische Spannung vollständig durch Lichtabsorption hervorgerufene Potentiale eines Photohalbleiters ersetzt. Verwendet man statt des Halbleitermaterials die Photoabsorption einer gelösten molekularen Verbindung oder einer Koordinationsverbindung spricht man von photosensitisierten Systemen.[9,52]

Die vorliegende Arbeit befasst sich mit der heterogenen Photokatalyse unter Verwendung von Halbleitermaterialien. Daher soll im Folgenden nur auf diese Form der Wasserstofferzeugung eingegangen werden.

Eine photokatalytische Wasserstofferzeugung lässt sich zum Beispiel mit Titanoxiden erreichen (vgl. Abb. 8). TiO_2 ist jedoch schlecht geeignet für die katalytische Reduktion von Protonen zu Wasserstoff, so dass Kokatalysatoren wie z. B. Platin oder Palladium benötigt werden. Diese Elemente sind jedoch teuer und weisen eine geringe Häufigkeit in der Erdkruste auf. Daher bietet es sich an Alternativen zu untersuchen, die eine ähnlich gute Fähigkeit zur Wasserstoffentwicklung aufweisen, jedoch besser verfügbare und günstigere Elemente enthalten.[9,52]

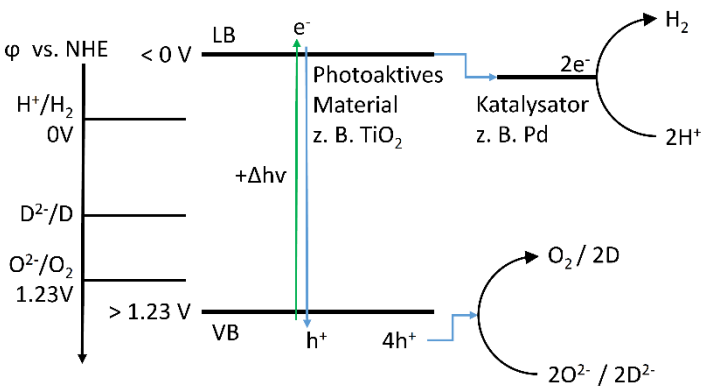

Abb. 8: Schematische Darstellung der photokatalytischen Wasserstoffgenerierung mit einem heterogenen Katalysator bestehend aus einem Halbleitermaterial und einem Kokatalysator. Die notwendigen Elektronen können dabei von organischen Elektronendonoren (D^{2-}) oder O^{2-} Ionen zurückgewonnen werden.

Ein weiteres Problem von TiO_2 ist die relativ große Bandlücke.[55,56] Diese lässt sich durch Dotieren, Substituieren oder durch Veränderung der Mikrostruktur modifizieren. Hierbei zeigte sich vor allem die Dotierung mit Stickstoff und Phosphor als einfach und zielführend. Allerding kann die Bandlücke nur in kleinem Rahmen verändert werden, sodass nach guten Alternativen für TiO_2 gesucht wird (siehe Tab. 1). Jedes Alternativmaterial bringt jedoch auch eigene Probleme mit sich. Die Verbindung CdS weist z.B. äußerst gute Bandpositionen (E_g = 2.4 eV, LB = -0.52 V vs. NHE, VB = 1.88 V vs. NHE)[51] auf, jedoch kommt es durch die hohen Potentiale während der Verwendung in der Photokatalyse zur Fotokorrosion.[9]

Tab. 1: Eine kleine Auswahl an Halbleitermaterialien die wie TiO_2 verwendbar für eine photokatalytische Wasserstoffentwicklung sind.

Halb-leiter	Kokatalysa-tor [gew.-%]	H_2-Entwick-lungs-rate [$\mu mol \cdot g^{-1} \cdot h^{-1}$]	Opferreagenz	Bestrahlung	Lit.
TiO_2	0.5 MoS_2 0.5 Graphen	460 371.25	25 % Ethanol	350 W Xe-Bogenlampe	[57]
		90			
	5 Pt	1533	50 % Methanol	500 W Xe-Bogenlampe	[38]
	5 Pd	7333			
ZnO		62.5	7 % Glycerol	Simuliertes Sonnenlicht	[58]
ZnS	40 ZnO	388	7 % Glycerol	Simuliertes Sonnenlicht	[58]
Ta_2O_5	5 NiO	915	9 % Methanol	300 W Hg-Hochdruckdampflampe	[59]
$KNbO_3$		100	20 % Methanol	350 W Hg-Hochdruckdampflampe	[60]
$SrTiO_3$	0.5 Pt	6000	42 % Methanol	UV unspezifiziert	[61]
$NaTaO_3$		36750	20 % Methanol	350 W Hg-Hochdruckdampflampe	[60]
CdS	0.5 Pt	11500	10 % Milchsäure-Lsg.	350 W Xe-Bogenlampe >420 nm	[62]
	0.5 Pt +1 Graphen	56000	10 % Milchsäure-Lsg.	350 W Xe-Bogenlampe >420 nm	[62]
C_3N_4	30 CdS +1 Pt	173	25 % Methanol	300 W Xe-Bogenlampe >400 nm	[63]

Da es schwierig ist in einem System aus Halbleitermaterialien, Katalysatoren und Katalysebedingungen einen Zusammenhang zur jeweilig beobachteten katalytischen Aktivität herzustellen, bietet es sich an das Katalysesystem zu vereinfachen. Es ist unter anderem einfacher sich bei der Forschung auf die Kinetik der Wasserstoffentwicklungskatalyse zu beschränken und die Oxidationsreaktion durch Wahl geeigneter sogenannter Opferreagenzien (engl.: Sacrificial Agents) zu vereinfachen (z. B. Amine oder Alkohole als Elektronendonoren). Andersherum sollte man die Wasserstoffentwicklung für die Untersuchung der Sauerstoffentwicklung unterdrücken, z. B. mit einer sauren $Fe_2(SO_4)_3$ Lösung als Opferreagenz.[9]

Die photokatalytische Wasserstoffentwicklung birgt daher noch ein großes Forschungspotential bevor es zu einer großtechnischen Anwendung kommen kann.

1.6. Zersetzung organischer Schadstoffe

Um die Belastung natürlicher Gewässer durch organische Schadstoffe zu verringern ist es möglich Abwässer durch eine photokatalytische Prozessierung zu reinigen. Es ist auch möglich solche Abwässer durch z. B. Elektrolyse oder Thermolyse zu reinigen, jedoch benötigen diese Prozesse sehr viel Energie. Eine photokatalytische Reinigung, oder auch photokatalytische Degradation von Schadstoffen, benötigt im Idealfall nur Sonnenlicht (Siehe Abb. 9). Als Photokatalysatoren können Halbleitermaterialien mit einer großen energetischen Bandlücke von 2.85 eV und einem Valenzbandpotential von 2.85 V vs. NHE eingesetzt werden. Diese Eigenschaften sind notwendig, um Wasser- oder Sauerstoffmoleküle zu reaktiven Sauerstoffspezies (ROS, reactive oxygen species) wie $HO^{\bullet}$ (2.85 V vs. NHE), H_2O_2 (1.76 V vs. NHE), O_3 (2.08 V vs. NHE), $O^{\bullet}$ (2.42 V vs. NHE) zu oxidieren.[23] Organische Moleküle werden durch den chemischen Angriff dieser Sauerstoffspezies oxidiert. Da auch C-C und C-H-Bindungen durch den Angriff gebrochen werden können, ist eine Oxidation bis zur Kohlensäure/Kohlendioxid und H_2O möglich. Zurück bleiben weniger giftige oder weniger persistente Substanzen wie Halogenide, NO_x und SO_x.[20,64–67]

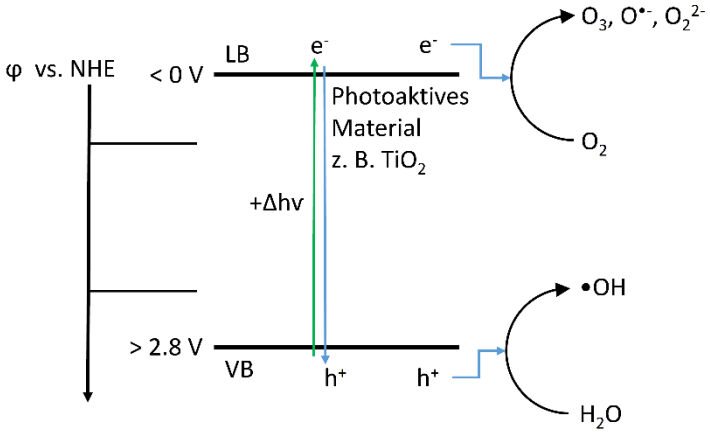

Abb. 9: Schematische Darstellung der photokatalytischen Abwasserreinigung mit einem heterogenen Katalysator bzw. Halbleitermaterial welches die angeregten Ladungsträger für die Generierung von reaktiven Sauerstoffspezies nutzen kann. Die reaktiven Sauerstoffspezies können in folgenden Reaktionen organische Substanzen im umgebenden Medium zu CO_2, H_2O etc. oxidieren bzw. zu weniger gefährlichen Substanzen umsetzen.

Persistente organische Schadstoffe (POPs), wie z. B. polyhalogenierte Alkansäuren sind nur in sehr geringen Konzentrationen in Wasser löslich und häufig nur durch aufwändige Methoden (z. B. HPLC/MS) in wässriger Lösung quantifizierbar. Daher verwendet man für

photokatalytische Degradationsexperimente in der Regel gut lösliche und einfach quantifizierbare Testsubstanzen wie z. B. Farbstoffe oder halogenierte Phenole. Deren Abbau lässt sich durch die vorhandenen π–Systeme vergleichsweise einfach durch zeitaufgelöste Messungen von UV/Vis-Spektren verfolgen, sodass nur die Endprodukte durch andere analytische Methoden nachgewiesen werden müssen.[66,68,69]

Typische Katalysatoren, die in Degradationsstudien hohe Effizienz aufweisen sind, TiO_2 und ZnO. Wie in der photokatalytischen Wasserstoffentwicklung (Kap. 1.5) sind diese Materialien jedoch nur fähig UV-Licht für die Photokatalyse in chemische Redox-Potentiale umzusetzen. Daher ist auch hier eine Modifizierung oder Änderung des Materials für eine Effizienzsteigerung nötig. Allerdings ist man hauptsächlich auf Oxide beschränkt, welche durch die hohen chemischen Potentiale nicht durch Photokorrosion desaktiviert werden können. Andere vieldiskutierte Materialien sind in Tab. 2 aufgelistet.[21,66,70,71]

Tab. 2: Beobachtete Aktivität verschiedener Photokatalysatoren zur Degradation diverser organischer Substanzen bei Bestrahlung durch die angegebenen Lichtquellen.

Katalysator	Organik	Reaktionsrate [min^{-1}]	Bestrahlung	Lit.
Fe_2O_3	4-Chlorphenol	5.55 *	Simuliertes Sonnenlicht	[72]
SnO_2	Rhodamin B Methylenblau	0.0096 0.0438	175 W Hg-Hochdruckdampflampe	[73]
ZnO	Methylenblau	0.0337	8 W LED 254 nm	[74]
	Bisphenol A	0.001*	300 W Xe-Bogenlampe	[75]
	2,4-Dichlorphenol	0.004*	55 W Fluoreszenzlampe	[76]
TiO_2	Methylenblau Methylorange	0.025* 0.02*	30 W Hg-Hochdruckdampflampe	[77]
	4-Chlorphenol	2.96*	Simuliertes Sonnenlicht	[72]
	Bisphenol A	0.0021*	300 W Xe-Bogenlampe	[75]
$LaFeO_3$	Rhodamin B	0.0085*	150 W Lampe unspezifiziert >400 nm	[78]
$LaCoO_3$	Methylenblau Methylorange	0.009* 0.009*	30 W Hg-Hochdruckdampflampe	[77]
$BiVO_4$	Rhodamin B	0.233	500 W Xe-Bogenlampe >420 nm	[79]

*Angegebene Werte sind umgerechnet zu einem repräsentativen Wert mit der Einheit min^{-1}.

1.7. Spinelle

Die Spinelle mit der allgemeinen Summenformel AB_2X_4 (A, B: Kationen mit Gesamtoxidationsstufe +8 und X: Anionen mit Gesamtoxidationsstufe -8) zeichnen sich durch ihre große Zusammensetzungsvielfalt und meistens hohe chemische und thermische Stabilität aus. Spinelle sind mit den Kationen Li^+, Na^+, Mg^{2+}, Al^{3+}, Si^{4+}, Ti^{4+}, $V^{3+/4+/5+}$, Cr^{3+}, $Mn^{2+/3+/4+}$, $Fe^{2+/3+}$,

$Co^{2+/3+}$, $Ni^{2+/3+}$, $Cu^{1+/2+}$, Zn^{2+}, Ga^{3+}, Ge^{4+}, Mo^{6+}, Ag^{+}, Cd^{2+}, In^{3+}, Sn^{4+} und W^{6+}, sowie den Anionen O^{2-}, S^{2-}, Se^{2-} und Te^{2-} bekannt. Allerdings lassen sich noch weitere Elemente durch Teilsubstitution einbringen. In der Struktur bilden die Anionen eine kubisch-dichteste Kugelpackung und die Kationen besetzen die Hälfte der Oktaederlücken und ein Achtel der Tetraederlücken (kubische Raumgruppe $Fd\bar{3}m$) (vgl. Abb. 10). Beim Namensgeber $MgAl_2O_4$ besetzen die Mg^{2+}-Ionen die Tetraederlücken und die Al^{3+}-Ionen die Oktaederlücken. Neben dieser normalen Besetzung der Plätze durch die Kationen kann sich ein Teil der A-Ionen auf Oktaederplätzen befinden (partiell inverser Spinell) oder alle A-Ionen haben den Platz gewechselt (inverser Spinell).[23,80,81]

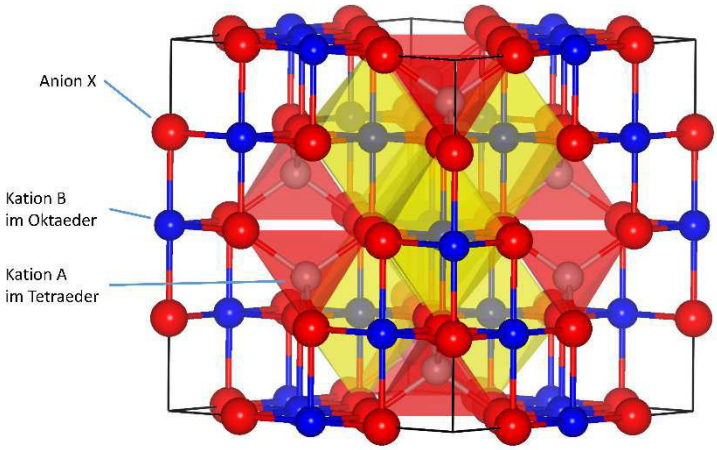

Abb. 10: Schematische Darstellung der Elementarzelle der normalen Spinellstruktur mit der Summenformel AB_2X_4. Vollständige Koordinationssphären der Oktaeder BX_6 sind gelb und vollständige Koordinationssphären der Tetraeder AX_4 rot schattiert.[80]

Mögliche Kombinationen an Kationoxidationszahlen sind mit abnehmender Häufigkeit 2 x +III und 1 x +II; 2 x +II und 1 x +IV; 1 x +I, 1 x +III und 1 x +IV; 1 x +I, 1 x +II und 1 x +V; sowie 2 x +I und 1 x +VI. Die Präferenz der Kationen für eine oktaedrische bzw. tetraedrische Umgebung führt dazu, dass nicht alle Kombinationen mit den oben genannten Kationen zur Ausbildung der Spinellstruktur unter normalen Bedingungen führen. So ist z.B. Zn_2SiO_4 nur bei hohen Drücken in der Spinellstruktur bekannt, während Mg_2SiO_4 und Fe_2SiO_4 unter Normalbedingungen in der Spinellstruktur kristallisieren. Grund dafür ist die bevorzugte oktaedrische Sauerstoffkoordination von Mg^{2+}- und Fe^{2+}-Ionen, während Zn^{2+} und Si^{4+} bevorzugt tetraedrisch von Sauerstoff umgeben sind.[23]

Die Kationen Mn^{3+}, (Ni^{2+}) und Cu^{2+} können leicht eine Verzerrung der Struktur durch den Jahn-Teller-Effekt bewirken.[23] Bei Berücksichtigung dieser Besonderheiten lässt sich eine Vielzahl von Verbindungen mit speziellen Eigenschaften herstellen. Dabei erlaubt die gezielte Mischung auch ein „Design“ der gewünschten chemischen und physikalischen Eigenschaften.

1.8. Polyoxothiostannate

In den Strukturen von Thiostannaten werden überwiegend SnS_4-Tetraeder oder SnS_3-trigonale-Pyramiden als primäre Baueinheiten beobachtet, wobei Sn(IV) die dominante Oxidationsstufe darstellt und Sn(II) deutlich seltener beobachtet wird. In einigen Thiostannaten liegen auch SnS_6-Oktaeder oder SnS_5-trigonale Bipyramiden vor. Diese primären Baueinheiten werden oft zu höher kondensierten Baueinheiten verknüpft, so dass 0D oder 1D Motive, und 2D bzw. 3D Netzwerke ausgebildet werden.[23,82–88]

Im Gegensatz zur Thiostannatchemie ist die Chemie der Oxostannate weniger vielfältig, aber in Analogie zu Thiostannaten werden auch in diesen Verbindungen SnO_x-Baugruppen mit x = 3, 4, 5 und 6 beobachtet.[23,89–91]

Die Oxothiostannate haben vergleichbare Strukturen wie die der Thiostannate mit der Ausnahme, dass erst wenige Vertreter dieser Substanzklasse bekannt sind. Einige Beispiele von Oxothiostannaten sind $[Sn_4Cl_4OS_5(S_3)]^{2-}$[92], $[Sn_8(Thiophenol)_6O_4S_{12}]^{6-}$[93] $[Sn_8Cl_6(\mu_2\text{-}OH)_2(\mu_4\text{-}O)_2S_{12}]^{8-}$[94], $[Sn_{10}O_4S_{20}]^{8-}$[95–97] und $[Sn_{10}Cl_4(\mu_4\text{-}O)_4(\mu_3\text{-}S)_4(\mu_2\text{-}S)_{12}]^{8-}$[94]. Bis auf die Strukturen von $[Sn_8(Thiophenol)_6O_4S_{12}]^{6-}$ und $[Sn_8Cl_6(\mu_2\text{-}OH)_2(\mu_4\text{-}O)_2S_{12}]^{8-}$ werden die Cluster aus eckenverknüpften Tetraedern gebildet, welche zu größeren Tetraedern kondensiert sind (so genannte Supertetraeder). In den Strukturen der beiden Ausnahmen sind SnX_6-Oktaeder (mit X = S, O) vorhanden, welche Baueinheiten aus SnX_4-Tetraedern (mit X = S, O, Cl) oder quadratischen $SnOS_4$-Pyramiden verknüpfen.

Oxothiostannate sollten die Eigenschaften von Thiostannaten, Zinnsulfiden und Oxostannaten in synergistischer Weise kombinieren, so dass im Vergleich zu den ‚reinen' Verbindungen unterschiedliche katalytische Eigenschaften vorliegen sollten.[98–110]

2. Methoden zur Charakterisierung

2.1. Photokatalysetests

Um Materialien auf ihre photokatalytischen Eigenschaften zu untersuchen muss zunächst überlegt werden, welche Rolle die Substanz in der Katalyse einnehmen soll. So kann das Material die photoaktive Komponente sein, sodass zusätzlich ein Kokatalysator benötigt wird. Handelt es sich bei dem Material um einen Katalysator ist ein photoaktives Material nötig welches die Energie für die Katalyse liefern muss. Ist das Material fähig Photonen zu absorbieren und energiereiche Ladungsträger zu generieren, sowie diese in einem katalytischen Prozess zu nutzen sind keine Hilfsmittel notwendig.

Für die katalytische Wirkung eines Materials ist dessen elektrochemisches Potential wichtig: es muss z. B. höher liegen als das eines erzeugten Produktes in einer Reduktionsreaktion, um die Reaktion vorantreiben zu können (vgl. Platin und Wasserstoff).[23]

Um entscheiden zu können für welche katalytischen Prozesse ein Halbleitermaterial geeignet ist, ist es hilfreich die ungefähren energetischen Niveaus des Leitungsbandes oder Valenzbandes abzuschätzen. Diese lassen sich über die Mullikenpotentiale abschätzen[50,51] und durch elektrochemische Untersuchungen (Mott-Schottky-Plot)[111] oder Photoelektronenspektroskopie (UPS/XPS)[112] ermitteln. Da letztere Methoden aufwändig und die Mullikenpotentiale nur für dicht gepackte Festkörper als Näherung gültig sind, bieten sich auch Untersuchungen nach dem Trial-and-Error-Prinzip an. In einem solchen Fall lassen sich jedoch keine Rückschlüsse ziehen, warum das Material nicht katalytisch aktiv ist.

Eignet sich ein Halbleitermaterial für einen Katalyseprozess ist es wichtig die optische Bandlücke zu bestimmen, da diese durch das eingestrahlte Licht überwunden werden muss. Ist die Energie des eingestrahlten Lichtes zu hoch kann es jedoch auch zu Photokorrosionsprozessen[9,74] kommen, welche die Effizienz des Materials vermindern.

Zusätzlich muss der Absorptionskoeffizient des Halbleitermaterials berücksichtigt werden, da eine hohe Absorptionsstärke die Eindringtiefe des Lichtes in eine Dispersion verringert und somit die photokatalytische Aktivität limitieren kann. Schlussendlich ist auch wichtig, dass der Katalysator unter den Reaktionsbedingungen stabil ist damit Nebenreaktionen, die eine Veränderung oder Inaktivierung des Katalysatormaterials verursachen, nicht die Kinetik des Katalyseprozesses beeinflussen.

Besonders wichtig ist auch, dass die Prozesstemperatur, der Druck (besonders bei Reaktionen in denen Gase auftreten) und die Bestrahlungsintensität während der katalytischen Reaktion konstant gehalten werden, um die Kinetik der Reaktion nicht zu beeinflussen.

2.1.1. Wasserstoffgenerierung mit Halbleitermaterialien

Um die verwendeten Halbleitermaterialien auf ihre photokatalytischen Eigenschaften zu untersuchen, wurden immer Konzentrationen von 0.2-1 mg/mL des Materials in Dispersion gewählt um eine Vergleichbarkeit mit Literaturdaten zu ermöglichen. Durchgeführt wurden die Untersuchungen in einem sogenannten Gasmesssystem (siehe Abb. 11). Dieses besteht im Wesentlichen aus einem abgeschlossen Gasvolumen, welches mit Hilfe eines Drucksensors und einer automatischen Bürette mit steuerbarem Schrittmotor isobar gehalten wird. Da schwankende Temperatureinflüsse von außen den Druck innerhalb der Apparatur stark beeinflussen, wird die gesamte Apparatur durch einen Glaskühlmantel isotherm gehalten. Die Veränderung des Volumens bei konstantem Druck und Temperatur wird dann in Abhängigkeit von der Zeit aufgezeichnet. Auf diese Weise lassen sich Reaktionen, bei denen es zu einem Gasumsatz kommt, auf ihre Kinetik untersuchen.

Um nun eine photokatalytische Wasserstoffgenerierung zu untersuchen, wird eine Dispersion des Katalysators in einer Reaktionsmischung (z.B. wässrige Ethanollösung) in den Kühlmantelkolben gefüllt. Um einen Einfluss des Luftsauerstoffs und Gasen wie CO_2 auf die Reaktion zu verhindern, muss die Luft in der Apparatur durch ein Inertgas (z.B. Argon) ersetzt werden. Daher bietet es sich an die Dispersion erst mit Argon zu spülen und dann über Spritzen in die mit Argon geflutete Apparatur einzubringen. Sobald sich ein konstanter Druck eingestellt hat, kann die Aufzeichnung der Volumenänderung beginnen und die Bestrahlung mit einer Lichtquelle (z.B. Xe-Bogenlampe mit UV-Filter) gestartet werden. Nach Ablauf der Reaktionszeit muss überprüft werden, ob es sich bei dem entwickelten Gas tatsächlich um Wasserstoff handelt. Dazu wird über ein Septum mit einer Gasspritze eine Probenmenge des Gasvolumens entnommen und mittels Gaschromatografie untersucht. Erfolgt eine Quantifizierung mittels Gaschromatografie, kann auch die Menge an entwickeltem Wasserstoff bestimmt durch den Gaschromatographen mit der Volumenentwicklung in der Apparatur verglichen werden.

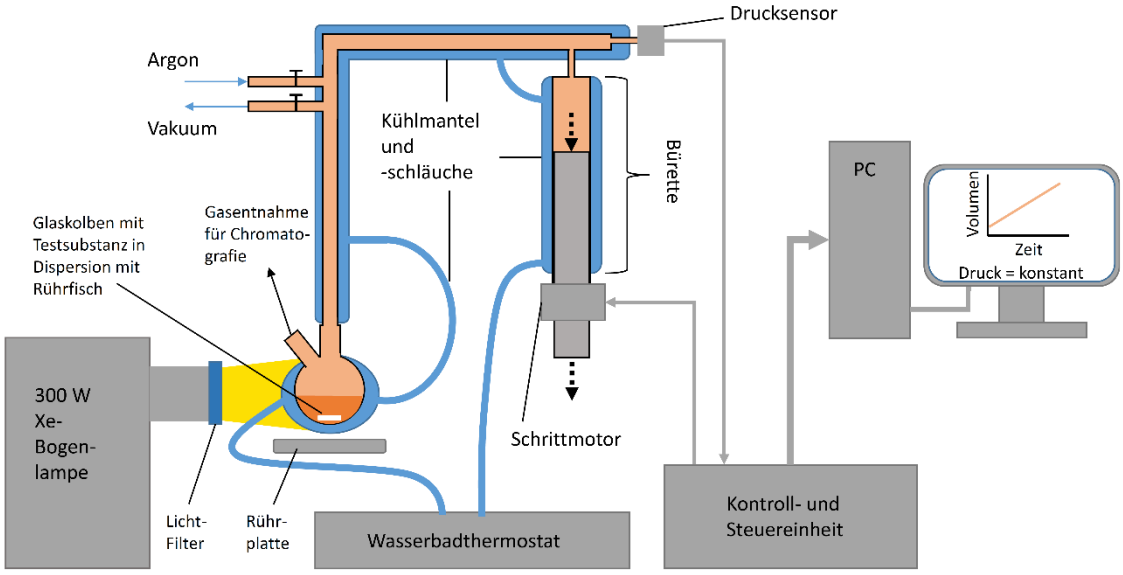

Abb. 11: Schematische Darstellung der Gasmessapparatur zur Untersuchung der photokatalytischen Wasserstoffgenerierung. In einem geschlossenen, thermostatierten System erzeugt der entwickelte Wasserstoff eine Druckerhöhung, welche durch eine automatische Bürette korrigiert wird. Aufgezeichnet wird der Verfahrweg der Bürette.

2.1.2. Wasserstoffgenerierung mit Photosensibilisator

Möchte man ein Material auf eine katalytische Wasserstoffgenerierung untersuchen welches keine adäquate Bandlücke für einen photokatalytischen Prozess aufweist, muss ein Photosensibilisator hinzugefügt werden. Diese sind in der Regel organische Farbstoffe oder Übergangsmetallkoordinationsverbindungen, welche einen $\pi \rightarrow \pi^*$ oder Chargetransfer-Übergang im gewünschten Wellenlängenbereich aufweisen.[9,37] Nach Anregung durch Photonen mit ausreichender Energie kann der Photosensibilisator ein angeregtes Elektron auf den Katalysator übertragen, welches dann für die Wasserstoffgenerierung genutzt werden kann. Der oxidierte Sensibilisator wird durch ein Elektronendonormolekül (z. B. Opferreagenz) regeneriert. Der Photosensibilisator kann wie in Kap. 2.1.1. beschrieben mit der Dispersion in das Gasmesssystem eingebracht werden. Zu berücksichtigen ist jedoch, dass Photosensibilisatoren häufig photolabil sind und daher geeignete Lichtfilter eingesetzt werden müssen, um das Eindringen höherenergetischer Photonen in die Reaktionslösung zu verhindern.

2.1.3. Zersetzung gelöster organischer Verbindungen

Die photokatalytische Degradation gelöster organischer Substanzen benötigt nur ein thermostatiertes Glasgefäß und eine geeignete Lichtquelle (siehe Abb. 12). Die Quantifizierung

der Substanz, die während oder nach der Reaktion gebildet wird, ist dagegen aufwändiger. Üblich ist eine Quantifizierung mittels UV/Vis-Spektroskopie, Massenspektrometrie oder Chromatografie. Im Vergleich zur UV/Vis-Spektroskopie ermöglichen die Chromatografie und Massenspektroskopie auch eine Quantifizierung etwaiger Abbauprodukte, jedoch sind diese analytischen Techniken bezüglich des Reaktionsgemisches eingeschränkt oder erfordern eine umfangreiche Probenvorbereitung nach Entnahme aus dem Reaktionskolben. Der Vorteil der UV/Vis-Spektroskopie ist dagegen die einfache und schnelle Durchführung. Es muss nur darauf geachtet werden, dass die zu detektierende Substanz einen elektronischen Übergang (z.B. π-System) aufweist, welcher *ex-situ* oder auch *in-situ* detektiert werden kann. Der Nachteil ist jedoch, dass die Abbauprodukte gängiger Testmoleküle in der Regel keine Absorption im UV/Vis-Bereich aufweisen. Daher sollte stets mit Chromatografie oder Massenspektrometrie überprüft werden, zu welchen Abbauprodukten die Zersetzung der organischen Moleküle geführt hat. Ein weiterer Nachteil ist die mögliche überlagerte Photoresponsivität des Halbleitermaterials mit dem organischen Molekül, sodass wechselseitige Beeinflussungen nicht immer ausgeschlossen werden können.[69,113] Am Ende einer Untersuchung wird ein Konzentrations-Zeit-Profil der Degradation des organischen Moleküls erhalten, welches mit den üblichen Kinetikmodellen ausgewertet werden kann.

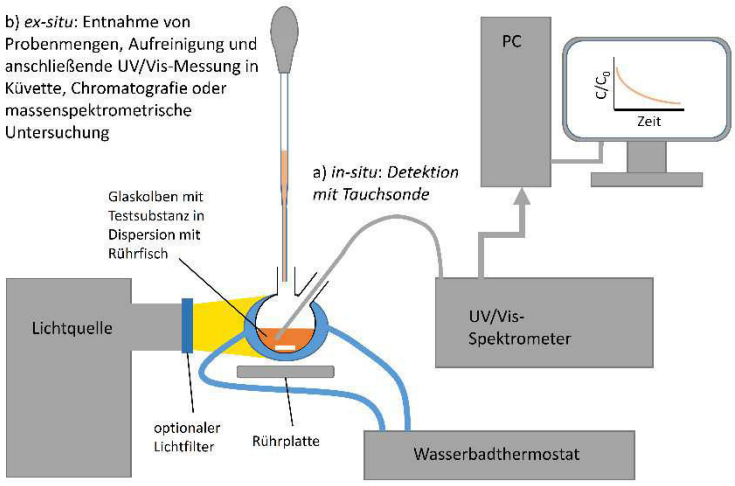

Abb. 12: Schematische Darstellung des Messaufbaus für die Untersuchung einer photokatalytischen Zersetzungsreaktion organischer Substanzen. In einem thermostatierten Glaskolben befindet sich der Katalysator in Dispersion in einer wässrigen Lösung einer organischen Substanz. Während der Bestrahlung kann *in-situ* mit einer UV/Vis-Tauchsonde oder *ex-situ* mit verschiedenen Techniken ein Konzentrations-Zeit-Profil bestimmt werden.

2.2. Actinometrie

Um eine gute Vergleichbarkeit der experimentellen Photokatalysedaten mit Literaturdaten zu erzielen, ist es nötig die für die Photokatalyse verwendeten Photonen zu quantifizieren.

Am einfachsten ist dies durch Verwendung eines Photometers. Jedoch ist mit diesem der Einfluss der verwendeten Glasapparatur und umgebender Bauteile (z.B.: spiegelnde Metalloberflächen) nur schwer zu quantifizieren. Der tatsächliche Photonenfluss im Reaktionskolben lässt sich mit chemischen Actinometern bestimmen. Diese sind stets auf gewisse Wellenlängenbereiche limitiert, sodass ein geeignetes Actinometer für den relevanten Wellenlängenbereich ausgewählt werden muss. Für den Wellenlängenbereich 250 – 500 nm, der übliche Wellenlängenbereich für photokatalytische Wasserstoffentwicklung und Degradation organischer Substanzen, ist $K_3[Fe^{III}(C_2O_4)_3]\cdot 3H_2O$ als Actinometer anwendbar.[114,115] Fe^{III} gelöst in einer schwefelsauren Lösung lässt sich mit Photonen leicht zu Fe^{II} reduzieren, während die Oxalatanionen oxidiert werden. Da diese Photoreduktionsreaktion im genannten Wellenlängenbereich eine Photoneneffizienz von ~1 aufweist, ist die Menge an gebildeten Fe^{II}-Ionen gleich der Anzahl an Photonen ($250\ nm < \lambda < 500\ nm$). Die Durchführung der Actinometrie ist durch die IUPAC standardisiert worden.[116]

3. Veröffentlichungen

3.1. „The Hazardous Origin of Photocatalytic Activity of $ZnCr_2O_4$“

$ZnCr_2O_4$ kommt in der Natur als Mineral Zinkchromit vor. Eine besonders einfache Synthese von $ZnCr_2O_4$ gelingt mit dem Precursor $NH_4Zn(CrO_4)_2 \cdot 2NH_3$, welcher sich bei moderaten Temperaturen von ca. 350 °C zu $ZnCr_2O_4$ zersetzen lässt. Die exakte Stöchiometrie des kristallinen Precursors führt zur Bildung von besonders reinem $ZnCr_2O_4$. In Abhängigkeit von der Zersetzungstemperatur werden Nanoteilchen zwischen 2 und 45 nm erhalten. Eine detaillierte Strukturanalyse belegt, dass die Stapelfehlerwahrscheinlichkeit bei den kleinsten Teilchen am größten ist und mit zunehmender Teilchengröße abnimmt. Die spezifische Oberfläche ist bei den kleinsten Teilchen am größten. Die Ergebnisse der Analyse der Pulverdiffraktogramme wird mit HR-TEM-Untersuchungen bestätigt. Photokatalytische Experimente (Photo-Fentonprozess) zur Degradation von γ-Eosin als Modellmolekül ergeben, dass die kleinsten Teilchen die höchste katalytische Aktivität aufweisen. Jedoch zeigte sich, dass bei den photokatalytischen Reaktionen geringe Mengen an CrO_4^{2-}-Anionen gebildet werden. Diese Anionen werden durch Photokorrosion gebildet und ergänzende Experimente belegen, dass nicht $ZnCr_2O_4$ der aktive Katalysator ist, sondern die CrO_4^{2-}-Anionen. Diese Anionen sind kanzerogen und daher ist zumindest $ZnCr_2O_4$ nicht als Katalysator für die photokatalytische Degradation organischer Moleküle geeignet. Mit MALDI-TOF Experimenten konnte der Degradationsmechanismus von γ-Eosin aufgeklärt werden.

Reprinted with permission from M. Poschmann, U. Schürmann, W. Bensch and L. Kienle, The Hazardous Origin of Photocatalytic Activity of $ZnCr_2O_4$, *Z. Anorg. Allg. Chem.*, **2018**, 644, 564-573. doi:10.1002/zaac.201800072.

Journal of Inorganic and General Chemistry
ZAAC
Zeitschrift für anorganische und allgemeine Chemie
DOI: 10.1002/zaac.201800072
ARTICLE

The Hazardous Origin of Photocatalytic Activity of $ZnCr_2O_4$

Michael Poschmann,[a] Ulrich Schürmann,[b] Wolfgang Bensch,*[a] and Lorenz Kienle[b]

Abstract. The $ZnCr_2O_4$ catalysts are synthesized by thermal decomposition of $(NH_4)_2[Zn(NH_3)_2(CrO_4)_2]$ and materials with high surface areas and particle sizes in the nano regime are obtained. A special structural feature of the materials are stacking faults with densities strongly depending on the synthesis temperature, i.e. the lower the temperature the larger the number of stacking faults. The catalyst prepared at the lowest decomposition temperature exhibiting the smallest particle size shows the highest catalytic activity in the photocatalytic degradation of y-Eosin in a photo-Fenton process. The results of different analytic methods demonstrate that the high catalytic activity is directly correlated with CrO_4^{2-} anions generated via photo-oxidation of the catalyst. Therefore, $ZnCr_2O_4$ cannot be regarded as an environmental friendly catalyst for advanced photocatalytic oxidation processes.

Introduction

Toxic organic compounds in waste water of industry and common households are a widely known hazard for the environment. The Environmental Protection Agency (EPA) of the United States of America published 2009 a report on water quality of US bays and estuaries. This report stated an impairment related to the area of 3.6% with polychlorinated biphenyls, pesticides, and other toxic organics in the year 2004.[1] As a result of such pollution these contaminants accumulate in aquatic life. An examination of the environmental agency of Germany (UBA) from 1994 to 2003 showed concentrations of polychlorinated dibenzodioxines and dibenzofuranes of 1.31 ng·kg^{-1} in fish and mussels.[2] Several probes (> 10%) of this evaluation exceeded even the critical value for these chemicals assigned by the European Union (4 ng·kg^{-1}).[2]

A possible method to reduce the concentration of persistent organic pollutants (POP's) in waste water is the photocatalytic degradation of such materials. Well-known catalysts for this application are TiO_2[3–15] and ZnO.[5,16,17] Less common degradation catalysts are perovskites (especially titanates, niobates, ferrites, and tantalates)[18–23] and iron oxides like Fe_2O_3[14,24] or spinels[25–27]. A drawback of TiO_2 and ZnO are the large optical bandgaps requiring light in the UV range to be catalytically active.[8,9,11,12,14,15,18,28] On the other hand, both compounds show high stability, good catalytic activity and they are inexpensive. A smaller optical bandgap would allow absorption of photons with energy in the visible light range enabling higher photon efficiency. Therefore, excessive research is ongoing in the field of bandgap engineering to increase the amount of photons absorbed from the solar spectrum. Different synthetic approaches are applied to obtain materials with a smaller bandgap like successive doping,[8,11,14,15,18,28] morphology modification,[8,11,13] (e.g. nanotubes etc.) or by deposition on support materials.[14,17]

At the surface of the photo-catalyst e^-/h^+ pairs are able to produce $OH^\bullet$, $O^\bullet$, O_3, and H_2O_2 from H_2O/O_2.[5] The minimum energy for the generation of these species is given by the standard electrode potentials of 2.85, 2.42, 2.08, and 1.76 V, respectively, vs. RHE at pH = 0.[29] In an aqueous environment H_2O is the prevalent possible reaction partner to be oxidized. Hence, for an effective catalytic degradation of organic molecules the energies for the generation of these active species have to be within the bandgap domain of the catalyst and the energetic position of the valence band must be larger than 2.85 V vs. RHE. Spinel-type oxides seem to be promising candidates because of their high stability in different media (acidic and basic), containing earth abundant elements and can be easily synthesized in large quantities. In some studies $ZnCr_2O_4$ showed very good performances in photo degradation of Reactive Blue 5,[30] Rhodamine B, Methylene blue and Methyl orange,[31] or y-Eosin,[32] due to a direct bandgap of ca. 3.4 eV and a low absorbance of visible light caused by d–d transitions of Cr^{3+} ions. Chromites are easily synthesized by thermal decomposition of crystalline precursors like e.g. $(NH_4)_2[Zn(NH_3)_2(CrO_4)_2]$.[33] The advantages of the decomposition synthesis are the very good reproducibility of the stoichiometry, the control of particle sizes and of surface areas, combined with high yields and easy scale up. However, a critical drawback of chromites is the possible photo oxidation of Cr^{III} to the highly soluble and hazardous Cr^{VI} species, especially in basic media.[34–36]

Herein we present results, which demonstrate the strong relation of the high catalytic activity of $ZnCr_2O_4$ in dye degradation (y-Eosin) with the chromate content and release during photo reaction as schematically shown in Figure 1. The mechanism postulated consists of a photo corrosion process of $ZnCr_2O_4$ and the Fenton-like Cr^{VI}-Cr^{III}/Cr^{IV}/Cr^{V} redox cycle, a type of Haber-Weiss cycle.[37,38] The e^-/h^+ pairs generated

* Prof. Dr. W. Bensch
Fax: +49-431-880-1520
E-Mail: wbensch@ac.uni-kiel.de
[a] Institut für Anorganische Chemie der Universität Kiel
Olshausenstr. 40
24098 Kiel, Germany
[b] Institute for Materials Science
Kaiserstrasse 2
24143 Kiel, Germany
Supporting information for this article is available on the WWW under **http://dx.doi.org/10.1002/zaac.201800072** or from the author.

from light absorption by $ZnCr_2O_4$ induce a photo oxidation of Cr^{III} to Cr^{VI} and a photo reduction of dissolved oxygen to superoxide radicals. These radicals attack dissolved molecules of y-Eosin used in the present studies. We present evidences that the more active species for photo degradation of y-Eosin is Cr^{VI} due to the Cr^{VI}-Cr^{III}/Cr^{IV}/Cr^{V} redox cycle, which produces two to six hydroxyl radicals per cycle from oxidation of H_2O, i.e. reduction of Cr^{VI} and reduction of H_2O_2 or $O_2^{\bullet-}$ by stepwise oxidation of Cr^{III}/Cr^{IV}/Cr^{V} back to Cr^{VI}.[34,35,37–44] All the generated radicals can react with surrounding organic molecules and initiate an advanced oxidation process (AOP) finally leading to nontoxic molecules like CO_2 and H_2O.[5]

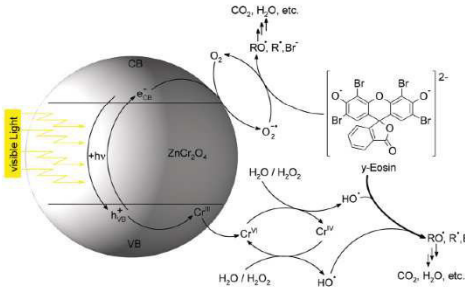

Figure 1. Schematic presentation of the degradation mechanism. Photons generate e /h^+ pairs, which oxidize Cr^{III} to Cr^{VI} or reduce O_2 to superoxide radicals. Cr^{VI} can react in a Fenton-like or Haber-Weiss type of mechanism to produce hydroxyl radicals. The generated radicals react with y-Eosin to organic radicals and finally to small nontoxic molecules.

Results and Discussion

XRD Diffraction Measurements

In the XRD patterns reflections of the spinel phase occur at calcining temperatures $T > 400$ °C (see Figure 2), whereas for $T < 400$ °C reflections of an unknown phase (200 °C) or just very broad reflections of low intensity (300 °C) were observed. Because no additional reflections are present in the XRD patterns of ZC400, ZC400w, ZC500, ZC600, and ZC750[45] phase pure samples were obtained with compositions in good agreement with the expected stoichiometry (EDX data see Table S4, Supporting Information). Rietveld refinements of the XRD patterns of these materials yield sizes of the coherently scattering domains ranging from 2 nm (ZC400w) to 45 nm

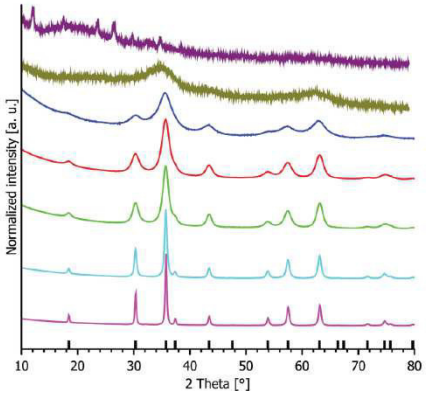

Figure 2. XRD diffraction patterns (bottom to top) of ZC750 (pink), ZC600 (cyan,), ZC500 (green), ZC400 (red), ZC400w (blue), ZC300 (dark yellow), and ZC200 (magenta). The decreasing particle sizes with lower calcining temperature (see Table 1) result in observable reflection broadening. There are no additional reflections in the thermally decomposed materials when compared to the calculated reflection positions for $ZnCr_2O_4$ (**I**).[45]

(ZC750) (see Table 1; procedure of Rietveld refinements is described in Supporting Information, Section S3). In addition to domain sizes the lognormal distribution of domain sizes was calculated applying the whole powder pattern modelling approach (WPPM) (see Figure 3).[46–48] With increasing calcination temperature the volume averaged domain sizes increase (Table 1). In addition, the distribution of the size of coherently scattering domains is broadened in the same direction (Figure 3).[47] The decrease of the volume averaged domain size for ZC400w compared to ZC400 suggests that during the treatment of the latter (see Experimental Section) particles are partially dissolved. Evaluation of the anisotropic broadening of Bragg reflections yields the volume averaged mean crystallite morphology (Figure 3).[49] At lower calcination temperatures the morphology is roughly spherical while for the sample prepared at $T = 750$ °C a nearly cubic shape is obtained.

During Rietveld refinement a notably difference in relative intensities of some reflections is observable, which is most pronounced for the {333/511} and {440} reflections. For of the catalyst ZC400 the {440}/{333/511} intensity ratio is 1.38, whereas ZC750 exhibits a ratio of 1.13 and the theoretical intensity ratio is 1.05. These observations indicate the presence

Table 1. Characteristic properties of the catalysts determined from XRD-measurements, N_2 sorption, and BET analysis as well as diffuse reflectance spectra.

Sample name	Volume averaged domain size (regarding stacking faults) /nm	Stacking fault probability /%	Cation vacancies in {111} plane /%	Surface area S_{BET} / $m^2 \cdot g^{-1}$	Band gap /eV
ZC400w	2 (3)	40	37	–	4.0
ZC400	4 (6)	29	8	58	4.0
ZC500	6 (8)	27	2	38	3.9
ZC600	16 (24)	5	0	14	3.8
ZC750	45 (66)	2	0	5	3.7

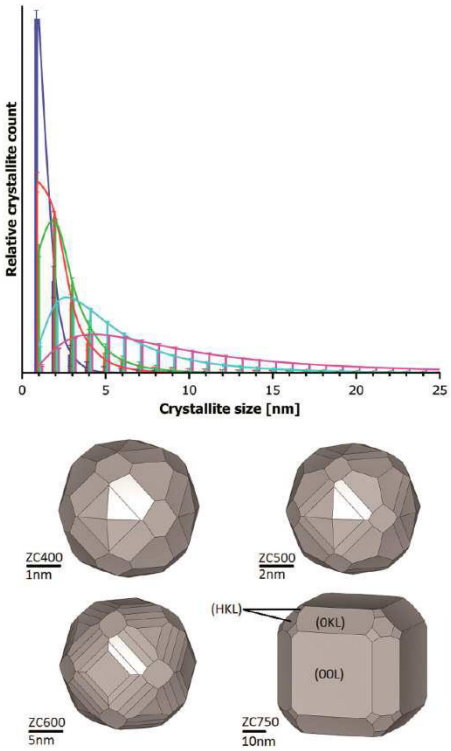

Figure 3. (Top) Logarithmic normal distribution of the crystallite sizes of ZC750 (pink), ZC600 (cyan), ZC500 (green) and ZC400 (red) determined by whole powder pattern modelling and (bottom) volume averaged mean crystallite morphology of ZC400, ZC500, ZC600, and ZC750 determined from anisotropic broadening with Topas Academic.[153] Visualization of crystallite morphologies using Vesta.[154]

of a notable amount of stacking faults,[150] especially for samples with smaller crystallites (ZC400w, ZC400, and ZC500). Oxidic spinels are known to bear stacking faults in the {110} and {111} plane,[150–52] which both increase the intensity of the {440} reflection relative to the {333/511} reflections. In addition, stacking faults of the {110} plane also increase the intensity of the {422} and {400} reflections relative to the {333/511} making them distinguishable from {111} stacking faults (see Figure S4, Supporting Information). Consequently taking {110} stacking faults into account in the XRD pattern refinements did not lead to satisfactory modeling of the reflection intensities. Consequently taking only {110} stacking faults into account in the XRD pattern refinements no satisfactory modeling of the reflection intensities could be achieved. A significant improvement was obtained considering {111} stacking faults. To adequately describe these stacking faults it is necessary to choose a unit cell of lower symmetry. Hence, a unit cell in space group $P1$ with lattice parameters a = b = 5.88815 Å, c = 14.42296 Å, $\alpha = \beta = 90°$ and $\gamma = 120°$ is suitable for tackling this problem. The transformation of the original cell is done with the matrix:

$$\begin{Bmatrix} -1/2 & 0 & 1 \\ 1/2 & -1/2 & 1 \\ 0 & 1/2 & 1 \end{Bmatrix} \quad (1)$$

Atomic positions of space group $Fd\bar{3}mZ$ are accordingly transformed using this matrix and the formerly (111) plane is transformed into the new (001) plane. The stacking faults can be described with the new unit cell as translation in a and/or b directions in combination with some cation vacancies (see Figure 4). Using this model the Rietveld refinements yield stacking fault probabilities of about 46% for ZC400w, which decrease with increasing crystallite size to ca. 1% for ZC750 (see Table 1 and Table S1, Supporting Information). The oc-

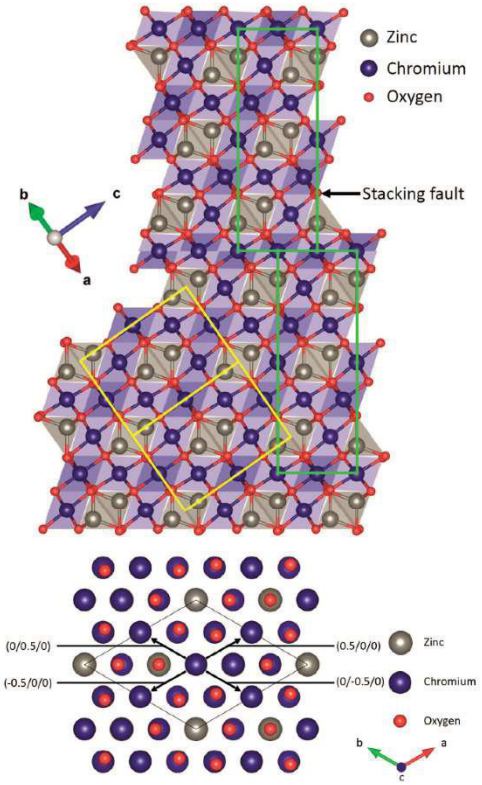

Figure 4. (Top) Projection onto the (110) plane of the spinel structure with the cubic unit cell (yellow) and the unit cell used for crystallographic description of stacking faults (green). (Bottom) Projection on the (001) plane of the spinel structure described in space group $P1$ {111} plane in $Fd\bar{3}mZ$) with translation vectors of possible stacking faults.

currence of stacking faults is accompanied by generation of cation vacancies in the plane of stacking faults of ca. 28 % in ZC400w and 0 % in ZC750.

The model explains the intensity of the {440} reflection very well but does not model intensity of {111} and {400} reflections. Hence, cation occupancy inversion was taken into account strongly improving the refinement (see Figures S5–S9, Supporting Information). The degree of inversion and of the stacking fault probability correlates the crystallite size: for the smallest coherently scattering domains (ZC400w) 20 % of the Cr^{3+} cations occupy tetrahedral sites, a value comparable to literature data for $ZnCr_2O_4$ with similar crystallite size.[55] The results of the analyses demonstrate that small crystallites are strongly affected by zero- and two-dimensional defects. This is a known effect of nanomaterials[51,55–57] because the relative number of disordered surface atoms and atoms at domain boundaries increases with decreasing domain size. Therefore, the influence of the ordering of these surface and interface atoms on reflection profiles and intensities of XRD patterns increases with decreasing domain size. Especially in the case of ZC400w there are just about 3–4 unit cells per crystallite in diameter. Therefore at least every forth unit cell must be defective.

Determination of sizes of coherently scattering domains is often performed assuming only contributions from size and strain. But stacking faults also lead to reflection broadening and taking this contribution into account the more realistic domain sizes are larger (Table 1).

TEM Analysis

In accordance with results obtained by Rietveld refinements of the XRD patterns, TEM micrographs show similar crystallite sizes for ZC400, ZC500, and ZC600 being 5.6, 7.8, and 17.6 nm, respectively (see Figure 5 and Figures S18 and S19, Supporting Information). The crystallites show fringes clearly demonstrating the crystalline nature of the samples. Most of the fringes can be assigned to the {111}, {311}, {222} lattice planes with d-values of 0.48, 0.30, and 0.25 nm, respectively. The electron diffraction patterns show a non-circular pattern for ZC400 changing to a spot pattern for ZC750 (see Figure 5 and Figures S14–S18, Supporting Information). The rotational averaged electron diffraction patterns display a sharpening of the diffraction rings with higher calcination temperature, as already observed in the XRD patterns. The d-values can all be assigned to lattice planes of cubic $ZnCr_2O_4$.

N_2 Sorption and BET Analysis

The N_2 sorption curves evidence larger adsorption-desorption hysteresis of type 3 for samples calcined at lower temperatures (see Figure S10, Supporting Information). With higher calcination temperature the hysteresis type changes from 3 to 4 in the case of ZC600, while ZC750 shows no hysteresis between adsorption and desorption curves. Because the spinel is non-porous the observed hysteresis may be explained by the presence of textural porosity with pores between 2 and 3 nm.

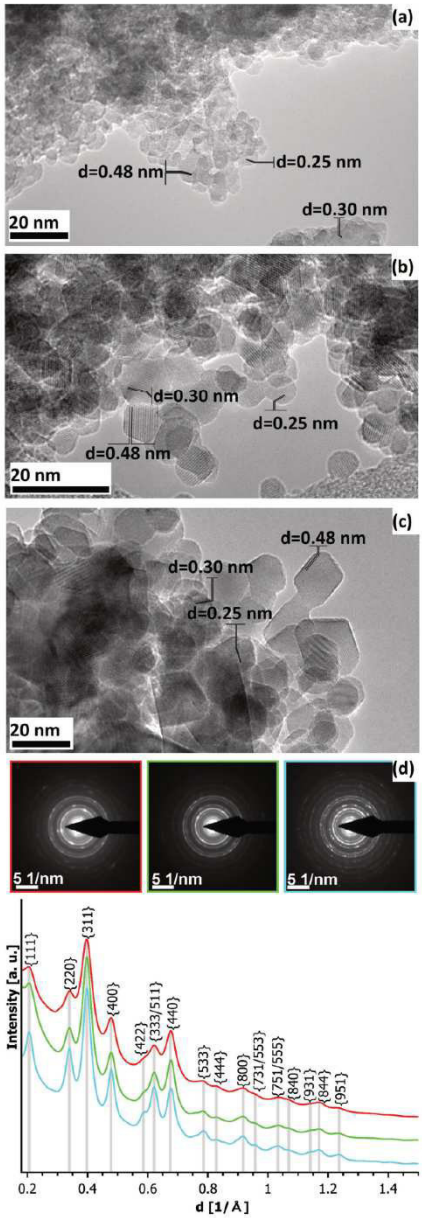

Figure 5. Transmission electron micrographs of typical regions of samples ZC400 (a), ZC500 (b), and ZC600 (c). Electron diffraction patterns and their rotational average of ZC400 (red), ZC500 (green) and ZC600 (cyan) with expected peak positions for $ZnCr_2O_4$[45] (d).

The corresponding surface areas range from 5 to 58 $m^2 \cdot g^{-1}$ (see Table 1).

UV/Vis Reflection Spectroscopy

The experimental reflectance data were converted to data for the Tauc-plots via the Kubelka-Munk function [Equation (2)]:[58]

$$\alpha = \frac{(1 - R_\infty)^2}{2R_\infty} \quad (2)$$

with the reflectance R_∞ of a sample with unlimited thickness [Equation (3)]:

$$R_\infty = \frac{R_{Sample}}{R_{Standard}} \quad (3)$$

where R_{Sample} is the reflectance of the sample mixed with a white standard (e.g. $BaSO_4$) and $R_{Standard}$ is the reflectance of the pure white standard. The determination of a bandgap is done by interpolating the linear part of the Tauc plot, which is a plot of $(\alpha E)^2$ vs. the energy $E = h\nu$ in the case of a direct bandgap.[59]

The UV/Vis absorbance spectra of the samples display typical d–d transitions of the Cr^{3+} cation in octahedral arrangement (see Figure 6 and Figure S11, Supporting Information).[60,61] Distinct absorption bands of Cr^{3+} located in tetrahedral sites are not observed. In addition, the expected bands of Cr^{3+} located on octahedral do not occur for ZC400 and ZC500, and it seems that the gradual inversion causes a blurred, undefined light absorption in the range of 1.7 to 3.0 eV. For ZC600 and more pronounced for ZC750, the Laporte forbidden $^2T_2 \leftarrow {}^4A_2$ transition accompanied by an electron-magnon phonon band is located at 1.86 eV and two broad absorptions caused by

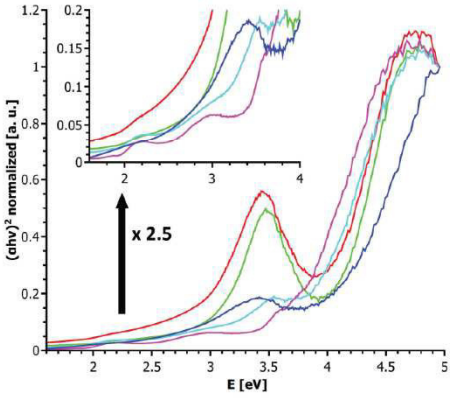

Figure 6. Tauc-plots of the diffuse reflectance spectra in the UV/Vis-range of ZC750 (pink), ZC600 (cyan), ZC500 (green), ZC400w (blue) and ZC400 (red). The inset shows the same spectra 2.5 times magnified in the region of d–d transitions. Additional to the absorption due to d–d transitions at 2.1 eV and 2.9 eV the absorption due to electronic transitions from the valence band to conduction band and the charge transfer transition of Cr^{VI} impurities is visible.

$^4T_2 \leftarrow {}^4A_2$ and $^4T_1 \leftarrow {}^4A_2$ transitions are centered on 2.15 eV and 2.87 eV, respectively. Like the bands in the IR spectra (see Figure S11, Supporting Information) the absorptions due to d–d transitions gain in intensity for the samples treated at higher temperatures. Interestingly, a band located at 3.43 eV is only observed for the samples calcined at 400 and 500 °C. This absorption indicates residual amorphous chromate species because there is no additional crystalline phase in the XRD and electron diffraction patterns of ZC400 and ZC500. A very small amount of such Cr^{VI} phase seems to persist in the material obtained at $T = 600$ °C giving rise to a not well pronounced signal located at ca. 3.5 eV. The direct bandgaps of the materials decrease with increasing calcining temperature from 4 eV (ZC400) to 3.7 eV (ZC750) (see Figure 6 and Table 1), with the latter value being larger than $E_g = 3.4$ eV as reported in literature for well crystalline $ZnCr_2O_4$.[61]

Infrared and Raman Spectroscopy

The MIR and FIR spectra of the samples calcined between 400 and 750 °C exhibit the expected vibration modes of $ZnCr_2O_4$ (see Figure S11): the F_{1u} vibration modes at 608, 471, 371 and 183 cm^{-1} as well as a F_{2u} vibration at 537 cm^{-1}.[62,63] With increasing crystallinity the absorption signals become more intense and narrower.

Like in the XRD and TEM analyses no hints are seen in the spectra on the nature of the Cr^{VI} species observed in the UV/Vis spectra of ZC400, ZC400w ZC500, and ZC600.

Catalytic Experiments

For photocatalytic degradation experiments y-Eosin was chosen as model compound in a neutral photo-Fenton process (see Figure 1).[64,65] y-Eosin is a xanthene based dye and therefore the structure and reactivity is similar to dioxins. In the catalytic photo-Fenton process not only the catalyst and a reacting substrate are used but also an oxidizing agent like H_2O_2 or O_3 is added. The catalyst cleaves these oxidizing agents or H_2O into highly reactive radicals (see Introduction), which chemically attack and decompose the organic substrate. Hence, the oxidizing agents provide the photo catalytically active species. The addition of the reagent does not significantly affect the cost of a potential photo catalytic waste water treatment, and e.g. ozone is already used for the disinfection of waste water.[66] Thus only the photo catalyst immobilized on a surface and a light source, sunlight at its best, has to be added to a continuous flow reactor for the efficient decontamination of waste water.

The catalysts prepared at the lowest temperatures exhibit the most efficient degradation of y-Eosin (see Figure 7 for data obtained with H_2O_2 and Figures S20 and S21, Supporting Information, showing results without additional H_2O_2 or without catalyst). After recovering the catalysts, no changes were observed in IR spectra and XRD patterns (see Figures S12 and S13, Supporting Information). The sample ZC750 reached a y-Eosin degradation of 24% after 1 h of illumination [$\ln(C/C_0) = -0.27$], while usage of ZC600 results in a degrada-

tion of 38 % after 1 h [$\ln(C/C_0) = -0.48$]. Both data sets can be fitted with nearly linear functions. Although the fit with a zeroth-order kinetic model leads to a R^2 value of 0.992, while assuming first order kinetics $R^2 = 0.997$ is obtained, but the reaction constants are comparable (see Table 2). Lower calcining temperatures lead to data which clearly follow first order kinetics. The catalysts ZC400 and ZC500 reach 92 % [$\ln(C/C_0) = -2.49$] and 83 % [$\ln(C/C_0) = -1.84$] degradation of y-Eosin after 1 h illumination. The first-order rate constant k can be determined from Equation (4):

$$\ln(C/C_0) = -k \cdot t \quad (4)$$

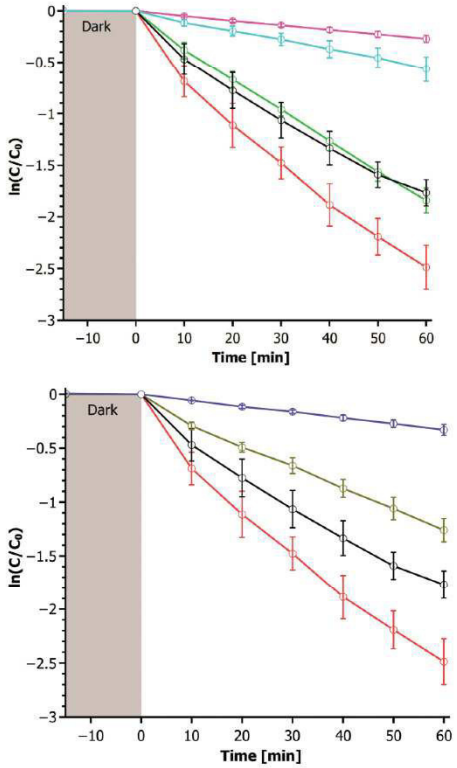

Figure 7. (Top) Decrease of the concentration of y-Eosin including standard deviation during catalytic experiments with different $ZnCr_2O_4$ catalysts and H_2O_2 in comparison to K_2CrO_4 and H_2O_2. (Bottom) Decrease of the concentration of y-Eosin including estimated standard deviations in presence of H_2O_2 during catalytic experiments with ZC400 as calcined and after washing process (ZC400w) with and without additional K_2CrO_4 in comparison to degradation with K_2CrO_4. The color coding is as follows: K_2CrO_4 (grey), ZC750 (pink), ZC600 (cyan), ZC500 (green), ZC400 (red), ZC400w (blue) and ZC400w with addition of K_2CrO_4 (olive). The grey area marks the time interval without illumination.

with initial concentration C_0 and concentration C at time t. As can be seen from the data in Table 2 the rate constant decreases drastically with higher calcination temperature from 47.1×10^{-3} min^{-1} to 4.6×10^{-3} min^{-1} for ZC400 and ZC750, respectively. The photo catalytic dye degradation performed with ZC400 in the presence of a small amount of H_2O_2 is ca. 25 times faster than without ZC400. We note that the rate constant of ZC400 without H_2O_2 is as good as that of ZC600 and about 5 times larger than the performance without catalyst and H_2O_2. In fact, the reaction constant of ZC400 without H_2O_2 is larger than that of TiO_2[67] (P25, catalyst concentration: 0.5 g·L^{-1}, light source: 500 W halogen lamp with < 470 nm cut off filter) and N:TiO_2[68] (catalyst concentration: 1 g·L^{-1}, light source: 150 W tungsten filament Lamp) despite that the light source applied during our studies has considerably less power. This is supported by our findings that P25 seems to inhibit the photolysis of y-Eosin when used in our setup, since the rate constant without P25 is four times higher than with P25 and H_2O_2 (see Table 2 and Figure S20, Supporting Information). When illuminated with UV light ($350 < \lambda < 400$ nm) the rate constant of TiO_2 is significantly increased to about 17.1×10^{-3} min^{-1}, as calculated from a photonic efficiency of 0.64 %, the given photon flux and initial y-Eosin concentration of 50 mg·L^{-1} at catalyst concentration of 1 g·L^{-1} and to 12.0×10^{-3} min^{-1} for ZnO with a photonic efficiency of 0.45 % and an amount of ZnO of 1 g·L^{-1}.[69] Maybe such gain can also be achieved for $ZnCr_2O_4$ but the use of visible light, which is the cheapest light source, is more favorable due to the fact that the fraction of UV light in the solar spectrum is only 3–4 % [8,9,11,12,14,15,18,28].

We note that the rate constants obtained during the present study are comparable with those of other ferrites reported for various dyes.[26,27,70–72] But similarly to the aforementioned investigations with TiO_2 the light sources used in the experiments were considerably more intense and/or the partially applied H_2O_2 concentrations were explicitly larger. Hence, $ZnCr_2O_4$ seems to be a good potential photo degradation catalyst.

Catalyst Corrosion

In UV/Vis spectra recorded in catalytic experiments an absorption band at 370 nm is observed, which can be assigned to CrO_4^{2-}.[38,43] The results of the catalytic experiments demonstrate that the amount of residual Cr^{VI} is crucial for the activity. After removal of CrO_4^{2-} from the sample ZC400 by extensive washing the reaction rate constant and therefore the catalytic activity decreased by a factor of 1/3 (1/8 with additional H_2O_2). Adding K_2CrO_4 to ZC400w matching the concentration of Cr^{VI} washed out from ZC400 leads to a higher catalytic activity with a rate constant of 20.5×10^{-3} min^{-1} (four times lower without H_2O_2) which is similar to the values obtained using only K_2CrO_4 (see Table 2). Therefore, it seems likely that the catalytic activity of $ZnCr_2O_4$ in the photo degradation of organic molecules stems from Cr^{VI} species. The catalyst ZC750 does not contain Cr^{VI} but still shows a reasonable catalytic activity.

Table 2. Conditions applied in catalytic experiments and photo catalytic properties of the catalysts in the degradation of y-Eosin. For comparison the reaction constants for dye degradation of y-Eosin with TiO_2[65] (catalyst concentration of 0.5 g·L^{-1}) and N:TiO_2[66] (catalyst concentration of 1 g·L^{-1}) are shown as well as the data obtained using P25 (TiO_2).

Sample name	H_2O_2 /µL	Reaction constant k 1. Ord. (min^{-1}) × 10^{-3}	0. Ord. (min^{-1}) × 10^{-3}	1. Ord./[CrO_4^{2-}] [min^{-1}/M(CrO_4^{2-})]
ZC400	10	47.1 ± 2.5	–	212.6 ± 37.6
ZC500	10	30.3 ± 0.7	–	281.0 ± 18.0
ZC600	10	7.7 ± 0.21	6 ± 0.12	123.8 ± 23.2
ZC750	10	4.6 ± 0.10	4 ± 0.08	128.1 ± 28.5
ZC400	0	7.4 ± 0.36	–	36.0 ± 3.6
ZC400w	0	2.29 ± 0.07	–	64.3 ± 11.9
ZC400w	10	5.47 ± 0.12	–	97.8 ± 28.7
ZC400w and $KCrO_4$	0	4.88 ± 0.13	–	10.7 ± 0.5
ZC400w and $KCrO_4$	10	20.5 ± 0.7	–	40.3 ± 4.7
$KCrO_4$	0	3.88 ± 0.15	–	10.7 ± 1.0
$KCrO_4$	10	32.3 ± 1.3	–	68.4 ± 7.3
Without catalyst	10	–	1.84 ± 0.06	–
Without catalyst	0	–	1.60 ± 0.04	–
TiO_2 [65]	0	5.1	–	–
N:TiO_2 [66]	0	2.4	–	–
P25 (TiO_2)	10	0.62 ± 0.1	0.43 ± 0.07	–

To understand this observation, the rate constants were normalized using the most intense UV/Vis absorbance of the CrO_4^{2-} anion charge-transfer band at 370 nm[38,43] as a measure of the Cr^{VI} content in the reaction medium. Applying this approach the resulting catalytic activity of ZC750 and H_2O_2 (see Table 2) is 1.9 times higher if only CrO_4^{2-} and H_2O_2 were used. Therefore, a co-catalytic mechanism as schematically drawn in Figure 1 can be postulated. The assumption of in-situ chromate generation is supported analyzing the change of UV/Vis spectra in the region 350–400 nm as function of reaction time (see Figure 8 and Figure S22, Supporting Information) concerning the concentrations of CrO_4^{2-} at the beginning of irradiation in catalytic tests (esp. ZC400 and ZC500).

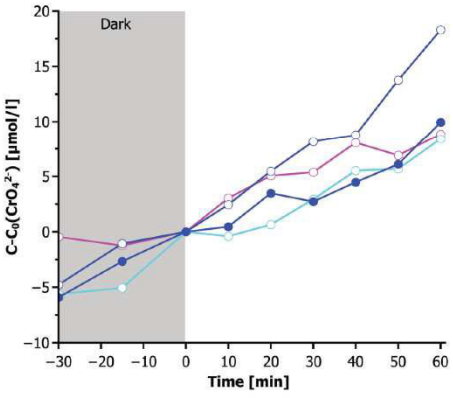

Figure 8. Time dependent evolution of the CrO_4^{2-} concentration observed in the degradation experiments with low to no CrO_4^{2-} content corrected by the value determined at t = 0. The color coding is as follows: ZC750 (pink), ZC600 (cyan), and ZC400w (blue). Data of experiments, which were done with addition of H_2O_2 are labeled with hollow circles. The grey area marks the time interval without illumination. Estimated error of the data points: ±10%.

Hence, the CrO_4^{2-} content in solution is composed of: (I) chromate dissolved before addition of y-Eosin, (II) formed chromate after addition of y-Eosin and processing of the suspension in the dark, and (III) generated CrO_4^{2-} during irradiation. An increase of the dissolution rate of CrO_4^{2-} during irradiation (e.g. ZC400w and ZC750) is a hint to a photo corrosion process. Huge amounts of dislocations observed especially in ZC400 and ZC500 may promote the photo corrosion process and therefore the dissolution rate of Cr^{VI}.[73,74] For the samples containing already relatively high CrO_4^{2-} contents no significant variation with time could be observed (see Figure S22, Supporting Information), while for low initial concentration (e.g. for ZC750) a steady increase of the concentration of CrO_4^{2-} anions is observed (see Figure 8 and Figure S23, Supporting Information). Quantification leads to dissolution rates of CrO_4^{2-} of 0.15 and 0.24 µM·min^{-1} for ZC400w and ZC400w with additional H_2O_2, respectively. Experiments performed with catalysts containing larger domain sizes (ZC600 and ZC750), CrO_4^{2-} dissolution rates of 0.12 and 0.16 µM·min^{-1} were estimated.

Especially for ZC750 the CrO_4^{2-} generation starts when illumination begins and after H_2O_2 was added. The actual guideline value for drinking water (0.05 mg·L^{-1})[75] as estimated by the World Health Organization is therefore exceeded after 5–10 min of catalytic reaction. Because a suitable photo catalytic decontamination of waste water lasts several hours, the use of $ZnCr_2O_4$ is not advisable. The photo corrosion is accompanied by a change of the volume averaged domain size determined by evaluation of the XRD patterns measured after the catalytic experiments: for ZC400w the sizes decreased from 2.0 to 1.9 nm (sample ZC400wPC) after 15 h of catalysis. The log normal distribution of the domain sizes shows a small shift to larger domains and a reduced relative number of small crystallites (see Figure S24, Supporting Information), i.e. the smallest particles are dissolved during the reaction by photo corrosion. While the mechanism of Cr^{III} oxidation was not investigated, one can propose that the oxidation may occur via (I) photo

excitation of $ZnCr_2O_4$ and generated holes h^+ oxidizing Cr^{III} on the catalyst surface, or (II) Cr^{III} is first dissolved and then oxidized by generated radicals ($HO^•$ and $O_2^{•-}$), photo excited $ZnCr_2O_4$ or y-Eosin, or (III) the radicals or photo excited y-Eosin molecules oxidize surface Cr^{III} of $ZnCr_2O_4$. The oxidation by y-Eosin is possible because the oxidation potential of photo excited y-Eosin (0.89 V vs. NHE at pH = 7)[76] is larger than the oxidation potential of $Cr_2O_7^{2-}$ (0.64 V vs. NHE at pH = 7)[129].

Degradation Mechanism

MALDI-TOF experiments were performed to elucidate the photocatalytic degradation mechanism. The spectrum collected at t = 0 shows several signals of brominated y-Eosin species like monobromide at 413 *m/z*, dibromide at 491 *m/z*, tribromide at 571 *m/z*, and tetrabromide at 649 *m/z* (see Figure 9). The signal of the mono sodium salt of the tetrabromo-y-Eosin molecule (671 *m/z*) is the most intense signal and is therefore used for data normalization. With progress of photocatalytic degradation new signals appear, while the intensity of signals for monobromide, dibromide and tribromide molecules rapidly decrease (see Figure S25, Supporting Information). Evidences for the degradation mechanism arise from mass signals at 586 and 664 *m/z*. Their quadruple/quintuple isotopic pattern allows assignment to hydroxylated y-Eosin species of the tribromide and tetrabromide species (see Figure 9). Signals with low intensity of the doubly hydroxylated y-Eosin occur at 680 and 602 *m/z* (see Figure S26, Supporting Information). These results are in accordance with the general postulated photodegradation mechanisms of organic molecules with conjugated π-systems.[4–6] Hydroxyl radicals mainly generated by the Cr^{VI}-Cr^{III}/Cr^{IV}/Cr^{V} redox cycle attack and bind to the sacrificial organic molecule. This attack occurs until the π-system and the molecular structure are fragmented.

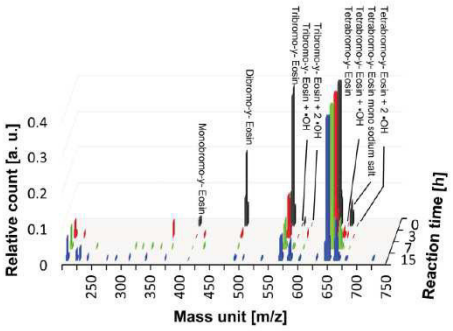

Figure 9. Mass spectra of y-Eosin solutions after t = 0 (black), 3 (pink), 7 (green) and 15 h (blue). Different bromide species of y-Eosin appear which decrease with increasing reaction time, while hydroxylated species are observed with increasing reaction time.

Conclusions

The synthesis of stoichiometric $ZnCr_2O_4$ by thermal decomposition of the crystalline precursor $(NH_4)_2[Zn(NH_3)_2(CrO_4)_2]$ allowed preparation of catalysts with varying microstructural and textural properties. Depending on the thermal treatment a large number of 0D and 2D defects is generated, especially for samples obtained at low temperatures. The detailed analyses of the XRD patterns reveal that the amount of stacking faults ranges between 46 and 1 %, which are accompanied by cation vacancies of up to 28 % in ZC400w. The observed domain sizes range from 3 to ca. 55 nm and specific surface areas vary from 5 to 60 $m^2 \cdot g^{-1}$. A partial inversion of the occupancies of tetrahedra and octahedra is also observed with about 20 % of Cr^{3+} being located on tetrahedra in the structure of the sample with the smallest size of coherently scattering domains. Additional to the known spectroscopic characteristics of highly crystalline $ZnCr_2O_4$, the absorption of photons with energies larger than 2.8 eV is observed due to amorphous Cr^{VI} residues in the oxides calcined at 400 and 500 °C, which can be removed by washing with water. The bandgap of the materials decreases from 4 to 3.4 with increasing calcination temperature from 400 to 750 °C. In photo degradation experiments the materials exhibit a high catalytic activity of up to 47.1×10^{-3} min^{-1}. Without addition of H_2O_2 the first-order rate constant and thus the catalytic activity for y-Eosin degradation with ZC400 is 4–5 times higher than observed for TiO_2[167] or N:TiO_2[168]. But the severe drawback of the present catalysts is the formation of the CrO_4^{2-} anions. Actually, CrO_4^{2-} emerged to be the active species in the degradation mechanism. The dissolution rate in the absence of H_2O_2 does not significantly differ between the catalysts and it is accelerated in the presence of H_2O_2 which is commonly used in photo catalytic degradation experiments. All the results presented here highly suggest that $ZnCr_2O_4$ is inappropriate for environmental friendly photo catalysis in aqueous media.

Experimental Section

Chemicals: Anhydrous $ZnCl_2$ (Merck), $(NH_4)_2CrO_4$ (Sigma Aldrich), 25 % NH_4OH solution (BCD), 35 % H_2O_2 solution (BCD), $BaSO_4$ (Merck), K_2CrO_4 (Merck), absolute ethanol (1 % MEK, Walter CMP), P25 (TiO_2, Evonik), potassium iodide (KI, Grüssing), hydrochloric acid (VWR), and y-Eosin sodium salt (Merck) were of reagents grade and were used without further purification. Ethyl acetate (98 %, Walter CMP) was purified by vacuum distillation with a rotary evaporator before use.

Preparation of the $(NH_4)_2[Zn(NH_3)_2(CrO_4)_2]$ Precursor and of the Catalysts: The synthesis of the precursor was done following the procedure reported by *Briggs* et al.[133] In a typical synthesis $(NH_4)_2CrO_4$ (4.87 g, 32 mmol) and $ZnCl_2$ (2.18 g, 16 mmol) were dissolved in 20 mL demineralized (demin.) water. After addition of 12 mL of concentrated (conc.) NH_3 solution the water and ammonia were slowly evaporated at room temperature. The precursor crystallized as dark yellow large crystals.

The catalysts were prepared by heating the precursor in an alumina crucible in a muffle furnace to T = 200, 300, 400, 500, 600, 750, and 1000 °C within 60 min and holding these temperatures for another 60 min. Subsequently the furnace was switched off. In the following the oxides are denoted as ZC for $ZnCr_2O_4$ and the respective calcination temperature.

Chromate residuals in ZC400 were removed adding ZC400 (ca. 1 g) to a mixture of 400 mL 1:1 demin. H_2O and absolute ethanol to obtain

ZC400w. The slurry was heated to reflux for at least 1 h before cooling down, followed by filtration and rinsing with 100 mL diluted aqueous KI solution and 500 mL of demin. H_2O.

Characterization Methods: X-ray diffraction patterns (XRD) were collected with a STOE Stadi-p (Cu-$K_{\alpha1}$ irradiadion, Ge monochromator and MYTHEN 1 K detector) in transmission geometry and with a PANalytical X'Pert Pro MPD Diffractometer (Cu-$K_{\alpha1,2}$ radiation) equipped with a PIXcel detector. Rietveld refinements were carried out applying the fundamental approach using the program Topas Academic.[15,31] The instrumental resolution function was determined with the LaB_6 SRM 660a NIST standard.

Energy Dispersive X-ray (EDX) analyses were made with an Environmental Scanning Electron Microscope Philips XL-30 equipped with an EDAX Detector.

Mid Infrared (MIR) spectra in the region of 375–4000 cm^{-1} were collected with a Bruker Alpha-P Platinum ATR spectrometer.

Far Infrared (FIR) spectra in the region from 75–400 cm^{-1} were measured with a Bruker IFS 66 spectrometer.

For the determination of diffuse Ultraviolet/Visible (UV/Vis) reflectance spectra the samples were mixed in a mortar with $BaSO_4$ as white standard (ratio 1:100) and the reflectance of the powders were measured with a Varian Cary 5000 in the region 200–2000 nm.

The specific surface areas were determined with N_2 sorption measurements with a Belsorp Max instrument and the data were evaluated with the BET method.

Transmission electron microscopy (TEM) analysis was done with a Tecnai F30 G^2 - STwin equipped with a field emission gun (FEG) operating at a 300 kV acceleration voltage.

Photocatalytic Experiments: The photocatalytic activity of the catalysts in degradation of y-Eosin was determined applying 30 mg of the oxides suspended in 2 mL of demin. H_2O. Suspensions were obtained applying ultrasound in a VWR USD600D at maximum power at room temperature for 60 s. The suspensions were added to 33 mL of demineralized H_2O in a round-bottomed flask equipped with a cooling jacket. The suspensions were magnetically stirred and equilibrated at 25 °C with a thermostat. After equilibrium was reached, y-Eosin solution (15 mL, 0.055 mM in demin. H_2O) was added, and the suspension (50 mL) was stirred in the dark for 30 min. At the beginning of the experiment, after 15 and 30 min, 3 mL of the suspension were removed and catalyst particles were separated by centrifugation. Afterwards, 10 µL of 35 % H_2O_2 solution (79 $mg{\cdot}L^{-1}$) was added and the setup was illuminated with a conventional halogen lamp (Osram Hal SST 116 W 240 V E27, photons with wavelength < 400 nm ≈ 0.3 %, the spectrum of lamp photons is shown in Figure S1, Supporting Information) for 60 min. During illumination, 3 mL of the suspension was removed every 10 min and the catalyst particles were separated by centrifugation. The residual concentration of y-Eosin was determined by measuring the UV/Vis spectra with a Varian Cary 5000 or a Varian Cary 8453. The offset caused by Mie scattering was estimated at 600 nm, subtracted, and the intensity of the absorption band at 517 nm was evaluated.

The influence of CrO_4^{2-} anions on the degradation of the dye was studied applying 2 mg of K_2CrO_4 instead of $ZnCr_2O_4$ or in addition to 30 mg of Zn400w in the photocatalytic experiments.

The photon flux directed into the round-bottomed flask was determined with ferrioxalate actinometry (experimental protocol, Supporting Information, Section S1) and a mean value of 22.7 ± 1.2 $\mu mol{\cdot}s^{-1}$ was obtained. For post catalytic characterizations the catalyst particles separated by centrifugation were washed with demin. H_2O and dried at 80 °C in air.

To obtain evidences for photo corrosion of $ZnCr_2O_4$, ZC400w (70 mg) was ultrasonically dispersed in 2 mL demin. H_2O and added to 1938 mL demin. H_2O and y-Eosin solution (60 mL, 0.555 mM). Afterwards 400 µL of 35 % H_2O_2 solution was added. This procedure yields an identical concentration of y-Eosin and H_2O_2 as in the other photo catalytic experiments. The dispersion was illuminated for 15 h followed by evaporation of the solvent in vacuo. The post catalytic material ZC400wPC was obtained by washing with 100 mL acetone and 500 mL demin. H_2O.

Mass Spectrometry: The photo degradation pathways of y-Eosin were analyzed applying the following experiments: 50 mg of ZC400 were dispersed by ultra sonication in 2 mL of 0.555 mM of y-Eosin solution and added to further 48 mL of 0.555 mM y-Eosin solution. The resulting suspension was treated as explained before (section photocatalytic experiments). After reaction times of 0, 3, 7, and 15 h, 2 mL ethanol was added to suppress any radical reaction. After filtration with Whatman Anodisc 0.1 µm syringe filters 2 mL concentrated aqueous HCl was added to precipitate the dissolved organic matter. The obtained liquid was extracted 10 times with 10 mL ethyl acetate, and the solvent was removed in vacuo to obtain the degradation products. Reddish brown solids were obtained, which were analyzed by Matrix Assisted Laser Desorption Ionization-Time of Flight Mass Spectroscopy (MALDI-TOF-MS) with a Bruker MALDI-TOF Bioflex. 4-Chloro-α-cyanocinnamic acid was used as the matrix and the sample was ionized with a Laser power of 38 %.

Supporting Information (see footnote on the first page of this article): Detailed description of actinometry and Rietveld refinement process as well as IR-, Raman spectra and XRD pattern of the precursor, N_2 sorption data, UV/Vis and IR spectra of the catalysts, postcatalytic measurements, TEM data, further data of degradation experiments and data of mass spectroscopy.

Acknowledgements

The authors are grateful to Christian-Albrechts-Universität zu Kiel for providing infrastructural facility and the state Schleswig-Holstein for financial support. We want to thank *Jacqueline Pick* and *Stefanie Pehlke* for their support in the measurements (IR-, Raman-, UV/Vis-reflection measurements) as well as *Inke Jess* for STA measurements. Additionally we thank *Christin Szillus* for preparing samples for TEM-measurements and *Rolf Schmied* and *Dirk Meyer* for mass spectrum analysis.

Keywords: Photocalatysis; X-ray diffraction; Chromates; Dye degradation; Nanoparticles

References

[1] United States Environmental Protection Agency Office of Water, *National Water Quality Inventory: Report to Congress – 2004 Reporting Cycle (EPA 841-R-08–001)*, can be found under https://www.epa.gov/sites/production/files/2015–09/documents/2009_01_22_305b_2004report_2004_305breport.pdf.

[2] A. Joas, E. Müller, Umweltbundesamt Germany, *Dioxine. Daten aus Deutschland*, can be found under http://

www.umweltbundesamt.de/sites/default/files/medien/publikation/long/3328.pdf **2007**.
[3] S. Debnath, N. Ballav, H. Nyoni, A. Maity, K. Pillay, *Appl. Catal. B* **2015**, *163*, 330–342.
[4] S. Das, M. Muneer, K. R. Gopidas, *J. Photochem. Photobiol. A: Chem.* **1994**, *77*, 83–88.
[5] M. R. Hoffmann, S. T. Martin, W. Choi, D. W. Bahnemann, *Chem. Rev.* **1995**, *95*, 69–96.
[6] I. K. Konstantinou, T. A. Albanis, *Appl. Catal. B* **2004**, *49*, 1–14.
[7] C. Chen, W. Ma, J. Zhao, *Chem. Soc. Rev.* **2010**, *39*, 4206.
[8] A. Ajmal, I. Majeed, R. N. Malik, H. Idriss, M. A. Nadeem, *RSC Adv.* **2014**, *4*, 37003.
[9] R. J. Tayade, T. S. Natarajan, H. C. Bajaj, *Ind. Eng. Chem. Res.* **2009**, *48*, 10262–10267.
[10] K. Tanaka, K. Padermpole, T. Hisanaga, *Water Res.* **2000**, *34*, 327–333.
[11] I. Paramasivam, H. Jha, N. Liu, P. Schmuki, *Small* **2012**, *8*, 3073–3103.
[12] M. Rochkind, S. Pasternak, Y. Paz, *Molecules* **2015**, *20*, 88–110.
[13] P. Pichat, *Molecules* **2014**, *19*, 15075–15087.
[14] S. Dong, J. Feng, M. Fan, Y. Pi, L. Hu, X. Han, M. Liu, J. Sun, J. Sun, *RSC Adv.* **2015**, *5*, 14610–14630.
[15] H. Zangeneh, A. A. L. Zinatizadeh, M. Habibi, M. Akia, M. Hasnain Isa, *J. Ind. Eng. Chem.* **2015**, *26*, 1–36.
[16] N. Daneshvar, D. Salari, A. R. Khataee, *J. Photochem. Photobiol. A: Chem.* **2004**, *162*, 317–322.
[17] S. Chowdhury, R. Balasubramanian, *Appl. Catal. B* **2014**, *160–161*, 307–324.
[18] W. Wang, M. O. Tadé, Z. Shao, *Chem. Soc. Rev.* **2015**, *44*, 5371–5408.
[19] X. Niu, H. Li, G. Liu, *J. Mol. Catal. A* **2005**, *232*, 89–93.
[20] S. Thirumalairajan, K. Girija, N. Y. Hebalkar, D. Mangalaraj, C. Viswanathan, N. Ponpandian, *RSC Adv.* **2013**, *3*, 7549.
[21] S. Li, L. Jing, W. Fu, L. Yang, B. Xin, H. Fu, *Mater. Res. Bull.* **2007**, *42*, 203–212.
[22] W. Wang, M. O. Tadé, Z. Shao, *Prog. Mater. Sci.* **2018**, *92*, 33–63.
[23] G. Zhang, G. Liu, L. Wang, J. T. S. Irvine, *Chem. Soc. Rev.* **2016**, *45*, 5951–5984.
[24] V. M. da Silva Rocha, M. de Godoi Pereira, L. R. Teles, M. O. da Guarda Souza, *Mater. Sci. Eng. B* **2014**, *185*, 13–20.
[25] M. H. Habibi, J. Parhizkar, *Spectrochim. Acta Part A* **2015**, *150*, 879–885.
[26] S. Bhukal, S. Bansal, S. Singhal, *Phys. B* **2014**, *445*, 48–55.
[27] S. Bhukal, S. Bansal, S. Singhal, *Mater. Sci. Semicond. Process.* **2014**, *26*, 467–476.
[28] R. Ullah, J. Dutta, *J. Hazard. Mater.* **2008**, *156*, 194–200.
[29] A. F. Hollemann, N. Wiberg, *Lehrbuch der anorganischen Chemie*, 102nd ed., Walter de Gruyter, Germany **2007**.
[30] M. Yazdanbakhsh, I. Khosravi, E. K. Goharshadi, A. Youssefi, *J. Hazard. Mater.* **2010**, *184*, 684–689.
[31] A. Abbasi, M. Hamadanian, M. Salavati-Niasari, S. Mortazavi-Derazkola, *J. Colloid Interface Sci.* **2017**, *500*, 276–284.
[32] Z. Mousavi, F. Soofivand, M. Esmacili-Zare, M. Salavati-Niasari, S. Bagheri, *Sci. Rep.* **2016**, *53*, 20071.
[33] S. H. C. Briggs, *J. Chem. Soc. Trans.* **1903**, *83*, 391–395.
[34] A. D. Bokare, W. Choi, *Environ. Sci. Technol.* **2011**, *45*, 9332–9338.
[35] Y. Inada, S. Funahashi, *Z. Naturforsch. B* **1997**, *52*, 711–718.
[36] B. Zydorczak, P. M. May, D. P. Meyrick, D. Bátka, G. Hefter, *Ind. Eng. Chem. Res.* **2012**, *51*, 16537–16543.
[37] X. Shi, N. S. Dalal, *Arch. Biochem. Biophys.* **1992**, *292*, 323–327.
[38] A. D. Bokare, W. Choi, *Environ. Sci. Technol.* **2010**, *44*, 7232–7237.
[39] B. L. Bartlett, D. Quane, *Inorg. Chem.* **1973**, *12*, 1925–1927.
[40] A. D. Bokare, W. Choi, *J. Hazard. Mater.* **2014**, *275*, 121–135.
[41] B. Jiang, Y. Liu, J. Zheng, M. Tan, Z. Wang, M. Wu, *Environ. Sci. Technol.* **2015**, *49*, 12363–12371.
[42] X. Shi, N. S. Dalal, *Environ. Health Persp.* **1994**, *102*, 231–236.
[43] M. I. Zaki, M. A. Hasan, N. E. Fouad, *Appl. Catal. A* **1998**, *171*, 315–324.
[44] L. Zhang, P. A. Lay, *Inorg. Chem.* **1998**, *37*, 1729–1733.
[45] H. Sawada, *Mater. Res. Bull.* **1997**, *32*, 873–878.
[46] P. Scardi, M. Leoni, *Acta Crystallogr., Sect. A* **2002**, *58*, 190–200.
[47] M. Leoni, R. Di Maggio, S. Polizzi, P. Scardi, *J. Am. Ceram. Soc.* **2004**, *87*, 1133–1140.
[48] B. David, M. Leoni, P. Scardi, *Mater. Sci. Forum* **2010**, *651*, 187–200.
[49] J. S. O. Evans, *Mater. Sci. Forum* **2010**, *651*, 1–9.
[50] V. I. Fadeeva, A. S. Kagan, L. S. Zevin, *Acta Crystallogr., Sect. A* **1977**, *33*, 386–389.
[51] A. Rečnik, I. Nyirő-Kósa, I. Dódony, M. Pósfai, *CrystEngComm* **2013**, *15*, 7539.
[52] S. V. Tsybulya, L. P. Solov'eva, G. N. Kryukova, E. M. Moroz, *J. Struct. Chem.* **1991**, *32*, 325–331.
[53] A. A. Coelho, *Topas Academic*, Coelho Software **2016**.
[54] K. Momma, F. Izumi, *J. Appl. Crystallogr.* **2011**, *44*, 1272–1276.
[55] S. Chen, Y. Wu, P. Cui, W. Chu, X. Chen, Z. Wu, *J. Phys. Chem. C* **2013**, *117*, 25019–25025.
[56] H. S. C. O'Neill, W. A. Dollase, *Phys. Chem. Minerals* **1994**, 541–555.
[57] D. Carta, C. Marras, D. Loche, G. Mountjoy, S. I. Ahmed, A. Corrias, *J. Chem. Phys.* **2013**, *138*, 54702.
[58] G. Kortüm, W. Braun, G. Herzog, *Angew. Chem. Int. Ed. Engl.* **1963**, *2*, 333–341.
[59] B. D. Viezbicke, S. Patel, B. E. Davis, D. P. Birnie, *Phys. Status Solidi B* **2015**, *252*, 1700–1710.
[60] P. Parhi, V. Manivannan, *J. Eur. Ceram. Soc.* **2008**, *28*, 1665–1670.
[61] M. Schmidt, Z. Wang, C. Kant, F. Mayr, S. Toth, A. T. M. N. Islam, B. Lake, V. Tsurkan, A. Loidl, J. Deisenhofer, *Phys. Rev. B* **2013**, *87*.
[62] J. Himmrich, H. D. Lutz, *Solid State Commun.* **1991**, *79*, 447–452.
[63] H. D. Lutz, B. Müller, H. J. Steiner, *J. Solid State Chem.* **1991**, *90*, 54–60.
[64] H. J. H. Fenton, *J. Chem. Soc. Trans.* **1894**, *65*, 899–910.
[65] G. Ruppert, R. Bauer, G. Heisler, *J. Photochem. Photobiol. A: Chem.* **1993**, *73*, 75–78.
[66] United States Environmental Protection Agency, *Wastewater Technology Fact Sheet Ozone Disinfection*, can be found under https://www3.epa.gov/npdes/pubs/ozon.pdf **1999**.
[67] F. Zhang, J. Zhao, T. Shen, H. Hidaka, E. Pelizzetti, N. Serpone, *Appl. Catal. B* **1998**, *15*, 147–156.
[68] A. T. Kuvarega, R. W. M. Krause, B. B. Mamba, *J. Phys. Chem. C* **2011**, *115*, 22110–22120.
[69] I. Poulios, E. Micropoulou, R. Panou, E. Kostopoulou, *Appl. Catal. B* **2003**, *41*, 345–355.
[70] C. G. Anchieta, E. C. Severo, C. Rigo, M. A. Mazutti, R. C. Kuhn, E. I. Muller, E. M. M. Flores, R. F. P. M. Moreira, E. L. Foletto, *Mater. Chem. Phys.* **2015**, *160*, 141–147.
[71] L. Han, X. Zhou, L. Wan, Y. Deng, S. Zhan, *J. Environ. Chem. Eng.* **2014**, *2*, 123–130.
[72] A. I. Borhan, P. Samoila, V. Hulea, A. R. Iordan, M. N. Palamaru, *J. Photochem. Photobiol. A: Chem.* **2014**, *279*, 17–23.
[73] H. M. Burt, A. G. Mitchell, *Int. J. Pharmaceutics.***1981**, *9*, 137–152.
[74] D. J. Fermín, E. A. Ponomarev, L. M. Peter, *J. Electroanal. Chem.* **1999**, *473*, 192–203.
[75] *Guidelines for Drinking-Water Quality*, 2nd ed., *Health Criteria and other Supporting Information*, World Health Organization, Geneva **1998**.
[76] R. Abe, K. Hara, K. Sayama, K. Domen, H. Arakawa, *J. Photochem. Photobiol. A: Chem. Chem.* **2000**, *137*, 63–69.

Received: March 2, 2018
Published online: June 12, 2018

Supporting information

On the Hazardous Origin of Photocatalytic Activity of $ZnCr_2O_4$

S.1. Ferrioxalate actinometry

The irradiation intensity was measured with ferrioxalate actinometry.[1–3] Fresh $K_3[Fe(C_2O_4)_3] \cdot 3\ H_2O$ was synthesized from 2.03 g $FeCl_3 \cdot 6\ H_2O$ (Sigma Aldrich) and 4.15 g $K_2C_2O_4 \cdot H_2O$ (Merck) in demin. water and purified by recrystallization from hot demin. water. 0.59 g of $K_3[Fe(C_2O_4)_3] \cdot 3\ H_2O$ (0.001 mmol) were dissolved in 50 mL diluted sulfuric acid (0.05 M, BCD) under dark conditions in the same round bottom flask with cooling jacket as used in the photo catalytic experiments. Before and during illumination every 20 to 25 sec 1 mL of the solution was extracted and added in each case to a solution of 1.2 mg (6.67 µmol) 1,10-phenanthroline (ABCR), 0.1155 g (1.50 mmol) ammonium acetate (Fluker) and 21.2 µL 96 % sulfuric acid filled up to 9 mL with demin. water. The samples were mixed in the dark and subsequently analyzed with UV/Vis spectroscopy. The maximum of the absorption peak at 511 nm gave the concentration of the generated amount of Fe^{2+} ions by photo reduction which is equal to the amount of photons passing the reaction vessel.

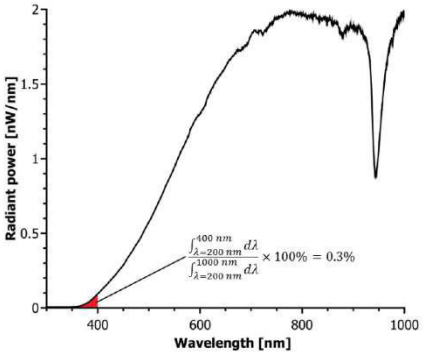

Fig. S1 Light spectrum of the halogen lamp Osram Hal SST 116 W 240 V E27 measured with a RPS-Mini-UV-CST Miniature USB Spectrometer

S.2. Analysis of the precursor $(NH_4)_2[Zn(NH_3)_2(CrO_4)_2]$

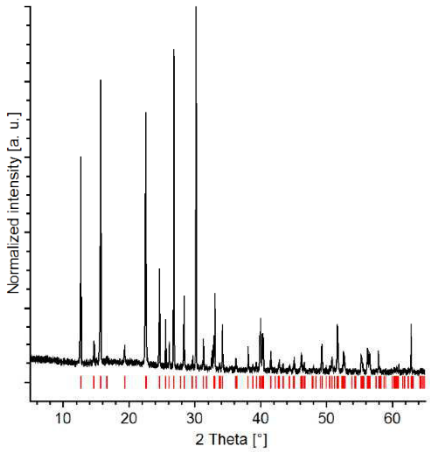

Fig. S2 XRD pattern of $(NH_4)_2[Zn(NH_3)_2(CrO_4)_2]$ (—) with reflection positions shown as vertical bars (—)[4].

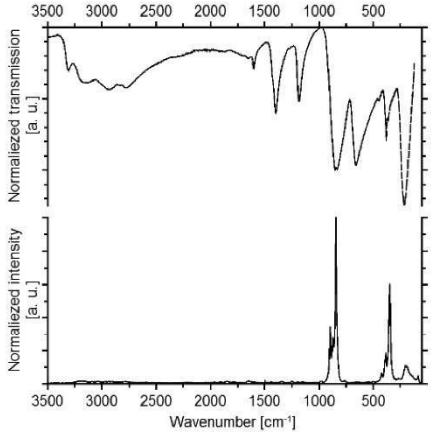

Fig. S3 MIR-/FIR (Top, —/ - -) and FT-Raman spectrum (Bottom, —) of the precursor $(NH_4)_2[Zn(NH_3)_2(CrO_4)_2]$. The MIR/FIR absorptions are: NH_4^+/NH_3 stretching modes at 2800 - 3300 cm^{-1}, NH_3 deformation vibration at 1603 cm^{-1}, NH_4^+/NH_3 deformation mode at 1398 cm^{-1}, NH_3 deformation vibration at 1184 cm^{-1}, Zn-NH_3 rocking at 655 cm^{-1}, Zn-NH_3 stretching at 375 cm^{-1}, H_3N-Zn-NH_3 bending at 209 cm^{-1}.[S2] The Raman modes are assigned: CrO_4^{2-} at 300 - 400 cm^{-1} and 800 - 900 cm^{-1}.[5]

S.3. Rietveld refinements

Rietveld refinements were done with *Topas Academic*[6] starting with structural data for $ZnCr_2O_4$[7]. The peak broadening was considered isotropic and anisotropic. In the anisotropic case we used an approach of Carlos Paiva-Santos, Selma G. Antonio and Alan Coelho (http://topas.dur.ac.uk/topaswiki/doku.php?id=anisotropic_hkl), which calculates values for crystallite sizes along sets of lattice planes (00l), (0kl) and (hkl) with the help of the Scherrer equation generalized by Stokes and Wilson[8]:

$$CS = \frac{K \cdot \lambda}{\beta \cdot \cos(\theta)} \quad (1)$$

with a shape factor K = 0.89, the wave length λ, the integral breadth β, the Bragg angle θ, resulting in the crystallite size CS. If the crystallite size along the {00l}, {0kl} and {hkl} planes is plotted in a 3D plot the averaged crystallite morphology is generated. In the case of isotropic line broadening a spherical morphology is expected, as seen for ZC400, ZC500 and ZC600.

For determination of the inversion parameter the atomic positions of the octahedral and tetrahedral site were doubled, and the occupancy of these positions was described as follows:

Zinc on tetrahedral site = 1- *Inv*;
Chromium on tetrahedral site = *Inv*;
Zinc on octahedral site = *Inv*/2;
Chromium on octahedral site = 1-*Inv*/2;

with the inversion parameter *Inv* representing the percentage amount of zinc atoms switched from the tetrahedral to the octahedral site. The stoichiometry is expected to be Zn:Cr = 1:2, so the total occupancy of the tetrahedral site and octahedral site is 1.

For the separately utilised WPPM (Whole Powder Pattern Modelling) analysis the implemented macro *"WPPM_Sphere_Ln_Normal"* was used, generating the μ and σ value of a log normal distribution:

$$N(CS) = \frac{1}{\sqrt{2\pi}\sigma CS} \exp\left(-\frac{(\ln(CS)-\mu)^2}{2\sigma^2}\right) \quad (2)$$

with *N* the relative count of crystallites with the size *CS* > 0, μ > 0.1 and σ > 0.1. The macro works with the assumption that each amount of crystallites with a defined crystallite size affects the shape of the reflections with an associated peak width and height at a fixed position.

Rietveld refinement of stacking faults:
The refinement of XRD data was first done with the spinel structure (see Tab. S2). Applying the matrix

$$\begin{Bmatrix} -1/2 & 0 & 1 \\ 1/2 & -1/2 & 1 \\ 0 & 1/2 & 1 \end{Bmatrix} \quad (3)$$

gives the spinel structure with a hexagonal unit cell in space group P1 (see Tab. S3). The former {111} plane in the cubic cell is now the (001) plane, a stacking of the unit cell along the c-axis gives a fault free structure. But a shift by certain vectors results in defined stacking faults, and there are three types of translation vectors:

$$v_1 = \begin{pmatrix} 0.5 \\ 0 \\ z \end{pmatrix} = \begin{pmatrix} -0.5 \\ 0 \\ z \end{pmatrix}, v_2 = \begin{pmatrix} 0 \\ 0.5 \\ z \end{pmatrix} = \begin{pmatrix} 0 \\ -0.5 \\ z \end{pmatrix}, v_3 = \begin{pmatrix} 0.5 \\ 0.5 \\ z \end{pmatrix} = \begin{pmatrix} -0.5 \\ -0.5 \\ z \end{pmatrix} \quad (4)$$

All these translations occur in a distinct quantity which is identical for v_1, v_2 and v_3 due to symmetry of the spinel lattice. But the translation leads to a postion of Cr^{III} sites in the (001) plane at a distance of 1.8 Å next to Zn^{II} sites of (0/0/0.875) of the cation layer below. This must be compensated by a sufficient number of cation vaccancies on these positions. Hence, a set of stacking sequences (choosen to be 100) is generated simulating different crystallites with different stackings to result in a satisfactory average. The amount of stacked unit cells was choosen to be in the range of the experimentally determined crystallite sizes. During the first runs of refinement the probability of stacking faults was chosen to match the intensities of the reflections at 58 and 62 °2Θ. A good refinement result was obtained with size and strain contributions. For further improvements parameters for partial inversion were added. Finally a fault free phase of $ZnCr_2O_4$ with the same domain size and strain was added and refined simultanously. This procedure reduced the total probabilty of stacking faults to a reasonable number leading to satisfactory modelling of the XRD data. The total probability $P_{(stacking\ faults\ total)}$ of stacking faults is calculated as the product of the mass fraction $W_{(weight\ fraction\ faulted\ phase)}$ and the stacking fault probability of the faulted phase $P_{(stacking\ faults\ local)}$.

$$P_{(stacking\ fault\ total)} = P_{(stacking\ faults\ local)} \times W_{(weight\ fraction\ faulted\ phase)} \quad (5)$$

The amount of cation vacancies in the plane of stacking faults $V_{Cations\ at\ (0,0,1)\ and\ (0,0,0.875)}$ is calculated as product of the weight fraction of the faulted phase $W_{(weight\ fraction\ faulted\ phase)}$ and the deviation of the occupancy of the atom sites $Occ_{(0,0,1)\ and\ (0,0,0.875)}$ from 1 at the stackingfault.

$$V_{Cations\ at\ (0,0,1)\ and\ (0,0,0.875)} = \left(1 - Occ_{(0,0,1)\ and\ (0,0,0.875)}\right) \times W_{(weight\ fraction\ faulted\ phase)} \quad (6)$$

The values obtained during the refinements are given in Tab. S1.

Tab. S1 $\chi 2$, stacking fault probability $P_{(stacking\ faults\ total)}$, cation vacancies, partial inversion and strain obtained by Rietveld refinements.

Sample	*χ2*	*Domain size [nm]*	$P_{(stacking\ faults\ total)}$ *[%]*	$V_{Cations\ at\ (0,0,1)\ and\ (0,0,0.875)}$ *[%]*	*Partial inversion [%]*	*Strain ε_0x1000*
ZC400w	*1.940*	*2.8±0.1*	*40*	*37.0*	*19.4±0.2*	*3.95±0.40*
ZC400	*2.381*	*6.1±0.1*	*29*	*7.9*	*10.5±0.2*	*1.59±0.05*
ZC500	*1.892*	*7.8±0.1*	*27*	*2.2*	*8.8±0.2*	*1.36±0.04*
ZC600	*2.312*	*24±0.7*	*5*	*0*	*4.8±0.2*	*1.26±0.05*
ZC750	*3.526*	*66±4*	*2*	*0*	*3.9±0.2*	*1.29±0.03*

Tab. S2 Starting lattice parameters for Rietveld refinements

Space group	*International Tables Number*	*Lattice parameter*	
		a=b=c	*α=β=γ*
Fd-3mZ	*227 setting 2*	*8.3267 Å*	*90°*
Atom type	*Site*	*x = y = z*	*Occupancy*
Zn^{II}	*8a*	*0.125*	*1*
Cr^{III}	*16d*	*0.500*	*1*
O^{-II}	*32e*	*0.26157*	*1*

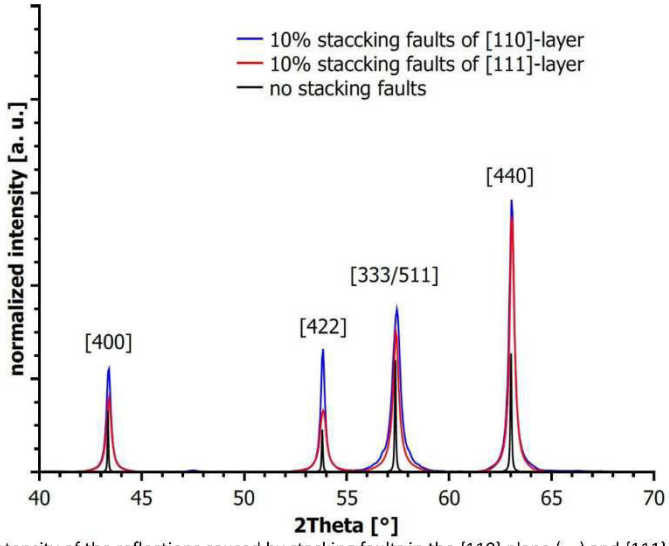

Fig. S4 Change in intensity of the reflections caused by stacking faults in the {110} plane (—) and {111} plane (—) compared with theoretical pattern for perfect $ZnCr_2O_4$(—). Simulations were done with Diffax[9].

Tab. S3 Lattice parameters and atomic positions for Rietveld refinements of stacking faults						
Space group	*Lattice parameter*					
	a	*b*	*c*	*α*	*β*	*γ*
P1	*5.8881 Å*	*5.8881 Å*	*14.423 Å*	*90°*	*90°*	*120°*
Atom type	*x*		*y*		*z*	
Zn^{II}	0.0		0.0		0.125	
Zn^{II}	0.0		0.0		0.875	
Zn^{II}	2/3		1/3		0.45833	
Zn^{II}	2/3		1/3		0.20833	
Zn^{II}	1/3		2/3		0.79167	
Zn^{II}	1/3		2/3		0.54167	
Cr^{III}	0.0		0.0		0.5	
Cr^{III}	2/3		1/3		5/6	
Cr^{III}	1/3		2/3		1/6	
Cr^{III}	1/6		1/3		1/3	
Cr^{III}	5/6		2/3		2/3	
Cr^{III}	2/3		5/6		1/3	
Cr^{III}	1/3		1/6		2/3	
Cr^{III}	1/6		5/6		1/3	
Cr^{III}	5/6		1/6		2/3	
Cr^{III}	0.5		0.0		0	
Cr^{III}	0.0		0.5		0	
Cr^{III}	0.5		0.5		0	
O^{-II}	0.0		0.0		0.2616	
O^{-II}	0.0		0.0		0.73842	
O^{-II}	2/3		1/3		0.5949	
O^{-II}	2/3		1/3		0.07176	
O^{-II}	1/3		2/3		0.92826	
O^{-II}	1/3		2/3		0.40506	
O^{-II}	0.84880		0.69760		0.4128	
O^{-II}	0.15120		0.30240		0.58722	
O^{-II}	0.30240		0.15120		0.4128	
O^{-II}	0.69760		0.84880		0.58722	
O^{-II}	0.84880		0.15120		0.4128	
O^{-II}	0.15120		0.84880		0.58722	
O^{-II}	0.51547		0.03093		0.7461	
O^{-II}	0.81787		0.63573		0.92052	
O^{-II}	0.96907		0.48453		0.7461	
O^{-II}	0.36427		0.18213		0.92052	
O^{-II}	0.51547		0.48453		0.7461	
O^{-II}	0.81787		0.18213		0.92052	
O^{-II}	0.18213		0.36427		0.0795	
O^{-II}	0.48453		0.96907		0.25386	
O^{-II}	0.63573		0.81787		0.0795	
O^{-II}	0.03093		0.51547		0.25386	
O^{-II}	0.18213		0.81787		0.0795	
O^{-II}	0.48453		0.51547		0.25386	

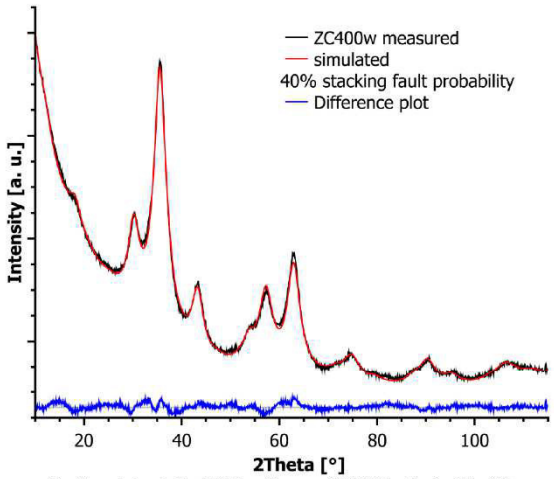

Fig. S5 Comparison of measured (—) and simulated XRD patterns of ZC400w (—) with difference plot (—).

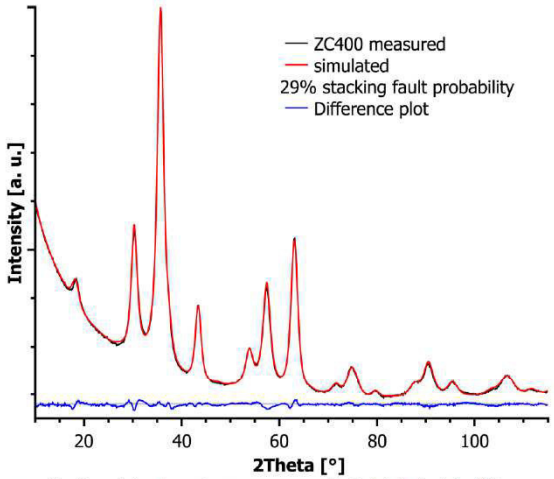

Fig. S6 Comparison of measured (—) and simulated XRD patterns of ZC400 (—) with difference plot (—).

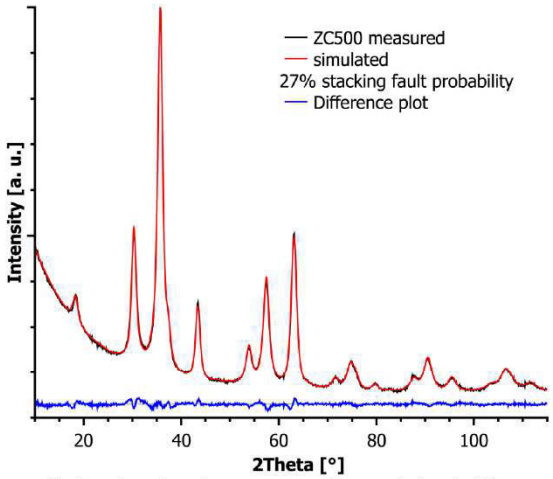

Fig. S7 Comparison of measured (—) and simulated XRD patterns of ZC500 (—) with difference plot (—).

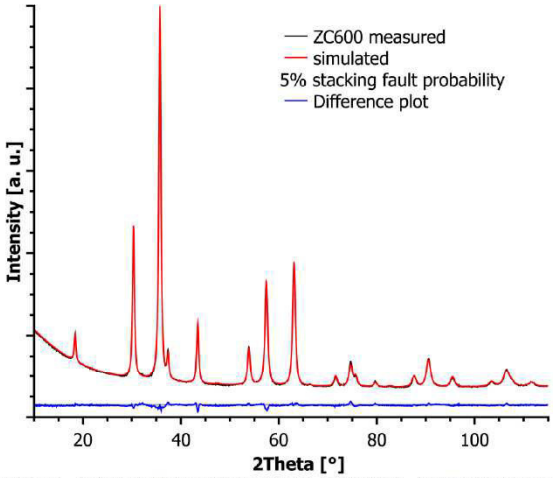

Fig. S8 Comparison of measured (—) and simulated XRD patterns of ZC600 (—) with difference plot (—).

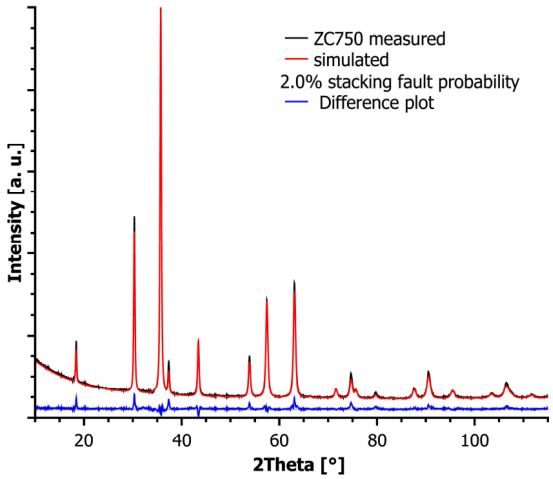

Fig. S9 Comparison of measured (—) and simulated XRD patterns of ZC750 (—) with difference plot (—).

S.4. Further characterization of the catalysts

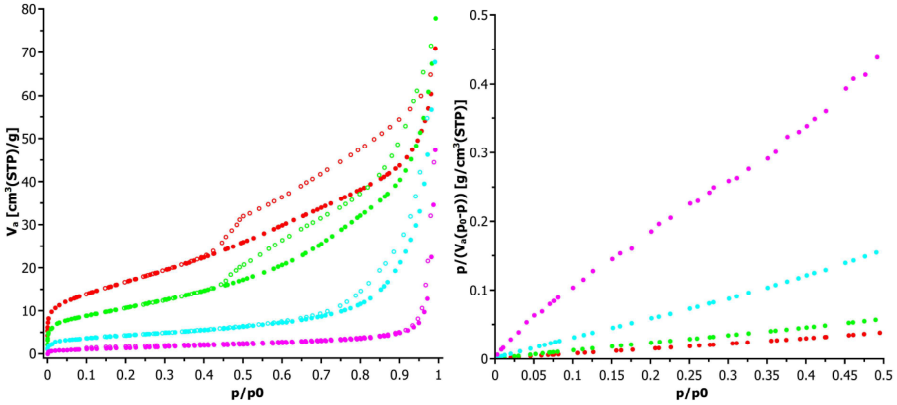

Fig. S10 N_2 sorption curves (left) and plot of the data according to the Method of Brunauer Emmett and Teller[10] (BET) of ZC750 (—), ZC600 (—), ZC500 (—) and ZC400 (—). The adsorption curves are presented as filled dots and the desorption curves are shown as empty spheres.

Tab. S4 Zink and Chromium content as percentage of the metal content determined with EDX measurements.

Sample	*Zn-content [%]*	*Cr-content [%]*
ZC400	*31.8±0.9*	*68.3±1.3*
ZC500	*32.2±0.4*	*67.8±0.4*
ZC600	*31.7±1.2*	*68.3±1.2*
ZC750	*31.2±1.8*	*68.8±1.8*

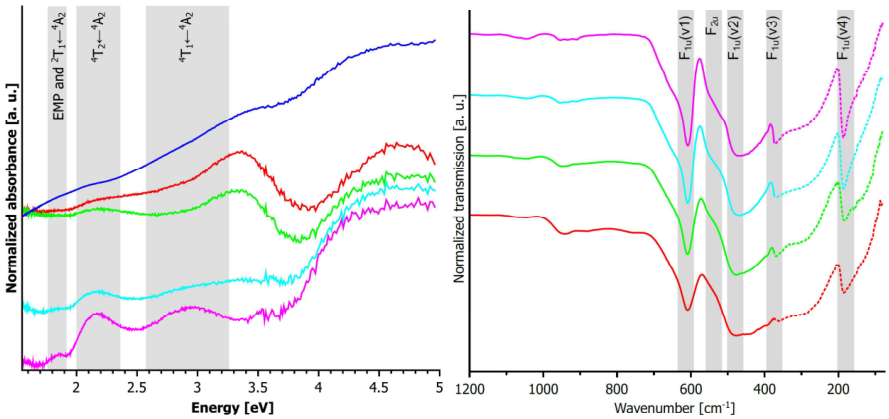

Fig. S11 (left) UV/Vis-Absorbance spectra of ZC750 (—), ZC600 (—), ZC500 (—), ZC400 (—) and ZC400w (—) mixed with $BaSO_4$ as internal white standard. The typical absorptions due to electron transitions can be observed[11]. The electron-magnon-phonon-absorption (EMP) at ~ 1.85 eV accompanied by $^2T_1 \leftarrow {}^4A_2$ is only visible for ZC750. An additional absorption at ~ 3.3 eV occurs for ZC400 and ZC500. (Right) MIR- and FIR-spectra of ZC750 (—/--), ZC600 (—/--), ZC500 (—/--) and ZC400 (—/--) show typical absorption bands of $ZnCr_2O_4$.[12,13]

S.5. Postcatalytic characterization

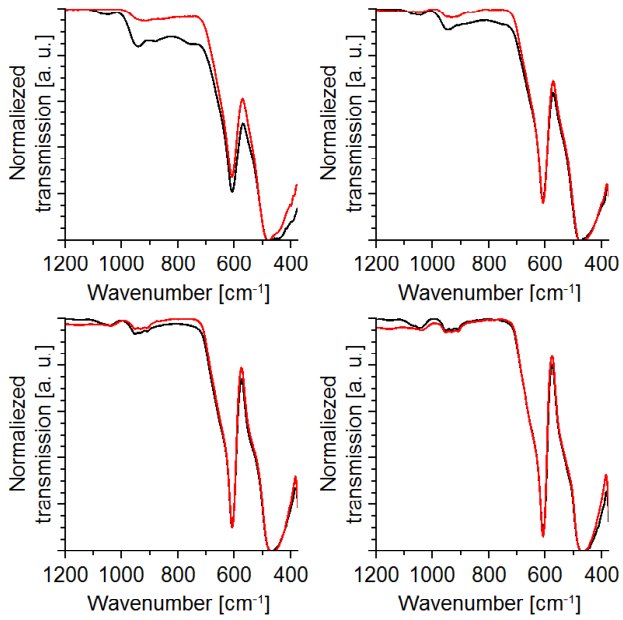

Fig. S12 MIR-spectra of the catalysts ZC750 (top left), ZC600 (top right), ZC500 (bottom left) and ZC400 (bottom right) before (—) and after photo catalysis (—).

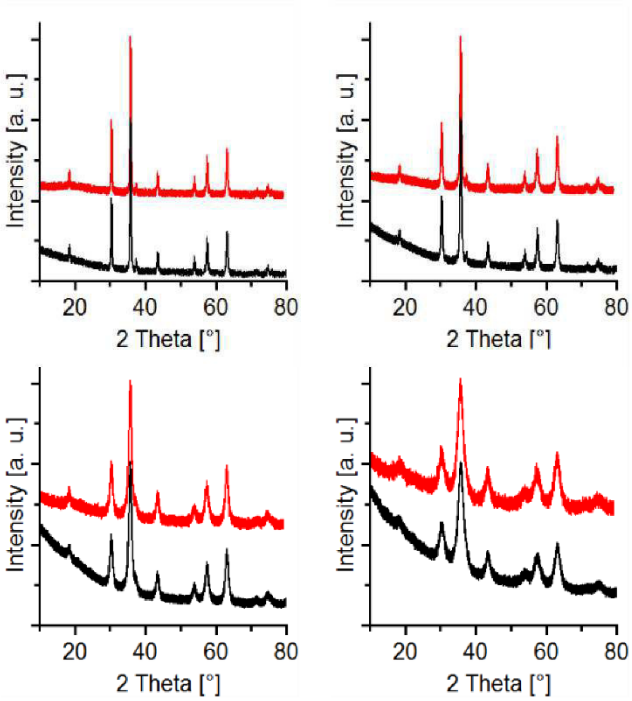

Fig. S13 XRD patterns of the photo catalysts ZC750 (top left), ZC600 (top right), ZC500 (bottom left) and ZC400 (bottom right) before (—) and after photo catalysis (—). It is obvious that the materials are still intact after the photocatalytic test.

S.6. TEM analysis

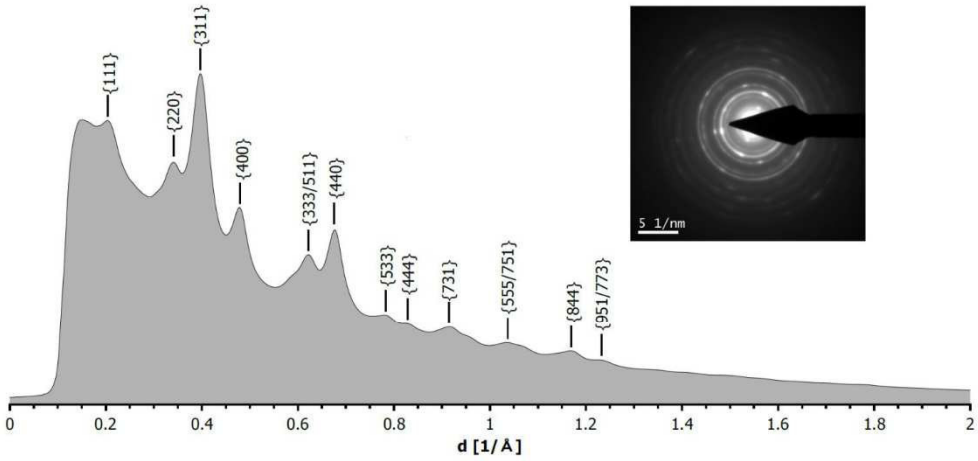

Fig. S1 Rotational average of the electron diffraction (inset) of ZC400 with indexing of the most intense reflections associated with $ZnCr_2O_4$ structure[7].

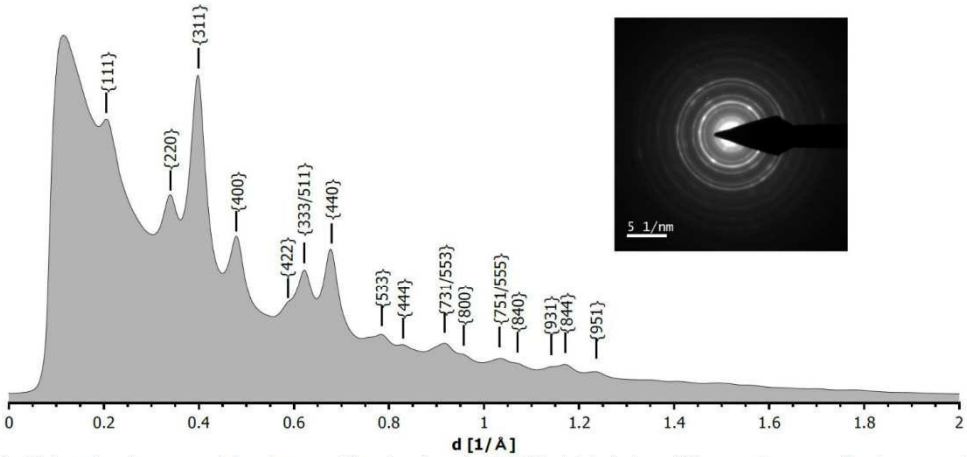

Fig. S2 Rotational average of the electron diffraction (inset) of ZC500 with indexing of the most intense reflections associated with $ZnCr_2O_4$ structure[7].

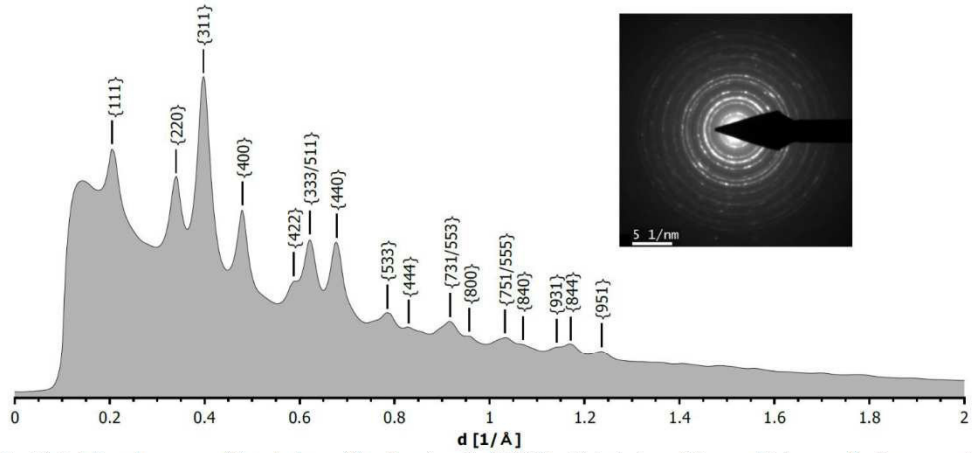

Fig. S3 Rotational average of the electron diffraction (inset) of ZC600 with indexing of the most intense reflections associated with $ZnCr_2O_4$ structure[7].

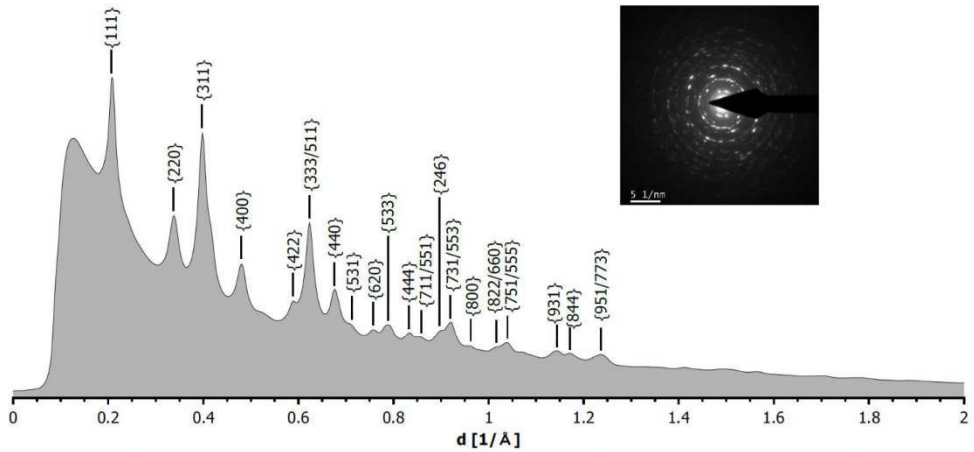

Fig. S17 Rotational average of the electron diffraction (inset) of ZC750 with indexing of the most intense reflections associated with $ZnCr_2O_4$ structure[7].

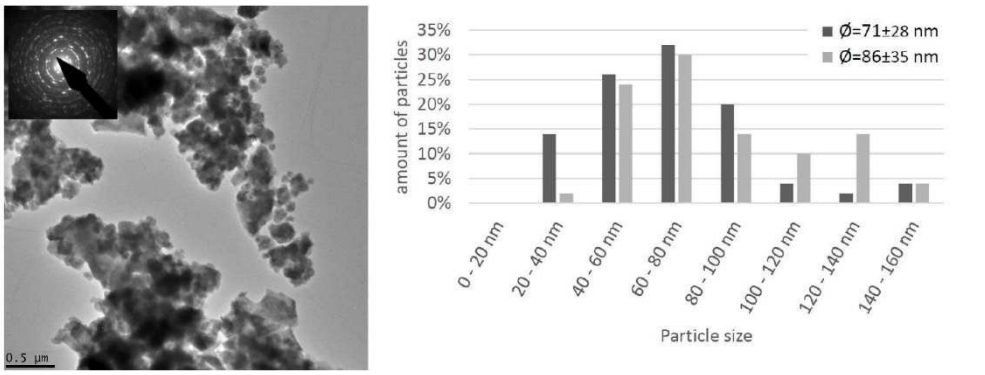

Fig. S18 Transmission electron microscope image of ZC750 (left) with electron diffraction pattern (inset) and statistical evaluation of particle sizes of ZC750 (right). The aspect ratio as quotient of long (light grey) to short (dark grey) diameter is 1.2.

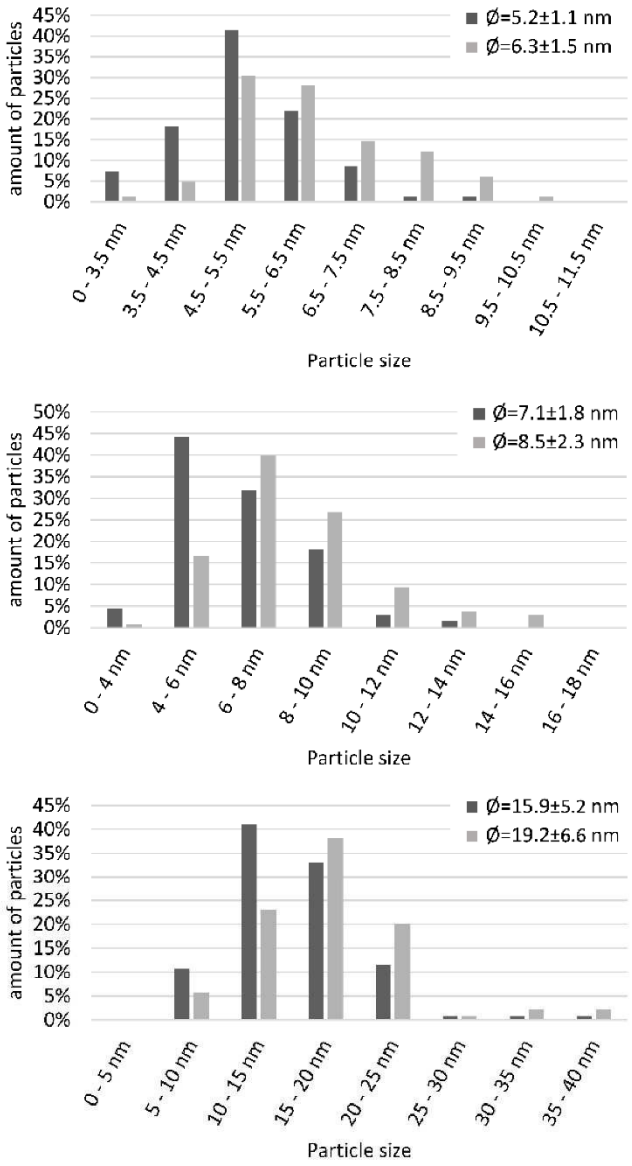

Fig. S19 Crystallite size distributions of ZC400, ZC500 and ZC600 (top to bottom). The aspect ratio as quotient of long (light grey) to short (dark grey) diameter is in all three cases 1.2.

S.7. Catalytic experiments

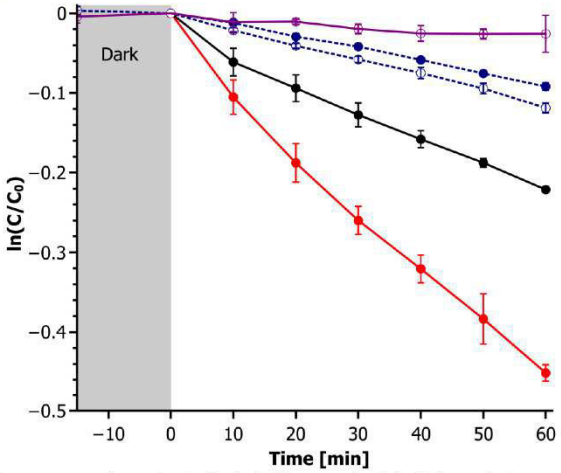

Fig. S20 Decrease of the concentration of y-Eosin including standard deviations during catalytic experiments with ZC400 without H_2O_2 (●) in comparison to P25 with H_2O_2 (○), K_2CrO_4 without H_2O_2 (●) and y-Eosin with (○) and without H_2O_2 (●). The grey area marks the time interval without illumination.

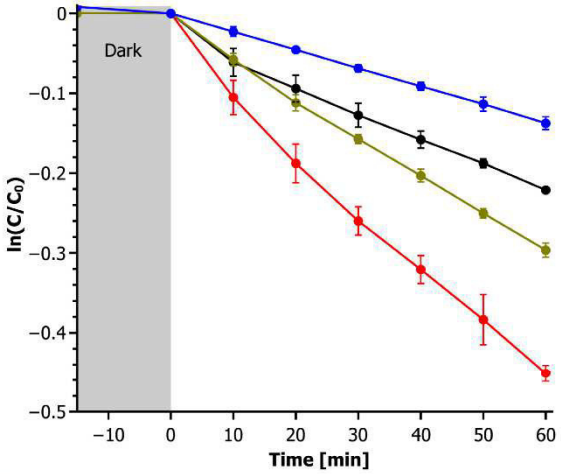

Fig. S21 Decrease of the concentration of y-Eosin including standard deviations without H_2O_2 during catalytic experiments with ZC400 as calcined (●) and after washing process (ZC400w) with (●) and without additional K_2CrO_4 (●) in comparison to degradation with K_2CrO_4 (●). The grey area marks the time interval without illumination.

S.8. Corrosion experiment

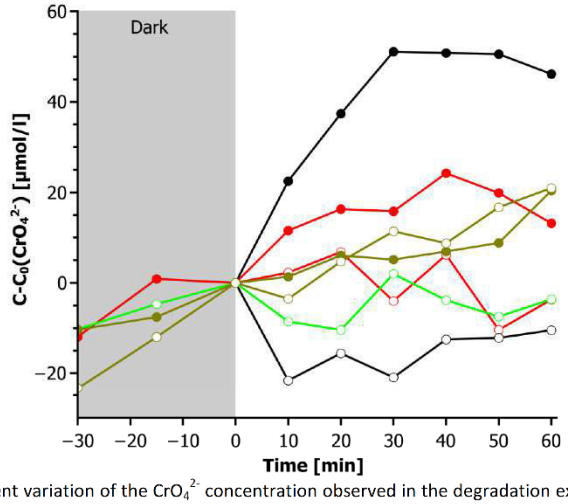

Fig. S22 Time dependent variation of the CrO_4^{2-} concentration observed in the degradation experiments with already high CrO_4^{2-} content corrected by the value at t=0. The colour coding is as follows: $KCrO_4$ (●/○), ZC500 (○), ZC400 (●/○), and ZC400w with addition of K_2CrO_4 (●/○). Data of experiments which were done with addition of H_2O_2 are displayed as hollow circles. The grey area marks time interval without illumination.

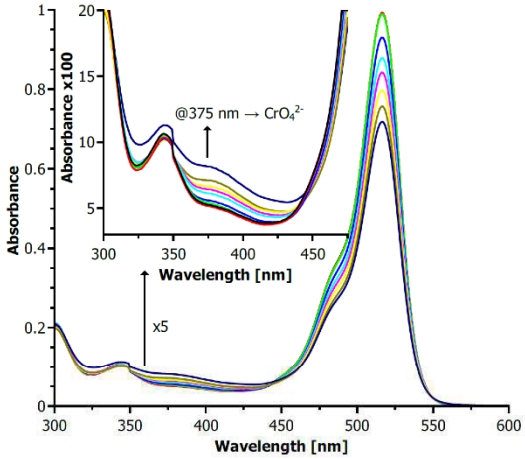

Fig. S23 Time dependent changes of UV/Vis spectra during photo catalysis with ZC750. Color coding is as follows: 30 min (—), 15 min (—) and 0 min (—) before irradiation and after 10 min (—), 20 min (—), 30 min (—), 40 min (—), 50 min (—) and 60 min (—) of irradiation. An increase of absorbance at 375 nm due to CrO_4^{2-} generation and dissolution is observable.

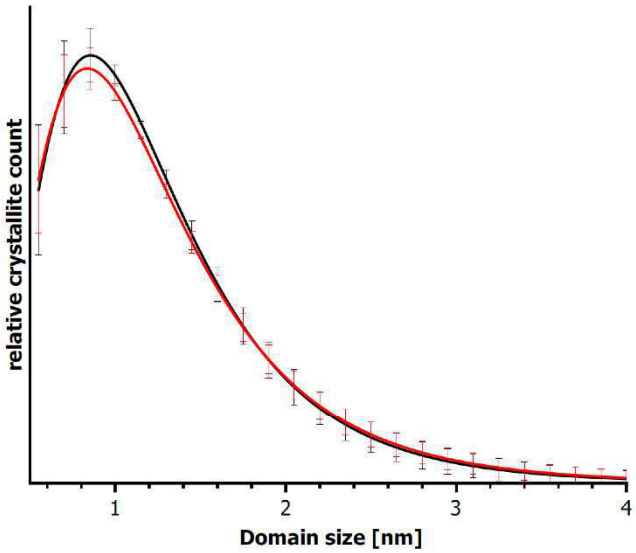

Fig. S24 log normal size distribution of crystallites of ZC400w (—) and ZC400wPC (—) after 15 hours of catalysis. There is a very small shift to lower domain sizes and lower relative amounts of small crystallites observable, which is an indication of corrosion of small crystallites.

S.9. mass spectrometry

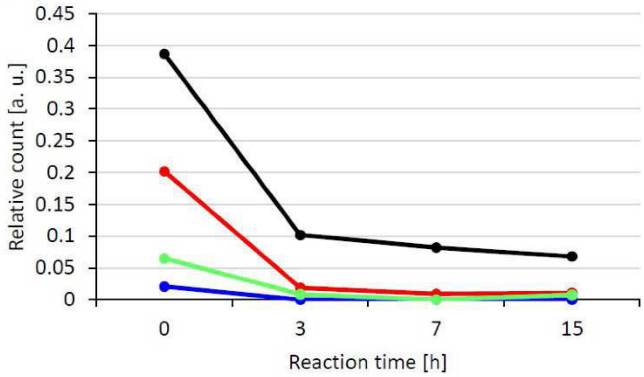

Fig. S25 Time dependent decrease of the mass signals of tribromide (●), dibromide (●), monobromide (●) and tetrabromide mono sodium salt (●) of y-Eosin in the MALDI-TOF spectra relative to the mass signal of the tetrabromide.

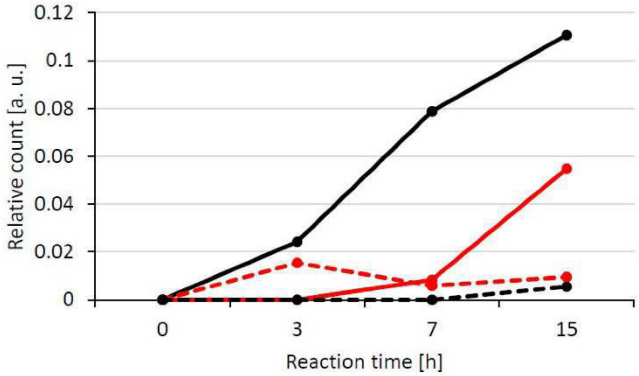

Fig. S26 Time dependent increase of the mass signals of the mono hydroxylated tribromide (584 m/z, —), tetrabromide (664 m/z, —) and double hydroxylated tribromide (602 m/z, - -) and tetrabromide (680 m/z, - -).

S.10. References

1 H. J. Kuhn, S. E. Braslavsky and R. Schmidt, Chemical Actinometry, *Pure Appl. Chem.*, **2004**, *76*, 2105–2146.

2 C. G. Hatchard and C. A. Parker, A new sensitive chemical actinometer, *Proc. R. Soc. London, Ser. A*, **1956**, *235*, 518–536.

3 C. A. Parker, A new sensitive chemical actinometer, *Proc. R. Soc. London, Ser. A*, **1953**, *220*, 104–116.

4 M. Harel, C. Knobler and J. D. McCullough, The Crystal Structure of the Ammonium Salt of Catena-di-μ-chromato-diamminezincate(II),$(NH_4)_2[Zn(NH_3)_2(CrO_4)_2]$, *Inorg. Chem.*, **1969**, *8*, 11–13.

5 G. Socrates, *Infrared and Raman Characteristic Group frequencies*, Wiley VCH, 3rd edn., **2004**.

6 A. A. Coelho, *Topas Academic*, Coelho Software, **2016**.

7 H. Sawada, Electron Density Study of Spinels: Zinc Chromium Oxide, *Mater. Res. Bull.*, **1997**, *32*, 873–878.

8 B. David, M. Leoni and P. Scardi, Domain size analysis in the Rietveld method, *Mater. Sci. Forum*, **2010**, *651*, 187–200.

9 M. M. J. Treacy, M. W. Deem and J. M. Newsam, *Diffax*, **2005**.

10 S. Brunauer, P. H. Emmett and E. Teller, Adsorption of Gases in Multimolecular Layers, *J. Am. Chem. Soc.*, **1938**, *60*, 309–310.
11 M. Schmidt, Z. Wang, C. Kant, F. Mayr, S. Toth, Islam, A. T. M. N., B. Lake, V. Tsurkan, A. Loidl and J. Deisenhofer, Exciton-magnon transitions in the frustrated chromium antiferromagnets $CuCrO_2$, α - $CaCr_2O_4$, $CdCr_2O_4$, and $ZnCr_2O_4$, *Phys. Rev. B*, **2013**, *87*.
12 J. Himmrich and H. D. Lutz, Normal coordinate analyses and lattice dynamical calculations of spinel-type $ZnCr_2O_4$, *Solid State Commun.*, **1991**, *79*, 447–452.
13 H. D. Lutz, B. Müller and H. J. Steiner, Lattice vibration spectra. LIX. Single crystal infrared and Raman studies of spinel type oxides, *J. Solid State Chem.*, **1991**, *90*, 54–60.

3.2. „New Transition Metal Oxo-Thiostannate: Synthesis, Characterization and Investigation of its Photocatalytic Properties“

Die Kristallstruktur der ungewöhnlichen Verbindung {[Ni(1,4,7,10-Tetraazacyclododecan)]$_6$[$Sn_6(OH)_6O_2S_{12}$]}·2(ClO_4)·19H_2O enthält das selten beobachtete [$Sn_6(OH)_6O_2S_{12}$]$^{10-}$-Anion, welches aus zwei $Sn(OH)_3OS_2$- und zwei SnO_2S_4-Oktaedern sowie zwei SnS_4-Tetraeder besteht. An das Anion sind die Ni^{2+}-zentrierten Komplexe über Ni-S- und Ni-OH-Bindungen gebunden. Diese Verbindung weist in einem Gemisch aus Triethylamin, Acetonitril, Wasser und dem Photosensibilisator [Ru(2,2‘-Bipyridin)$_3$](PF_6)$_2$ bei Bestrahlung mit Licht eine hohe photokatalytische Aktivität auf und nach 3 Stunden werden 26.6 mmol/g_{cat} H_2 generiert. Nach der Photokatalyse konnten in dem Lösungsmittelgemisch qualitativ Nanoteilchen nachgewiesen werden, welche während der Reaktion gebildet werden. Wegen der Komplexität des Systems und der vielen Einflussfaktoren konnte jedoch nicht geklärt werden, ob der Wasserstoff katalytisch durch {[Ni(1,4,7,10-Tetraazacyclododecan)]$_6$[$Sn_6(OH)_6O_2S_{12}$]}·2(ClO_4)·19H_2O generiert wird, oder ob die Nanoteilchen dafür verantwortlich sind.

Journal of Inorganic and General Chemistry
ZAAC
Zeitschrift für anorganische und allgemeine Chemie
DOI: 10.1002/zaac.201800475
ARTICLE

New Transition Metal Oxo-Thiostannate: Synthesis, Characterization, and Investigation of its Photocatalytic Properties

Assma Benkada,[a] Michael Poschmann,[a] Christian Näther,[a] and Wolfgang Bensch*[a]

Abstract. The new transition metal oxo-thiostannate $\{[Ni(cyclen)]_6[Sn_6S_{12}O_2(OH)_6]\}\cdot 2(ClO_4)\cdot 19H_2O$ (1) was prepared under hydrothermal conditions using $Na_4SnS_4\cdot 14H_2O$ and $[Ni(cyclen)](ClO_4)_2$ as reactants. In the crystal structure the rare $[Sn_6S_{12}O_2(OH)_6]^{10-}$ anion is observed, which is composed of $SnS_2O(OH)_3$ and SnS_4O_2 octahedra, and SnS_4 tetrahedra sharing edges and corners. The anion is expanded by six Ni^{2+} centered complexes via Ni–S and Ni–OH bonds. The photocatalytic properties for the visible light driven hydrogen evolution reaction shows that 26.6 mmol·g^{-1} H_2 were evolved after 3 h.

Introduction

Thiostannates and oxo-thiostannates and tin-sulfur compounds are an interesting group among the group of thiometalates compounds that show a versatile structural behavior and are promising candidates as catalysts, ion exchangers, absorbers and as sensors.[1–4] Due to the variable coordination number and oxidation state of tin, the different tin building units like tetrahedron, trigonal bipyramid, and octahedron are observed in the crystal structures of thiostannates.[5] The most thiostannates(IV) and tin-sulfur compounds contain the $[Sn_2S_6]^{4-}$ anion,[6] which is formed by two edge-sharing $[SnS_4]^{4-}$ tetrahedra. The $[Sn_2S_6]^{4-}$ anion is either isolated as in $Na_4Sn_2S_6\cdot 14H_2O$,[7] $[Ni(2amp)_3][Sn_2S_6]\cdot 9.5H_2O$,[8] $[Ni(tren)(amine)]_2[Sn_2S_6]\cdot nH_2O$ [amine = 1,2-diaminocyclohexane (1,2-dach); 2-(aminomethyl)pyridine (2amp); ethylendiamine (en); 1,2-diaminopropane (1,2-dap); n = 2, 3, 4, 6, 10],[9] $[Ni(aepa)_2]_2[Sn_2S_6]$ (aepa = *N*-2-aminoethyl-1,3-propandiamine), $[Ni(peha)][Sn_2S_6]\cdot H_2O$ (peha = pentaethylenehexamine), $[Co(dien)_2]_2[Sn_2S_6]$ (dien = diethylenetriamine),[10] $[M(en)_3]_2[Sn_2S_6]$ (M = Co, Mn, Zn),[11] or is bonded covalently to transition metal cations such as in $\{[M(tepa)]_2[Sn_2S_6]\}$ (M = Co, Fe, Ni; tepa = tetraethylenepentamine)[12] forming neutral complexes.

In addition to the $[Sn_2S_6]^{4-}$ anion, different other thiostannate anions like $[SnS_3]^{2-}$, $[SnS_4]^{4-}$, $[Sn_2S_5]^{2-}$, $[Sn_2S_7]^{6-}$, $[Sn_2S_8]^{2-}$, $[Sn_3S_7]^{2-}$, $[Sn_4S_9]^{2-}$, $[Sn_5S_{12}]^{4-}$ [13–17] or the tetrameric adamantane-like unit $[Sn_4S_{10}]^{4-}$ are known.[13] In the above mentioned anions tin is in the oxidation state IV. However, in the compounds $BaLnSn_2S_6$ (Ln = Ce, Pr, Nd),[18] $(trenH_3)Cu_7Sn_4S_{12}$,[19] $[(Ph_3PCu)_6\{(CH_2)_4SnS_2\}_6Cu_4Sn]$,[20] $[(R^2Sn)_2SnS_4]$, $\{[(R^2Sn)(R^{fC4}Sn)SnS_4]_2FeR^{fCO}\}$ {R^2 = $C(Me)_2CH_2C(Me)=NNH_2$, R^{fC4} = $[C(Me)_2CH_2C(Me)=N–NHC(O)]fC[C(O)NH–NH_2$, and R^{fCO} = $[fC(COO)_2]^{2-}$},[21] $[(CuPPh_3)_2(Sn^{II}Cl)_2\{(RSn^{IV})_2Se_4\}_2]$, $[(CuPPh_3)_2(Sn^{II}Cu_2)\{(R^1Sn^{IV})_2Se_4\}_3]$, $[(CuPPh_3)_2(Sn^{II}Cl)_2\{(R^1Sn^{IV}Cl)Se_2\}_2]$ and $[Cu(CuPPh_3)(Sn^{II}Cu_2)\{(R^1Sn^{IV})_2Se_4\}_3]$ [R^1 = $CMe_2CH_2C(O)Me$] [22] tin adopts the oxidation states II and IV, whereas in $[\{(CMe_2CH_2COMe)Sn\}_2(\mu\text{-}S)_2\}Sn_2S_6]$,[23] Sn^{III} and Sn^{IV} cations are observed.

In contrast to $[Sn_xS_y]^{n-}$ anions, oxo-thiostannate anions $[Sn_xS_yO_z]^{n-}$ are relatively rare and much less investigated. Prominent representatives are $[Sn_{10}S_{20}O_4]^{8-}$,[24,25] $[Sn_{10}S_{16}O_4Cl_4]_n$,[26] $[Sn_8S_{12}O_4(SPh)_6]^{6-}$,[27] $[Sn_8S_{12}O_2(OH)_2Cl_6]^{4-}$,[26] and $[Sn_4S_5(S_3)OCl_4]^{2-}$.[28] Among these anions the $[Sn_{10}S_{20}O_4]^{8-}$ anionic cluster is most common. It has an idealized T_d symmetry and can be described as a supertetrahedral cluster (denoted as T3) formed by ten corner-linked SnS_4 polyhedra. Four empty sites are occupied by O^{2-} anions expanding the coordination number of Sn from four to five or six.[24,25,29] All Sn-O-S compounds contain isolated $[Sn_{10}S_{20}O_4]^{8-}$ anionic clusters with inorganic cations compensating the negative charges like in $[Cs_8(H_2O)_{13}][Sn_{10}S_{20}O_4]$[29] and $[Li_8(H_2O)_{29}][Sn_{10}S_{20}O_4]\cdot 2H_2O$,[24] and only in $\{[Ni(1,2\text{-dach})_2(ma)]_4[Sn_{10}S_{20}O_4]\}$ (1,2-dach = 1,2-diaminocyclohexane; ma = methylamine)[30] the cluster is expanded via sulfur atoms to Ni^{2+} centered complexes.

In this context, we have reported on a new oxo-thiostannate with the composition $[Ni(cyclen)(H_2O)_2]_4[Sn_{10}S_{20}O_4]\cdot ca\cdot 13H_2O$ that consists of a T3-type $[Sn_{10}S_{20}O_4]$ cluster anion. The negative charge is compensated by Ni^{2+} cations that are coordinated by four nitrogen atoms of a cyclen ligand. The octahedral Ni coordination is completed by two additional water molecules that occupies the axial positions, leading to the formation of a $[Ni(cyclen)(H_2O)_2]^{2+}$ cation. Therefore, they are not connected to the cluster anion. Surprisingly, the oxothiostannate cluster has formed only by the reaction of $[Ni(cyclen)(H_2O)_2](ClO_4)_2\cdot H_2O$ with $Na_4SnS_4\cdot 14H_2O$ in water. The reaction mechanism for the formation of this oxo-

* Prof. Dr. W. Bensch
Fax: +49-431-880-1520
E-Mail: wbensch@ac.uni-kiel.de
[a] Institute of Inorganic Chemistry
Christian-Albrechts-University of Kiel
Max-Eyth-Str. 2
<postCode/24118 Kiel, Germany
Supporting information for this article is available on the WWW under **http://dx.doi.org/10.1002/zaac.201800475** or from the author.

cluster is still not fully understood, but it is assumed that $[SnS_3(OH)]^{3-}$ is formed, which condense to generate $[Sn_2S_5O]^{4-}$ that further reacts with $[Sn_2S_7]^{6-}$ yielding $[Sn_4S_{10}O]^{6-}$ anions. These anions might be further linked by sulfur atoms leading to the formation of the $[Sn_{10}S_{20}O_4]^{8}$ cluster.[31] Based on these assumptions the question arises, whether additional oxo-thiostannate clusters can be synthesized using these reactants and if bond formation between the Ni^{2+} cations and the cluster anions can be enforced by using slightly different synthesis conditions, e.g. less water in the slurry. Therefore, we reacted $Na_4SnS_4{\cdot}14H_2O$ with $[Ni(cyclen)](ClO_4)_2$ under hydrothermal conditions and we obtained a new oxo-thiostannate cluster with the composition $\{[Ni(cyclen)]_6[Sn_6S_{12}O_2(OH)_6]\}$. Finally, the compound shows promising photocatalytic properties and therefore, such investigations were also conducted. Herein we report on these investigations.

Experimental Section

$Na_4SnS_4{\cdot}14H_2O$ and $[Ni(cyclen)](ClO_4)_2$ were synthesized according to literature methods.[32,33] Generally, the reaction products were filtered off, washed with tiny amounts of water, and dried at ambient conditions.

Caution: Perchlorates are potentially explosive if heated and must be handled with care.

Synthesis of $\{[Ni(cyclen)]_6[Sn_6S_{12}O_2(OH)_6]\}{\cdot}2(ClO_4){\cdot}19H_2O$ (1): $Na_4SnS_4{\cdot}14H_2O$ (147.8 mg, 0.25 mmol) and $[Ni(cyclen)](ClO_4)_2$ (107.5 mg, 0.25 mmol) were reacted in a glass tube with 2 mL H_2O for 7 d at 120 °C. The mixture was cooled down to room temperature, filtered off, and the blue-green mother liquor was kept in a refrigerator until blue-green block-like crystals were formed (12 % yield based on Sn). Elemental analysis: calcd. C: 18.26, H 5.23, N 10.64 %; found C 17.33, H 4.94, N 10.07 %.

Structure Determination: Data for compound **1** were collected with a STOE IPDS-1 (Imaging Plate Diffraction System) with graphite monochromated Mo-K_α radiation (λ = 0.7107 Å) at 170(2) K. The structure was solved with direct methods using the program SHELXS-97,[34] and the refinements were done against and SHELXL-2014.[35] All non-hydrogen atoms were refined anisotropically. The C–H hydrogen atoms were positioned with idealized geometry and were refined isotropically with $U_{iso}(H) = 1.2\ U_{eq}(C)$ using a riding model. The O–H hydrogen atoms were located in the difference Fourier maps, their bond lengths were set to ideal values and finally they were refined isotropically with $U_{iso}(H) = 1.5\ U_{eq}(O)$ using a riding model. The water hydrogen atoms were not located but considered in the calculation of the formula and the molecular weight. One of the perchlorate anions is disordered on a center of inversion and was refined using a split model. The position of the other perchlorate anion seems to be disordered with water molecules and was refined with only half occupation. Several water molecules are also disordered and were refined using a split model with in part not full occupation (Table S1, Supporting Information).

Crystallographic data (excluding structure factors) for the structure in this paper have been deposited with the Cambridge Crystallographic Data Centre, CCDC, 12 Union Road, Cambridge CB21EZ, UK. Copies of the data can be obtained free of charge on quoting the depository number CCDC-1863370 (Fax: +44-1223-336-033; E-Mail: deposit@ccdc.cam.ac.uk, http://www.ccdc.cam.ac.uk).

Characterization Methods

X-ray powder Diffractometry: The powder diffraction patterns were collected with a STOE Stadi P diffractometer equipped with a MYTHEN 1 K detector (DECTRIS) using germanium monochromatized Cu-$K_{\alpha1}$ radiation (λ = 1.540598 Å). The experimental and the calculated patterns using the single-crystal X-ray data match perfectly indicating phase purity of the samples (Figure S1, Supporting Information).

Energy dispersive X-ray Spectroscopy (EDX): EDX analyses (Table S2, Supporting Information) were performed with a Philips Environmental Scanning Electron Microscope ESEM XL30 equipped with an EDX detector.

Elemental Analysis: CHNS elemental analyses were performed with a EURO EA Elemental Analyzer (EURO VECTOR Instruments and Software).

Infrared Spectroscopy: IR spectra were measured in a region from 400 to 4000 cm^{-1} with a Bruker Alpha P spectrometer.

UV/Vis Spectroscopy: UV/Vis analyses were performed at room temperature with an UV/Vis/NIR two channel spectrometer Cary 5 (Varian Techtron Pty., Darmstadt, 200–3000 cm^{-1}) using $BaSO_4$ as reference material. The UV/Vis reflectance data were transformed applying the Kubelka–Munk function.

Thermogravimetric Analysis: Thermogravimetric analysis was performed with a Linseis STA PT1600 instrument. The sample was heated in a nitrogen atmosphere with a heating rate of 4 K·min^{-1}.

Photocatalytic Hydrogen Evolution: In the photocatalytic experiments, **1** (10 mg, 3.2 µmol) or $[Ni(cyclen)(H_2O)_2](ClO_4)_2{\cdot}H_2O$ (9.3 mg, 19.2 µmol) and $[Ru(bpy)_3](PF_6)_2$ (8.6 mg, 1 µmol) as photosensitizer were transferred in a double-walled thermostatically controlled vessel. Triethylamine (10 mL) and acetonitrile (10 mL) were dried with CaH_2, distilled in a nitrogen atmosphere, and added to the mixture. Subsequently, degassed H_2O (3 mL) was added. The reaction mixture was stirred in the dark for 1 h and irradiated with UV light (330 W Xe lamp with a 400 nm cut-off filter) at 30 °C. The evolved gas was collected after distinct reaction times and was quantified by gas chromatography using an Agilent 6890 Plus gas chromatograph with a 5 Å molecular sieves column and TCD detector with argon as carrier gas.

Supporting Information (see footnote on the first page of this article): ■■ ((<=Author: please give a short description of the supporting information.)) ■■

Results and Discussion

Crystal Structure

The compound $\{[Ni(cyclen)]_6[Sn_6S_{12}O_2(OH)_6]\}{\cdot}2(ClO_4){\cdot}19H_2O$ (**1**) crystallizes in the monoclinic space group *C*2/*c* with four formula units per unit cell. The $[Sn_6S_{12}O_2(OH)_6]^{10-}$ anionic building unit is located on a center of inversion and consists of three crystallographically independent Sn cations that exhibits different coordination arrangements (Figure 1 top).

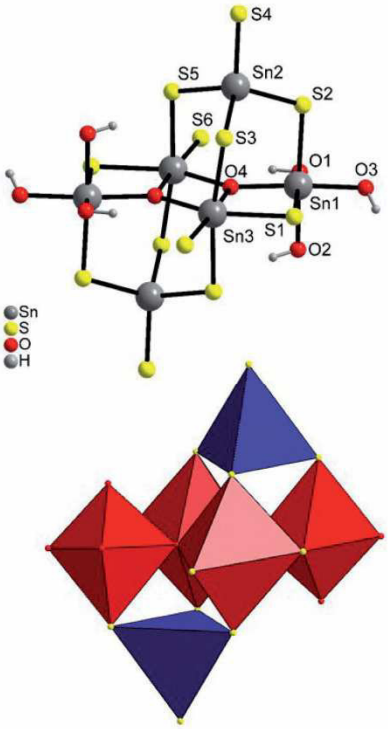

Figure 1. The structure of the $[Sn_6S_{12}O_2(OH)_6]^{10-}$ anion with labelling (top) and in polyhedral representation (bottom) in compound **1**. Only the crystallographically unique atoms are labeled.

Sn1 is coordinated by three terminally bonded OH^- anions, two μ_2-bridging S atoms, and one μ_3-O atom to form a $SnS_2O(OH)_3$ octahedron. Sn3 is also octahedrally coordinated, but by ~~two~~ terminal and ~~two~~ μ_2-bridging S atoms as well as two μ_3-O atoms forming SnS_4O_2 units. Sn2 is in a tetrahedral environment of four S atoms. Each two SnS_4O_2 octahedra are linked via two O atoms sharing common edges forming a double octahedron (Figure 1 bottom). The double octahedron is further connected to two $SnS_2O(OH)_3$ units by μ_3-oxo and μ_2-S atoms sharing common edges into tetranuclear units, in which the Sn atoms are coplanar. The two SnS_4 tetrahedra are located above and below this plane and are linked to two SnS_4O_2 and one $SnS_2O(OH)_3$ octahedra by common corners.

The Sn–S bond lengths are in the range of 2.386(2) to 2.623(2) Å for bridging S^{2-}, whereas the bonds to terminal S^{2-} are between 2.327(2) and 2.408(2) Å (Table S3, Supporting Information). The μ_3-O-Sn bonds are between 2.075(5) and 2.128(5) Å. Similar values have also been reported in literature.[7,30,36,37,38] The Sn–OH bond lengths range from 2.066(6) to 2.102(6) Å and are significantly shorter than for bridged OH^- anions (2.310 and 2.348 Å) (Figure S2, Supporting Information). According to BVS. analysis, the oxidation states of the O atoms of the hydroxyl groups are between 0.68 and 0.77 (average: 0.71) and the oxidation state of the μ_3-O atom is 2.08, which is in agreement with bridging O^{2-} and terminal OH^- anions **1**. In the two different ~~octahedral~~, the angles around Sn indicate a severe distortion (Table S3). The S–Sn–S angles in the SnS_4 tetrahedron are between 105.42(7) and 109.05(9)° indicating a moderate distortion.

The $Sn_6S_{12}O_2(OH)_6$ cluster anions are expanded by six $[Ni(cyclen)]^{2+}$ cations, of which four are coordinated by S^{2-} and two OH^- anions into $\{[Ni(cyclen)]_6[Sn_6S_{12}O_2(OH)_6]\}^{2+}$ cations and the positive charge is compensated by two ClO_4^- anions (Figure 2). The Ni^{2+} cations within these clusters form a trigonal antiprism (Figure S3, Supporting Information). The cluster is stabilized by strong intramolecular O–H···S and N–H···S hydrogen bonds between the S atoms and the hydroxyl and amino hydrogen atoms (Figure 2 bottom and Table S4, Supporting Information). There are additional weak C–H···S contacts but the H···S distances and C–H···S angles

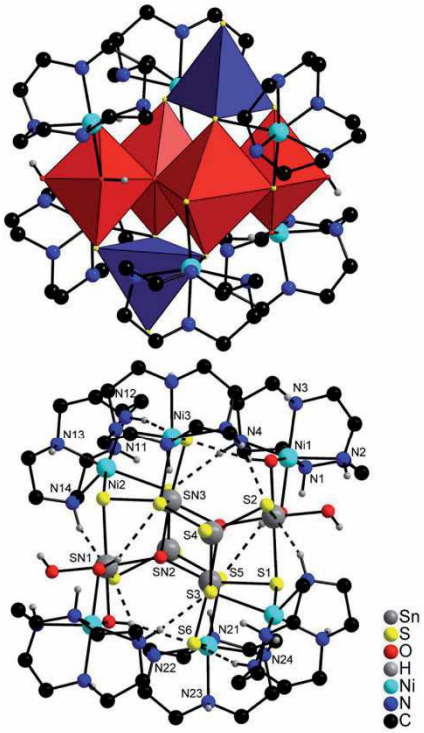

Figure 2. $\{[Ni(cyclen)]_6[Sn_6S_{12}O_2(OH)_6]\}^{2+}$ cluster cation with view along (top) and perpendicular (bottom) to the plane formed by the octahedral coordinated Sn cations in the crystal structure of **1**. Intramolecular O–H···S and N–H···S hydrogen bonding is shown as dashed lines and C–H hydrogen atoms are omitted for clarity.

indicate that this is only a weak interaction (Table S5, Supporting Information).

In the [Ni(cyclen)S_2] and [Ni(cyclen)$(OH)_2$] units the Ni–N, Ni–O, and Ni–S bond lengths are in the range of 2.071(9)–2.144(10), 2.107(6)–2.115(6), and 2.459(2)–2.543(2) Å agreeing well with literature data.[39–41] The octahedra NiN_4S_2 and $NiN_4(OH)_2$ (Figure 3) are distorted as evidenced by the angles around the Ni^{2+} cations (Table S6, Supporting Information). These values are in good agreement with those reported in literature.[41–43] The distortion of NiN_4S_2 and $NiN_4(OH)_2$ can be quantified using two parameters: the octahedral angle variance $\sigma_{\theta<oct>}^2$ and the mean octahedral quadratic elongation λ_{oct}.[44] The values of $\sigma_{\theta<oct>}^2$ = 85.310, λ_{oct} = 1.025 for Ni1, $\sigma_{\theta<oct>}^2$ = 95.035, λ_{oct} = 1.037 for Ni2, and $\sigma_{\theta<oct>}^2$ = 103.119, λ_{oct} = 1.039 for Ni3 confirm a strong distortion of the octahedra. In this context, it is important to notice that Sn–OH–Ni units have been rarely observed so far.

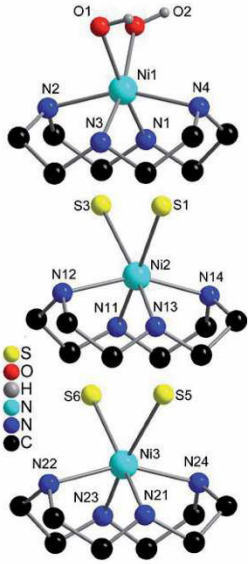

Figure 3. Coordination sphere of the three octahedrally coordinated Ni cations in the crystal structure of **1**. The C–H hydrogen atoms are omitted for clarity.

In the crystal structure of **1** the $\{[Ni(cyclen)]_6[Sn_6S_{12}O_2(OH)_6]\}^{2+}$ cations are linked into chains by centrosymmetric pairs of C–H···S hydrogen bonds (Figure S4 and Table S5, Supporting Information). Between the chains the perchlorate anions are located that are hydrogen bonded to the cations (Figure 4). This includes one strong N–H···O hydrogen bond with a H···O distance of 2.32 Å and the corresponding N–H···O angle of 158.4° as well as a number of weaker C–H···O interactions (Table S5). By this arrangement cavities are formed, in which the water molecules are embedded. These water molecules are linked only to the perchlorate ~~cations~~ anions via strong intermolecular N–H···O and weaker C–H···O hydrogen bonding (Table S5).

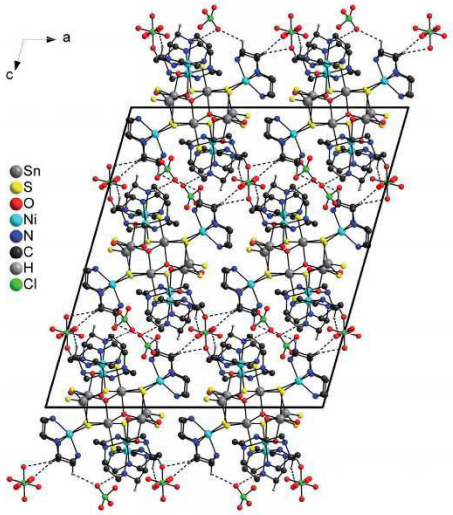

Figure 4. Crystal structure of **1** with view along the crystallographic *b* axis showing the arrangement of the $\{[Ni(cyclen)]_6[Sn_6S_{12}O_2(OH)_6]\}^{2+}$ cations and the perchlorate anions with intermolecular hydrogen bonding shown as dashed line. For clarity, only the hydrogen atoms involved in intermolecular hydrogen bonding are shown. Please note, that the one of the two crystallographically independent ClO_4^- anions is disordered.

Since the hydrogen atoms of the H_2O molecules could not be located, for all O···O separations up to 3.2 Å intermolecular O–H···O hydrogen bonding interactions were assumed, which is also supported experimentally by IR spectroscopic investigations, where a broad band is observed at about 3387 cm^{-1} (see below). If all hydrogen bonds are considered a complex hydrogen bonding network is formed (Figure 5).

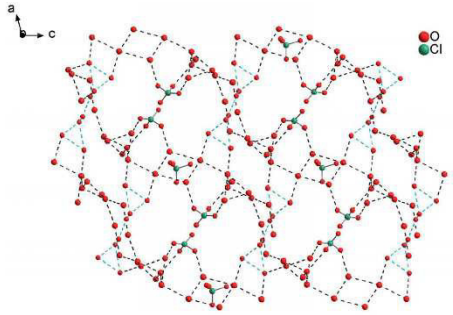

Figure 5. View of the hydrogen-bonded network generated by intermolecular O···O interactions between the water molecules, perchlorate anions, and the anionic $[Sn_6S_{12}O_2(OH)_6]^{10-}$ ~~cations~~ anions (dotted grey lines) as well as within the anionic unit (dotted turquoise lines).

Spectroscopic Properties

The typical bands of the cyclen molecule in compound **1** can be identified in the IR spectra (Figure S5 and Table S7, Supporting Information). The broad absorption at approximately 3387 cm^{-1} is assigned to the OH stretching vibration of the water molecules. The N–H stretching vibration of cyclen occurs around 3149 cm^{-1} and the Ni–N stretching mode is observed around 426 cm^{-1}. The UV/Vis spectrum shows the expected d–d transitions. For the high spin complex $[Ni(H_2O)_6]^{2+}$ these transitions are located at about 1.05 eV (1176 nm, $^3A_{2g} \rightarrow {}^3T_{2g}$), 1.71 eV (724 nm, $^3A_{2g} \rightarrow {}^3T_{1g}$ (F)) and 3.14 eV (395 nm, $^3A_{2g} \rightarrow {}^3T_{1g}$ (P)).[45] For **1** the d–d transitions occur at 1.21 eV (1024 nm), 2.11 eV (587 nm) and 3.45 eV (359 nm) (Figure S6, Supporting Information). The latter absorption seems to be too intense and too broad for a d–d transition indicating that a charge-transfer band is superimposed. The color of the crystals is caused by the transition at 2.11 eV (587 nm) which corresponds to green. The strong absorption at 4.11 eV may be regarded as HOMO–LUMO transition.

Thermogravimetric Analysis

To get some information on the stability of compound **1** and to investigate if the water molecules can be reversibly removed, measurements using simultaneously differential thermoanalysis and thermogravimetry (DTA-TG) were performed. Upon heating two mass steps are observed in the TG curve, of which the first one is accompanied by two endothermic signals in the DTA curve at peak temperatures of ca. 75 and 106 °C (Figure 6). The mass loss of 10.5 % in the first step is in good agreement with that calculated for the removal of nineteen H_2O molecules (calcd. 10.8 %). In the second TG step the anhydrate formed as intermediate decomposes at 250 °C in an exothermic reaction. In a further experiment, heating was stopped after the first TG step at 150 °C and the residue was investigated by X-ray powder diffraction, and the powder pattern reveals some similarities to that of the pristine compound. The anhydrate does not show water uptake on storage at room temperature and therefore, it was treated with small amounts of water. The X-ray powder pattern of this residue consists of a mixture of the pristine compound **1** as the major phase and a small amount of an additional unknown crystalline phase (Figure S7, Supporting Information).

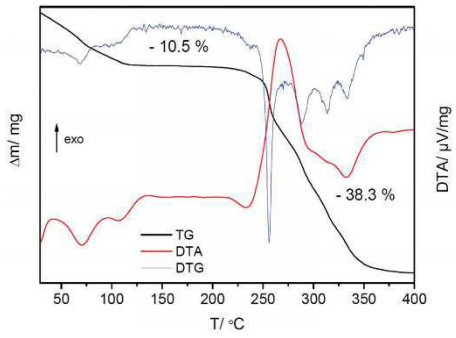

Figure 6. TG (black), DTA (red), and DTG (blue) curves of compound **1**.

Photocatalytic Hydrogen Evolution

The photocatalytic experiments were performed using **1**, $[Ru(bpy)_3](PF_6)_2$ as photosensitizer, the sacrificial agent triethylamine as electron donor, H_2O as proton source, and CH_3CN as solvent for the photosensitizer. The photocatalytically evolved H_2 (Figure 7) increases with increasing irradiation time, and then levels-off reaching 29.6 mmol·g^{-1} after 3 h irradiation. During the reaction the orange solution turned brown leading to a reduced absorption of the incident light, which may explain the decline of the initially steep evolution curve. Such color change demonstrates the photodegradation of $[Ru(bpy)_3](PF_6)_2$ as reported previously.[46–51] Because **1** is soluble in water one may assume that the photocatalytic reaction is homogeneous. Hence, the stability of **1** in both H_2O and a mixture of trimethylamine, acetonitrile and H_2O was investigated by storing the sample for 1 d at room temperature, but **1** could not be recovered after evaporation of the solvents indicating decomposition of the compound.

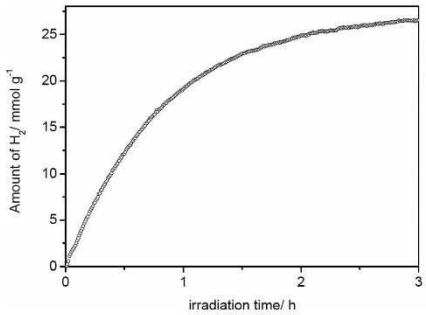

Figure 7. Photocatalytic hydrogen evolution using compound **1**, $[Ru(bpy)_3](PF_6)_2$ as photosensitizer, triethylamine as sacrificial, water as proton donor, and acetonitrile as solvent.

Indeed, the Tyndall effect could be detected after the photocatalytic reaction confirming the presence of nanoparticles, i.e. such particles were generated during the catalytic test. It was reported in the literature that transition metal complexes may be destroyed during the photocatalytic reaction and nanoparticles are generated, which are the active species.[52] Such complexes may be regarded as pre-catalysts which are in-situ transformed into the catalytically active species. Therefore, we assumed that during chemical decomposition the Ni^{2+} centered complex is released, and therefore a photocatalytic experiment was performed with the mixture $[Ni(cyclen)(H_2O)_2](ClO_4)_2 \cdot H_2O$/$[Ru(bpy)_3](PF_6)_2$ (Figure S8, Supporting Information). For this system 14.2 mmol·g^{-1} H_2 were obtained after 1.5 h irradiation time. In the present case the situation is more com-

Table 1. Comparison of the photocatalytic activity of different catalysts at various conditions.

Catalyst	Reaction mixture / Light source	Activity/TON
1	Triethylamine, acetonitrile, water, $[Ru(bpy)_3](PF_6)_2$/ 330 W Xe lamp, cut-off filter ($\lambda > 400$ nm)	83.1
$[Ni(cyclen)(H_2O)_2](ClO_4)_2 \cdot H_2O$ [a]	Triethylamine, acetonitrile, water, $[Ru(bpy)_3](PF_6)_2$/ 330 W Xe lamp, cut-off filter ($\lambda > 400$ nm)	44.4
$[Co(N4Py)(OH_2)]^{3+}$ [54]	H_2A/NaHA, pH = 4, $[Ru(bpy)_3]Cl_2$/ 150 W Xe lamp, cut-off filter ($\lambda > 400$ nm)	65
$[Co(N4Py)(NCMe)]^{3+}$ [54]	H_2A/NaHA, pH = 4, $[Ru(bpy)_3]Cl_2$/ 150 W Xe lamp, cut-off filter ($\lambda > 400$ nm)	67
$[Co(N4Py)(N_3)]^{2+}$ [54]	H_2A/NaHA, pH = 4, $[Ru(bpy)_3]Cl_2$/ 150 W Xe lamp, cut-off filter ($\lambda > 400$ nm)	75
$[Co(N4Py)(NCS)]^{2+}$ [54]	H_2A/NaHA, pH = 4, $[Ru(bpy)_3]Cl_2$/ 150 W Xe lamp, cut-off filter ($\lambda > 400$ nm)	73
$[Co(N4Py)Cl]^{2+}$ [54]	H_2A/NaHA, pH = 4, $[Ru(bpy)_3]Cl_2$/ 150 W Xe lamp, cut-off filter ($\lambda > 400$ nm)	65
$[Co(N4Py)Br]^{2+}$ [54]	H_2A/NaHA, pH = 4, $[Ru(bpy)_3]Cl_2$/ 150 W Xe lamp, cut-off filter ($\lambda > 400$ nm)	68
$[Ni(bpy)_3]^{2+}$ [55]	Acetonitrile-water: 8/2, TEOA, pH = 9, $[Ir(dfppy)_2(Hdcbpy)]$ [b] / 30 W white LED lamp ($\lambda = 420$ nm)	118
$[Ni(bpet)(CH_3CN)_2](ClO_4)_2$ [56] [c]	DMA/ascorbate buffer (pH = 4.0), $[Ru(bpy)_3]Cl_2$/ 6 W diode LED lamp ($\lambda = 450$ nm)	36
$[Ni(bppt)(CH_3CN)_2](BPh_4)_2$ [56] [c]	DMA/ascorbate buffer (pH = 4.0), $[Ru(bpy)_3]Cl_2$/ 6 W diode LED lamp ($\lambda = 450$ nm	3.8

a) N4Py = 1,1-bis(pyridin-2-yl)-*N*,*N*-bis(pyridin-2ylmethyl)methanamine. b) dfppy = 2-(3,4-difluorophenyl)pyridine; Hdcbpy = 4-carboxy-2,2′-bipyridine-4′-carboxylate. c) bpet = bis(2-pyridylmethyl)-1,2-ethanedithiol, bppt = bis(2-pyridylmethyl)-1,3-propane-dithiol.

plex than only using a Ni^{2+} centered complex and the sensitizer because the anion may also decompose and the nanoparticles generated contain both Ni and Sn.

A comparison of the photocatalytic activity with data reported in literature is difficult because the activity depends on a large number of parameters like, e.g., the solvents, the amount of the catalyst, the co-catalyst, the photosensitizer, the intensity and wavelength of the light source, the sacrificial compound, pH value etc. In addition, the amount of hydrogen produced is reported as different quantities like e·g·mmol·g^{-1}, mmol, mL, TON (turnover number, Table 1) or TOF (turnover frequency).[53] Nevertheless, the TON of 83.1 for the title compound is in the range of data reported for Ni^{2+} and Co^{2+} centered complexes (Table 1).

Conclusions

The presented work was motivated by previous investigations, in which a new oxo-thiostannate was accidently obtained simply by the reaction of $[Ni(cyclen)(H_2O)_2](ClO_4)_2 \cdot H_2O$ with $Na_4SnS_4 \cdot 14H_2O$. Therefore, we investigated if other oxo-thiostannate compounds can be synthesized by this route and whether the Ni^{2+} cations can be bonded to the cluster anion. Under similar conditions the new oxo-thiostannate $\{[Ni(cyclen)]_6[Sn_6S_{12}O_2(OH)_6]\} \cdot 2(ClO_4) \cdot 19H_2O$ was obtained, in which the Ni^{2+} cations are covalently bonded to the cluster anion. The photocatalytic experiments show a high activity for H_2 generation. Since the catalytic system is complex the nature of the catalytic process could not be determined.

Acknowledgements

Financial support by the State of Schleswig-Holstein is gratefully acknowledged. We thank *Aleksej Jochim* for the TG measurements.

Keywords: $[Sn_6S_{12}O_2(OH)_6]^{10-}$; Hydrothermal synthesis; Single crystal structure; Spectroscopic and thermal properties; Photocatalytic hydrogen evolution

References

[1] T. Jiang, A. Lough, G. A. Ozin, *Adv. Mater.* **1998**, *10*, 42–46.
[2] H. Ahari, G. A. Ozin, R. L. Bedard, S. Petrov, D. Young, *Adv. Mater.* **1995**, *7*, 370–374.
[3] P. Enzel, G. S. Henderson, G. A. Ozin, R. L. Bedard, *Adv. Mater.* **1995**, *7*, 64–68.
[4] J. B. Parise, Y. H. Ko, J. Rijssenbeek, D. M. Nellis, K. M. Tan, S. J. Koch, *J. Chem. Soc. Chem. Commun. Chem. Soc. Chem. Commun.* **1994**, 527.
[5] W. S. Sheldrick, *J. Chem. Soc., Dalton Trans.* **2000**, *18*, 3041–3052.
[6] B. Seidlhofer, N. Pienack, W. Bensch, *Z. Naturforsch. B* **2010**, *65*, 937–975.
[7] B. Krebs, S. Pohl, W. Schiwy, *Z. Anorg. Allg. Chem.* **1972**, *393*, 241–252.
[8] J. Hilbert, C. Näther, W. Bensch, *Z. Anorg. Allg. Chem.* **2017**, *643*, 1861–1866.
[9] J. Hilbert, C. Näther, W. Bensch, *Cryst. Growth Des.* **2017**, *17*, 4766–4775.
[10] N. Pienack, H. Lühmann, B. Seidlhofer, J. Ammermann, C. Zeisler, F. Danker, C. Näther, W. Bensch, *Solid State Sci.* **2014**, *33*, 67–72.
[11] D. X. Jia, Y. Zhang, J. Dai, Q. Y. Zhu, Y. M. Gu, *Z. Anorg. Allg. Chem.* **2004**, *630*, 313–318.
[12] N. Pienack, S. Lehmann, H. Lühmann, M. El-Madani, C. Näther, W. Bensch, *Z. Anorg. Allg. Chem.* **2008**, *634*, 2323–2329.
[13] B. Krebs, *Angew. Chem.* **1983**, *95*, 113–134.
[14] W. Schiwy, S. Pohl, B. Krebs, *Z. Anorg. Allg. Chem.* **1973**, *402*, 77–86.
[15] J.-H. Liao, C. Varotsis, M. G. Kanatzidis, *Inorg. Chem.* **1993**, *32*, 2453–2462.
[16] T. Jiang, A. Lough, G. A. Ozin, R. L. Bedard, R. Broach, *J. Mater. Chem.* **1998**, *8*, 721–732.
[17] Y. Ko, C. L. Cahill, J. B. Parise, *J. Chem. Soc., Chem. Commun.* **1994**, *1*, 69–70.

[18] K. Feng, X. Zhang, W. Yin, Y. Shi, J. Yao, Y. Wu, *Inorg. Chem.* **2014**, *53*, 2248–2253.
[19] M. Behrens, M.-E. Ordolff, C. Näther, W. Bensch, K.-D. Becker, C. G.-Deudon, A. Lafond, J. A. Cody, *Inorg. Chem.* **2010**, *49*, 8305–8309.
[20] H. P. Nayek, W. Massa, S. Dehnen, *Inorg. Chem.* **2008**, *47*, 9146–9148.
[21] Z. You, K. Harms, S. Dehnen, *Eur. J. Inorg. Chem.* **2015**, 5322–5328.
[22] N. Rinn, L. Guggolz, J. Lange, S. Chatterjee, T. Block, R. Pöttgen, S. Dehnen, *Chem. Eur. J.* **2018**, *24*, 5840–5848.
[23] Z. H. Fard, C. Müller, T. Harmening, R. Pöttgen, S. Dehnen, *Angew. Chem.* **2009**, *121*, 4507–4511.
[24] T. Kaib, M. Kapitein, S. Dehnen, Z. *Anorg. Allg. Chem.* **2011**, *637*, 1683–1686.
[25] J. B. Parise, Y. Ko, *Chem. Mater.* **1994**, *6*, 718–720.
[26] J.-J. Zhang, S.-M. Hu, X.-T. Wu, W.-X. Du, R.-B. Fu, L.-S. Wang, *Inorg. Chem. Commun.* **2003**, *6*, 744–747.
[27] L. Wu, L. Chen, J. Dai, C. Cui, Z. Fu, X. Wu, *Inorg. Chem. Commun.* **2001**, *4*, 574–576.
[28] W. Bubenheim, U. Müller, Z. *Anorg. Allg. Chem.* **1993**, *619*, 779–785.
[29] W. Schiwy, B. Krebs, *Angew. Chem.* **1975**, *87*, 451–452.
[30] J. Hilbert, C. Näther, W. Bensch, *Curr. Inorg. Chem.* **2016**, *6*, 181–186.
[31] A. Benkada, H. Reinsch, M. Poschmann, J. Krahmer, N. Pienack, W. Bensch, *Inorg. Chem.* **2018**, under revision.
[32] Y. Oh, S. Bag, C. D. Malliakas, M. G. Kanatzidis, *Chem. Mater.* **2011**, *23*, 2447–2456.
[33] J. H. Coates, D. A. Hadi, S. F. Lincoln, H. W. Dodgen, J. P. Hunt, *Inorg. Chem.* **1981**, *20*, 707–711.
[34] G. M. Sheldrick, *SHELXS-97*, Program for the Solution of Crystal Structures; University of Göttingen, Göttingen, Germany, **1997**.
[35] G. M. Sheldrick, *SHELXL-2014*, Program for the Refinement of Crystal Structures, University of Göttingen, Göttingen, Germany, **2014**.
[36] B. Krebs, W. Schiwy, Z. *Anorg. Allg. Chem.* **1973**, *398*, 63–71.
[37] H. Puff, H. Reuter, *J. Organomet. Chem.* **1989**, *368*, 173–183.
[38] H. Puff, H. Reuter, *J. Organomet. Chem.* **1989**, *373*, 173–184.
[39] M. Behrens, S. Scherb, C. Näther, W. Bensch, Z. *Anorg. Allg. Chem.* **2003**, *629*, 1367–1373.
[40] B. Scott, K. J. Brewer, L. O. Spreer, C. A. Craig, J. W. Otvos, M. Calvin, S. Taylor, *J. Coord. Chem.* **1990**, *21*, 307–313.
[41] J. Hilbert, C. Näther, W. Bensch, *Dalton Trans.* **2015**, *44*, 11542–11550.
[42] J. Hilbert, N. Pienack, H. Lühmann, C. Näther, W. Bensch, Z. *Anorg. Allg. Chem.* **2016**, *642*, 1427–1434.
[43] J. Hilbert, C. Näther, R. Weihrich, W. Bensch, *Inorg. Chem.* **2016**, *55*, 7859–7865.
[44] K. Robinson, G. V. Gibbs, P. H. Ribbe, *Science* **1971**, *172*, 567–570.
[45] F. A. Holleman, E. Wiberg, N. Wiberg, *Lehrbuch der Anorganischen Chemie*, 102nd., Walter de Gruyter, Berlin, **2007**.
[46] B. B. Beyene, C.-H. Hung, *Sustainable Energy Fuels* **2018**, 2, 2036–2043.
[47] M. Nippe, R. S. Khnayzer, J. A. Panetier, D. Z. Zee, B. S. Olaiya, M. Head-Gordon, C. J. Chang, F. N. Castellano, J. R. Long, *Chem. Sci.* **2013**, *4*, 3934–3945.
[48] B. Durham, J. V. Caspar, J. K. Nagle, T. J. Meyer, *J. Am. Chem. Soc.* **1982**, *104*, 4803–4810.
[49] L. J. Henderson, M. Ollino, V. K. Gupta, G. R. Newkome, W. R. Cherry, *J. Photochem.* **1985**, *31*, 199–210.
[50] A. Vaidyalingam, P. K. Dutta, *Anal. Chem.* **2000**, *72*, 5219–5224.
[51] F. Niefind, J. Djamil, W. Bensch, B. R. Srinivasan, I. Sinev, W. Grünert, M. Deng, L. Kienle, A. Lotnyk, M. B. Mesch, J. Senker, L. Dura, T. Bewerics, *RSC Adv.* **2015**, *5*, 67742–67751.
[52] M. A. Asraf, H. A. Younus, M. Yusubove, F. Verpoort, *Catal. Sci. Technol.* **2015**, *5*, 4901–4925.
[53] M. Dave, A. Rajagopal, M. Damm-Ruttensperger, B. Schwarz, F. Nägele, L. Daccache, D. Fantauzzi, T. Jacob, C. Streb, *Sustainable Energy Fuels* **2018**, 2, 1020–1026.
[54] W. K. C. Lo, C. E. Castillo, R. Gueret, J. Fortage, M. Rebarz, M. Sliwa, F. Thomas, C. J. McAdam, G. B. Jameson, D. A. McMorran, J. D. Crowley, M.-N. Collomb, A. G. Blackman, *Inorg. Chem.* **2016**, *55*, 4564–4581.
[55] Y.-J. Yuan, H.-W. Lu, J.-R. Tu, Y. Fang, Z.-T. Yu, X.-X. Fan, Z.-G. Zou, *ChemPhysChem* **2015**, *16*, 2925–2930.
[56] D. Hong, Y. Tsukakoshi, H. Kotani, T. Ishizuka, K. Ohkubo, Y. Shiota, K. Yoshizawa, S. Fukuzumi, T. Kojima, *Inorg. Chem.* **2018**, *57*, 7180–7190.

Received: November 12, 2018

Journal of Inorganic and General Chemistry
ZAAC
Zeitschrift für anorganische und allgemeine Chemie

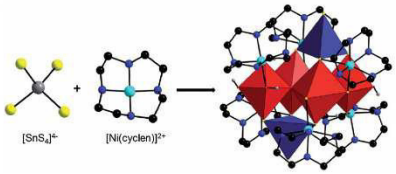

Supporting Information

New Transition Metal Oxo-Thiostannate: Synthesis, Characterization and Investigation of its Photocatalytic Properties

Assma Benkada, Michael Poschmann, Christian Näther, Wolfgang Bensch

Content

Table S1: Crystal and refinement data for compound **1**.

Crystal system	Monoclinic
Empirical formula	C48 H164 Cl2 N24 Ni6 O35 S12 Sn6
Space group	*C*2/*c*
M (g/mol)	3158.04
a (Å)	25.7223(9)
b (Å)	15.6522(3)
c (Å)	29.0703(10)
α (°)	90
β (°)	105.879(3)
γ (°)	90
V ($Å^3$)	11257.4(6)
Temperature (K)	170(2)
Z	4
Dcalc (g/cm^3)	1.863
μ (mm^{-1})	2.632
Scan range (deg)	1.457≤ θ ≤25.099
Reflections collected	36263
Independent reflections	9966
Observed reflections	7886
Goodness-of-fit on F^2	1.069
R values (I>2σ(I))	R1 = 0.0584, wR2 = 0.1460
R values (all data)	R1 = 0.0766, wR2 = 0.1552
Res. Elec. Dens. ($e.Å^{-3}$)	1.080 and -0.717

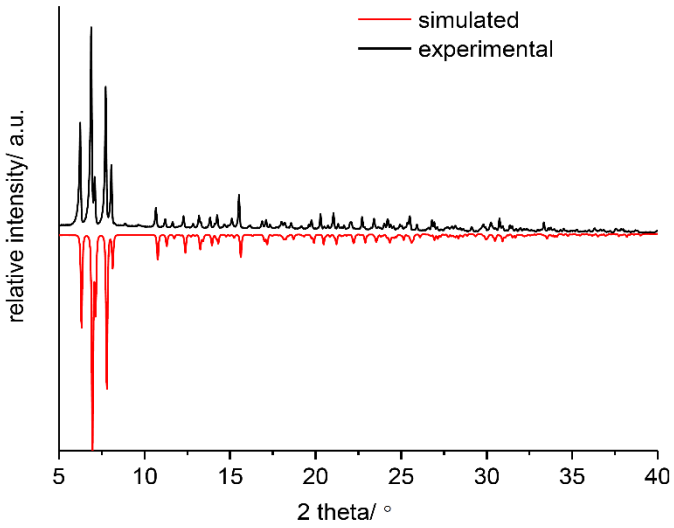

Figure S1: Experimental PXRD patterns of compound **1** (black) compared with the pattern calculated from single-crystal X-ray data (red).

Table S2: EDX data for compound **1**

		Ni	Sn	S
Compound **1**	calculated	1	1	2
	measured	0.83	1	1.90

Table S3: Bond lengths [Å] and angles [°] of the {[Ni(cyclen)]$_6$[Sn$_6$S$_{12}$O$_2$(OH)$_6$]} cation in compound **1**

Sn(1)-O(3)	2.066(6)	Sn(1)-O(2)	2.102(6)
Sn(1)-O(4)#1	2.080(5)	Sn(1)-S(2)	2.491(2)
Sn(1)-O(1)	2.097(6)	Sn(1)-S(1)	2.528(2)
O(4)-Sn(1)#1	2.080(5)	O(4)#1-Sn(1)-S(2)	93.67(16)
O(3)-Sn(1)-O(4)#1	175.4(2)	O(1)-Sn(1)-S(2)	88.33(18)
O(3)-Sn(1)-O(1)	87.9(2)	O(2)-Sn(1)-S(2)	167.01(17)
O(4)#1-Sn(1)-O(1)	95.8(2)	O(3)-Sn(1)-S(1)	93.09(18)
O(3)-Sn(1)-O(2)	87.9(2)	O(4)#1-Sn(1)-S(1)	82.74(15)
O(4)#1-Sn(1)-O(2)	90.2(2)	O(1)-Sn(1)-S(1)	169.02(18)
O(1)-Sn(1)-O(2)	78.9(2)	O(2)-Sn(1)-S(1)	90.19(16)
O(3)-Sn(1)-S(2)	89.2(2)	S(2)-Sn(1)-S(1)	102.60(7)
Sn(2)-S(4)	2.327(2)	Sn(2)-S(5)	2.394(2)
Sn(2)-S(3)	2.386(2)	Sn(2)-S(2)	2.399(2)
S(4)-Sn(2)-S(3)	114.31(9)	S(4)-Sn(2)-S(2)	109.05(9)
S(4)-Sn(2)-S(5)	105.56(9)	S(3)-Sn(2)-S(2)	108.32(8)
S(3)-Sn(2)-S(5)	105.42(7)	S(5)-Sn(2)-S(2)	114.30(8)
Sn(3)-O(4)#1	2.075(5)	Sn(3)-S(1)#1	2.525(2)
Sn(3)-O(4)	2.128(5)	Sn(3)-S(5)	2.561(2)
Sn(3)-S(6)	2.408(2)	Sn(3)-S(3)#1	2.623(2)
S(1)-Sn(3)#1	2.525(2)	S(3)-Sn(3)#1	2.623(2)
O(4)-Sn(3)#1	2.075(5)	O(4)-Sn(3)-S(5)	91.04(15)
O(4)#1-Sn(3)-O(4)	73.3(2)	S(6)-Sn(3)-S(5)	86.79(7)
O(4)#1-Sn(3)-S(6)	101.32(16)	S(1)#1-Sn(3)-S(5)	89.64(7)
O(4)-Sn(3)-S(6)	174.06(15)	O(4)#1-Sn(3)-S(3)#1	96.48(15)
O(4)#1-Sn(3)-S(1)#1	154.94(16)	O(4)-Sn(3)-S(3)#1	93.24(15)
O(4)-Sn(3)-S(1)#1	81.89(15)	S(6)-Sn(3)-S(3)#1	89.86(7)
S(6)-Sn(3)-S(1)#1	103.61(7)	S(1)#1-Sn(3)-S(3)#1	81.15(7)
O(4)#1-Sn(3)-S(5)	94.26(15)	S(5)-Sn(3)-S(3)#1	169.19(7)
Ni(2)-S(1)-Sn(3)#1	95.69(8)	Sn(2)-S(5)-Sn(3)	105.31(8)
Ni(2)-S(1)-Sn(1)	114.94(9)	Ni(3)-S(5)-Sn(3)	90.49(7)
Sn(3)#1-S(1)-Sn(1)	85.76(6)	Sn(3)-S(6)-Ni(3)	96.24(8)
Sn(2)-S(2)-Sn(1)	105.09(8)	Sn(1)-O(1)-Ni(1)	100.7(3)
Sn(2)-S(3)-Ni(2)	107.95(8)	Sn(1)-O(2)-Ni(1)	100.2(2)
Sn(2)-S(3)-Sn(3)#1	104.29(7)	Sn(3)#1-O(4)-Sn(1)#1	143.6(3)
Ni(2)-S(3)-Sn(3)#1	92.64(8)	Sn(3)#1-O(4)-Sn(3)	106.7(2)
Sn(2)-S(5)-Ni(3)	105.48(8)	Sn(1)#1-O(4)-Sn(3)	109.6(2)

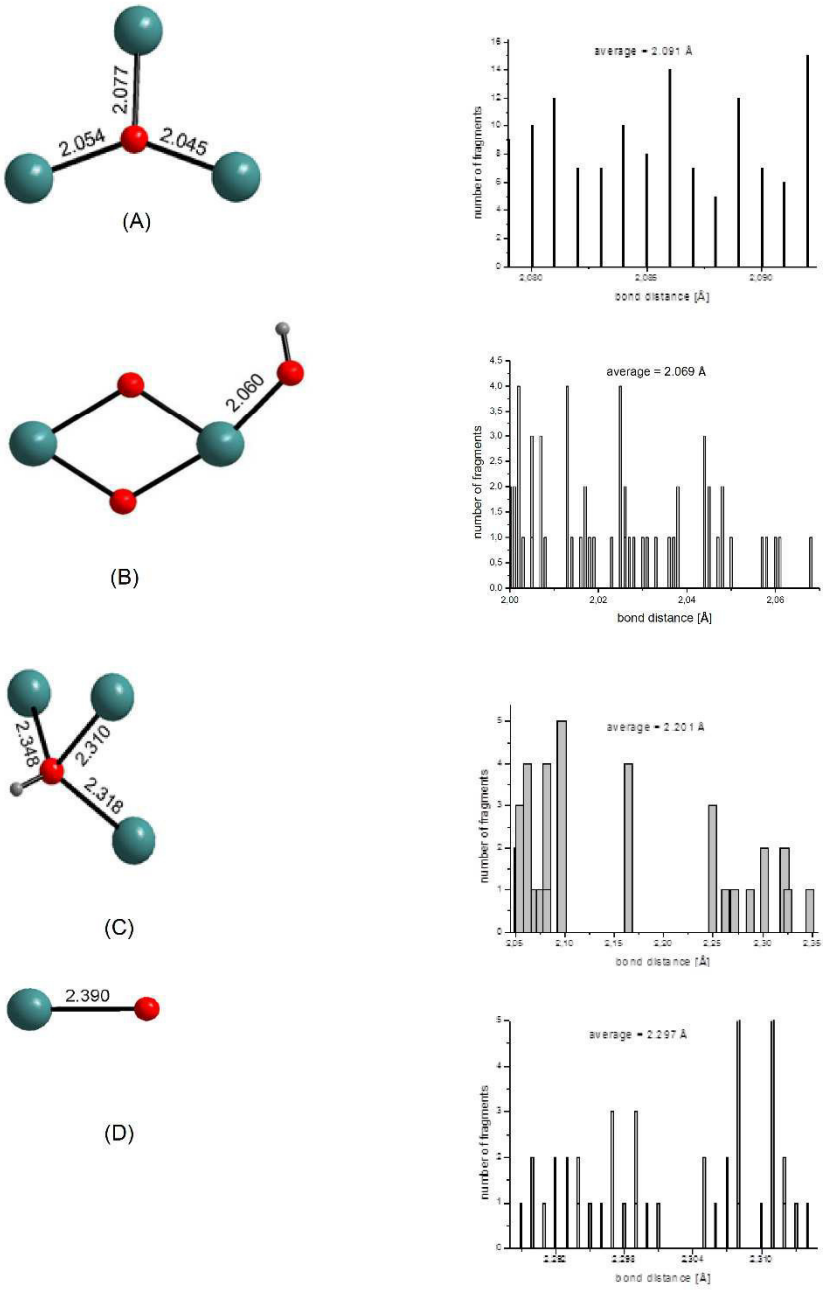

Figure S2: Distribution of the SnO distances and their average values for μ_3-oxo (A), terminal OH (B), μ_3-hydroxo (C) and terminal oxo (D) fragments in crystal structures retrieved from the Cambridge Crystallographic Database (CSD).

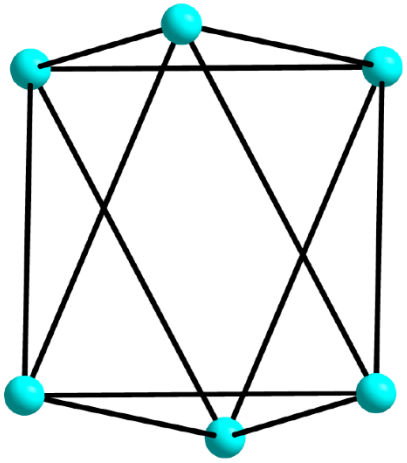

Figure S3: View of the trigonal antiprismatic arrangement of the Ni(II) cations.

Table S4: Intramolecular hydrogen bonds [Å and °] in compound **1**

D-H...A	d(D-H)	d(H...A)	d(D...A)	<(DHA)
O(1)-H(1)...S(6)	0.84	2.50	3.302(6)	160.9
O(2)-H(2)...S(5)#1	0.84	2.67	3.461(6)	156.5
N(4)-H(4N)...S(3)#1	1.00	2.37	3.297(8)	154.6
N(12)-H(12N)...S(6)#1	1.00	2.38	3.364(7)	167.7
N(14)-H(14N)...S(2)	1.00	2.30	3.270(8)	162.1
N(21)-H(21N)...S(4)	1.00	2.74	3.668(10)	155.4
N(22)-H(22N)...S(2)	1.00	2.42	3.304(9)	147.1
N(2)-H(2N)...O(3)	1.00	2.02	2.932(10)	150.2

Symmetry transformations used to generate equivalent atoms: #1 -x+3/2,-y+3/2,-z+1

Table S5: Intermolecular hydrogen bonds [Å and °] in compound **1**

D-H...A	d(D-H)	d(H...A)	d(D...A)	<(DHA)
N(23)-H(23N)...O(24)	1.00	2.32	3.28(3)	158.4
C(21)-H(21A)...O(11)#10	0.99	2.62	3.38(2)	133.2
C(14)-H(14B)...O(12)#8	0.99	2.44	3.37(2)	155.8
C(28)-H(28B)...O(13)#1	0.99	2.64	3.38(2)	131.2
C(3)-H(3B)...O(14)#5	0.99	2.58	3.50(2)	153.7
C(11)-H(11A)...O(14)#7	0.99	2.63	3.51(2)	149.0
C(24)-H(24A)...O(22)	0.99	2.66	3.42(2)	133.5
C(13)-H(13A)...O(24)#1	0.99	2.62	3.19(2)	116.7
O(3)-H(3)...O(39)#3	0.84	2.05	2.872(19)	167.7
N(1)-H(1N)...O(40)#3	1.00	2.24	3.20(2)	160.2
N(1)-H(1N)...O(40')#3	1.00	2.07	3.04(3)	162.0
C(3)-H(3A)...O(34)#4	0.99	2.53	3.428(19)	151.3
N(3)-H(3N)...O(37)#4	1.00	2.35	3.17(3)	138.8
N(11)-H(11N)...O(31)#6	1.00	2.63	3.450(14)	138.8
N(13)-H(13N)...O(36)#3	1.00	2.18	3.12(2)	155.5
C(16)-H(16B)...O(39)#8	0.99	2.59	3.408(19)	140.1
C(17)-H(17B)...O(38)#9	0.99	2.51	3.45(3)	157.8
C(27)-H(27B)...O(40)#11	0.99	2.63	3.57(3)	157.7
C(6)-H(6B)...S(6)	0.99	3.03	3.851(12)	141.5
C(18)-H(18A)...S(4)#6	0.99	2.93	3.752(12)	141.1
C(22)-H(22A)...S(2)	0.99	2.97	3.604(13)	122.7
C(27)-H(27B)...S(5)	0.99	2.99	3.506(12)	113.2

Symmetry transformations used to generate equivalent atoms:
#1 -x+3/2,-y+3/2,-z+1 #2 -x+1,y,-z+1/2 #3 -x+3/2,-y+1/2,-z+1
#4 -x+3/2,y+1/2,-z+3/2 #5 x+1/2,-y+1/2,z+1/2
#6 -x+2,-y+2,-z+1 #7 -x+3/2,y+1/2,-z+1/2 #8 x+1/2,y+1/2,z
#9 -x+2,y,-z+3/2 #10 x+1/2,-y+3/2,z+1/2 #11 x,y+1,z

Table S6: Bond lengths [Å] and angles [°] around the Ni cations in compound **1**

Ni(1)-N(1)	2.071(9)	Ni(1)-N(2)	2.108(7)
Ni(1)-N(3)	2.094(8)	Ni(1)-N(4)	2.133(7)
O(1)-Ni(1)	2.107(6)	O(2)-Ni(1)	2.115(6)
N(1)-Ni(1)-N(3)	102.9(4)	O(1)-Ni(1)-O(2)	78.4(2)
N(1)-Ni(1)-O(1)	166.8(3)	N(2)-Ni(1)-O(2)	95.0(3)
N(3)-Ni(1)-O(1)	90.0(3)	N(1)-Ni(1)-N(4)	82.8(3)
N(1)-Ni(1)-N(2)	82.8(3)	N(3)-Ni(1)-N(4)	82.4(3)
N(3)-Ni(1)-N(2)	81.9(3)	O(1)-Ni(1)-N(4)	102.2(3)
O(1)-Ni(1)-N(2)	96.2(3)	N(2)-Ni(1)-N(4)	155.8(3)
N(1)-Ni(1)-O(2)	88.6(3)	O(2)-Ni(1)-N(4)	104.0(3)
N(3)-Ni(1)-O(2)	167.6(3)	Ni(2)-N(14)	2.112(8)
Ni(2)-N(13)	2.092(7)	Ni(2)-N(12)	2.129(7)
Ni(2)-N(11)	2.110(8)	N(23)-Ni(3)-S(6)	88.2(3)
S(1)-Ni(2)	2.494(2)	S(3)-Ni(2)	2.520(2)
N(13)-Ni(2)-N(11)	100.8(3)	N(14)-Ni(2)-S(1)	98.1(2)
N(13)-Ni(2)-N(14)	82.0(3)	N(12)-Ni(2)-S(1)	101.5(2)
N(11)-Ni(2)-N(14)	80.2(3)	N(13)-Ni(2)-S(3)	166.0(2)
N(13)-Ni(2)-N(12)	81.4(3)	N(11)-Ni(2)-S(3)	88.5(2)
N(11)-Ni(2)-N(12)	83.0(3)	N(14)-Ni(2)-S(3)	110.1(2)
N(14)-Ni(2)-N(12)	153.7(3)	N(12)-Ni(2)-S(3)	89.5(2)
N(13)-Ni(2)-S(1)	87.6(2)	S(1)-Ni(2)-S(3)	83.82(7)
N(11)-Ni(2)-S(1)	171.1(3)		
Ni(3)-N(21)	2.105(9)	Ni(3)-N(22)	2.135(9)
Ni(3)-N(23)	2.109(9)	Ni(3)-N(24)	2.144(10)
S(5)-Ni(3)	2.543(2)	S(6)-Ni(3)	2.459(2)
N(21)-Ni(3)-N(23)	100.5(4)	N(22)-Ni(3)-S(6)	93.8(3)
N(21)-Ni(3)-N(22)	80.9(4)	N(24)-Ni(3)-S(6)	105.9(3)
N(23)-Ni(3)-N(22)	82.0(3)	N(21)-Ni(3)-S(5)	86.8(3)
N(21)-Ni(3)-N(24)	82.2(4)	N(23)-Ni(3)-S(5)	166.2(3)
N(23)-Ni(3)-N(24)	81.0(4)	N(22)-Ni(3)-S(5)	110.9(2)
N(22)-Ni(3)-N(24)	153.4(4)	N(24)-Ni(3)-S(5)	88.5(3)
N(21)-Ni(3)-S(6)	169.0(3)	S(6)-Ni(3)-S(5)	86.11(8)

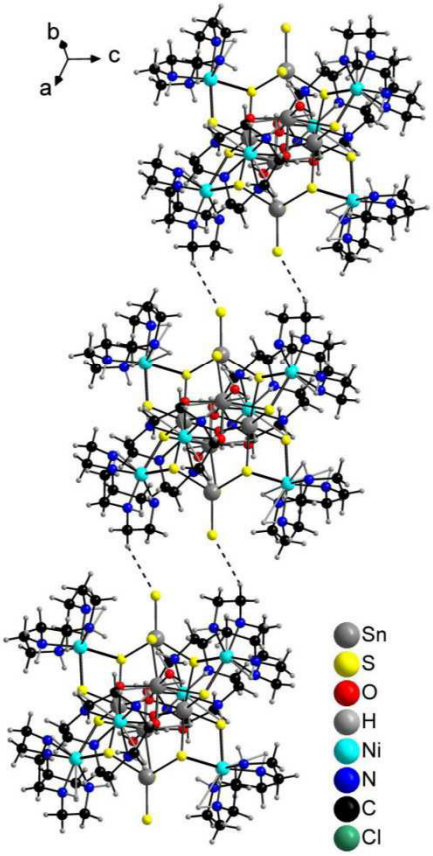

Figure S4: View of the chains with intermolecular C-H···S hydrogen bonding shown as dashed lines.

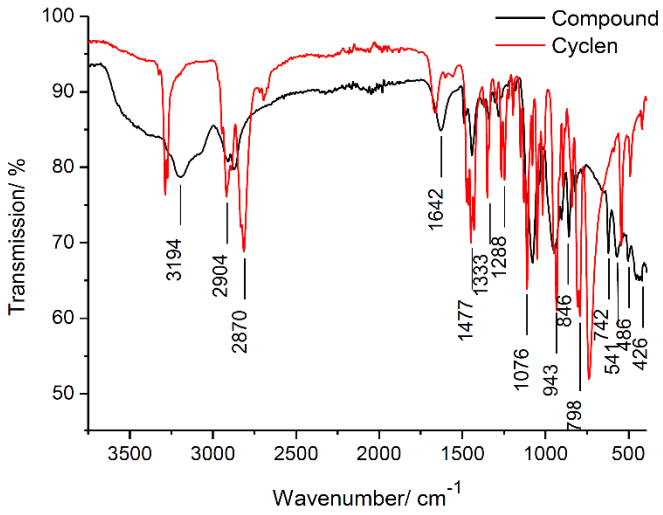

Figure S5: IR spectra of compound **1** (black) and 1,4,7,10-tetraazacyclododecane (cyclen, red).

Table S7: Values of the absorption observed in the IR spectrum of compound **1** together with their assignment

Cyclen	**Compound 1**	**Assignment**
3285m	3194m	ν (NH)
2915s, 2804s	2904w, 2870m	ν (CH_2)
1667m	1642m	δ (NH)
1433m	1477w	δ (CH_2)
1333m	1333w	δ (CH_2)
1255m	1288w	ν (C-N)
1099s	1076s	ν (C-N)
932s	943s	skeleton vib. cyclohex.
831m	864m	δ (C-C-C)
725w, 619w, 564w, 497w	798m, 742s, 541m, 486w	δ (C-C-C)
430w	426w	ν (M-N)

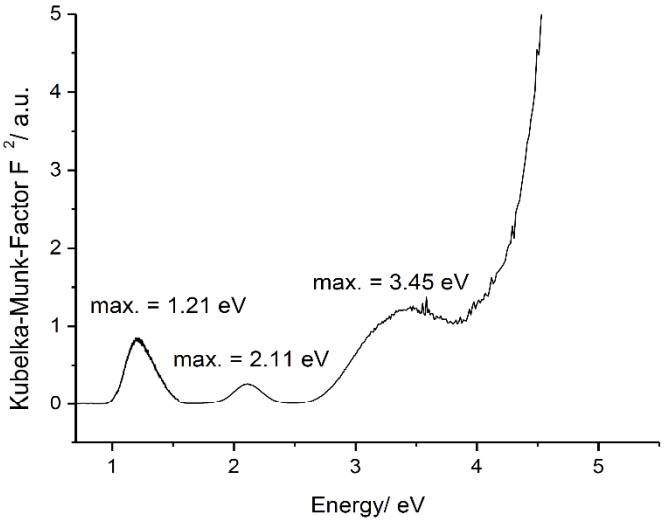

Figure S6: Kubelka-Munk-Factor F^2 as function of energy retrieved form UV/Vis spectroscopic data.

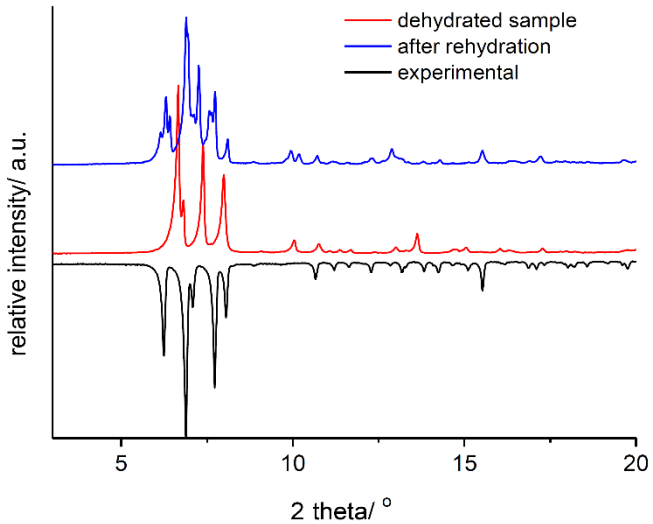

Figure S7: Experimental X-ray powder patterns of compound **1** (black), of the dehydrated sample (red) and of the sample after rehydration (blue).

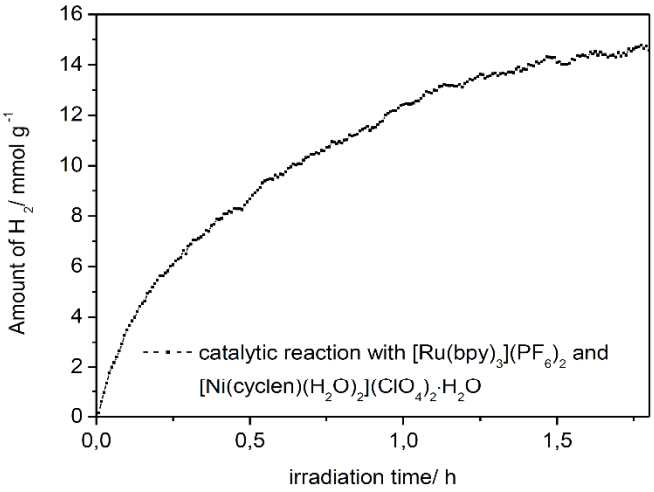

Figure S8: Amount of H_2 as function of time in the photocatalytic hydrogen evolution using $[Ni(cyclen)(H_2O)_2](ClO_4)_2 \cdot H_2O$. Triethylamine was used as sacrificial, $[Ru(bpy)_3](PF_6)_2$ as photosensitizer, water as proton donor and acetonitrile as solvent for the photosensitizer.

3.3. „Synthesis and Characterization of a Rare Transition-Metal Oxothiostannate and Investigation of its Photocatalytic Properties“

Diese Arbeit befasst sich mit dem neuen Oxothiostannat mit der Summenformel [Ni(1,4,7,10-Tetraazacyclododecan)$(H_2O)_2]_4[Sn_{10}S_{20}O_4]\cdot\sim 13H_2O$. Das Material wird durch hydrothermale Reaktion von $Na_4SnS_4\cdot 14H_2O$ mit [Ni(1,4,7,10-Tetraazacyclododecan)$(H_2O)_2](ClO_4)_2\cdot H_2O$ bei 90 °C erhalten. Das zentrale Strukturmotiv stellt der Cluster $[Sn_{10}S_{20}O_4]^{8-}$ dar, welcher von vier Ni^{2+}-Komplexen umgeben ist. Die Struktur des Clusters kann als [Sn10S20] T3-Typ Supertetraeder mit einem $[Sn_{10}O_4]$ anti-T2 Cluster beschrieben werden. Durch Untersuchungen mit ^{119}Sn NMR Spektroskopie konnte gezeigt werden, dass die Clusterbildung erst durch die Anwesenheit der Ni^{2+}-Komplexe ermöglicht wird. Die Cluster und Komplexe sind in der Struktur so angeordnet, dass Kanäle gebildet werden, in denen ca. 13 Kristallwassermoleküle pro Formeleinheit vorhanden sind. Die Kristallwassermoleküle können thermisch unter Erhalt der Kristallinität entfernt werden. Wird die entwässerte Probe in H_2O-Atmosphäre gelagert, werden die H_2O-Moleküle wieder in die Struktur eingebaut. Die photokatalytischen Untersuchungen ergaben eine Wasserstoffgenerierung von 18.7 mmol/g_{cat} in 3 Stunden. Allerdings nimmt die photokatalytische Aktivität mit zunehmender Bestrahlzeit ab, sodass ein Photokorrosionsprozess vermutet werden muss.

Inorganic Chemistry
Cite This: Inorg. Chem. 2019, 58, 2354−2362
Article
pubs.acs.org/IC

Synthesis and Characterization of a Rare Transition-Metal Oxothiostannate and Investigation of Its Photocatalytic Properties

Assma Benkada, Helge Reinsch, Michael Poschmann, Jan Krahmer, Nicole Pienack, and Wolfgang Bensch*

Institute of Inorganic Chemistry, Christian-Albrechts University of Kiel, Max-Eyth-Strasse 2, 24118 Kiel, Germany

Supporting Information

ABSTRACT: The new transition-metal oxothiostannate $[Ni(cyclen)(H_2O)_2]_4[Sn_{10}S_{20}O_4]\cdot\sim 13H_2O$ (**1**) was prepared under hydrothermal conditions using $Na_4SnS_4\cdot 14H_2O$ as the precursor in the presence of $[Ni(cyclen)(H_2O)_2](ClO_4)_2\cdot H_2O$. Compound **1** comprises the $[Sn_{10}S_{20}O_4]^{8-}$ anion constructed by the T3-type supertetrahedron $[Sn_{10}S_{20}]$ and the $[Sn_{10}O_4]$ anti-T2 cluster. Channels host the H_2O molecules, and the sample can be reversibly dehydrated and rehydrated without significantly affecting the crystallinity of the material. ^{119}Sn NMR spectroscopy of an aqueous solution of $Na_4SnS_4\cdot 14H_2O$ evidences that between 25 and 120 °C only $[SnS_4]^{4-}$ and $[Sn_2S_6]^{4-}$ anions are present. In further experiments, hints were found that the formation of tin oxosulfide ions depends on the Ni^{2+}-centered complexes. Compound **1** exhibits promising photocatalytic properties for the visible-light-driven hydrogen evolution reaction, with 18.7 $mmol\cdot g^{-1}$ H_2 being evolved after 3 h.

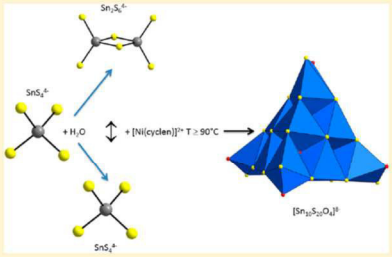

INTRODUCTION

Thiostannates exhibit a pronounced structural flexibility due to the variable oxidation state and coordination of Sn^{n+} (n = 2, 4) cations. Hence, SnS_x primary structural building units like a tetrahedron, a trigonal bipyramid, and an octahedron are observed.[1] In the crystal structures of thiostannates(IV), mainly the $[SnS_4]^{4-}$ tetrahedron occurs, which is either isolated as in $Na_4SnS_4\cdot 14H_2O$,[2] $K_4SnS_4\cdot 4H_2O$, $Rb_4SnS_4\cdot 4H_2O$, or $Cs_4SnS_4\cdot 3H_2O$[3] or condensed, forming the $[Sn_2S_6]^{4-}$ anion such as in $Na_4Sn_2S_6\cdot 14H_2O$.[4] Compounds with isolated $[Sn_2S_6]^{4-}$ anions combined with inorganic, organic, or complex cations for charge compensation form the most frequent class of thiostannates(IV). Depending on the pH value, various SnS_x polyhedra are formed in aqueous solution. Thus, in addition to the $[SnS_4]^{4-}$ and $[Sn_2S_6]^{4-}$ anions, different condensation products are observed like, e.g., $[SnS_3]^{2-}$, $[Sn_2S_5]^{2-}$, $[Sn_2S_7]^{6-}$, $[Sn_2S_8]^{2-}$, $[Sn_3S_7]^{2-}$, $[Sn_4S_9]^{2-}$, and $[Sn_5S_{12}]^{4-}$ anions[5−8] or the tetrameric adamantane-like moiety $[Sn_4S_{10}]^{4-}$.[5] In thiostannate compounds, three types of cations for charge compensation are distinguished: (i) metal cations, (ii) protonated organic molecules and metal complexes, or (iii) transition-metal cations with bonds to the anionic frameworks. Examples for group i are $Na_4SnS_4\cdot 14H_2O$,[2] $Na_4Sn_2S_6\cdot 14H_2O$,[4] $Cs_4Sn_5S_{12}\cdot 2H_2O$[8] or $Rb_2Sn_3S_7\cdot 2H_2O$,[9] with isolated anions like $[SnS_4]^{4-}$, $[Sn_2S_6]^{4-}$, $[Sn_5S_{12}]^{4-}$, and $[Sn_3S_7]^{2-}$, layered materials like $M_2Cu_2Sn_2S_6$ (M = Na, K, Cs, and Rb)[10] or three-dimensional structures as observed in $K_2Sn_2S_5$[6] and $Na_4Sn_3S_8$.[11] Group ii covers materials like $[Ni(dap)_3]_2Sn_2S_6\cdot 2H_2O$ (dap = 1,2-diaminopropane),[12] $[M(en)_3]_2Sn_2S_6$ (M = Ni, Co, Mn, and Zn; en = ethylenediamine),[12,13] and $[M(dien)_2]_2Sn_2S_6$ (M = Ni and Mn; dien = diethylenetriamine)[14,15] with discrete $[Sn_2S_6]^{4-}$ anions and compounds with layered anions, e.g., $(Et_4N)_2Sn_3S_7$, $(DABCOH)_2Sn_3S_7$ (DABCO = 1,4-diazabicyclo[2.2.2]-octane),[7] and $(trenH)_2Sn_3S_7$.[16] In group iii, transition-metal cations have bonds to the anionic framework exemplified by $Rb_2Cu_2SnS_4$, $M_2Cu_2Sn_2S_6$ (M = Na, K, Cs, and Rb)[10] $Cu_2CdSn_3S_8$,[17] $\{[Mn(2,2'\text{-bipy})_2]_2[Sn_2S_6]\}$ (2,2′-bipy = 2,2′-bipyridine),[18] $\{[M(1,10'\text{-phen})_2]_2[Sn_2S_6]\}$ (M = Mn, Fe, and Co; 1,10′-phen = 1,10′-phenanthroline),[19,20] $\{[Ni(cyclam)]_2[Sn_2S_6]\}_n\cdot 2nH_2O$ (cyclam = 1,4,8,11-tetraazacyclotetradecane),[18] $(1,4\text{-dabH}_2)Ag_2SnS_4$ (1,4-dab = 1,4-diaminobutane),[21] or $(dienH_2)Cu_2Sn_2S_6$.[22]

In most thiostannates, Sn adopts oxidation state IV, but there are some mixed-valent thiostannates in which Sn occurs in oxidation states II/IV or III/IV, e.g., $BaLnSn_2S_6$ (Ln = Ce, Pr, and Nd),[23] $(trenH_3)Cu_7Sn_4S_{12}$ (tren = tris(2-aminoethyl)-amine),[24] $[(Ph_3PCu)_6\{(CH_2)_4SnS_2\}_6Cu_4Sn]$,[25] and $[\{(CMe_2CH_2COMe)Sn_2(\mu\text{-}S)_2\}Sn_2S_6]$.[26] In the first five compounds, $Sn^{II/IV}$ is observed, while in the sixth Sn adopts oxidation states III and IV.

Another group of tin compounds contain sulfide and oxide anions, and prominent representatives are $[Sn_{10}S_{20}O_4]^{8-}$,[27,28] $[Sn_{10}S_{16}O_4Cl_4]^{4-}$,[29] $[Sn_8S_{12}O_4(SPh)_6]^{6-}$,[30] $[Sn_8S_{12}O_2(OH)_2Cl_6]^{4-}$,[29] and $[Sn_4S_5(S_3)OCl_4]^{2-}$.[31] Among these anions, the $[Sn_{10}S_{20}O_4]^{8-}$ moiety is the most common. It has an idealized T_d symmetry and can be described as a

Received: September 29, 2018
Published: January 31, 2019

DOI: 10.1021/acs.inorgchem.8b02773
Inorg. Chem. 2019, 58, 2354−2362

supertetrahedral cluster (denoted as T3) formed by 10 corner-linked SnS_4 polyhedra. Four empty sites are occupied by O^{2-} anions expanding the coordination number of Sn^{IV} from 4 to 5 or 6.[27,28,32]

While many thiostannate compounds were prepared using the molten flux approach like, e.g., $Cs_2Sn_4S_9$, $Rb_2Sn_4S_9$, $K_2Sn_4S_9$, and Li_2CdSnS_4[33,34] or high-temperature synthesis, e.g., $AGaSnS_4$ (A = Na, K, Rb, Cs, and Tl),[35] $BaCdSnS_4$,[36] and Au_2BaSnS_4,[37] the solvothermal approach allows the preparation of inorganic−organic hybrid compounds containing amine molecules and/or in situ generated transition-metal complexes, and this synthetic method led to an enormous expansion of the chemical and structural diversity of thiostannates.[38] Many of these compounds were synthesized by applying the elements Sn and S and transition metals or salts like $SnCl_4{\cdot}SH_2O$ and $Na_2S{\cdot}9H_2O$ in aqueous amine solutions.[38] Here we present a new rare oxothiostannate, which was synthesized under hydrothermal conditions using $Na_4SnS_4{\cdot}14H_2O$ as the precursor and the $[Ni(cyclen)(H_2O)_2](ClO_4)_2{\cdot}H_2O$ complex. The potential of $Na_4SnS_4{\cdot}14H_2O$ as single-source precursor for the generation of thiostannates has only been explored a little. Hence, we investigated the behavior of this salt in H_2O from room temperature up to 120 °C using ^{119}Sn NMR spectroscopy in order to monitor the stability. In addition to the synthesis and crystal structure of the new compound $[Ni(cyclen)(H_2O)_2]_4[Sn_{10}S_{20}O_4]{\cdot}{\sim}13H_2O$ (**1**), we report an in situ investigation of the formation of **1**, its thermal and H_2O sorption behavior, and the photocalytic properties of the title compound as well.

EXPERIMENTAL SECTION

$Na_4SnS_4{\cdot}14H_2O$ and $[Ni(cyclen)](ClO_4)_2$ were synthesized according to literature methods.[39,40] $[Ni(cyclen)(H_2O)_2](ClO_4)_2{\cdot}H_2O$ was prepared by dissolving $[Ni(cyclen)](ClO_4)_2$ in a H_2O/ethanol (1:1) mixture and allowing the solvent to evaporate slowly until purple crystals formed. Cyclen (Strem Chemicals, Inc., 98%) and $Ni(ClO_4)_2{\cdot}6H_2O$ (abcr, 99%) were used without further purification. Generally, the reaction product was filtered off, washed with tiny amounts of H_2O, and dried at ambient conditions. ***Caution!*** *One should keep in mind that perchlorate compounds are potentially explosive if heated and must be handled with care.*

Synthesis of $[Ni(cyclen)(H_2O)_2]_4[Sn_{10}S_{20}O_4]{\cdot}{\sim}13H_2O$ (1). For the synthesis of **1**, 120.9 mg (0.25 mmol) of $[Ni(cyclen)(H_2O)_2](ClO_4)_2{\cdot}H_2O$ was dissolved in 10 mL of H_2O. A total of 147.8 mg (0.25 mmol) of $Na_4SnS_4{\cdot}14H_2O$ also dissolved in 10 mL of H_2O was added dropwise to the $[Ni(cyclen)(H_2O)_2](ClO_4)_2{\cdot}H_2O$ solution. The mixture was filtered off to remove the black solid, and the reaction was then carried out under dynamic conditions (2 h at 120 °C). The product was cooled to room temperature, the green powder of compound **1** was filtered off, and the green mother liquor was again heated for 2 h to 120 °C until the solution became light pink and green crystals of **1** were formed (27% yield based on Sn). Compound **1** could also be obtained by using $Ni(ClO_4)_2{\cdot}6H_2O$ (91.0 mg, 0.25 mmol) and cyclen (43.0 mg, 0.25 mmol) instead of the complex. The salt and ligand were dissolved in 10 mL of H_2O and stirred at room temperature for 20 min. $Na_4SnS_4{\cdot}14H_2O$ (147.8 mg, 0.25 mmol) was added portionwise to the solution. The slurry was filtered to remove a black solid, and the clear brown solution was heated under dynamic conditions (120 °C). Compound **1** crystallized as green crystals after 2 h in a similar yield. We performed syntheses below 120 °C and observed that crystallization of compound **1** already occurred at 90 °C. Elem anal. Found: C, 12.58%; H, 3.21%; N, 7.33%; S. 20.54%. Calcd: C, 12.03%; H, 3.85%; N, 7.02%; S, 20.08%.

Structure Determination from Powder X-ray Diffraction (PXRD) Data. The PXRD pattern of compound **1** could be successfully indexed with a tetragonal unit cell using *TOPAS Academics*,[41] and the reflection extinction conditions point to space group $I4_1/a$. Using the lattice parameters and composition based on the energy-dispersive X-ray (EDX) data and CHNS analysis, the positions of the heavy Sn, S/O, and Ni atoms could be determined using direct methods, as implemented in *EXPO2009*.[42] This initial model was further complemented by the missing atoms of the cyclen ligand and the H_2O molecules of the nickel complex, which were inserted using the molecular modeling software *Materials Studio*.[43] The obtained model was further optimized by force-field calculations using the universal force field,[44] as implemented in the forcite routine in *Materials Studio*. The structurally optimized starting model was subsequently refined by the Rietveld method using a Thompson−Cox−Hasting profile shape function and an 18th-order polynomial background function. The positions of all atoms of the $\{Sn_{10}S_{20}O_4\}$ cluster were freely refined using only bond restraints. The nickel complex was refined as rigid body. Attempts to position the complex so that Ni−O/S bonds to the cluster are formed led to a significant decline of the figures of merit. The comparably high values for the displacement parameters were refined element-specific or as a group for the nickel complex. The crystallographic details and resulting reliability factors are summarized in Table S1, and the results of the Rietveld refinement are shown in Figure S1. In the difference Fourier map, only weak electron densities could be observed, indicating that for disordered H_2O, which was not considered in the refinement. Hence, the final structure contained voids, and using the program suite *PLATON*, a solvent-accessible space of 2050 $Å^3$ was calculated (23% of the unit cell volume).[45] Assuming that a H_2O molecule requires 40 $Å^3$ space, app. 13 H_2O molecules occupy the voids (Figure S2). The structural data have been deposited in the Cambridge Crystallographic Data Centre as CCDC 1863577 (**1**).

Characterization Methods. *PXRD.* The PXRD patterns were collected with a STOE Stadi-P diffractometer equipped with a MYTHEN 1K detector (DECTRIS) using monochromatized Cu $K\alpha_1$ radiation (λ = 1.540598 Å). The experimental and calculated patterns using the results of the Rietveld refinement matched perfectly, indicating the phase purity of the sample (Figure S3).

EDX Spectroscopy. EDX analysis (Table S2) was performed with a Philips ESEM XL30 environmental scanning electron microscope equipped with an EDX detector.

Elemental Analysis. CHNS elemental analyses were performed with a EURO EA elemental analyzer (EURO VECTOR Instruments and Software).

^{119}Sn NMR Spectroscopy. ^{119}Sn NMR spectra were recorded in D_2O at 149 MHz using a Bruker Avance3 400 HD spectrometer (T_{max} = 80 °C) and at different temperatures. The pulse width was 11 μs at 30.974 W, the relaxation delay 1 s, and the number of scans 256. The NMR samples were prepared in a 5 mm tube and referenced to $SnCl_4$ [$\delta(^{119}Sn)$ = −150 ppm]. To be consistent with literature data, the NMR shifts were corrected using $SnMe_4$ as the standard (0 ppm).

In Situ Investigation of the Formation of Compound 1. The crystallization of compound **1** was investigated in situ using an EasyMax reactor system (Mettler Toledo GmbH, Giessen, Germany), which allowed control of the temperature, dosing of the solution, and stirring. With this cell, simultaneous measurements of, e.g., pH value, redox potential, ion conductivity, in situ IR spectroscopy, and in situ luminescence, can be performed.[46,47] In the present experiment, the precursor was dissolved in H_2O and placed inside the glass reactor vessel. $[Ni(cyclen)(H_2O)_2](ClO_4)_2{\cdot}H_2O$ was also dissolved in H_2O and then added dropwise to the reactor vessel under constant stirring (300 rpm). The solution was slowly heated to 90 °C (5 $K{\cdot}min^{-1}$). The pH value and redox potential were measured with a pH electrode [InLab Semi-Micro, Mettler Toledo; sensor type, combined pH electrode; reference system, Argenthal (0−100 °C as the temperature range)] and a redox electrode [InLab Redox Micro (Mettler Toledo); sensor type, combined ORP electrode with platinum ring; reference system, Argenthal (ceramic diaphragm, 3 M KCl as the reference electrolyte, and 0−100 °C as the temperature range)].

IR Spectroscopy. IR spectra were measured in the region from 400 to 4000 cm^{-1} with a Bruker Alpha P spectrometer.

DOI: 10.1021/acs.inorgchem.8b02773
Inorg. Chem. 2019, 58, 2354−2362

UV/Vis Spectroscopy. UV/vis analysis was performed at room temperature with a Cary 5 UV/vis−near-IR two-channel spectrometer (Varian Techtron Pty., Darmstadt, Germany, 200−3000 cm^{-1}) using $BaSO_4$ as the reference material. The UV/vis diffuse-reflectance data were transformed by applying the Kubelka−Munk function.

Thermogravimetric Analysis (TGA). TGA was performed with a Linseis STA PT1600 instrument. The samples were heated in a N_2 atmosphere with a heating rate of 4 $K \cdot min^{-1}$.

N_2 and H_2O Sorption Measurements. The N_2 and H_2O sorption isotherms of compound **1** were measured by a Belsorpmax instrument (BEL Japan Inc., Toyonaka, Japan) at 77 K (N_2) and 303 K (H_2O). The samples were pretreated by heating to 130 °C in a vacuum for 16 h to remove H_2O molecules.

Photocatalytic Hydrogen Evolution. In the photocatalytic experiments, a double-walled thermostatically controlled vessel with **1** (10 mg, 3.13 μmol) or $[Ni(cyclen)(H_2O)_2](ClO_4)_2 \cdot H_2O$ (6.0 mg, 12.5 μmol) and $[Ru(bpy)_3](PF_6)_2$ (8.6 mg, 1.00 μmol) as the photosensitizer were used. Triethylamine (10 mL) and acetonitrile (10 mL) were dried with CaH_2, distilled under N_2, and added to the mixture. Subsequently, degassed H_2O (3 mL) was added. The system was stirred in the dark for 1 h and irradiated after equilibration with UV light (330 W Xe lamp with a 400 nm cutoff filter) at 30 °C. Evolved gas was collected after a distinct reaction time and quantified by gas chromatography (Agilent 6890 Plus gas chromatograph with a 5 Å molecular sieve column and a thermal conductivity detector; the carrier gas was argon).

RESULTS AND DISCUSSION

Synthetic Aspects and In Situ Investigations. To prove which species might form when the precursor was dissolved in H_2O, measurements using ^{119}Sn NMR spectroscopy were performed. Depending on the reaction conditions, one can expect that different thiostannates or oxothiostannates can form, which can easily be distinguished because the chemical shift is sensitive whether only S^{2-} anions or mixed anions are present. In the ^{119}Sn NMR spectra, the chemical shifts of thiostannate and oxothiostannate ions are in the range of −1000 to +1000 ppm.[48,49] If the precursor $Na_4SnS_4 \cdot 14H_2O$ is dissolved in H_2O, two signals occur at approximately 69 and 74 ppm, indicating that the Sn^{IV} cations in the solution are in a tetrahedral environment (literature data: 49−74 ppm;[50] Figures 1 and S4). The signal at 69 ppm can be assigned to the $[Sn_2S_6]^{4-}$ anion and that at 74 ppm to $[SnS_4]^{4-}$. This observation suggests that a relatively fast protonation and condensation reaction must occur, in which H_2S is emitted and

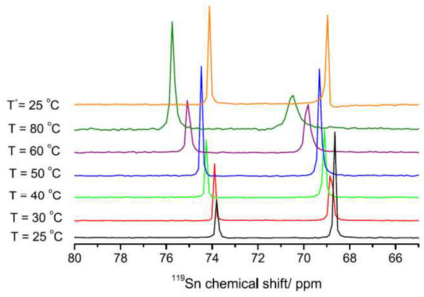

Figure 1. ^{119}Sn NMR spectra of the precursor $Na_4SnS_4 \cdot 14H_2O$ dissolved in D_2O measured at the indicated temperatures in the range of 80 to 65 ppm (*: ^{119}Sn NMR spectrum of the precursor solution, which was heated at 120 °C for 1 h and cooled to room temperature).

$[Sn_2S_6]^{4-}$ anions are formed. The evolution of H_2S could be proven with wet lead acetate paper. With increasing temperature, the signals occurred at slightly larger chemical shifts because the Sn−S bond lengths increased, leading to a change of the nuclear magnetic shielding.[51] Upon heating of $[Sn_2S_6]^{4-}$, the equilibrium was shifted to $[SnS_4]^{4-}$, and integration of both signals confirmed that with increasing temperature the amount of $[Sn_2S_6]^{4-}$ was reduced (Table S3). However, no tin oxosulfide ions were detected, demonstrating the stability of Sn^{IV} in the S^{2-} environment up to at least 80 °C. In another experiment, the precursor solution was heated at 120 °C for 1 h, and after cooling to room temperature, the ^{119}Sn NMR spectrum (Figure 1) showed only the signals of $[Sn_2S_6]^{4-}$ and $[SnS_4]^{4-}$, while tin oxosulfide species were absent because they should show signals between −200 and −500 ppm.[49] The two signals exhibited different intensities compared to the spectrum recorded at the beginning of the experiments (T = 25 °C) and now the two anions were present in a nearly 1:1 ratio (Table S3). The main conclusions of the ^{119}Sn NMR investigations are that, in the presence of H_2O, no tin oxosulfides are generated and that $[SnS_4]^{4-}$ and $[Sn_2S_6]^{4-}$ anions are stable up to 120 °C.

In the following, an in situ experiment monitoring the redox potential, pH value, and temperature of the solution simultaneously was performed (Figure 2). Dissolution of the

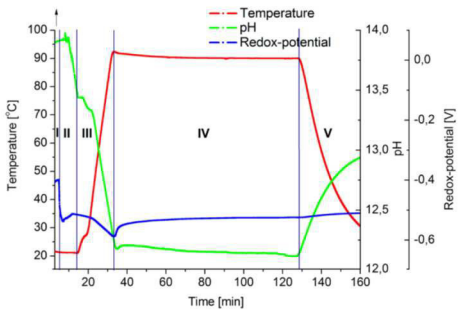

Figure 2. In situ investigation of the crystallization of compound **1**. The temperature (red), pH value (green), and redox potential (blue) were recorded simultaneously: (I) showing the precursor solution before the solution containing the Ni^{2+} complex was added (II); (III) heating the solution to 90 °C; (IV) keeping the temperature constant; (V) cooling the solution to room temperature.

precursor in H_2O (region I) yields an initial pH value of 13.9 and a redox potential of −0.40 V. After addition of the dissolved Ni^{2+} complex (region II), the pH value drops to 13.4, which can be explained by dilution of the solution. Simultaneously the redox potential reaches −0.51 V, indicating the release of reducing species like, e.g., HS^- formed according to $H_2S + H_2O \Leftrightarrow HS^- + H_3O^+$.[52] In region III, the temperature is successively increased, which is accompanied by a reduction of the pH value to 12.3 and of the redox potential to −0.59 V at T = 90 °C (region III). The pH value drop is caused by the temperature dependence of the pH and eventually by further release of H_2S. Alteration of the redox potential can also be traced back to the increased temperature. In region IV, the slight decrease of the pH (12.1) can be explained by further generation of H_2S, and the minute change

DOI: 10.1021/acs.inorgchem.8b02773
Inorg. Chem. 2019, 58, 2354−2362

of the redox potential may be caused by the consumption of, e.g., HS^-. Finally, lowering the temperature to room temperature (region V) is accompanied by an increase of the pH value. The PXRD pattern of the solid recovered from the slurry demonstrates that **1** already crystallized at 90 °C (Figure S5).

For an explanation of the formation of the tin oxosulfide species, the chemical reactivity of organotin compounds R_3SnX (R = organic molecule; X = electronegative ligand) in H_2O may serve as a model. For example, the hydrolysis of R_3SnX leads to the formation of $R_3Sn(OH)$, which further reacts to $R_3SnOSnR_3$.[53,54] In analogy, one may propose that $[SnS_3(OH)]^{3-}$ is formed and then condenses to generate $[Sn_2S_5O]^{4-}$. This anion reacts with $[Sn_2S_7]^{6-}$, yielding $[Sn_4S_{10}O]^{6-}$. The connection of these anions via S atoms leads to formation of the $[Sn_{10}S_{20}O_4]^{8-}$ cluster (Scheme 1).

Scheme 1. Proposed Mechanism for the Formation of $[Sn_{10}S_{20}O_4]^{8-}$ Starting from the $[SnS_4]^{4-}$ Anion

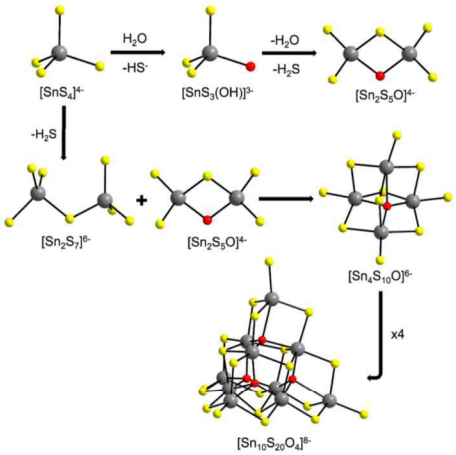

To confirm this suggestion, the pH value of the precursor solution without the Ni^{2+} complex was adjusted to 12.3 (with 0.2 M HCl) and the solution was heated at 90 °C for 1 h. After cooling to room temperature, a ^{119}Sn NMR spectrum was recorded (Figure S6), which shows only the signal of $[Sn_2S_6]^{4-}$ at 55 ppm and no signal for $[SnS_4]^{4-}$ or any possible oxo species. Therefore, one may assume that the Ni^{2+} complex plays a crucial role for the formation of the oxosulfide species.

Crystal Structures. Compound **1** crystallizes in the tetragonal space group $I4_1/a$ with three unique Sn atoms, five independent S atoms, three unique O atoms, and one independent Ni atom. The structure of the $[Sn_{10}S_{20}O_4]^{8-}$ anion consists of ten $[SnS_4]^{4-}$ tetrahedra, which are linked via corners, yielding the T3-type supertetrahedron $[Sn_{10}S_{20}]$[55−57] (Figure 3, top). The O atoms are located between the SnS_4 tetrahedra (Figure 3, bottom) and are in a tetrahedral environment of Sn atoms. The arrangement of the O atoms can be described as an anti-T2 cluster[57] (Figure 4, bottom).

In the $[Sn_{10}S_{20}O_4]^{8-}$ cluster, Sn1 and Sn3 are in an octahedral environment, while a trigonal-bipyramidal coordi-

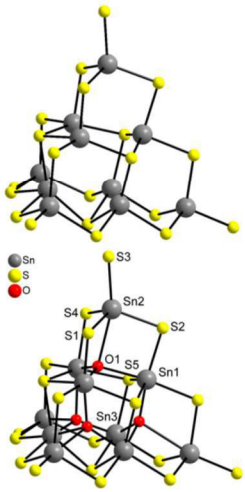

Figure 3. View of the T3 supertetrahedral cluster $[Sn_{10}S_{20}]$ in the structure of **1** (top) and the O atoms located in the voids of the cluster (bottom). Only crystallographically unique atoms are labeled.

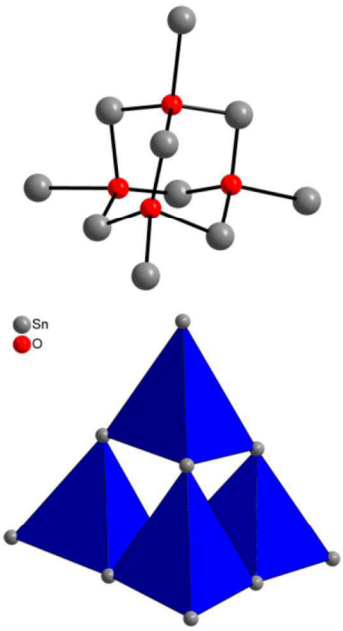

Figure 4. Structure (top) and a polyhedral representation (bottom) of the anti-T2 cluster formed by the tetrahedral environments of the O atoms in the structure of **1**.

DOI: 10.1021/acs.inorgchem.8b02773
Inorg. Chem. 2019, 58, 2354−2362

nation is observed for Sn2. In the $Sn1S_4O_2$ octahedron, the O atoms are in the trans positions, while in $Sn3S_4O_2$, the O atoms occupy the cis positions. In the two octahedra, the Sn−S/Sn−O bonds in the basal plane and Sn−S/Sn−O bonds to the apical atoms (Table S4) are comparable with data reported in the literature.[32,55] For the SnS_4O trigonal bipyramid, the Sn−O/S bonds are slightly larger than those in the octahedra. The S−Sn−S/S−Sn−O/O−Sn−O angles (Table S4) in the three polyhedra indicate distortions from ideal geometry, as were also observed in similar compounds.[32,55] The Sn_4O tetrahedron is strongly distorted, as evidenced by the Sn−O bond lengths (2.001(7)−2.681(1) Å) and the Sn−O−Sn angles (92.95(6)−128.77(6)°). One cluster of **1** is located on each corner and another in the middle of the unit cell, and two clusters are positioned on the middle of the faces (010) and (001) (Figure 5).

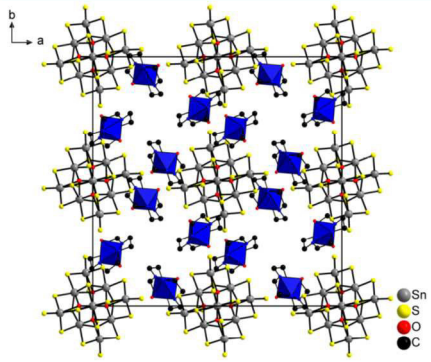

Figure 5. View of the arrangement of the $\{Sn_{10}S_{20}O_4\}$ moieties and Ni^{2+}-centered complexes (blue octahedra) in the unit cell of compound **1**. H atoms are not shown.

The $[Sn_{10}S_{20}O_4]^{8-}$ clusters on the corner and in the middle of the unit cell are arranged in rods along the *b* axis, and the remaining clusters form rods along [100]. The cations and H_2O molecules occupy the empty spaces between the anions. The size of the channel along [001] is about 5.5 $Å^2$ measured from coordinate-to-coordinate. In **1**, charge compensation is achieved by the Ni^{2+} cation, which is in an octahedral environment of four N atoms of the cyclen ligands and two O atoms of the H_2O molecules (Figure 6).

We note that all Sn−O−S compounds contain isolated $[Sn_{10}S_{20}O_4]^{8-}$ clusters with inorganic cations compensating for the negative charges like in $[Cs_8(H_2O)_{13}][Sn_{10}S_{20}O_4]$[32] and $[Li_8(H_2O)_{29}][Sn_{10}S_{20}O_4]\cdot 2H_2O$,[27] and only in $\{[Ni(1,2\text{-dach})_2(ma)]_4[Sn_{10}S_{20}O_4]\}$ (1,2-dach = 1,2-diaminocyclohexane; ma = methylamine)[55] is the cluster expanded via S atoms to Ni^{2+}-centered complexes. In this compound, the Ni^{2+} cation is in an octahedral environment of five N atoms of the amine ligands and of one S atom of the $[Sn_{10}S_{20}O_4]^{8-}$ cluster.

Spectroscopy Properties. The typical bands of the cyclen molecule in **1** can be identified in the IR spectrum (Figure S7 and Table S5). The OH band of H_2O molecules in compound **1** is located at 3373 cm^{-1}. The N−H stretching vibration of cyclen occurs around 3199 cm^{-1}, and the Ni−N stretching mode is observed around 417 cm^{-1}. The UV/vis spectrum

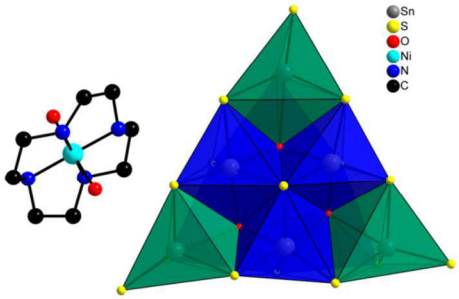

Figure 6. Views of the $[Ni(cyclen)(H_2O)_2]^{2+}$ complex (left) and the $[Sn_{10}S_{20}O_4]^{8-}$ anion (right). Nearly trigonal-bipyramidal SnS_4O: polyhedra, green; octahedra, blue.

shows the expected d−d transitions. For the high-spin complex $[Ni(H_2O)_6]^{2+}$, the d−d transitions are located at 1.05 eV (1176 nm, $^3A_{2g} \rightarrow {}^3T_{2g}$), 1.71 eV (724 nm, $^3A_{2g} \rightarrow {}^3T_{1g}$ (F)), and 3.14 eV (395 nm, $^3A_{2g} \rightarrow {}^3T_{1g}$ (P)).[52] For **1**, these transitions are found at 1.16 eV (1068 nm), 2.03 eV (610 nm), and 3.11 eV (398 nm) (Figure S8); i.e., the color stems from d−d transitions at 2.03 eV (610 nm), explaining the green color of the crystals. The absorption band at 3.11 eV is too intense for a d−d transition and is mostly the sum of the d−d and HOMO−LUMO transition.[52] The strong absorption at 3.72 eV may be regarded as a charge-transfer band.[58]

TGA. The TGA, differential thermal analysis (DTA), and derivative thermogravimetry curves of **1** are displayed in Figure S9. A mass loss of 4.5% is observed in the first step, which is accompanied by a broad endothermic event ($T_{peak} \approx 75$ °C) and corresponds to the removal of eight crystal H_2O molecules (calcd 4.6%). The second decomposition step with a mass loss of 26.7% is also accompanied by an endothermic event (T_{peak} = 335 °C) and corresponds to the removal of eight H_2O molecules that coordinate to the Ni^{2+} cation and four cyclen ligands (calcd 26.6%). To confirm the emission of individual constituents of the compound, the black residue of the decomposition product (T = 500 °C) was investigated by PXRD and IR spectroscopy. According to the PXRD pattern, the residue consists of NiO, SnS, $Ni_3Sn_2S_2$, and an unknown phase (Figure S10). Furthermore, in the IR spectrum, no bands of H_2O molecules and cyclen ligands are observed (Figure S11). According to the void space, the crystal H_2O content should be app. 13. An experiment was performed with a freshly prepared compound, which was weighed at room temperature for about 1 day at regular time intervals. The weight was reduced within several minutes, which may explain the difference between the observed and expected H_2O content in the TGA curve. In a further experiment, decomposition was stopped at 130 °C and a PXRD pattern was collected. Afterward, the residue was stored for 1 day in a H_2O atmosphere, and again a PXRD pattern was measured (Figures S12 and S13). The removal of H_2O is accompanied by a slight shift of the positions of the Bragg reflections (Figure S12, bottom), while rehydration leads to a PXRD pattern in full agreement with that of the pristine material.

N_2 and H_2O Sorption. The N_2 adsorption−desorption curves of **1** were recorded, but the Brunauer−Emmett−Teller surface area was only app. 20 $m^2 \cdot g^{-1}$; i.e., the sample is

DOI: 10.1021/acs.inorgchem.8b02773
Inorg. Chem. 2019, 58, 2354−2362

nonporous (Figure S14, bottom). Nevertheless, the H_2O sorption−desorption was measured, and ca. 13 H_2O molecules were adsorbed at $p/p_0 = 0.9$ (Figure S14, top). The desorption branch exhibits a divergent shape, and at $p/p_0 = 0.1$, the sample still contained about 4 H_2O molecules. After H_2O uptake, a PXRD pattern was recorded that matches that collected for the pristine material (Figure S15); i.e., the sample is stable. The observed H_2O isotherm does not follow the typical isotherms according to the IUPAC nomenclature. At the moment, no straightforward explanation can be given, but we will assume that kinetics play an important role and strong interactions between H_2O and atoms of the host material lead to the observed isotherm. Similarly, the low N_2 adsorption (Figure S14, bottom) may be a kinetic phenomenon because the measurement is performed at 77 K, and additionally N_2 and H_2O exhibit different kinetic diameters (N_2, 3.64 Å; H_2O, 2.65 Å[59]). We note that the observation made here is not unusual, and, e.g., MOF-802,[60] Ni-CAU-29,[61] or STA-12[62] did not show N_2 adsorption but good H_2O uptake. We calculated the Connolly surface (Figure S16) for H_2O as the probe molecule (probe radius 1.32 Å) using *Materials Studio*. The calculated accessible volume for this guest molecule is 19.3% of the total volume, being proportional to a maximum H_2O content of approximately 9 wt %. These data clearly support the experimental findings.

Photocatalytic Hydrogen Evolution. Photocatalytic experiments were carried out with **1**, $[Ru(bpy)_3](PF_6)_2$ as the photosensitizer, the sacrificial agent triethylamine as the electron donor, H_2O as the proton source, and CH_3CN as the solvent for the photosensitizer. The photocatalytically evolved H_2 (Figure 7) increases with increasing irradiation and then

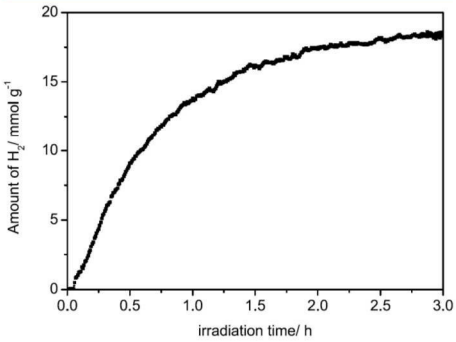

Figure 7. Photocatalytic hydrogen evolution using compound **1**, $[Ru(bpy)_3](PF_6)_2$ as the photosensitizer, triethylamine as the sacrificial agent, H_2O as the proton donor, and acetonitrile as the solvent.

levels off, reaching 18.7 mmol·g^{-1} after 3 h of irradiation time, and longer irradiation yields a constant H_2 evolution up to 5 h. During the reaction, the light-orange solution turned brown, leading to a reduced absorption of incident light, which may explain the decline of the initially steep curve. Such a color change indicates photodegradation of the sensitizer, as reported in several publications.[63−68] The compound could be recovered after photocatalysis, but the PXRD pattern indicates low crystallinity (Figure S17). When new solvents are applied to the recovered material, the hydrogen evolution reaches only 3.2 mmol·g^{-1}. This observation is an indication that the compound is destroyed during the photocatalytic reaction. Therefore, the stability of **1** in the solution of triethylamine/acetonitrile/H_2O was investigated by storing the sample for 1 day at room temperature. The PXRD pattern shows a modulated background besides reflections of **1**, suggesting the formation of an amorphous solid. This observation supports the assumption that **1** is not stable under the basic conditions for a longer time and irradiation may accelerate the amorphization process. We assume that during chemical decomposition the Ni^{2+}-centered complex is released, and therefore a photocatalytic experiment was performed with the mixture $[Ni(cyclen)(H_2O)_2](ClO_4)_2 \cdot H_2O/[Ru(bpy)_3](PF_6)_2$ (Figure S18). For this system, 18.9 mmol·g^{-1} H_2 was obtained after 3 h of irradiation time, and longer irradiation yields a constant H_2 evolution up to 5 h. However, it was reported that transition-metal complexes may be destroyed during the photocatalytic reaction and nanoparticles are generated, which are the active species.[69] Such complexes may be regarded as precatalysts, which are in situ transformed into the catalytically active species. The appearance of the Tyndall effect after the photocatalytic reaction confirms the presence of nanoparticles. In the present case, the situation is more complex than only using a Ni^{2+}-centered complex because the anion may also be decomposed and the amorphous particles generated may contain both Ni and Sn. A possible photocatalytic mechanism has already been discussed for the $[Ni(bpy)_3]^{2+}$ complex (bpy = 2,2′-bipyridine)[70] and on the basis of this proposed mechanism, we assume a similar mechanism for the $[Ni(cyclen)(H_2O)_2]^{2+}$ complex (Scheme 2).

Scheme 2. Proposed Mechanism for Photocatalytic Hydrogen Generation Using the $[Ni(cyclen)(H_2O)_2]^{2+}$ Complex[a]

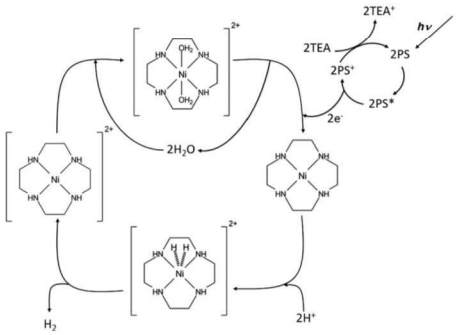

[a]PS = $[Ru(bpy)_3](PF_6)_2$; TEA = triethylamine. The scheme was adapted from ref 70.

A comparison of the photocatalytic activity with data reported in the literature is difficult because the activity depends on a large number of parameters like solvents, the amount of the catalyst, the cocatalyst, the photosensitizer, the intensity and wavelength of the light source, the sacrificial compound, the pH value, etc. In addition, the amount of H_2

DOI: 10.1021/acs.inorgchem.8b02773
Inorg. Chem. 2019, 58, 2354−2362

produced is reported as different quantities like, e.g., mmol·g^{-1}, mmol, mL, turnover number, or turnover frequency.[71] Nevertheless, the amount of H_2 of 138 μmol·h^{-1} is in the range of data reported for sulfidic compounds or composites (Table 1).

Table 1. Comparison of the Photocatalytic Activity of Different Catalysts at Various Conditions

catalyst	reaction mixture/light source	activity/ μmol·h^{-1}
compound **1**	triethylamine, acetonitrile, H_2O, $[Ru(bpy)_3](PF_6)_2$, 330 W Xe lamp, cutoff filter (λ > 400 nm)	138
colloidal MoS_2[72]	scorbic acid, acetonitrile, methanol, $[Ru(bpy)_3](PF_6)_2$, 300 W Xe lamp, cutoff filter (λ > 420 nm)	420
TiO_2/MoS_2/graphene[73]	ethanol, H_2O, 350 W Xe lamp	165
MoS_xC_y[74]	triethylamine, acetonitrile, H_2O, $[Ru(bpy)_3](PF_6)_2$, 300 W Xe lamp, cutoff filter (λ > 420 nm)	120
MoS_2/SiO_2[75]	KOH, TiO_2, H_2O, methanol, medium-pressure Hg lamp	860
CoS_x/graphene[76]	TEOA, H_2O, Eosin Y/300 W Xe lamp, cutoff filter (λ > 455 nm)	300
$[Co_4(C_6H_{14}N)_4(\mu_4\text{-}S_2)_2(\mu_2\text{-}S_2)_4]\cdot 4H_2O$[77]	triethylamine, acetonitrile, H_2O, $[Ru(bpy)_3](PF_6)_2$, 330 W Xe lamp	98
CoS/mpg-CN (mpg = mesoporous graphitic)[78]	H_2O, triethanolamine, 300 W Xe lamp	37

CONCLUSION

In this work, we present the structure of a new rare oxothiostannate **1**, which was prepared by the reaction of $Na_4SnS_4\cdot 14H_2O$ with $[Ni(cyclen)(H_2O)_2](ClO_4)_2\cdot H_2O$ under hydrothermal conditions. The anion is constructed by a T3 supertetrahedron and an anti-T2 cluster. In the structure, tunnels are directed along [001], which host H_2O molecules. The sample can be reversibly dehydrated and rehydrated without significant loss of crystallinity. ^{119}Sn NMR investigations of an aqueous solution of $Na_4SnS_4\cdot 14H_2O$ demonstrate that only $[SnS_4]^{4-}$ and $[Sn_2S_6]^{4-}$ anions exist in solution, and they are stable up to 120 °C. The formation of $[Sn_2S_6]^{4-}$ occurs via a condensation reaction, and H_2S is released. One must postulate that generation of the oxosulfide $[Sn_{10}S_{20}O_4]^{8-}$ ion requires the presence of the Ni^{2+}-centered complex in the reaction mixture. In situ investigations of the formation show that crystallization already occurs at 90 °C and pH 12.3. The photocatalytic experiments show a high activity for hydrogen generation, and the catalysis is most probably heterogeneous.

ASSOCIATED CONTENT

Supporting Information

The Supporting Information is available free of charge on the ACS Publications website at DOI: 10.1021/acs.inorgchem.8b02773.

Crystal data and refinement results, tables with interatomic distances, IR and UV/vis spectra, DTA–TGA curves, N_2 and H_2O sorption curves, PXRD patterns of the pristine samples (dehydrated and rehydrated), and additional photocatalytic curves (PDF)

Accession Codes

CCDC 1863577 contains the supplementary crystallographic data for this paper. These data can be obtained free of charge via www.ccdc.cam.ac.uk/data_request/cif, or by emailing data_request@ccdc.cam.ac.uk, or by contacting The Cambridge Crystallographic Data Centre, 12 Union Road, Cambridge CB2 1EZ, UK; fax: +44 1223 336033.

AUTHOR INFORMATION

Corresponding Author

*E-mail: wbensch@ac.uni-kiel.de. Phone: +49 431 880-2419. Fax: +49 431 880-1520.

ORCID

Helge Reinsch: 0000-0001-5288-1135

Wolfgang Bensch: 0000-0002-3111-580X

Notes

The authors declare no competing financial interest.

ACKNOWLEDGMENTS

Financial support by the State of Schleswig-Holstein is gratefully acknowledged. We thank Aleksej Jochim for the TGA measurements and Philipp Polzin and Dr. Huayna Terraschke for support.

REFERENCES

(1) Sheldrick, W. S. Network self-assembly patterns in Main Group metal chalcogenide-based materials. *J. Chem. Soc., Dalton Trans.* **2000**, 3041–3052.

(2) Schiwy, W.; Pohl, S.; Krebs, B. Darstellung und Struktur von $Na_4SnS_4\bullet 14H_2O$. *Z. Anorg. Allg. Chem.* **1973**, *402*, 77–86.

(3) Ruzin, E.; Jakobi, S.; Dehnen, S. Syntheses, Structures and Reactivity of Novel Hydrates of *ortho*-Sulfidostannate Salts. *Z. Anorg. Allg. Chem.* **2008**, *634*, 995–1001.

(4) Krebs, B.; Pohl, S.; Schiwy, W. Darstellung und Struktur von $Na_4Ge_2S_6\bullet 14H_2O$ und $Na_4Sn_2S_6\bullet 14H_2O$. *Z. Anorg. Allg. Chem.* **1972**, *393*, 241–252.

(5) Krebs, B. Thio- und Selenoverbindungen von Hauptgruppenelementen – neue anorganische Oligomere und Polymere. *Angew. Chem.* **1983**, *95*, 113–134.

(6) Liao, J.-H.; Varotsis, C.; Kanatzidis, M. G. Syntheses, Structures, and Properties of Six Novel Alkali Metal Tin Sulfides: $K_2Sn_2S_5$, α-$Rb_2Sn_2S_5$, β-$Rb_2Sn_2S_5$, $K_2Sn_2S_5$, $Cs_2Sn_2S_5$, and Cs_2SnS_{14}. *Inorg. Chem.* **1993**, *32*, 2453–2462.

(7) Jiang, T.; Lough, A.; Ozin, G. A.; Bedard, R. L.; Broach, R. Synthesis and structure of microporous layered tin(IV) sulfide materials. *J. Mater. Chem.* **1998**, *8*, 721–732.

(8) Ko, Y.; Cahill, C. L.; Parise, J. B. Novel Layered Sulfides of Tin: Synthesis and Structural Characterization of $Cs_4Sn_5S_{12}\bullet 2H_2O$ and $Sn_5S_{12}(N_2C_4H_{11})_2(N_4C_{10}H_{24})$. *J. Chem. Soc., Chem. Commun.* **1994**, 69–70.

(9) Sheldrick, W. S.; Schaaf, B. Darstellung und Kristallstruktur von $Rb_2Sn_3S_7\bullet 2H_2O$ und $Rb_4Sn_2Se_6$. *Z. Anorg. Allg. Chem.* **1994**, *620*, 1041–1045.

(10) Liao, J.-H.; Kanatzidis, M. G. Quaternary $Rb_2Cu_2SnS_4$, $A_2Cu_2Sn_2S_6$ (A = Na, K, Rb, Cs), $A_2Cu_2Sn_2Se_6$ (A = K, Rb), $K_2Au_2SnS_4$, and $K_2Au_2Sn_2S_6$. Syntheses, Structures, and Properties of New Solid-state Chalcogenides Based on Tetrahedral $[SnS_4]^{4+}$ Units. *Chem. Mater.* **1993**, *5*, 1561–1569.

(11) Jumas, J.-C.; Philippot, E.; Maurin, M. Etude Structurale de $Na_4Sn_3S_8$. Evolution de la Coordination de l'Etain dans le Système Na_2S-SnS_2. *J. Solid State Chem.* **1975**, *14*, 152–159.

(12) Behrens, M.; Scherb, S.; Näther, C.; Bensch, W. On the Incorporation of Transition Metal Atoms into Thiostannates: Synthesis, Crystal Structures and Spectroscopic Properties of $[Ni(en)_3]_2Sn_2S_6$, $[Ni(dap)_3]_2Sn_2S_6\cdot 2H_2O$, $[Co(tren)]_2Sn_2S_6$, and $[Ni(tren)]_2Sn_2S_6$. *Z. Anorg. Allg. Chem.* **2003**, *629*, 1367–1373.

DOI: 10.1021/acs.inorgchem.8b02773
Inorg. Chem. 2019, 58, 2354–2362

(13) Jia, D.-X.; Zhang, Y.; Dai, J.; Zhu, Q.-Y.; Gu, Y.-M. Solvothermal Syntheses and Characterization of Thiostannates $[M(en)_3]_2Sn_2S_6$ (M = Mn, Co, Zn), the Influence of Metal Ions on the Crystal Structure. *Z. Anorg. Allg. Chem.* **2004**, *630*, 313−318.
(14) Jia, D.-X.; Dai, J.; Zhu, Q.-Y.; Zhang, Y.; Gu, X.-M. Syntheses, crystal structures and thermoanalyses of thiostannates $[Ni(en)_3]_2Sn_2S_6$ and $[Ni(dien)_2]_2Sn_2S_6$. *Polyhedron* **2004**, *23*, 937−942.
(15) Fu, M.-L.; Guo, G.-C.; Liu, B.; Wu, A.-Q.; Huang, J.-S. Two New Thiostannates Templated by Transition Metal Complexes. *Chin. J. Inorg. Chem.* **2005**, *21*, 25−29.
(16) Pienack, N.; Schinkel, D.; Puls, A.; Ordolff, M.-E.; Lühmann, H.; Näther, C.; Bensch, W. New Thiostannates Synthesized Under Solvothermal Conditions: Crystal Structures of $(trenH)_2Sn_3S_7$ and $\{[Mn(tren)]_2Sn_2S_6\}$. *Z. Naturforsch., B: J. Chem. Sci.* **2012**, *67b*, 1098−1106.
(17) Chykhrij, S. I.; Sysa, L. V.; Parasyuk, O. V.; Piskach, L. V. Crystal structure of the $Cu_2CdSn_3S_8$ compound. *J. Alloys Compd.* **2000**, *307*, 124−126.
(18) Hilbert, J.; Pienack, N.; Lühmann, H.; Näther, C.; Bensch, W. Transition Metal Complexes with Linkage to the Thiostannate Units Forced by Suitable Amine Molecules. *Z. Anorg. Allg. Chem.* **2016**, *642*, 1427−1434.
(19) Hilbert, J.; Näther, C.; Bensch, W. Influence of the Synthesis Parameters onto Nucleation and Crystallization of Five New Tin−Sulfur Containing Compounds. *Inorg. Chem.* **2014**, *53*, 5619−5630.
(20) Hilbert, J.; Näther, C.; Bensch, W. The $[Sn_2S_6]^{4-}$ Anion Acting as Tetradentate Linker: Solvothermal Synthesis and Selected Properties of $\{[TM(phen)_2]_2Sn_2S_6\}$ and $\{[TM(phen)_2]_2Sn_2S_6\}\cdot phen\cdot H_2O$ (TM = Fe, Co). *Z. Anorg. Allg. Chem.* **2014**, *640*, 2858−2863.
(21) Pienack, N.; Bensch, W. The new silver thiostannate $(1,4\text{-}dabH_2)Ag_2SnS_4$: Solvothermal Synthesis, Crystal Structure and Spectroscopic Properties. *Z. Anorg. Allg. Chem.* **2006**, *632*, 1733−1736.
(22) Pienack, N.; Puls, A.; Näther, C.; Bensch, W. The layered thiostannate $(dienH_2)Cu_2Sn_2S_6$ − a Photoconductive Inorganic-Organic Hybrid Compound. *Inorg. Chem.* **2008**, *47*, 9606−9611.
(23) Feng, K.; Zhang, X.; Yin, W.; Shi, Y.; Yao, J.; Wu, Y. New Quaternary Rare-Earth Chalcogenides $BaLnSn_2Q_6$ (Ln = Ce, Pr, Nd, Q = S; Ln = Ce, Q = Se): Synthesis, Structure, and Magnetic Properties. *Inorg. Chem.* **2014**, *53*, 2248−2253.
(24) Behrens, M.; Ordolff, M.-E.; Näther, C.; Bensch, W.; Becker, K.-D.; Guillot-Deudon, C.; Lafond, A.; Cody, J. A. New Three-Dimensional Thiostannates Composed of Linked Cu_8S_{12} Clusters and the First Example of a Mixed-Metal Cu_2SnS_{12} Cluster. *Inorg. Chem.* **2010**, *49*, 8305−8309.
(25) Nayek, H. P.; Massa, W.; Dehnen, S. A Heterometallic, Heterovalent $Cu^{I}/Sn^{II/IV}/S$ Cluster with an Unprecedented Cu_4Sn Core and Stannacyclopentane Units. *Inorg. Chem.* **2008**, *47*, 9146−9148.
(26) Hassanzadeh Fard, Z.; Müller, C.; Harmening, T.; Pöttgen, R.; Dehnen, S. Knüpfung von Thiostannat-Sn-Sn-Bindungen in Lösung: In-situ-Bildung des gemischtvalenten funktionalisierten Komplexes $[\{(RSn^{IV})_2(\mu\text{-}S)_2\}_3Sn^{III}{}_2S_6]$. *Angew. Chem.* **2009**, *121*, 4507−4511.
(27) Kaib, T.; Kapitein, M.; Dehnen, S. Synthesis and Crystal Structure of $[Li_8(H_2O)_{29}][Sn_{10}O_4S_{20}]\cdot 2H_2O$. *Z. Anorg. Allg. Chem.* **2011**, *637*, 1683−1686.
(28) Parise, J. B.; Ko, Y. Material Consisting of Two Interwoven 4-Connected Networks: Hydrothermal Synthesis and Structure of $[Sn_5S_9O_2][HN(CH_3)_3]_2$. *Chem. Mater.* **1994**, *6*, 718−720.
(29) Zhang, J.-J.; Hu, S.-M.; Wu, X.-T.; Du, W.-X.; Fu, R.-B.; Wang, L.-S. A simple method for the preparation of octanuclear tin (IV) oxosulfide cluster and the conversion of it to decanuclear cluster. *Inorg. Chem. Commun.* **2003**, *6*, 744−747.
(30) Wu, L.; Chen, L.; Dai, J.; Cui, C.; Fu, Z.; Wu, X. The first octanuclear tin(IV)-oxosulfide cluster. *Inorg. Chem. Commun.* **2001**, *4*, 574−576.
(31) Bubenheim, W.; Müller, U. Reaktionen von Zinnchloriden mit Polysulfiden. Die Kristallstrukturen von $(PPh_4)_2[SnCl_2(S_6)_2]$, $(PPh_4)_2[Sn_4Cl_4S_5(S_3)O]$ und $(PPh_4)_2[SnCl_6]\bullet S_8\bullet 2CH_3CN$. *Z. Anorg. Allg. Chem.* **1993**, *619*, 779−785.
(32) Schiwy, W.; Krebs, B. $[Sn_{10}O_4S_{20}]^{8-}$: Ein neuer Typ eines Polyanions. *Angew. Chem.* **1975**, *87*, 451−452.
(33) Marking, G. A.; Evain, M.; Petricek, V.; Kanatzidis, M. G. New Layered Compounds through Polysulfide Flux Synthesis; $A_2Sn_4S_9$ (A = K, Rb, Cs) Present a New Form of the $[Sn_4S_9]^{2-}$ Network. *J. Solid State Chem.* **1998**, *141*, 17−28.
(34) Devi, M. S.; Vidyasagar, K. First examples of sulfides in the quaternary A/Cd/Sn/S (A = Li, Na) systems: molten flux synthesis and single crystal X-ray structures of Li_2CdSnS_4, Na_2CdSnS_4 and $Na_6CdSn_4S_{12}$. *J. Chem. Soc., Dalton Trans.* **2002**, 2092−2096.
(35) Kumari, A.; Vidyasagar, K. Solid-state synthesis, structural variants and transformation of three-dimensional sulfides, $AGaSnS_4$ (A = Na, K, Rb, Cs, Tl) and $Na_{1.263}Ga_{1.263}Sn_{0.737}S_4$. *J. Solid State Chem.* **2007**, *180*, 2013−2019.
(36) Teske, C. L. Darstellung und Kristallstruktur von Barium-Cadmium-Thiostannat (IV) $BaCdSnS_4$. *Z. Anorg. Allg. Chem.* **1980**, *460*, 163−168.
(37) Teske, C. L. Darstellung und Kristallstruktur von Gold-Barium-Thiostannat (IV), Au_2BaSnS_4. *Z. Anorg. Allg. Chem.* **1978**, *445*, 193−201.
(38) Seidlhofer, B.; Pienack, N.; Bensch, W. Synthesis of Inorganic-Organic Hybrid Thiometallate Materials with a Special Focus on Thioantimonates and Thiostannates and in *situ* X-Ray Scattering Studies of their Formation. *Z. Naturforsch., B: J. Chem. Sci.* **2010**, *65b*, 937−975.
(39) Oh, Y.; Bag, S.; Malliakas, C. D.; Kanatzidis, M. G. Selective Surfaces: High-Surface-Area Zinc Tin Sulfide Chalcogels. *Chem. Mater.* **2011**, *23*, 2447−2456.
(40) Coates, J. H.; Hadi, D. A.; Lincoln, S. F.; Dodgen, H. W.; Hunt, J. P. Oxygen-17 Magnetic Resonance and Temperature-Jump Spectrophotometric Study of the Square Planar-Octahedral Equilibrium in the 1,4,7,10-Tetraaza-cyclododecanenickel(II) System. *Inorg. Chem.* **1981**, *20*, 707−711.
(41) *Topas Academics 4.2*; Coelho Software: Brisbane, Australia, 2007.
(42) Altomare, A.; Camalli, M.; Cuocci, C.; Giacovazzo, C.; Moliterni, A.; Rizzi, R. EXPO2009: structure solution by powder data in direct and reciprocal space. *J. Appl. Crystallogr.* **2009**, *42*, 1197−1202.
(43) *Materials Studio*, version 5.0; Accelrys Inc.: San Diego, CA, 2009.
(44) Rappe, A. K.; Casewit, C. J.; Colwell, K. S.; Goddard, W. A., III; Skiff, W. M. UFF, a full periodic table force field for molecular mechanics and molecular dynamics simulations. *J. Am. Chem. Soc.* **1992**, *114*, 10024−10035.
(45) Spek, A. L. Single-crystal structure validation with the program PLATON. *J. Appl. Crystallogr.* **2003**, *36*, 7−13.
(46) Pienack, N.; Ruiz Arana, L.; Bensch, W.; Terraschke, H. In Situ Studies on Phase Transitions of Tris(acetylacetonato)-Aluminum(III) $Al(acac)_3$. *Crystals* **2016**, *6*, 157−158.
(47) Terraschke, H.; Ruiz Arana, L.; Lindenberg, P.; Bensch, W. Development of a new *in situ* analysis technique applying luminescence of local coordination sensors: principle and application for monitoring metal-ligand exchange processes. *Analyst* **2016**, *141*, 2588−2594.
(48) Mundus, C.; Taillades, G.; Pradel, A.; Ribes, M. A ^{119}Sn solid-state nuclear magnetic resonance study of crystalline tin sulphides. *Solid State Nucl. Magn. Reson.* **1996**, *7*, 141−146.
(49) Davies, A. G.; Gielen, M.; Pannell, K. H.; Tiekink, E. R. T. *Tin Chemistry: Fundamentals, Frontiers, and Applications*, 1st; John Wiley & Sons, Ltd.: London, 2008.
(50) Protesescu, L.; Nachtegaal, M.; Voznyy, O.; Borovinskaya, O.; Rossini, A. J.; Emsley, L.; Copéret, C.; Günther, D.; Sargent, E. H.; Kovalenko, M. V. Atomistic Description of Thiostannate-Capped CdSe Nanocrystals: Retention of Four-Coordinate SnS4Motif and Preservation of Cd-Rich Stoichiometry. *J. Am. Chem. Soc.* **2015**, *137*, 1862−1874.

DOI: 10.1021/acs.inorgchem.8b02773
Inorg. Chem. 2019, 58, 2354−2362

(51) Mason, J. *Multinuclear NMR*, 1st; Plenum Press: New York, 1987.
(52) Holleman, F. A.; Wiberg, E.; Wiberg, N. *Lehrbuch der Anorganischen Chemie*, 102nd; Walter de Gruyter: Berlin, 2007.
(53) Haj, S. B. Functionalized Organotin Compounds as Synthons for Tin-containing Heterocycles and Periphery-functionalized Organotinoxo Clusters. Ph.D. Thesis, University of Dortmund, Dortmund, Germany,2015.
(54) Powell, P. *Principles of Organometallic Chemistry*, 2nd; Springer: London, 1988.
(55) Hilbert, J.; Näther, C.; Bensch, W. {[Ni(1,2-dach)$_2$(ma)]$_4$[$Sn_{10}S_{20}O_4$]} An Example of the Tin-Oxo-Sulfide Cluster with Uncommon Connection Mode Towards the Charge Compensating Ni(II) Complex. *Curr. Inorg. Chem.* **2017**, *6*, 181−186.
(56) Cahill, C. L.; Parise, J. B. On the formation of framework indium sulfides. *J. Chem. Soc., Dalton Trans.* **2000**, 1475−1482.
(57) Bu, X.; Zheng, N.; Feng, P. Tetrahedral Chalcogenide Clusters and Open Frameworks. *Chem. - Eur. J.* **2004**, *10*, 3356−3362.
(58) Vijayan, P.; Viswanathamurthi, P.; Velmurugan, K.; Nandhakumar, R.; Balakumaran, M. D.; Kalaichelvan, P. T.; Malecki, J. G. Nickel(II) and copper(II) complexes constructed with N_2S_2 hybrid benzamidine−thiosemicarbazone ligand: synthesis, X-ray crystal structure, DFT, kinetico-catalytic and *in vitro* biological applications. *RSC Adv.* **2015**, *5*, 103321−103342.
(59) Ismail, A. F.; Khulbe, K. C.; Matsuura, T. *Gas Separation Membranes: Polymeric and Inorganic*; Springer International Publishing, 2015.
(60) Furukawa, H.; Gandara, F.; Zhang, Y.-B.; Jiang, J.; Queen, W. L.; Hudson, M. R.; Yaghi, O. M. Water Adsorption in Porous Metal−Organic Frameworks and Related Materials. *J. Am. Chem. Soc.* **2014**, *136*, 4369−4381.
(61) Rhauderwiek, T.; Wolkersdörfer, K.; Øien-Ødegaard, S.; Lillerud, K.-P.; Wark, M.; Stock, N. Crystalline and permanently porous porphyrin-based metal tetraphosphonates. *Chem. Commun.* **2018**, *54*, 389−392.
(62) Wharmby, M. T.; Pearce, G. M.; Mowat, J. P. S.; Griffin, J. M.; Ashbrook, S. E.; Wright, P. A.; Schilling, L.-H.; Lieb, A.; Stock, N.; Chavan, S.; Bordiga, S.; Garcia, E.; Pirngruber, G. D.; Vreeke, M.; Gora, L. Synthesis and crystal chemistry of the STA-12 family of metal N,N′-piperazinebis(methylenephosphonate)s and applications of STA-12(Ni) in the separation of gases. *Microporous Mesoporous Mater.* **2012**, *157*, 3−17.
(63) Beyene, B. B.; Hung, C.-H. Photocatalytic hydrogen evolution from neutral aqueous solution by a water-soluble cobalt(II) porphyrin. *Sustainable Energy Fuels* **2018**, *2*, 2036−2043.
(64) Nippe, M.; Khnayzer, R. S.; Panetier, J. A.; Zee, D. Z.; Olaiya, B. S.; Head-Gordon, M.; Chang, C. J.; Castellano, F. N.; Long, J. R. Catalytic proton reduction with transition metal complexes of the redox-active ligand bpy2PYMe. *Chem. Sci.* **2013**, *4*, 3934−3945.
(65) Durham, B.; Caspar, J. V.; Nagle, J. K.; Meyer, T. J. Photochemistry of tris(2,2′-bipyridine)ruthenium(2+) ion. *J. Am. Chem. Soc.* **1982**, *104*, 4803−4810.
(66) Henderson, L. J.; Ollino, M.; Gupta, V. K.; Newkome, G. R.; Cherry, W. R. Effect of chelate ring size on the photoanation reaction of polypyridine ruthenium complexes. *J. Photochem.* **1985**, *31*, 199−210.
(67) Vaidyalingam, A.; Dutta, P. K. Analysis of the Photodecomposition Products of $[Ru(bpy)_3]^{2+}$ in Various Buffers and upon Zeolite Encapsulation. *Anal. Chem.* **2000**, *72*, 5219−5224.
(68) Niefind, F.; Djamil, J.; Bensch, W.; Srinivasan, B. R.; Sinev, I.; Grünert, W.; Deng, M.; Kienle, L.; Lotnyk, A.; Mesch, M. B.; Senker, J.; Dura, L.; Beweries, T. Room temperature synthesis of an amorphous MoS_2 based composite stabilized by N-donor ligands and its light-driven photocatalytic hydrogen production. *RSC Adv.* **2015**, *5*, 67742−67751.
(69) Asraf, Md. A.; Younus, H. A.; Yusubov, M.; Verpoort, F. Earth-abundant metal complexes as catalysts for water oxidation; is it homogeneous or heterogeneous? *Catal. Sci. Technol.* **2015**, *5*, 4901−4925.
(70) Yuan, Y.-J.; Lu, H.-W.; Tu, J.-R.; Fang, Y.; Yu, Z.-T.; Fan, X.-X.; Zou, Z.-G. A Noble-Metal-Free Nickel(II) Polypyridyl Catalyst for Visible-Light-Driven Hydrogen Production from Water. *ChemPhysChem* **2015**, *16*, 2925−2930.
(71) Dave, M.; Rajagopal, A.; Damm-Ruttensperger, M.; Schwarz, B.; Nägele, F.; Daccache, L.; Fantauzzi, D.; Jacob, T.; Streb, C. Understanding homogeneous hydrogen evolution reactivity and deactivation pathways of molecular molybdenum sulfide catalysts. *Sustainable Energy Fuels* **2018**, *2*, 1020−1026.
(72) Zong, X.; Na, Y.; Wen, F.; Ma, G.; Yang, J.; Wang, D.; Ma, Y.; Wang, M.; Sun, L.; Li, C. Visible light driven H_2 production in molecular systems employing colloidal MoS_2 nanoparticles as catalyst. *Chem. Commun.* **2009**, 4536−4538.
(73) Xiang, Q.; Yu, J.; Jaroniec, M. Synergetic Effect of MoS_2 and Graphene as Cocatalysts for Enhanced Photocatalytic H_2 Production Activity of TiO_2 Nanoparticles. *J. Am. Chem. Soc.* **2012**, *134*, 6575−6578.
(74) Djamil, J.; Segler, S. A.; Dabrowski, A.; Bensch, W.; Lotnyk, A.; Schürmann, U.; Kienle, L.; Hansen, S.; Beweries, T. The influence of carbon content on the structure and properties of MoS_xC_y photocatalysts for light driven hydrogen generation. *Dalton Trans.* **2013**, *42*, 1287−1292.
(75) Sobczynski, A. Molybdenum Disulfide as a Hydrogen Evolution Catalyst for Water Photodecomposition on Semiconductors. *J. Catal.* **1991**, *131*, 156−166.
(76) Kong, C.; Min, S.; Lu, G. Dye-sensitized cobalt catalysts for high efficient visible light hydrogen evolution. *Int. J. Hydrogen Energy* **2014**, *39*, 4836−4844.
(77) Pienack, N.; Lühmann, H.; Djamil, J.; Permien, S.; Näther, C.; Haumann, S.; Weihrich, R.; Bensch, W. Two Pseudopolymorphic Star-Shaped Tetranuclear Co^{3+} Compounds with Disulfide Anions Exhibiting Two Different Connection Modes and Promising Photocatalytic Properties. *Chem. - Eur. J.* **2015**, *21*, 13637−13645.
(78) Zhu, Y.; Xu, Y.; Hou, Y.; Ding, Z.; Wang, X. Cobalt sulfide modified graphitic carbon nitride semiconductor for solar hydrogen production. *Int. J. Hydrogen Energy* **2014**, *39*, 11873−11879.

DOI: 10.1021/acs.inorgchem.8b02773
Inorg. Chem. 2019, 58, 2354−2362

Supporting Information

Synthesis and Characterization of a rare Transition Metal Oxo-Thiostannate and Investigation of its Photocatalytic Properties

Assma Benkada, Helge Reinsch, Jan Krahmer, Michael Poschmann, Nicole Pienack, Wolfgang Bensch

Content

Table S1: Crystallographic parameters obtained by structure solution and Rietveld refinement of the X-ray powder pattern of **1**

Crystal system	Tetragonal
Space group	$I4_1/a$
a (Å)	26.8992(8)
b (Å)	26.8992(8)
c (Å)	12.3616(6)
V (Å^3)	8944.7(7)
Z	4
Dcalc (g/cm^3)	2.13
Diffractometer	STOE Stadi P
Detector	Dectris Mythen
Radiation	Cu-$K_{\alpha 1}$, λ = 154.0598 pm
Temperature (K)	293
Range of data collection	$3 < 2\theta < 50$
Independent atoms	24
R_{WP} (%)	8.3
R_p (%)	6.5
R_{Bragg} (%)	3.0
R_{Exp} (%)	2.9
GoF	2.9

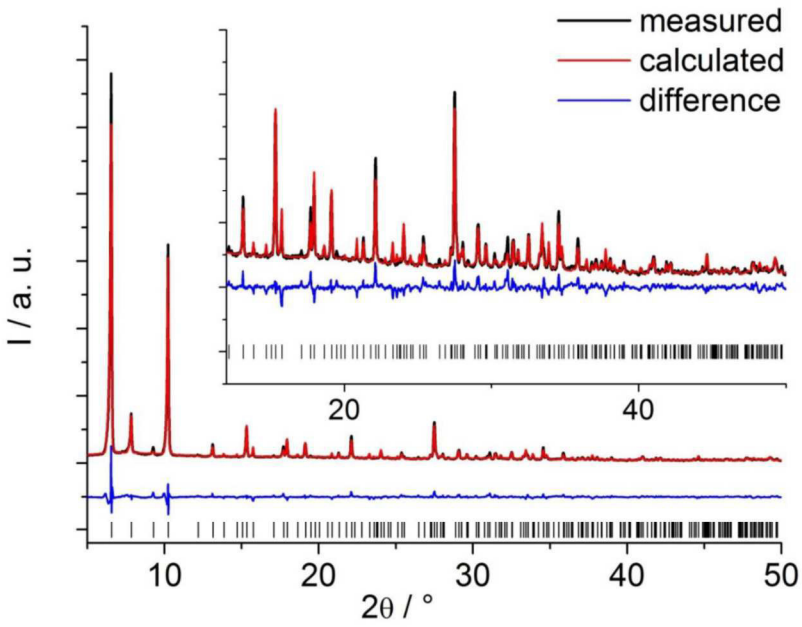

Figure S1: Final Rietveld plot with experimental data shown in black, calculated fit shown in red and difference curved shown in blue. The vertical bars indicate the allowed peak positions.

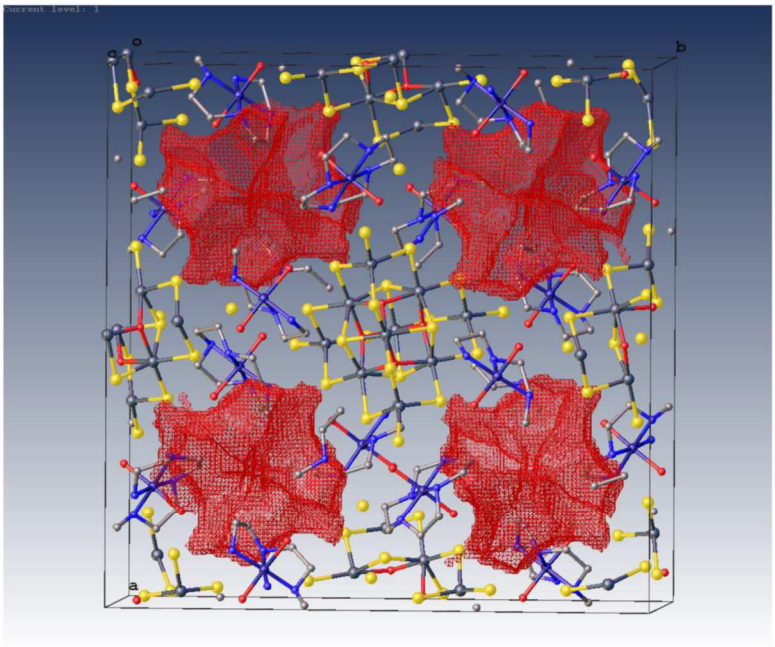

Figure S2: Solvent accessible space in compound **1** calculated using OLEX2 [1].

[1]: O. V. Dolomanov, L. J. Bourhis, R. J. Gildea, J. A. K. Howard, H. Puschmann, *J. Appl. Cryst.* **2009**, *42*, 339-341.

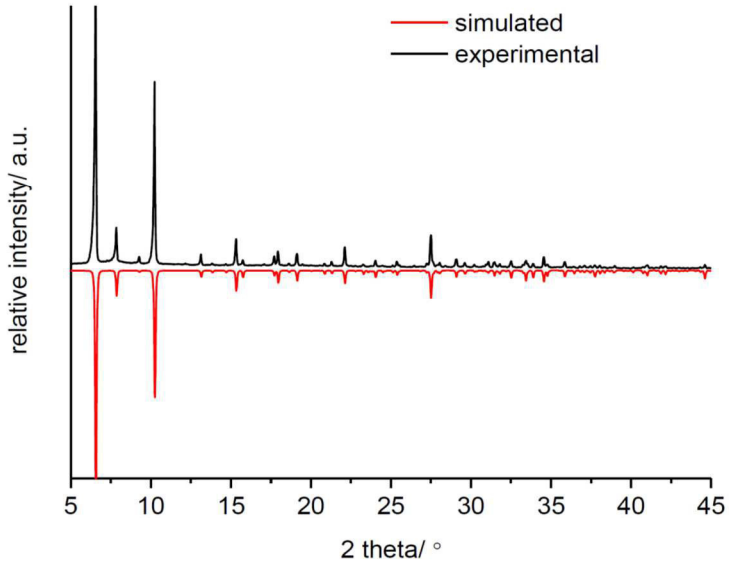

Figure S3: Experimental PXRD pattern of compound **1** (black) compared with the simulated pattern calculated from the results of the Rietveld refinement (red).

Table S2: EDX data for compound **1**

		Ni	Sn	S
Compound **1**	Calculated	4 11.38 %	10 57.54 %	20 31.08 %
	Measured	4.11 11.72 %	10.07 57.95 %	19.51 30.32 %

^{119}Sn-NMR

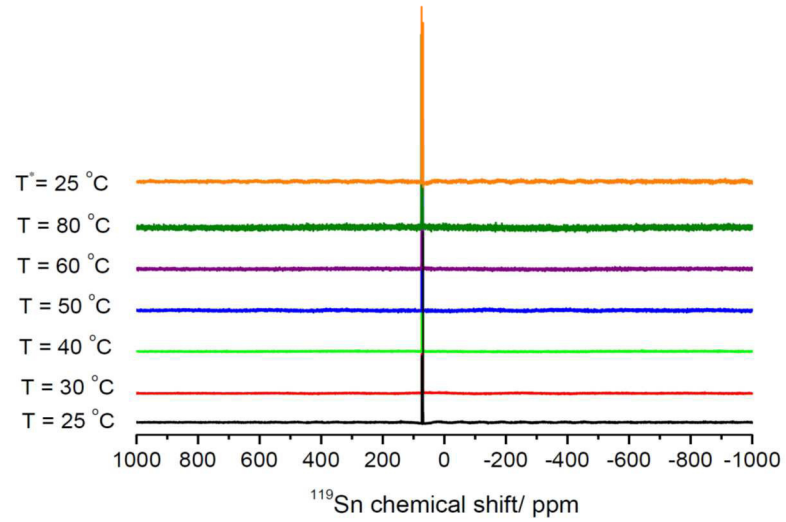

Figure S4: ^{119}Sn-NMR spectra of the precursor $Na_4SnS_4 \cdot 14H_2O$ dissolved in D_2O measured at indicated temperatures in the range of 1000 to -1000 ppm (*: ^{119}Sn-NMR spectrum of the precursor solution, which was heated at 120 °C for 1 h and cooled to room temperature).

Table S3: ^{119}Sn NMR Integrals of $[SnS_4]^{4-}$ and $[Sn_2S_6]^{4-}$ anions

T/ °C	$[Sn_2S_6]^{4-}$	$[SnS_4]^{4-}$
25	2.69	1
30	1.42	1
40	1.52	1
50	1.41	1
60	1.36	1
80	0.92	1
120	0.98	1

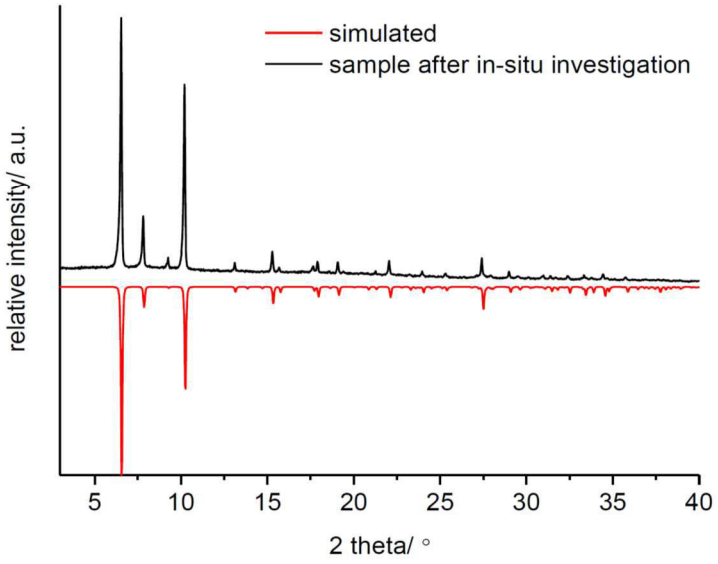

Figure S5: Calculated X-ray powder pattern of compound **1** (red) and experimental powder pattern of a sample isolated after 40 min reaction time in an *in-situ* experiment at 90°C (black).

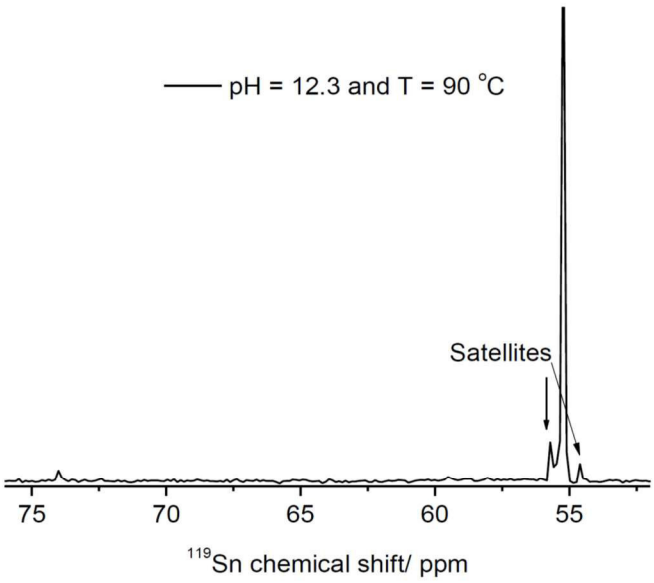

Figure S6: ^{119}Sn-NMR spectrum of the $Na_4SnS_4 \cdot 14H_2O$ dissolved in D_2O. The pH value of the solution was adjusted to 12.3 and the solution was heated to 90 °C.

Table S4: Bond lengths [Å] and angles [°] of compound **1**

Sn(1)-O(5)	2.003(6)	Sn(1)-S(7)	2.459(2)
Sn(1)-O(5)#1	2.263(7)	Sn(1)-S(8)	2.443(6)
Sn(1)-S(4)	2.419(9)	Sn(1)-S(8)#1	2.460(1)
O(5)-Sn(1)-O(5)#1	96.89(6)	O(5)-Sn(1)-S(4)	168.28(7)
O(5)-Sn(1)-S(8)	67.13(7)	O(5)-Sn(1)-S(7)	77.81(4)
O(5)#1-Sn(1)-S(4)	91.07(9)	O(5)-Sn(1)-S(8)#1	83.36(5)
O(5)#1-Sn(1)-S(8)	78.69(8)	O(5)#1-Sn(1)-S(7)	172.67(4)
S(4)-Sn(1)-S(7)	94.93(6)	O(5)#1-Sn(1)-S(8)#1	79.00(5)
S(4)-Sn(1)-S(8)	106.33(3)	S(8)-Sn(1)-S(7)	103.51(6)
S(4)-Sn(1)-S(8)#1	106.65(9)	S(8)-Sn(1)-S(8)#1	140.17(7)
S(7)-Sn(1)-S(8)#1	95.23(1)	S(6)-Sn(2)-S(4)	116.03(6)
Sn(2)-S(3)	2.493(9)	S(6)-Sn(2)-S(3)	96.49(9)
Sn(2)-S(4)	2.467(2)	S(4)-Sn(2)-S(3)	114.58(4)
Sn(2)-S(6)	2.449(8)	Sn(3)-S(3)	2.395(9)
Sn(3)-O(5)	2.001(7)	Sn(3)-S(8)	2.461(5)
O(5)-Sn(3)-O(5)#1	95.54(1)	O(5)-Sn(3)-S(8)	84.09(6)
O(5)-Sn(3)-S(3)	89.40(5)	O(5)#1-Sn(3)-S(8)	66.78(5)
O(5)#1-Sn(3)-S(3)	168.65(4)	S(3)-Sn(3)-S(8)#1	107.24(6)
S(3)-Sn(3)-S(3)#1	87.61(4)	S(8)-Sn(3)-S(8)#1	136.59(7)
S(3)-Sn(3)-S(8)	103.72(3)		
Ni(9)-O(22)	1.882(2)	Ni(9)-N(11)	1.938(3)
Ni(9)-O(23)	1.973(1)	Ni(9)-N(12)	2.021(9)
Ni(9)-N(10)	1.924(8)	Ni(9)-N(13)	1.933(1)
O(22)-Ni(9)-N(10)	87.06(8)	N(10)-Ni(9)-N(12)	91.84(1)
O(22)-Ni(9)-N(11)	90.72(2)	N(10)-Ni(9)-N(13)	88.17(3)
O(22)-Ni(9)-N(12)	89.98(2)	N(10)-Ni(9)-O(23)	93.38(1)
O(22)-Ni(9)-N(13)	95.59(3)	N(11)-Ni(9)-N(12)	87.87(7)
O(23)-Ni(9)-N(12)	82.72(8)	N(11)-Ni(9)-O(23)	88.76(9)
O(22)-Ni(9)-O(23)	172.70(6)	N(13)-Ni(9)-N(12)	174.41(9)
N(10)-Ni(9)-N(11)	177.77(9)	N(13)-Ni(9)-O(23)	91.69(9)

Infrared spectroscopy

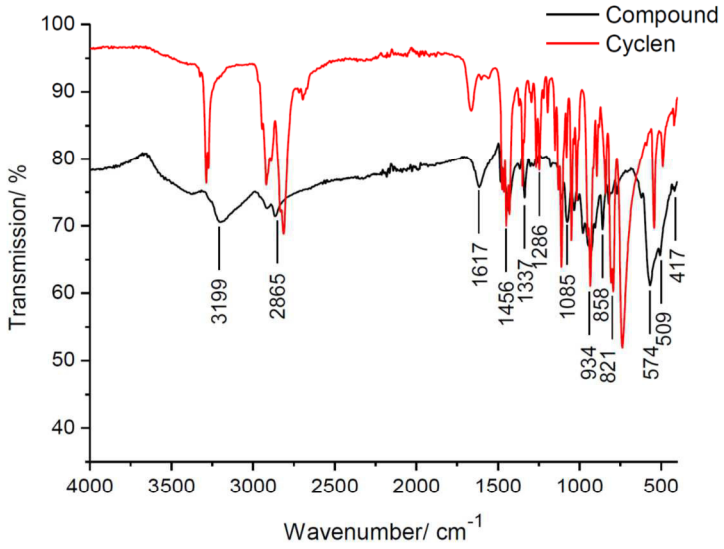

Figure S7: IR spectra of compound **1** (black) and 1,4,7,10-tetraazacyclododecane (cyclen, red).

Table S5: Values of the absorption observed in the IR spectrum of compound **1** together with their assignment

Cyclen	Compound 1	Assignment
3285m	3199m	ν (NH)
2915s, 2804s	2910w, 2865m	ν (CH_2)
1667m	1671m	δ (NH)
1433m	1456w	δ (CH_2)
1333m	1337w	δ (CH_2)
1255m	1286w	ν (C-N)
1099s	1085s	ν (C-N)
932s	934s	skeleton vib. cyclohex.
831m	858m	δ (C-C-C)
725w, 619w, 564w, 497w	821m, 574m, 509w	δ (C-C-C)
430w	417w	ν (M-N)

UV/Vis spectroscopy

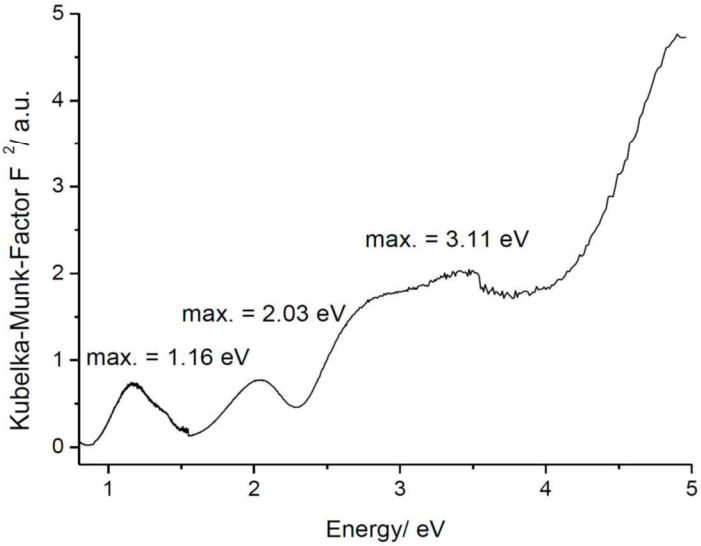

Figure S8: UV-Vis spectrum of **1** plotted as Kubelka-Munk-Factor vs. energy.

Thermogravimetric analysis

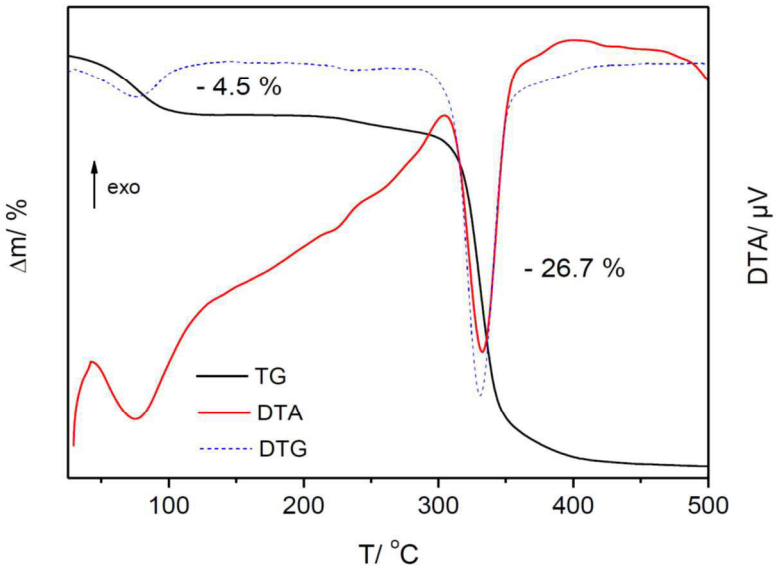

Figure S9: TG (black), DTA (red) and DTG (blue) curves of compound **1**.

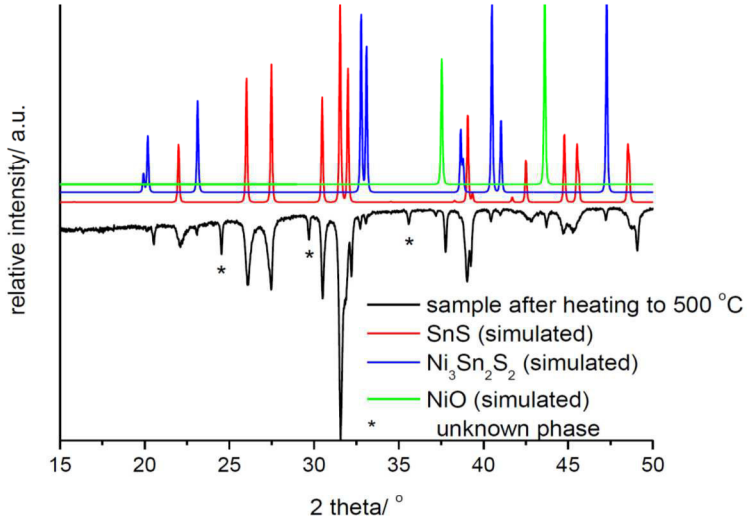

Figure S10: Experimental X-ray powder pattern of the sample after heating to 500 °C (black) compared with simulated X-ray powder patterns of SnS (red), $Ni_3Sn_2S_2$ (blue) and NiO (green).

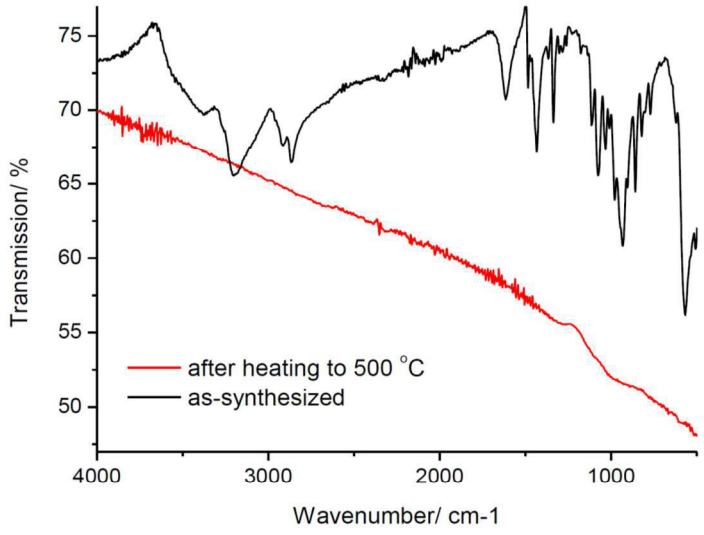

Figure S11: IR-spectra of the samples bevor (black) and after heating to 500 °C (red).

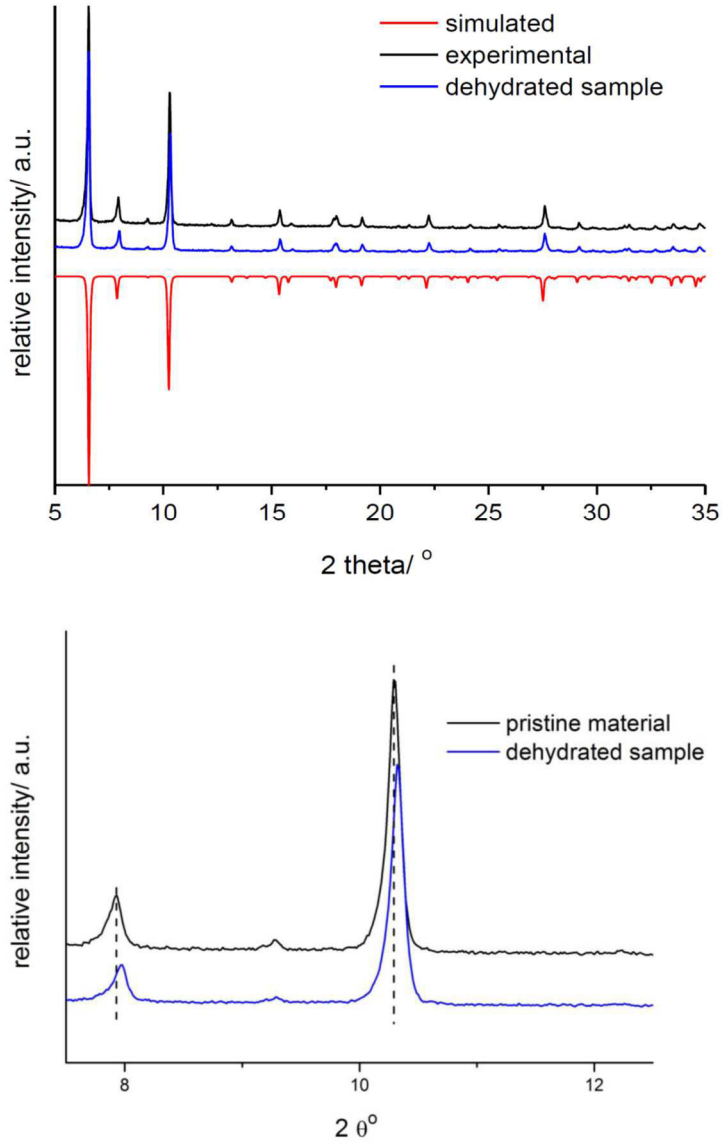

Figure S12: top: Experimental X-ray powder pattern of compound **1** (black), of the dehydrated compound (blue) and calculated X-ray powder pattern for compound **1** (red); bottom: enlarged view of a region of the powder patterns of pristine and dehydrated sample showing the shift of the Bragg reflections.

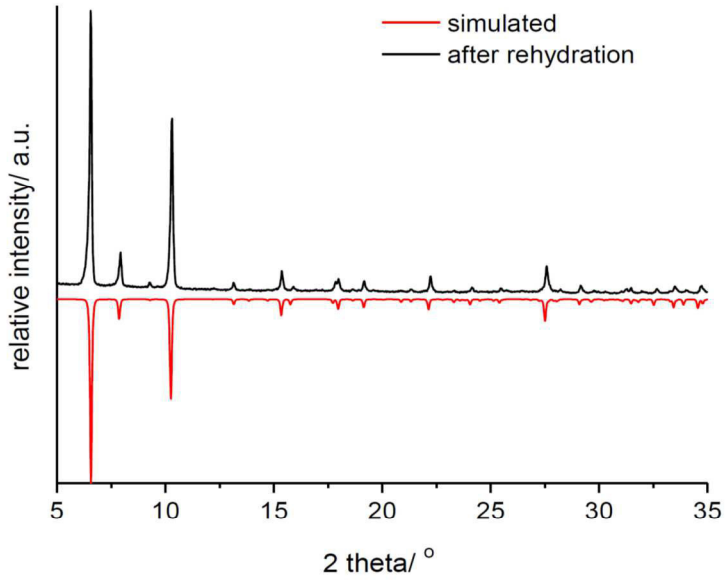

Figure S13: Calculated X-ray powder pattern of compound **1** (red) and experimental powder pattern of the sample after rehydration (black).

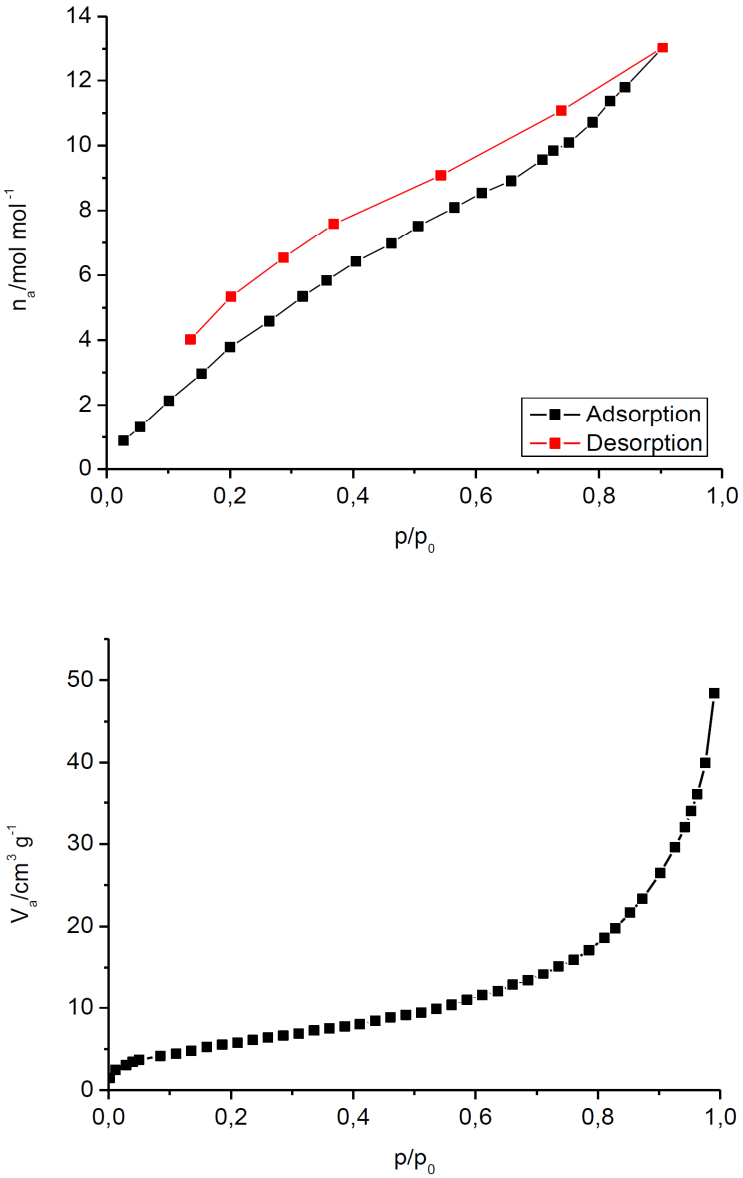

Figure S14: Adsorption isotherms of compound **1** with H_2O (top) and N_2 (bottom).

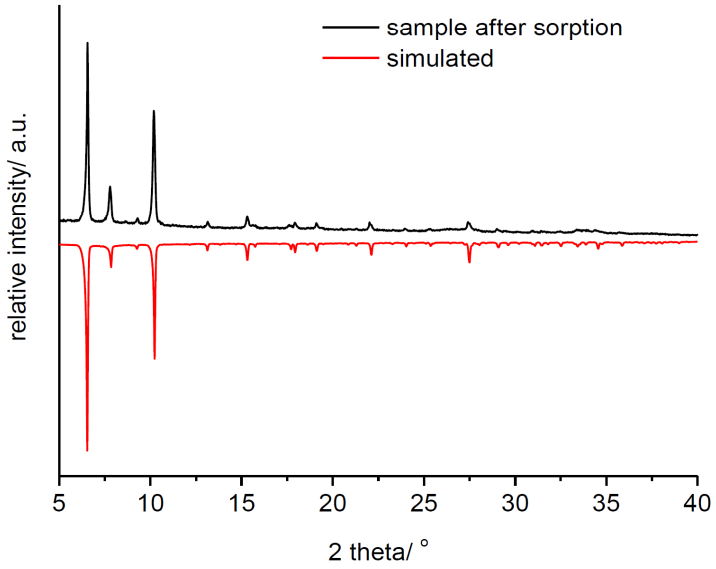

Figure S15: Calculated X-ray powder pattern of compound **1** (red) and experimental powder pattern of the sample after sorption (black).

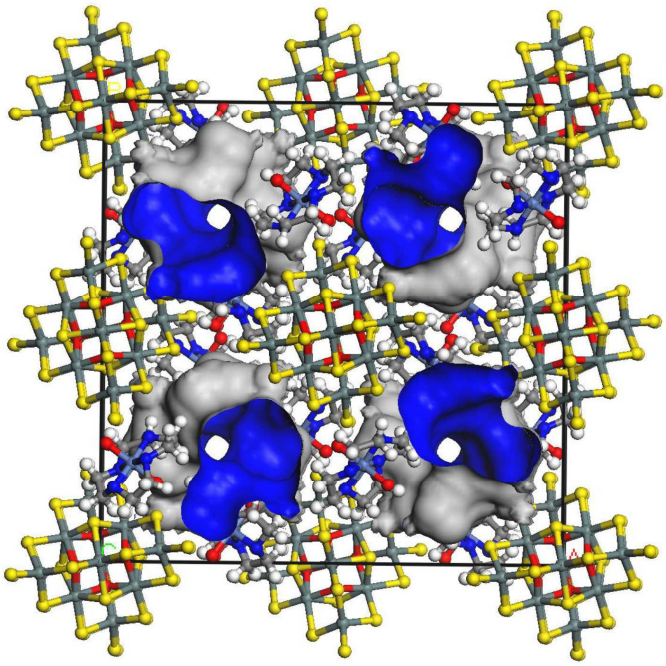

Figure S16: Calculated Connolly surface for **1** using water as probe molecule using Materials Studio.

Photocatalysis

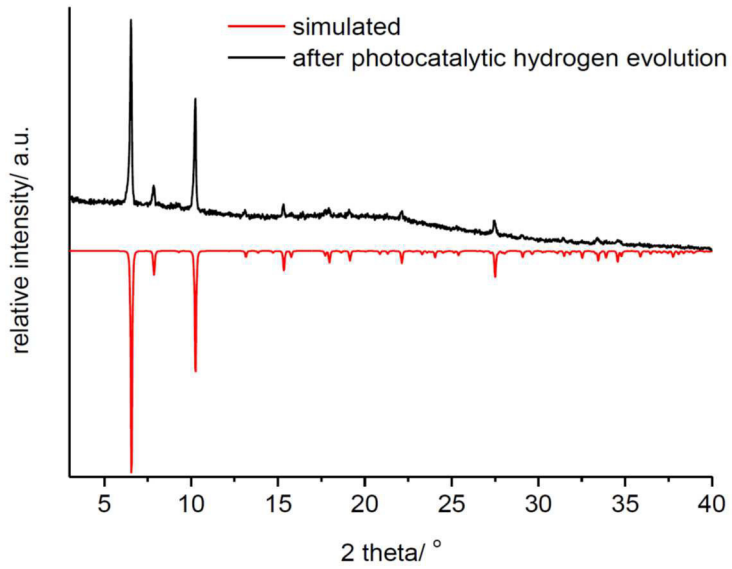

Figure S17: Experimental PXRD pattern of compound **1** (black) after phototcatalytic hydrogen evolution compared with their simulated from X-ray data (red).

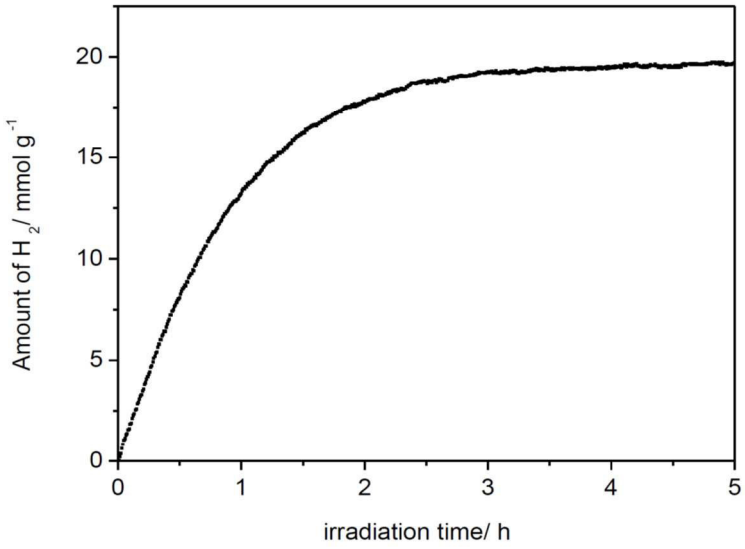

Figure S18: Amount of H_2 as function of time in the photocatalytic hydrogen evolution using $[Ni(cyclen)(H_2O)_2](ClO_4)_2 \cdot H_2O$.

4. Manuskripte

4.1. "$CuCo_2S_4$ on TiO_2 leading to high photocatalytic H_2 evolution" eingereicht in Dalton Transactions

Der metallische Spinell $CuCo_2S_4$ ist in elektrokatalytischen Experimenten aktiv für eine katalytische Wasserstoffentwicklung und bei der katalytischen Sauerstoffentwicklung aktiver als Einzelkomponenten wie z.B. Cu_2S und Co_3S_4. Damit ist $CuCo_2S_4$ auch ein möglicher bifunktionaler Kokatalysator für eine photokatalytische Wasserspaltung und simultane Entwicklung von Sauerstoff und Wasserstoff. In er vorliegenden Arbeit wurde $CuCo_2S_4$ als Ko-Katalysator auf dem Halbleiter TiO_2 in unterschiedlichen Konzentrationen deponiert und umfassend charakterisiert. Die kohärent streuenden Domänen von $CuCo_2S_4$ liegen im Nanometerbereich und bilden mit TiO_2 Nanokomposite. Bei optimalem Verhältnis $CuCo_2S_4$:TiO_2 konnten 1680 $\mu mol \cdot h^{-1} \cdot g^{-1}$ H_2 (40 $mL \cdot h^{-1} \cdot g^{-1}$) photokatalytisch erzeugt werden. Nach 80 Stunden Bestrahlzeit wurden 60000 $\mu mol/g_{cat}$ H_2 produziert, was deutlich mehr ist als für z.B. C_3N_4@Pt or C_3N_4@MoS_2. Der synergistische Effekt des in-situ Hergestellten Komposits konnte durch Untersuchung einer mechanischen Mischung von $CuCo_2S_4$/TiO_2, welches deutlich weniger katalytisch aktiv ist, nachgewiesen werden. Nach mehr als 80 Stunden Bestrahlung nimmt die katalytische Aktivität ab, was vermutlich auf Photokorrosion zurückgeführt werden kann. In der Literatur werden oft die teuren Platinmetalle als Ko-Katalysatoren verwendet. Ein TiO_2/Pd Komposit zeigte in der Tat eine bessere katalytische Aktivität als $CuCo_2S_4$/TiO_2. Allerdings ist Pd ca. 600 mal teurer als Co, welches das teuerste Element von $CuCo_2S_4$ ist. Die Optimierung des katalytischen Systems sollte zu einer noch besseren Stabilität führen als schon jetzt beobachtet.

$CuCo_2S_4$ deposited on TiO_2 nanoparticles leading to high photocatalytic H_2 evolution

Michael Poschmann[a], Hendrik Groß[b], Reza Amin[c], Torben Dankwort[b], Lorenz Kienle[b], Wolfgang Bensch[a]

[a] Institute of Inorganic Chemistry, Kiel University, Max-Eyth Straße 2, D-24118 Kiel, Germany E-mail: wbensch@ac.uni-kiel.de

[b] Institute of Materials Science, Kiel University, Kaiserstraße 2, D-24143 Kiel, Germany

[c] Department of Chemistry, Faculty of Sciences, University of Guilan, P.O. Box 41335-1914, Rasht, Guilan, Iran

Abstract

We report the deposition of metallic spinel type $CuCo_2S_4$ on nanocrystalline TiO_2 resulting in the formation of heterostructure nanocomposites. The syntheses were performed under solvothermal conditions leading to an in-situ coverage of the surface of P25® (TiO_2) with nanosized $CuCo_2S_4$ particles. The nanocomposites were characterized in detail by X-ray powder diffraction (XRD), high resolution transmission electron microscopy (HRTEM), nitrogen sorption (BET) and UV-Vis spectroscopy. By varying the $CuCo_2S_4/TiO_2$ ratio to an optimum value a catalyst could be obtained which shows a very high photocatalytic H_2 production rate of 1680 $\mu mol \cdot h^{-1} \cdot g^{-1}$ (40 $mL \cdot h^{-1} \cdot g^{-1}$) which is much larger than for pure TiO_2. After 80 h irradiation time about 60000 $\mu mol/g_{cat}$ H_2 were generated. An increased light absorption and an efficient charge separation for the sample with the optimal $CuCo_2S_4$:TiO_2 ratio is most probably responsible for the high catalytic activity.

Introduction

With the increasing shortage of mineral oil and fossil fuels increasing efforts are undertaken for development of alternative, ecofriendly and renewable fuels. One intensively discussed process is the catalytic hydrogen evolution[1–9], beside biorefinery[10,11] or CO_2-fixation[12,13] or conversion[14].

Nowadays hydrogen gas is produced mainly by steam reforming/water-gas shift reaction using natural gas, which is therefore neither renewable nor ecofriendly. Ecofriendly catalytic hydrogen evolution can be achieved by electrocatalysis, photocatalysis or the combined photo-electro-catalysis.[1] In the present work we

focus on photocatalysis. The goal of photocatalytic hydrogen production (see Fig. 1) is the reduction of protons from water using sunlight.[1]

$$2\ H^+ + D^{2-} \longrightarrow H_2 + D \qquad \text{(eq. 1)}$$

with D^{2-} being an electron donor.

When using just H_2O the electron donor would be O^{2-} producing O_2 by oxidation according to eq. 2.

$$2\ H_2O \longrightarrow 2\ H_2 + O_2 \qquad \Delta G^0 = 1.23\ eV \qquad \text{(eq. 2)}$$

But this reaction needs high oxidation potentials, is energetically demanding and kinetically challenging.[1,2] Because both gases are produced in the identical environment the back reaction may occur and water is formed.[15] Additionally, the oxygen produced is economically of no importance, and more useful electron donors may be organic substances which are chemically modified (oxidized) in the hydrogen evolution reaction (HER) thus leading to formation of useful organic products.[16,17]

A widely applied electron donor is triethanolamine (TEOA) which is first oxidized to the radical cation which decomposes via hydrolysis to glycoaldehyde and diethanolamine (Scheme 1).[18–21]

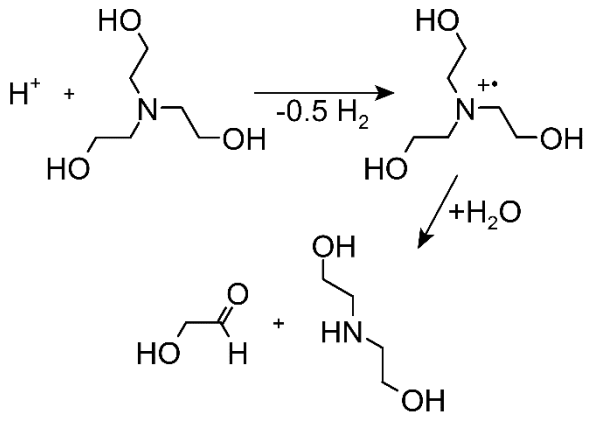

Scheme 1: Reaction pathways of oxidation of TEOA.

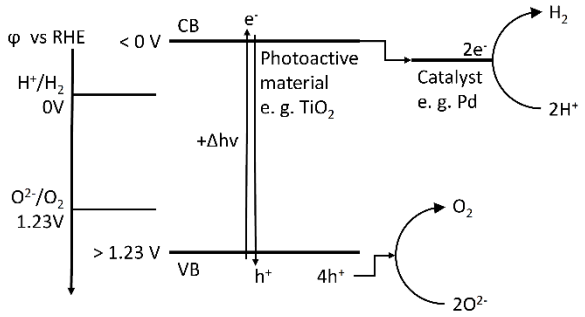

Fig. 1: Schematic mechanism of photocatalytic water splitting using a photoactive water oxidation catalyst and a co-catalyst for hydrogen evolution.

For this reaction a catalyst is needed, and one of the most prominent photoactive materials is TiO_2 providing a structure dependent band gap of 3 - 3.2 eV[1,22–24], and good stability in aqueous media. In addition, the valence band (VB, 2.6 - 2.7 V vs. RHE) and conduction band (CB, -0.67 to -0.9 V vs. RHE) exhibit positions suitable for O^{2-} oxidation and hydrogen reduction, respectively. The most active pure TiO_2 seems to be a mixture of rutile and anatase phases. An explanation for this observation is that charge carriers excited in anatase (indirect band gap, E_g = ~3.2 eV)[1] can be accumulated in rutile (direct band gap E_g = 3.0 eV).[1] Although being a direct band gap semiconductor rutile seems to exhibit a higher life time for electron-hole pairs than anatase.[25] Additionally, rutile shows higher catalytic activity for water oxidation, while anatase has higher activity for hydrogen evolution catalysis if co-catalysts are applied.[26] TiO_2 itself is a poor catalyst for hydrogen evolution while a combination with Pt or Pd as co-catalysts yields very active materials which are often used as benchmarks for comparison with different catalytic systems and setups.[1,27] Because the noble metals Pd and Pt are precious and costly, an intense search is going on to replace these metals by cheaper and more abundant materials. Materials fulfilling these needs and exhibiting high catalytic activities are transition metal sulfides like MoS_2[28,29], WS_2[29,30], NiS_x[31–33], CuS[34–36] or CoS_x[37]. All of them show synergistic effects when combined with semiconductors like TiO_2.[28–38] Copper is the cheapest metal of these sulfides showing high activities for photocatalytic hydrogen evolution.[35,39–43] In contrast, CoS_x exhibits multi-functionality for hydrogen evolution, oxygen evolution (OER), oxygen reduction (ORR) and carbon dioxide reduction.[44–47] A combination of copper and cobalt sulfides possibly shows both properties, i.e. multi-functionality and high activity for

hydrogen evolution. But research applying Cu- and Co-sulfides in photocatalysis is mostly focused on the binary sulfides. Therefore a study using the ternary sulfide $CuCo_2S_4$ as co-catalyst fills a gap of knowledge between CuS and CoS used in photocatalysis. $CuCo_2S_4$ crystallizes in the spinel structure in the cubic space group *Fd*-3*m*, and unit cell parameter *a* = 9.4504 Å.[48] The sulfide ions are arranged in distorted cubic close packed topology generating octahedral and tetrahedral vacancies. The Co cations occupy ½ of the octahedral sites and Cu is located in 1/8 of the tetrahedral vacancies, with Wyckoff positions 16d and 8a respectively.[48] The charge neutrality of the compound was intensively investigated in the past and led to different oxidation states assigned to the constituents like $Cu^{1.2}(Co_2)^{4.8}(S_4)^{-VI}$[49], $Cu^{II}Co^{III}{}_2(S_4)^{-VIII}$[50–53], $Cu^{I}Co^{III}{}_2(S_4)^{-VII}$[48,54].

An important characteristic property of $CuCo_2S_4$ is its electrical conductivity which can turn into superconductivity at very low temperatures when a small excess of Cu cations is present.[48,50] A good conductivity is important for a good and fast electron transfer to surface sites, being able to use excited electrons for catalytic reactions. On the other hand the conductivity is accompanied with high light absorptivity and reflectivity. Therefore, the amount of $CuCo_2S_4$ on TiO_2 should be limited to low percentages. In some studies $CuCo_2S_4$ showed activity for electrochemical HER and OER making it a bifunctional catalyst for water splitting and a very interesting material for further investigations.[55–57]

We deposited different amounts of $CuCo_2S_4$ as co-catalyst on TiO_2 using a solvothermal approach and observed a strong concentration dependence of the photocatalytic activity of the composites for the hydrogen evolution reaction. The results of the investigations together with the characterization of the materials are presented here.

Experimental

Chemicals

$CoCl_2$•$6H_2O$ (>98 %, Fluka), $CuCl_2$•$2H_2O$ (≥99%, Merck), P25® (TiO_2, 99.5 %, Degussa), thiourea (≥98 %, Merck), triethanolamine (TEOA, ≥99 %, Fluka), $FeCl_3$•$6H_2O$ (>98 %, Sigma Aldrich), $K_2C_2O_4$•H_2O (99 %, Merck), K_2PdCl_4 (>98 %, Degussa), H_2SO_4 (96 %, Walter CMP), acetone (97 %, Walter CMP), ammonium

acetate (≥98 %, Fluka), Ethanol (99 %, methylated, Walter CMP), 1,10-phenanthroline (99 %, ABCR), NaCl (>99.5 %, Grüssing) were used without further purification.

Synthesis of Photocatalysts

The synthetic procedure for P25@$CuCo_2S_4$ 10 wt-% (CCS10) is related to that reported by Qizhao *et al.* and was as follows.[58] 340 mg of P25® was stirred for one hour in 10 mL of deionized water. Then 18.8 mg (0.11 mmol) of $CuCl_2$•$2H_2O$, 52.4 mg (0.22 mmol) of $CoCl_2$•$6H_2O$ and 50 mg (0.66 mmol) thiourea dissolved in 3 mL deionized water and 2 mL conc. aqueous ammonia were added and stirred for one hour. The resulting dispersion was ultrasonicated for 0.5 h and then transferred into a Teflon-lined steel autoclave with a total volume of 30 mL. The sealed autoclaves were then heated to 180 °C for 12 h. Afterwards the formed solid was filtrated and washed multiple times with demineralized water and ethanol and dried in air at ambient temperature. Greyish black powders were obtained (yield ca. 67 %). After characterization of the samples with EDX and XRD individual batches were combined for further usage.

Samples with higher and lower loading of $CuCo_2S_4$ were synthesized in a similar way but using the half or double amount of Cu, Co and S sources. These samples are denoted as CCS5 and CCS20.

A sample of pure $CuCo_2S_4$ was prepared by using the same procedure as for CSS10 but without P25®.

For comparison a sample P25@Pd 1 wt-% was prepared as follows.[27] 15 mg of K_2PdCl_4 were dissolved in 5 mL demineralized water and 45 mL ethanol. 500 mg P25® are added and the mixture is stirred until a good dispersion is obtained. Then the dispersion is stirred and irradiated for 2 h with a 300 W Xe lamp in a round bottom flask equipped with a cooling jacket keeping the temperature constant at 30 °C. Afterwards the material was separated by centrifugation, washed with demineralized water and ethanol, and then dried at 90 °C in an oven. Characterization of this material is presented in the supporting information (see supporting information Chap. S1).

Characterization

X-ray powder patterns (XRD) of all samples were recorded with a PANalytical Empyrean MPD diffractometer with Cu $K\alpha_{1,2}$ irradiation in reflection geometry. The profile function of the instrument was determined using LaB_6 SRM 660a NIST standard. Rietveld refinements of the patterns were done using the program TOPAS Academic v6[59] in combination with coding program jEdit[60].

For nanostructure investigation, Transmission Electron Microscopy (TEM) was performed using a FEI Tecnai F30 G^2 STwin equipped with a field emission gun operated at 300 kV. For contrast enhancement, scripts for Gatan Digital Micrograph were used as described by Mitchell[61]. Diffraction data was simulated using the software jems[62].

Energy Dispersive X-ray (EDX) analyses were carried out within the TEM (Li:Si Detector, EDAX) or with an Environmental Scanning Electron Microscope Philips XL-30 and an Li:Si EDAX detector.

For the diffuse reflectance spectroscopy and collection of the UV/Vis spectra the samples were ground as 1 wt-% mixture with NaCl as white standard. The powder was measured in reflection geometry using an integrating sphere in a Varian Cary 5000 in the region 250-2000 nm.

The specific surface areas of the samples were determined with the Brunauer-Emmett-Teller (BET) method[63] using data obtained by sorption measurements with N_2 using a Belsorp Max apparatus. Before the measurements the samples were dried in vacuum at 10^{-3} mbar at T = 90 °C for 16 h.

Photocatalytic Measurements

Measurements of the photocatalytic activity were undertaken with a Gasmess system of the Messen Nord GmbH. It consists of an enclosed glass tube system connected to a round bottom flask, a membrane pressure sensor, a vacuum pump, argon supply and an automatic syringe. The system monitors pressure increases and uses the automatic syringe to correct the pressure to the starting value to keep the setup isobar. Every part of the setup is surrounded by a cooling jacket keeping the system at a constant temperature of 30 °C applying a thermostatic water bath. In each catalytic run 20 mg of catalyst were added into the flask. Afterwards the gas phase was purged with Argon followed by addition of 50 mL of degassed 10 Vol-%

aqueous triethanolamine (TEOA) solution. After stabilization of the pressure a 300 W Xe arc lamp equipped with low pass 320 nm cut off filter in a distance of 15 cm was switched on to irradiate the flask. The volume increase is detected versus time. After each measurement 10 mL of the gas phase were extracted and injected into a gas chromatograph (Agilent 6890 Plus with 5 Å molsieve column and TCD detector) to determine the hydrogen content. Errors are given as standard deviations of single measurements or as linear error propagations.

To show the synergism between P25® and $CuCo_2S_4$ additional experiments were done using pure P25®, pure $CuCo_2S_4$ and a mechanical mixture of both. In these experiments 20 mg P25® and/or 2 mg $CuCo_2S_4$ were used as catalyst. All other conditions were the same as in the experiments mentioned above.

To evaluate the influence of dissolved Cu^{II}- and/or Co^{II}-species on the photocatalytic activity of CCS5, CCS10 and CCS20, photocatalysis measurements were done using 20 mg P25®, 1 mg $CuCl_2 \cdot 2H_2O$ and 3 mg $CoCl_2 \cdot 6H_2O$, matching the amount of Cu- and Co-ions in CCS10, as catalyst. All other conditions were identical as in experiments mentioned above.

Actinometry

The measurement of the photon flux of the setup for photocatalytic investigations was done with the chemical actinometer system $K_3Fe(C_2O_4)_3 \cdot 3H_2O$ in 0.05 M H_2SO_4 solution as suggested by IUPAC for the wavelength range from 450 to 250 nm. Therefore, $K_3Fe(C_2O_4)_3 \cdot 3H_2O$ was prepared freshly by dissolving $K_2C_2O_4$ (22.5 mmol) in water and adding a solution of $FeCl_3 \cdot 9H_2O$ (7.5 mmol) in the dark. After crystallization at 0 °C and after two times recrystallization from 20 mL demineralized water, large green crystals of pure $K_3Fe(C_2O_4)_3 \cdot 3H_2O$ were obtained (yield 78 %). For the actinometry 0.49 g of $K_3Fe(C_2O_4)_3 \cdot 3H_2O$ were dissolved in the dark in 50 mL of 0.05 M sulfuric acid. Every 10 seconds of irradiation 1 mL of the solution was removed with a micropipette and added to a mixture of 1 mL 0.12 wt-% aqueous phenanthroline solution, 1.5 mL demineralized water, 2.5 mL buffer solution (ammonium acetate 46.2 g/L and 5 mL/L sulfuric acid) and 4.5 mL 0.05 M sulfuric acid. After some hours in the dark the UV/Vis spectra of the samples were recorded with a modular UV/Vis spectrometer consisting of a Lamp (StellarNet STE-

SL5-DH), probe tip with 1 cm transmission depth and spectrometer (Laser 2000 RPS-Mini-UV-CST).

Post catalytic characterization

For post catalytic characterization the reaction slurry containing the catalyst after irradiation was added to 50 mL acetone for sedimentation of catalyst particles. The latter where separated via centrifugation at 5000 rpm and washed several times with acetone. The catalyst was then characterized like the as synthesized material using XRD, EDX and TEM.

Results and Discussion

X-Ray powder diffraction

The X-Ray powder patterns show reflections of anatase and rutile (see Fig. 2 and supporting information Fig. S5 and S6), together with reflections of $CuCo_2S_4$ exhibiting a relatively low intensity. Results of the Rietveld refinement of CCS10 (Table 1) demonstrate that the sample consists of ≈82 wt-% anatase, ≈12 wt-% rutile and ≈6 wt-% $CuCo_2S_4$. For determination of the quantities the linear absorption coefficients, formula weights and unit cell volumes were considered. But one should keep in mind that P25® is known to contain 8-13 wt-%[64–66] of amorphous titania. Therefore the $CuCo_2S_4$ content may be slightly overestimated. As expected the samples CCS5 and CCS20 have the same anatase to rutile ratio and the $CuCo_2S_4$ were determined as 1.2 resp. 14.8 wt-% (see supporting information Tab. S2). The unit cell parameters of anatase, rutile and $CuCo_2S_4$ are in the range reported in literature (see Tab. 1).[67–69] The volume weighted mean diameter of the coherently scattering domains was estimated from the observed integral breadth of the Bragg reflections using a shape factor of 0.89, valid for spherical crystallites. For anatase and rutile the volume averaged domain diameters are 23 and 32 nm, respectively. Both values are slightly larger than reported for P25®, but it is mentioned in literature that P25® is characterized by fluctuations in composition and domain diameters.[64–66] For $CuCo_2S_4$ an isotropic domain diameter of 14 nm is obtained. CCS5 and CCS20 have similar coherently scattering domain sizes for the two TiO_2 phases,

while the values are in the same region CCS5 and CCS20 (see supporting information Tab. S2).

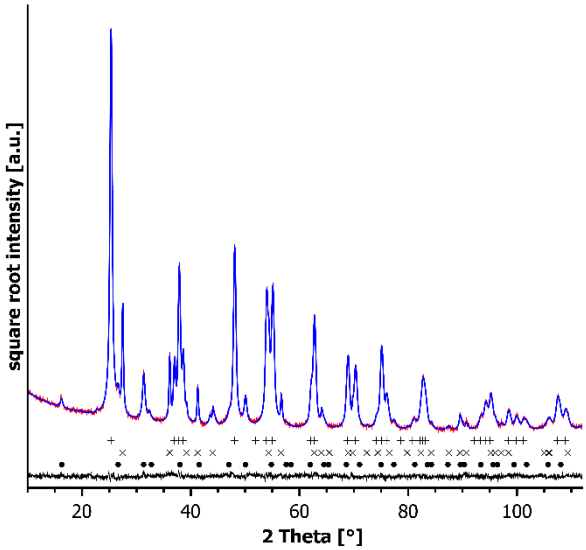

Fig. 2: Rietveld refinement data of CCS10. (Red) measured data, (blue) simulated data and (black) difference curve. Marks correspond to reflection postitions of anatase[67] (+), rutile[68] (x), $CuCo_2S_4$[69] (●). The difference curve shows that the experimental and simulated patterns match perfectly.

Tab. 1: Selected structural data obtained by Rietveld refinements of XRD data of the sample CCS10. Estimated standard deviations are given in parentheses.

Parameter	Anatase	Rutile	$CuCo_2S_4$
Cell parameter [Å]	a = b = 3.78646(3) (3.7842(13)[65]) c = 9.50690(12) (9.5146(15)[65])	a = b = 4.59480(10) (4.595(1)[65]) c = 2.95970(13) (2.959(1)[65])	a = b = c = 9.4701(4) (9.478(5)[69])
Chalcogen position	x = y = 0 z = 0.20732 (0.2081(2)[67])	x = y = 0.30479 (0.30479(10)[68]) z = 0	x = y = z = 0.263 (0.263[69])
Space group	$I4_1/amdS$	$P4_2/mnm$	Fd-3mZ
R-Bragg	0.910	1.784	1.257
Weight fraction [%]	82.0	11.5	6.0
Volume averaged domain size [nm]	23	33	14

Transmission and scanning electron microscopy

Transmission electron micrographs of the samples show the presence of large agglomerates on a micrometer length scale, consisting of nano-crystallites. From HRTEM micrographs, d-spacings of the crystallites were obtained to allow

differentiation between different phases. Accordingly, rutile and anatase crystallites could be identified (Fig. 3a and supporting information Fig. S4). Further, HRTEM micrographs and corresponding FFT (zone axis [112]) verify the presence of $CuCo_2S_4$ crystallites. The polydisperse crystallites exhibit diameters of 10 nm to 40 nm and the results are therefore in good agreement with XRD data. The nano-crystallites do not exhibit prominent crystal defects like intergrown domains and shear structures.

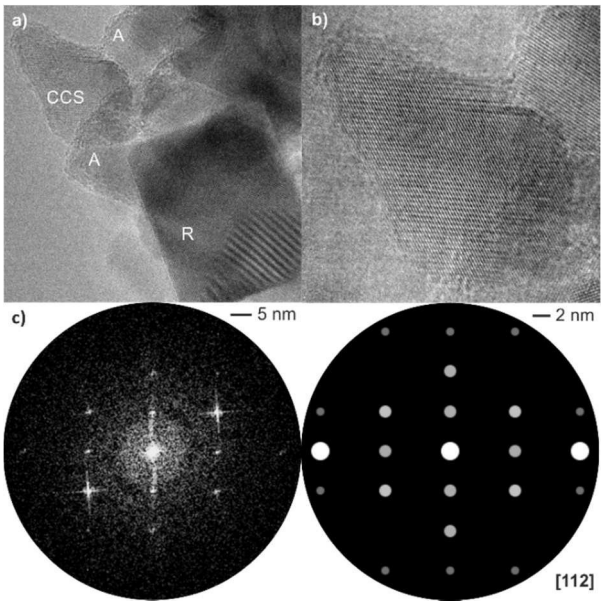

Fig. 3: Transmission electron micrographs and electron diffraction patterns of a particle cluster of CCS10. a) Overview micrograph showing the occurrence of crystallites whose d-spacings could be attributed to anatase (A)[67], rutile (R)[68], and $CuCo_2S_4$ (CCS)[69]. b) HRTEM micrograph of the $CuCo_2S_4$ crystallite found in figure a). c) Corresponding FFT and simulated diffraction pattern of $CuCo_2S_4$ in zone axis [112], showing good agreement. Differences in intensity may occur due to misalignment of the crystallite and the impact of the contrast transfer function on the peak intensity of FFT.

Diffuse Reflectance Spectroscopy

The experimental diffuse reflectance data are transformed into absorption data via the Kubelka-Munk function using the equation:

$$\alpha = \frac{(1 - R_\infty)^2}{2R_\infty} \quad , \qquad \text{(Eq.4)}$$

with the Kubelka-Munk absorptivity α and R∞ as relative diffuse reflectivity calculated by:

$$R_{\infty} = \frac{R_{Sample}}{R_{Standard}} \quad , \qquad \text{(Eq.5)}$$

with the reflectivity of the sample R_{Sample} and the reflectivity of the pure white standard $R_{Standard}$, in this case NaCl.[70]

The Kubelka-Munk curve of CCS10 (see Fig. 4) shows a very broad diffuse photon absorption in the low energy range from 0.6 to 3.2 eV. For CCS5 the curve for the absorptivity is less intense, while for CCS20 the absorptivity is increased due to higher loading of $CuCo_2S_4$ compared to CCS10 (see supporting information Fig. S7). This explains the greyish black color of the samples and is a result of $CuCo_2S_4$ being an electrical conductor.[48,50] At higher energies a strong increase of the absorptivity is observed due to the absorption edge of rutile.[1] A Tauc-plot (see Fig. 4) gives a linear dependency of the band edge.[71] With this plot the band edge can be determined as 3.3 eV (365 nm), which is similar to values reported for rutile in P25® (3.35 eV).[66] The band gap of anatase could not be determined because it is not possible to accurately determine additionally an indirect band gap at higher energies due to the low absorptivity. The photon absorptivity of titania material in CCS5 and CCS20 is similar to that of CCS10 (see supporting information Fig. S8).

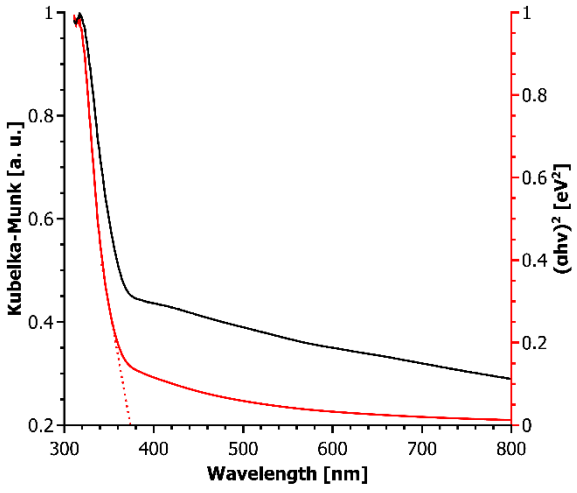

Fig. 4: Kubelka-Munk term (black) and Tauc-plot (red) calculated from the observed diffuse reflectivity data of CCS10 showing the broad absorbtion of $CuCo_2S_4$ at low eneries and the absorption edge of TiO_2 at high energies (dotted line).

Nitrogen Sorption experiments

The N_2 sorption data of CCS5, CCS10 and CCS20 show type II isotherms, a typical dependency for nonporous or macroporous materials having no limitation of

multilayer adsorption (see Fig. 5).[72] The BET analysis[63] (see Fig. 6) yields a specific surface area of 40 m^2/g, 39 m^2/g and 38 m^2/g for CCS5, CCS10 and CCS20, respectively. The specific surface area is reduced by ~ 26 % compared to P25® having a specific surface area of 49 m^2/g. A reasonable explanation is that $CuCo_2S_4$ is deposited on TiO_2 particles increasing the particle diameter and weight while not increasing the surface area. But the amount of $CuCo_2S_4$ seems to not strongly affect the specific surface area.

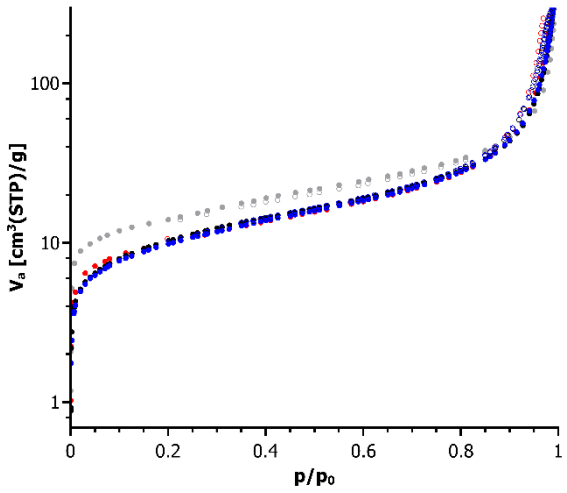

Fig. 5: Detected N_2-sorption data of P25® (grey), CCS5 (black), CCS10 (red) and CCS20 (blue) showing typical characteristics of a nonporous material.

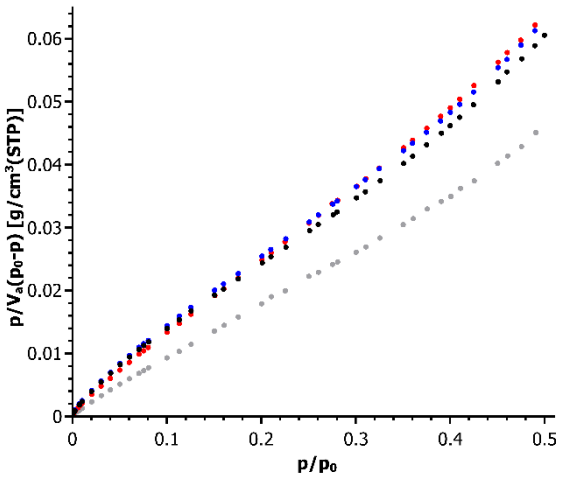

Fig. 6: Form N_2-sorption data derived BET-plot revealing the decreased surface area of CCS5 (black), CCS10 (red) and CCS20 (blue) compared to P25® (grey).

Photocatalytic experiments

At the beginning of the photocatalytic measurement the evolution of a discrete gas volume is observed, which is related to light induced heating of the reaction mixture.

Afterwards a very pronounced gas volume evolution of 40 mL/(g_{cat}•h) is observed over more than 9.5 h (see Fig. 7) which is caused by H_2 generation as evidenced by gas chromatographic analysis. Assuming an ideal gas the amount of H_2 is 1680±70 µmol/(g_{cat}•h) for CCS10. This value is only about 2.8 times lower than the H_2 production of P25@Pd 1 wt-% (4730±690 µmol/(g_{cat}•h), see Tab. 2 and supporting information Fig. S13), but comparable to reported activities for similar TiO_2@Pd catalysts.[73–75] As mentioned above TiO_2 itself exhibits only very low photocatalytic activity for HER which is explained by fast recombination of electrons and holes, a pronounced back reaction and a large overpotential on the surface for H_2 production. Hence, the high catalytic activity of CCS10 is caused by a synergistic effect. The catalyst loading of 10 wt-% seems to be almost ideal because of the significantly higher activity compared to the other two catalysts (see Tab. 2 and Fig. 7). With CCS5 no catalytic activity could be observed indicating that the loading with the spinel material is too low for generating a synergy with TiO_2. Using CCS20 a H_2 evolution rate of 1240±100 µmol/(g_{cat}•h) is obtained, which is about 25 % less than for CCS10. The observation of an optimal loading was also made for CoS_x deposited on TiO_2 [38], for mixtures of NiS and CuS on TiO_2 [58], or Cu_xS on TiO_2[76]. Possible explanations for this behavior are a decreased absorption of light by TiO_2, the introduction of more recombination centers and/or a decrease of the number of active sites on the TiO_2 surface, a incomplete dispersion of the particles on the surface, and increased particles sizes.[77]

A comparison of the catalytic activity of materials is not straightforward due to the differing experimental setups, the different numbers reported for the activity and the sacrifical agents applied. The effect of the latter was recently sumarized in a review showing that the catalytic activity of pure P25® strongly depend on the sacrifical agents.**[78]** The highest activity was observed for TiO_2/ethylene glycol (190.2 µmol H_2 in 6 h) and the lowest for lactic acid (27.6 µmol in 6 h), while TiO_2/TEOA produced a low amount of 61.8 µmol H_2 in 6 h. Keeping all the difficulties in mind we compare the performances of selected catalytic systems in Table 2 to give the reader an impression about the activity of CCS10. As can be seen from the data CCS10 and CCS20 show a far higher activity for hydrogen evolution compared to other catalysts under comparable conditions (300 W Xe arc lamp and triethanolamine as sacrificial agent). Especially, the higher activity compared to co-catalysts like Pt, MoS_2 and NiS reveals $CuCo_2S_4$ as promising co-catalyst for

photocatalytic hydrogen evolution. The effects of the different light filters is hard to be considered. For example the band gap of C_3N_4 (2.7 eV[79–81]) is smaller than that of TiO_2. Therefore the used light filter has a great effect on the photocatalytic activity and the amount of photons has to be considered for better comparability.

The chemical actinometry with $K_3Fe(C_2O_4)_3 \cdot 3H_2O$ gave a value for the photon flux of the used 300 W Xe arc lamp with used 320 nm low pass filter in the relevant wavelength range from 250 to 500 nm of 5.36±0.42 mol/s. Using the formula:

$$PE\ (250-500\ nm) = \frac{2 \cdot R^{in}}{\mathrm{R}_{O,250-500\ nm}}\ , \qquad \text{(Eq. 6)}$$

the photonic efficiency (PE) can be calculated, with the initial H_2 production rate R^{in} and photon flux $R_{O,250\text{-}500\ nm}$ determined by the actinometry system.[8,82–86] The photonic efficiency of CCS10 is 0.35±0.02 %, and for P25@Pd 1 wt-% tested for comparison the value is 0.98±0.14 %. A much larger efficiency cannot be expected because the majority of the photons (see supporting information Fig. S2) has not a sufficient energy to excite TiO_2. For the catalyst with the higher loading the photonic efficiency is 0.26±0.02 %.

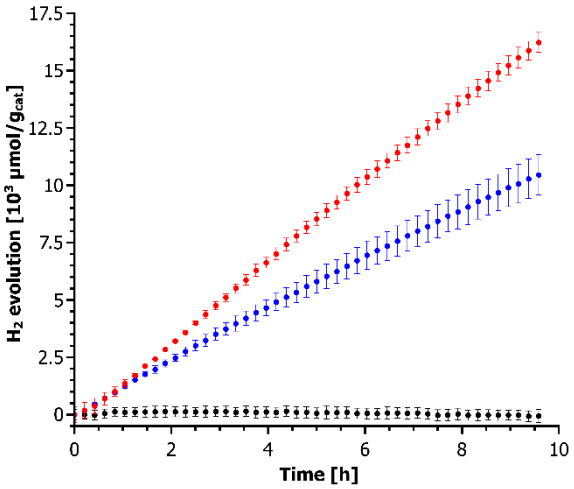

Fig. 7: Mean hydrogen evolution observed during irradiation of CCS5 (black), CCS10 (Red) and CCS20 (blue) dispersed in 10 Vol-% aqueous TEOA solution. Error bars represent the standard deviation.

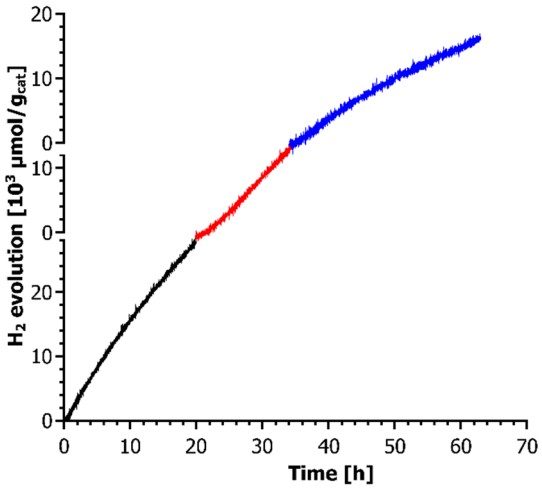

Fig. 8: H_2-evolution when CCS10 is used as photocatalyst in aqueous TEOA solution for the first (black), second (red) and third (blue) time showing the slowly decreasing activity with time.

Tab. 2: Obtained photocatalytic hydrogen evolution rates and photonic efficiency compared to data reported in literature for selected similar systems using 300 W Xe Lamp irradiation and triethanolamine as sacrificial agent.

Sample	Low pass light filter [nm]	Sacrificial agent used in aqueous solution	Hydrogen evolution rate [µmol/(g_{cat}•h)]
$(Cu,In)_{0.2}Zn_{1.6}S_2$@Pt[87]	420	10 Vol-% TEOA	720
C_3N_4@Carbon@NiS[81]	420	15 Vol-% TEOA	992
C_3N_4@MoS_2[79]	420	10 Vol-% TEOA	500
TiO_2@MWCNT@Pt[88]	420	15 Vol-% TEOA	378
C_3N_4[80]	420	20 Vol-% TEOA	279
TiO_2[80]	420	20 Vol-% TEOA	18
$Zn_{0.5}Cd_{0.5}S$[80]	420	20 Vol-% TEOA	1197
P25@Pd	320	10 Vol-% TEOA	4730[a]
CCS5	320	10 Vol-% TEOA	traces
CCS10	320	10 Vol-% TEOA	1680[a] 28000[b]
CCS20	320	10 Vol-% TEOA	1240[a] 8373b
P25®	320	10 Vol-% TEOA	traces
$CuCo_2S_4$	320	10 Vol-% TEOA	traces
P25® and $CuCo_2S_4$	320	10 Vol-% TEOA	26400[a,b]
P25® with Cu^{II}/Co^{II}-chloride	320	10 Vol-% TEOA	traces

[a:] estimated standard deviations calculated from different measurements are between 3 and 8 %. Note for the Pd sample the value is slightly larger.

[b:] evolution rate given in µmol/($g_{CuCo2S4}$•h)

The hydrogen evolution rate of CCS10 decreases slowly with time which may be explained by an increasing shortage of the sacrificial agent or due to deactivation of the catalyst. After the first catalytic test the catalyst was reused in a second test and after this run the material was recovered for the third time (see Fig. 8). The experiments show that the activity of the catalyst is slowly decreasing over time during the very long irradiation time of 70 to 80 h and even about ~60 mmol per gram catalyst were produced. Assuming a linear decrease of H_2 evolution rate a half life time of activity can be estimated to be ~42 h. We note that in many studies irradiation of the catalytic system is restricted to only a few hours which does not allow judgement of the stability.

The synergism in photocatalytic activity of $CuCo_2S_4$ and TiO_2 becomes apparent when using pure P25®, $CuCo_2S_4$ or a mechanical mixture of both materials (for characterization of these materials see supporting information Fig. S9 and S10 and Tab. S4). Pure P25® or $CuCo_2S_4$ show no sufficient ability for photocatalytic hydrogen evolution under the conditions applied in the other experiments (see supporting information Fig. S11), and only traces of H_2 could be detected. A mechanical mixture of 10 wt-% $CuCo_2S_4$ and P25® shows a lower hydrogen evolution rate (26400±900 µmol/($g_{CuCo_2S_4}$•h)) compared to CSS10 (28000±1200 µmol/($g_{CuCo_2S_4}$•h)) based on the $CuCo_2S_4$ content determined by XRD. Additionally the half life time of hydrogen evolution rate with the mechanical mixture (20.3 ± 0.9 h) is lower compared to CCS10. This results can be explained with the better interaction and connection of TiO_2 and $CuCo_2S_4$ in CCS10 due to the chosen synthesis procedure.

Post catalytic characterization

Analyzing XRD patterns of CCS10 after the catalytic test it is observable that the intensity of the reflections of $CuCo_2S_4$ are reduced compared to the pattern before catalysis (see Fig. 9). This finding can be explained by either amorphization of $CuCo_2S_4$, a dissolution or a detachment of the spinel particles from the TiO_2 surface. Chemical analyses of the liquid phases and of the recovered $CuCo_2S_4/TiO_2$ nanocomposites revealed a decrease of the Cu, Co and S content with increasing irradiation time. After 80 h of irradiation Cu vanished and only 1.1±0.2 wt-% of Co

could be detected via EDX on the catalyst material (see supporting information Tab. S1). One may speculate that dissolution and oxidation of S^{2-} ions are responsible for the H_2 evolution. But this would only account for a maximum H_2 evolution of 8 mmol/g_{cat}, which is much less than the value obtained after 80 h irradiation time (compare Fig. 8). To gain insight into the catalyst deactivation CCS10 was stirred in the dark for 20 h under the same conditions as a photocatalytic measurement and EDX data were collected. Indeed, the amount of Cu, Co, and S was reduced which indicates slow dissolution of the spinel material. In the used aqueous TEOA solution traces of Cu^{2+} and Co^{2+} ions could be detected (see supporting information Fig. S3). These results demonstrate that the basic TEOA solution is responsible for the catalyst deactivation. Hence, a more suitable sacrificial agent must be identified which will be the task of future work. To demonstrate that dissolved metal ions are not the active catalysts, photocatalytic experiments with P25® and dissolved Cu^{II} and Co^{II}-salts were done under the standard conditions applied here (see supporting information Fig. S12). In these experiments no hydrogen evolution could be observed like using only P25®. That proves that $CuCo_2S_4$ is the active co-catalyst.

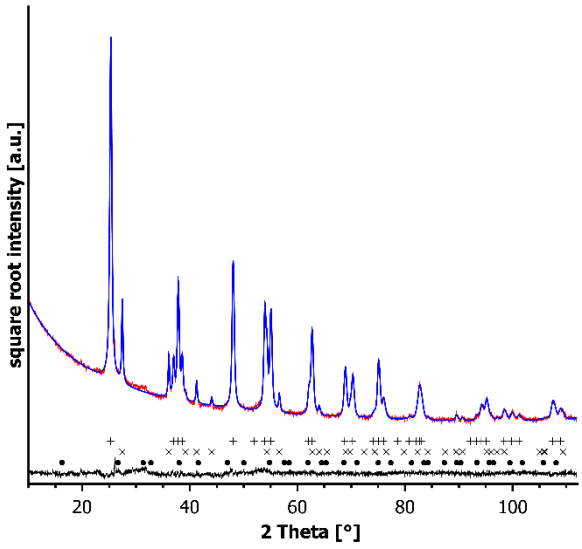

Fig. 9: Rietveld refinement data of CCS10 after used in catalysis experiment with 20 h irradiation. (Red) measured data, (blue) simulated data and (black) difference curve. Marks correspond to reflection postitions of Anatase[67] (+), Rutile[68] (x), $CuCo_2S_4$[69] (✳). Intensity of reflections of $CuCo_2S_4$ are explicitly lowered compared to the as synthesized material.

Conclusion

Phase pure $CuCo_2S_4$ seems to be easily synthesizable on Titania materials. The material gets a greyish black color originating from the metallic characteristics of $CuCo_2S_4$ interfering with the bandgap of P25® being 3.3 eV. The accessible surface area is not strongly reduced to 38-40 m^2/g. In photocatalytic measurements CCS10 and CCS20 show high catalytic activities when TEOA is used as sacrificial agent. The rate constant of hydrogen evolution with catalyst loading of 10 wt-% calculates to 1680±70 µmol/(g_{cat}•h) corresponding to 40 mL/g_{cat} per hour with a photonic efficiency of 0.35±0.02 %. With 5 wt-% and 20 wt-% catalyst loading the Materials show lower activity for H_2 evolution. The catalytic activity of CSS10 is only 2.8 times lower than using Pd as co-catalyst. But Pd (34000 US-$/kg)[89] is far more expensive than Co (55.5 US-$/kg)[90], which is the most expensive element in $CuCo_2S_4$. Therefore, the use of $CuCo_2S_4$ instead of Pd is very promising. In summary a schematic mechanism can be suggested as shown in Fig. 10. Electron-hole pairs are generated by light absorption by TiO_2. The electrons are transferred to the co-catalyst $CuCo_2S_4$ and H^+ ions are readily reduced to H_2. The valence band holes are filled by electrons due to oxidation of TEOH.

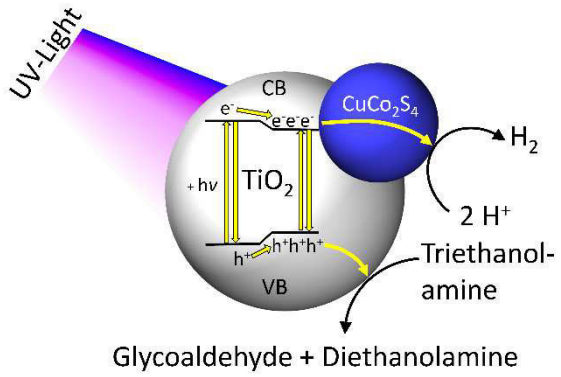

Fig. 10: Schematic representation of the suggested mechanism of hydrogen evolution with P25@$CuCo_2S_4$ in aqueous triethanolamine solution.

Acknowledgements

The authors are grateful to Christian-Albrechts-Universität zu Kiel for providing infrastructural facility and the state Schleswig-Holstein for financial support. We want to thank Jacqueline Pick and Stefanie Pehlke for their support in the spectroscopic measurements.

Literature

[1] A. Kudo, Y. Miseki, *Chem. Soc. Rev.*, **2009**, *38*, 253–278.
[2] X. Zou, Y. Zhang, *Chem. Soc. Rev.*, **2015**, *44*, 5148–5180.
[3] T. Jafari, E. Moharreri, A. S. Amin, R. Miao, W. Song, S. L. Suib, *Molecules*, **2016**, *21*.
[4] T. Shinagawa, K. Takanabe, *ChemSusChem*, **2017**, *10*, 1318–1336.
[5] S. Y. Tee, K. Y. Win, W. S. Teo, L.-D. Koh, S. Liu, C. P. Teng, M.-Y. Han, *Adv. Sci.*, **2017**, *4*, 1600337.
[6] C. Acar, I. Dincer, G. F. Naterer, *Int. J. Energy Res.*, **2016**, *40*, 1449–1473.
[7] Y. Miseki, K. Sayama, *Adv. Energy Mater.*, **2018**, *443*, 1801294.
[8] K. Maeda, *J. Photoch. Photobio. C*, **2011**, *12*, 237–268.
[9] H. Ahmad, S. K. Kamarudin, L. J. Minggu, M. Kassim, *Renew. Sust. Energ. Rev.*, **2015**, *43*, 599–610.
[10] A. J. Ragauskas, C. K. Williams, B. H. Davison, G. Britovsek, J. Cairney, C. A. Eckert, W. J. Frederick, J. P. Hallett, D. J. Leak, C. L. Liotta, J. R. Mielenz, R. Murphy, R. Templer, T. Tschaplinski, *Science*, **2006**, *311*, 484–489.
[11] J. J. Bozell, G. R. Petersen, *Green Chem.*, **2010**, *12*, 539–554.
[12] A. M. Appel, J. E. Bercaw, A. B. Bocarsly, H. Dobbek, D. L. DuBois, M. Dupuis, J. G. Ferry, E. Fujita, R. Hille, P. J. A. Kenis, C. A. Kerfeld, R. H. Morris, C. H. F. Peden, A. R. Portis, S. W. Ragsdale, T. B. Rauchfuss, J. N. H. Reek, L. C. Seefeldt, R. K. Thauer, G. L. Waldrop, *Chem. Rev.*, **2013**, *113*, 6621–6658.
[13] R. L. Paddock, S. T. Nguyen, *J. Am. Chem. Soc.*, **2001**, *123*, 11498–11499.
[14] J. K. Stolarczyk, S. Bhattacharyya, L. Polavarapu, J. Feldmann, *ACS Catal.*, **2018**, *8*, 3602–3635.
[15] F. Dionigi, P. C.K. Vesborg, T. Pedersen, O. Hansen, S. Dahl, A. Xiong, K. Maeda, K. Domen, I. Chorkendorff, *J. Catal.*, **2012**, *292*, 26–31.
[16] D. S. P. Cardoso, B. Šljukić, D. M. F. Santos, C. A. C. Sequeira, *Org. Process Res. Dev.*, **2017**, *21*, 1213–1226.
[17] K. D. Moeller, T. Wu, B. H. Nguyen, M. C. Daugherty, *Angew. Chem. Int. Ed.*, **2019**.
[18] T. Lazarides, T. McCormick, P. Du, G. Luo, B. Lindley, R. Eisenberg, *J. Am. Chem. Soc.*, **2009**, *131*, 9192–9194.
[19] G. Liu, P. Niu, C. Sun, S. C. Smith, Z. Chen, G. Q. Lu, H.-M. Cheng, *J. Am. Chem. Soc.*, **2010**, *132*, 11642–11648.
[20] M. Schwarze, D. Stellmach, M. Schröder, K. Kailasam, R. Reske, A. Thomas, R. Schomäcker, *Phys. Chem. Chem. Phys.*, **2013**, *15*, 3466–3472.
[21] Z. Zhang, A. Li, S.-W. Cao, M. Bosman, S. Li, C. Xue, *Nanoscale*, **2014**, *6*, 5217–5222.
[22] M. Landmann, E. Rauls, W. G. Schmidt, *J. Phys.: Condens. Matter*, **2012**, *24*, 195503.
[23] A. Fujishima, K. Honda, *Nature*, **1972**, *238*, 37–38.
[24] A. L. Linsebigler, G. Lu, J. T. Yates, *Chem. Rev.*, **1995**, *95*, 735–758.
[25] X. Wang, A. Kafizas, X. Li, S. J. A. Moniz, P. J. T. Reardon, J. Tang, I. P. Parkin, J. R. Durrant, *J. Phys. Chem. C*, **2015**, *119*, 10439–10447.
[26] Y. Kakuma, A. Y. Nosaka, Y. Nosaka, *Phys. Chem. Chem. Phys.*, **2015**, *17*, 18691–18698.
[27] Q. Fan, S. He, L. Hao, X. Liu, Y. Zhu, S. Xu, F. Zhang, *Sci. Rep.*, **2017**, *7*, 42172–42186.
[28] L. Guo, Z. Yang, K. Marcus, Z. Li, B. Luo, L. Zhou, X. Wang, Y. Du, Y. Yang, *Energy Environ. Sci.*, **2018**, *11*, 106–114.
[29] W. Ho, J. C. Yu, J. Lin, J. Yu, P. Li, *Langmuir*, **2004**, *20*, 5865–5869.
[30] B. Mahler, V. Hoepfner, K. Liao, G. A. Ozin, *J. Am. Chem. Soc.*, **2014**, *136*, 14121–14127.
[31] F. Xu, L. Zhang, B. Cheng, J. Yu, *ACS Sustain. Chem. Eng.*, **2018**, *6*, 12291–12298.
[32] X. Zhang, Y. Chen, Y. Xiao, W. Zhou, G. Tian, H. Fu, *Nanoscale*, **2018**, *10*, 4041–4050.
[33] L. Zhang, B. Tian, F. Chen, J. Zhang, *Int. J. Hydrogen Energ.*, **2012**, *37*, 17060–17067.
[34] Y. Im, S. Kang, K. M. Kim, T. Ju, G. B. Han, N.-K. Park, T. J. Lee, M. Kang, *Int. J. Photonenergy*, **2013**, *2013*, 1–10.
[35] S. Yu, J. Liu, Y. Zhou, R. D. Webster, X. Yan, *ACS Sustain. Chem. Eng.*, **2016**, *5*, 1347–1357.
[36] M. Chandra, K. Bhunia, D. Pradhan, *Inorg. Chem.*, **2018**, *57*, 4524–4533.
[37] F. Chen, W. Luo, Y. Mo, H. Yu, B. Cheng, *Appl. Surf. Sci.*, **2018**, *430*, 448–456.
[38] Z. Yu, J. Meng, J. Xiao, Y. Li, Y. Li, *Int. J. Hydrogen Energ.*, **2014**, *39*, 15387–15393.

[39] A. M. Huerta-Flores, L. M. Torres-Martínez, E. Moctezuma, A. P. Singh, B. Wickman, *J. Mater. Sci.: Mater. Electron.*, **2018**, *29*, 11613–11626.
[40] N. Li, W. Fu, C. Chen, M. Liu, F. Xue, Q. Shen, J. Zhou, *ACS Sustain. Chem. Eng.*, **2018**, *6*, 15867–15875.
[41] S. Shen, X. Chen, F. Ren, C. X. Kronawitter, S. S. Mao, L. Guo, *Nanoscale Res. Lett.*, **2011**, *6*, 290.
[42] L. Zhang, T. Jiang, S. Li, Y. Lu, L. Wang, X. Zhang, D. Wang, T. Xie, *Dalton Trans.*, **2013**, *42*, 12998–13003.
[43] InfoMine Inc., *Copper Price*, http://www.infomine.com/investment/metal-prices/copper/5-year/, Accessed on 2019/02/08.
[44] H. Liang, D. Jiang, S. Wei, X. Cao, T. Chen, B. Huo, Z. Peng, C. Li, J. Liu, *J. Mater. Chem. A*, **2018**, *6*, 16235–16245.
[45] R. Souleymen, Z. Wang, C. Qiao, M. Naveed, C. Cao, *J. Mater. Chem. A*, **2018**, *6*, 7592–7607.
[46] Y. Yan, K. Li, X. Chen, Y. Yang, J.-M. Lee, *Small*, **2017**, *13*.
[47] M. Zheng, Y. Ding, L. Yu, X. Du, Y. Zhao, *Adv. Funct. Mater.*, **2017**, *27*, 1605846.
[48] T. Oda, M. Shirai, N. Suzuki, K. Motizuki, *J. Phys.: Condens. Matter*, **1995**, *7*, 4433–4446.
[49] R. A.D. Pattrick, V. S. Coker, C. I. Pearce, N. D. Telling, G. van der Laan, *Can. Mineral.*, **2008**, *46*, 1317–1322.
[50] K. Miyatani, T. Tanaka, S. Sakita, M. Ishikawa, N. Shirakawa, *Jpn. J. Appl. Phys.*, **1993**, *32*, 448–450.
[51] Y. Furukawa, S. Wada, K. Miyatani, T. Tanaka, M. Fukugauchi, M. Ishikawa, *Phys. Rev. B*, **1995**, *51*, 6159–6162.
[52] S. Wada, H. Sugita, K. Miyatani, T. Tanaka, T. Nishikawa, *J. Phys.: Condens. Matter*, **2002**, *14*, 219–230.
[53] H. Sugita, S. Wada, K. Miyatani, T. Tanaka, M. Ishikawa, *Physica B*, **2000**, *284-288*, 473–474.
[54] A. N. Buckley, W. M. Skinner, S. L. Harmer, A. Pring, L.-J. Fan, *Geochim. Cosmochim. Ac.*, **2009**, *73*, 4452–4467.
[55] M. Chauhan, K. P. Reddy, C. S. Gopinath, S. Deka, *ACS Catal.*, **2017**, *7*, 5871–5879.
[56] Y. Ge, J. Wu, X. Xu, M. Ye, J. Shen, *Int. J. Hydrogen Energ.*, **2016**, *41*, 19847–19854.
[57] A. M. Wiltrout, C. G. Read, E. M. Spencer, R. E. Schaak, *Inorg. Chem.*, **2016**, *55*, 221–226.
[58] Q. Wang, G. Yun, Y. Bai, N. An, Y. Chen, R. Wang, Z. Lei, W. Shangguan, *Int. J. Hydrogen Energ.*, **2014**, *39*, 13421–13428.
[59] Alan Coelho, *Topas Academic v6*, Coelho Software, **2016**.
[60] *jEdit*, http://www.jedit.org/index.php?page=features, Accessed on 2018/11/21.
[61] D. R. G. Mitchell, *Microsc. Res. Tech.*, **2008**, *71*, 588–593.
[62] P. A. Stadelmann, *Ultramicroscopy*, **1987**, *21*, 131–145.
[63] S. Brunaer, Emmett, Paul H., Teller, Edward, S. Brunauer, P. H. Emmett, E. Teller, *J. Am. Chem. Soc.*, **1938**, *60*, 309–319.
[64] B. Ohtani, O. O. Prieto-Mahaney, D. Li, R. Abe, *J. Photoch. Photobio. A*, **2010**, *216*, 179–182.
[65] D. M. Tobaldi, R. C. Pullar, M. P. Seabra, J. A. Labrincha, *Mater. Lett.*, **2014**, *122*, 345–347.
[66] J. Yu, H. Yu, B. Cheng, M. Zhou, X. Zhao, *J. Molec. Catal. A*, **2006**, *253*, 112–118.
[67] M. Horn, C. F. Schwerdtfeger, E. P. Meagher, *Z. Krist.*, **1972**, *136*, 273–281.
[68] S. C. Abrahams, J. L. Bernstein, *J. Chem. Phys.*, **1971**, *55*, 3206–3211.
[69] D. P. Williamson, N. W. Grimes, *J. Phys. D: Appl. Phys.*, **1974**, *7*, 1–6.
[70] G. Kortüm, W. Braun, G. Herzog, *Angew. Chem. Int. Ed.*, **1963**, *2*, 333–341.
[71] P. A. Lee, G. Said, R. Davis, T. H. Lim, *Solid State Commun.*, **1969**, *7*, 2719–2729.
[72] M. Thommes, K. Kaneko, A. V. Neimark, J. P. Olivier, F. Rodriguez-Reinoso, J. Rouquerol, K. S.W. Sing, *Pure Appl. Chem.*, **2015**, *87*, 160–178.
[73] T. Kawai, T. Sakata, *J. Chem. Soc., Chem. Commun.*, **1980**, 694-695.
[74] A. L. Luna, D. Dragoe, K. Wang, P. Beaunier, E. Kowalska, B. Ohtani, D. Bahena Uribe, M. A. Valenzuela, H. Remita, C. Colbeau-Justin, *J. Phys. Chem. C*, **2017**, *121*, 14302–14311.
[75] J. Wu, S. Lu, D. Ge, L. Zhang, W. Chen, H. Gu, *RSC Adv.*, **2016**, *6*, 67502–67508.
[76] H. Dang, Z. Cheng, W. Yang, W. Chen, W. Huang, B. Li, Z. Shi, Y. Qiu, X. Dong, H. Fan, *J. Alloy Compd.*, **2017**, *709*, 422–430.
[77] K. C. Christoforidis, P. Fornasiero, *ChemCatChem*, **2017**, *9*, 1523–1544.
[78] V. Kumaravel, M. Imam, A. Badreldin, R. Chava, J. Do, M. Kang, A. Abdel-Wahab, *Catalysts*, *9*, 276.

[79] M. Li, L. Zhang, X. Fan, M. Wu, Y. Du, M. Wang, Q. Kong, L. Zhang, J. Shi, *Appl. Catal. B: Environ.*, **2016**, *190*, 36–43.
[80] M. Wang, S. Shen, L. Li, Z. Tang, J. Yang, *J. Mater. Sci.*, **2017**, *52*, 5155–5164.
[81] J. Wen, X. Li, H. Li, S. Ma, K. He, Y. Xu, Y. Fang, W. Liu, Q. Gao, *Appl. Surf. Sci.*, **2015**, *358*, 204–212.
[82] N. Serpone, A. Salinaro, *Pure Appl. Chem.*, **1999**, *71*, 303–320.
[83] N. Serpone, *J. Photoch. Photobio. A*, **1997**, *104*, 1–12.
[84] H. Kisch, D. Bahnemann, *J. Phys. Chem. Lett.*, **2015**, *6*, 1907–1910.
[85] M. J. Muñoz-Batista, A. Kubacka, A. B. Hungría, M. Fernández-García, *J. Catal.*, **2015**, *330*, 154–166.
[86] M. Qureshi, K. Takanabe, *Chem. Mater.*, **2016**, *29*, 158–167.
[87] X. Zhang, M. Yang, J. Zhao, L. Guo, *Int. J. Hydrogen Energ.*, **2013**, *38*, 15985–15991.
[88] K. Dai, X. Zhang, K. Fan, P. Zeng, T. Peng, *J. Nanomater.*, **2014**, *2014*, 1–8.
[89] InfoMine Inc., *Palladium price*, http://www.infomine.com/investment/metal-prices/palladium/5-year/, Accessed on 2018/10/09.
[90] InfoMine Inc., *Cobalt price*, http://www.infomine.com/investment/metal-prices/cobalt/5-year/, Accessed on 2018/10/09.

Supporting information to

$CuCo_2S_4$ on TiO_2 leading to high photocatalytic H_2 evolution

S1. P25@Pd characterization

P25@Pd 1 wt-% was characterized with XRD using a PANalytical Empyrean MPD Diffractometer with Cu K_α irradiation in reflection geometry. Rietveld refinement was done with the program Topas academic v6 in combination with jEdit. The refinement of the X-ray powder pattern leads to 0.33 wt% Pd deposited on TiO_2 and size of coherently scattering domains of 9±2 nm (GOF: 1.175,see Fig. S1) For simplicity, the sample is still called P25@Pd 1 wt-%.

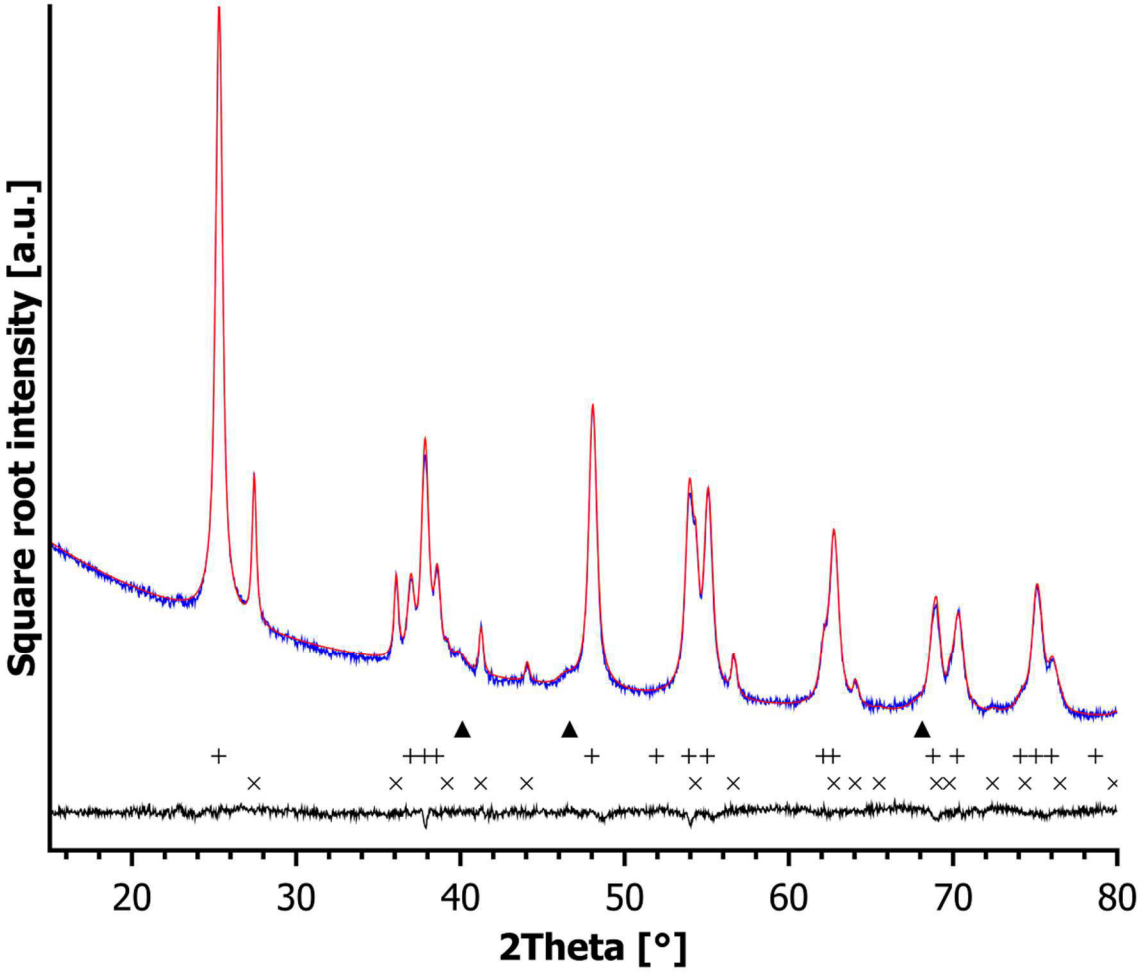

Fig. S1: Rietveld refinement data of XRD measurement of P25@Pd 1 wt-% (blue), the obtained fitting (red) and the difference curve (black). The reflection positions are marked as follows: Palladium[1] ▲, Anatase[2] + and Rutile[3] x.

S2. EDX and XRD data of CCS10 catalysts

Tab. S1: Percentual weight fractions expected from 10 wt-% $CuCo_2S_4$ on TiO_2 and detected with EDX spectroscopy for CCS10 before and after the first and third catalytic test in SEM Philips XL-30. Observable is a good accordance between expected and synthesized sample while catalysis leads to a decrease of Cu, Co and S-Content.

Sample	Expected for 10 wt-% $CuCo_2S_4$ on TiO_2	CCS10 as synthesized	CCS10 after 1. catalysis run 20 h	CCS10 after 3. catalysis run 80 h	CCS10 stirred in dark 20 h
	wt-%				
Cu rel to TiO_2	2.1	2.3±0.1	1.2±0.4	Not detectable	0.5±0.3
Co rel. to TiO_2	3.9	3.9±0.1	3.2±0.4	1.1±0.3	1.1±0.3
S rel. to TiO_2	4.3	4.2±0.2	1.8±0.4	0.5±0.3	0.8±0.3
TiO_2 calc. from Ti	90	89.7±0.9	93.8±0.4	98.4±0.3	97.6±0.3

Tab. S2: From Rietveld refinements of XRD data determined parameters for phases observed in CCS5 and CCS20.

Parameter	CCS5			CCS20		
	Anatase	Rutile	$CuCo_2S_4$	Anatase	Rutile	$CuCo_2S_4$
Cell parameter [Å]	a = b = 3.78689(7) c = 9.50686(21)	a = b = 4.59538(19) c = 2.96021(22)	a = b = c = 9.4798(18)	a = b = 3.78691(8) c = 9.50695(22)	a = b = 4.59538(20) c = 2.96020(23)	a = b = c = 9.47636(26)
Chalcogen position	x = y = 0 z = 0.20732	x = y = 0.30479 z = 0	x = y = z = 0.263	x = y = 0 z = 0.20732	x = y = 0.30479 z = 0	x = y = z = 0.263
Space group	*$I4_1/amdS$*	*$P4_2/mnm$*	*Fd*-3*mZ*	*$I4_1/amdS$*	*$P4_2/mnm$*	*Fd*-3*mZ*
R-Bragg	1.712	1.825	2.987	1.041	1.282	1.912
Weight fraction [%]	87.0	11.8	1.2	74.8	10.4	14.8
Volume averaged domain size [nm]	23	31	21	24	31	20

Tab. S3: Percentual atomic contents determined with EDX spectroscopy for CCS10, CCS5 and CCS20 in SEM Philips XL-30.

Sample	CCS5	CCS10	CCS20
	at-%		
Cu	3.2±0.5	2.6±0.3	5.5±0.2
Co	3.1±0.3	4.8±0.3	8.7±0.2
S	3.37±1.3	9.7±0.8	15.9±0.8
Ti	90.3±2.0	82.9±0.7	68.9±1.2
	wt-%		
Cu/Co-sulfide	6.1±0.2	2.6±0.3	19.8±0.2
TiO_2	93.9±0.2	4.8±0.3	80.2±0.2
	atomic ratio relative to Cu		
Cu	Traces	1.0±0.1	1.0±0.04
Co	Traces	1.8±0.1	1.6±0.04
S	Traces	3.7±0.3	2.9±0.1

S3. Lamp spectum

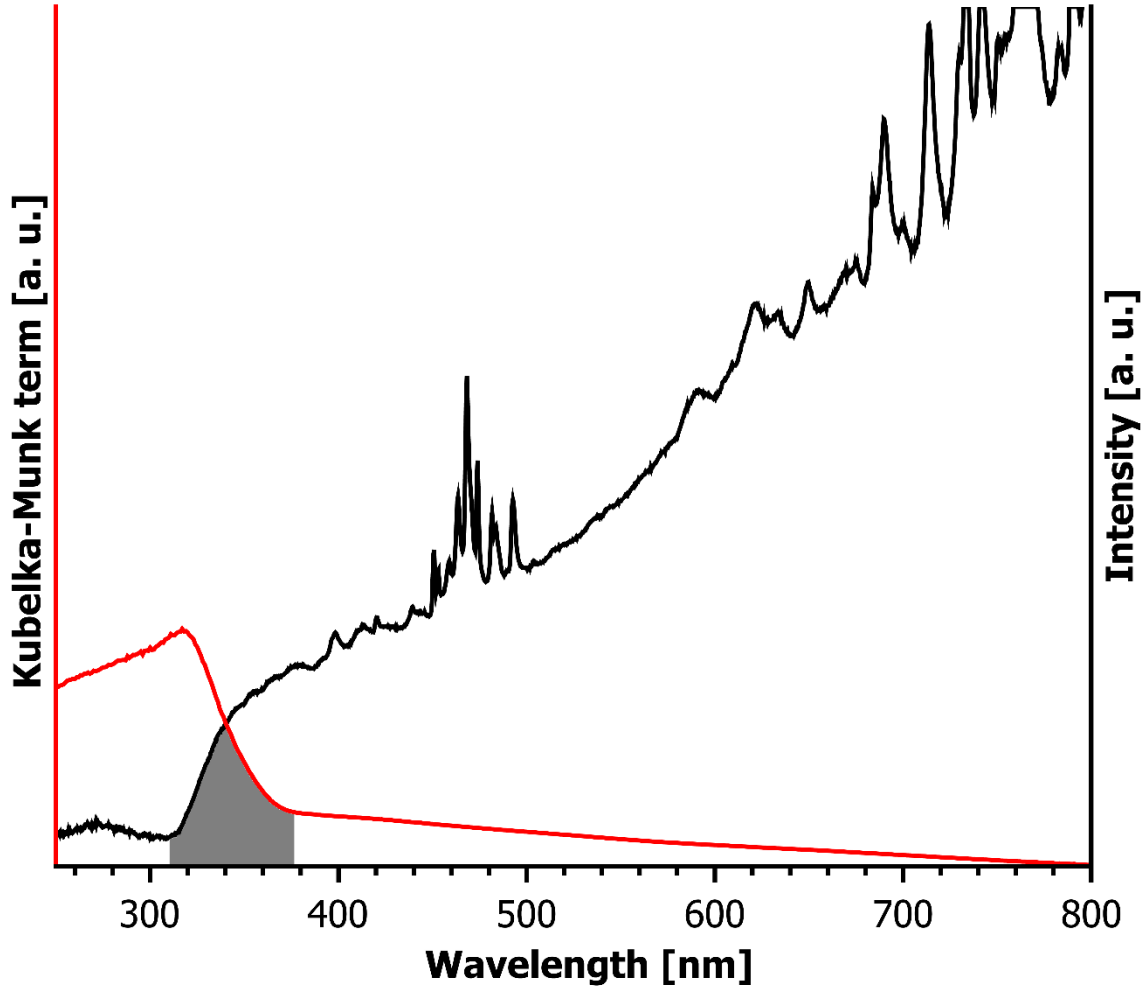

Fig. S2 Observed spectrum (black) of the used 300 W Xe-lamp combined with a 320 nm low pass filter compared to the absorption spectrum of CCS10 (red). The overlap between the spectrum and the absorption region is shaded in grey.

S4. UV/Vis-data

A catalysis experiment with CCS10 in aqueous 10 Vol-% TEOA solution is done without irradiation for 20 h under same conditions as in other catalysis experiments. Afterwards 50 mL acetone are added to easily separate the catalyst via centrifugation. The acetone is separated by evaporation to obtain the reaction mixture after process. For comparison two small crystals ~1 mg of $CuCl_2 \cdot 2H_2O$ and $CoCl_2 \cdot 6H_2O$ are dissolved in 5 mL aqueous 10-Vol-% TEOA solution.

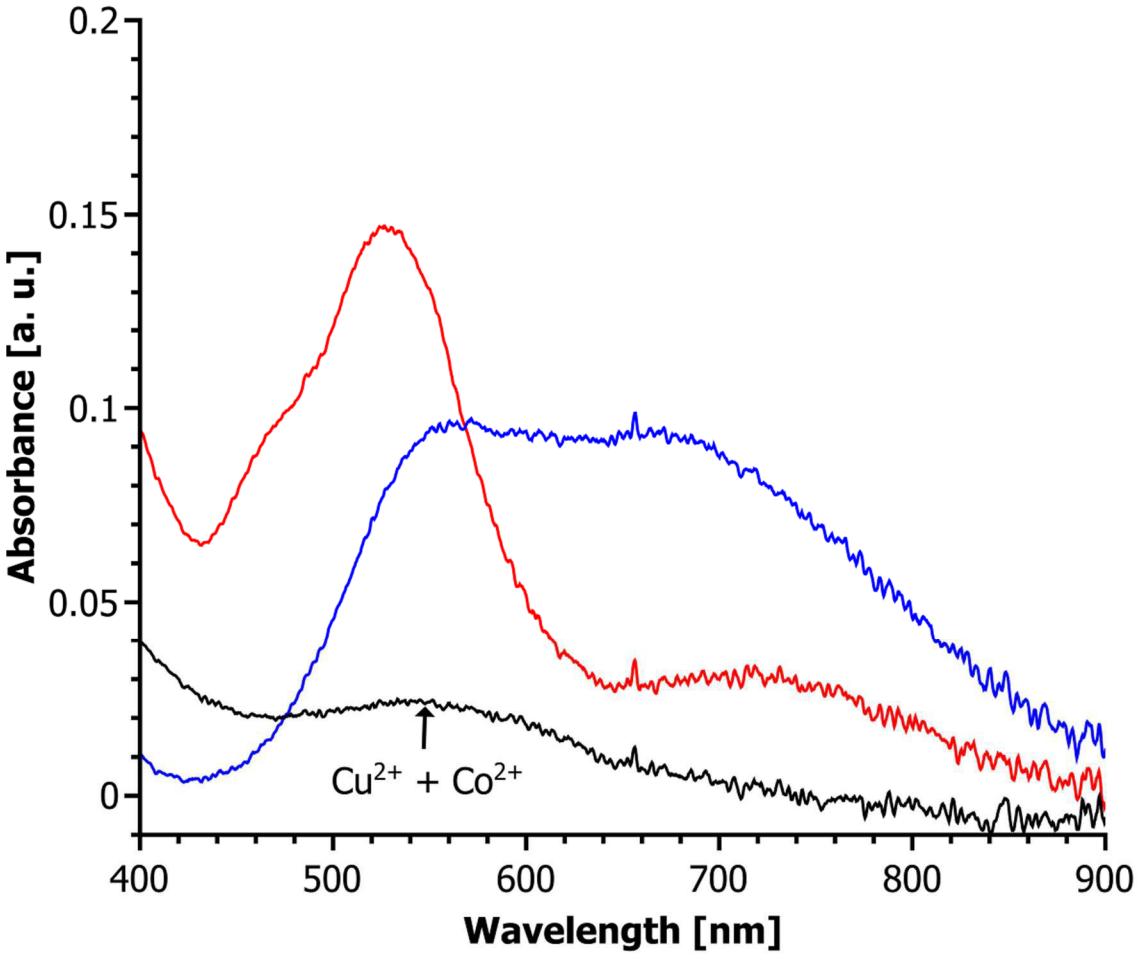

Fig. S3: UV/Vis data of the reaction mixture after reaction with CCS10 in the dark (black) in comparison to Cu^{2+} (blue) and Co^{2+} (red) in aqueous 10 Vol-% TEOA solution. Aqueous 10 Vol-% TEOA solution is used as reference. A small absorption band is observed related to traces of Cu^{2+} and Co^{2+}-TEOA complexes occurring due to catalyst dissolution.

S5. Transmission Electron Microscopy

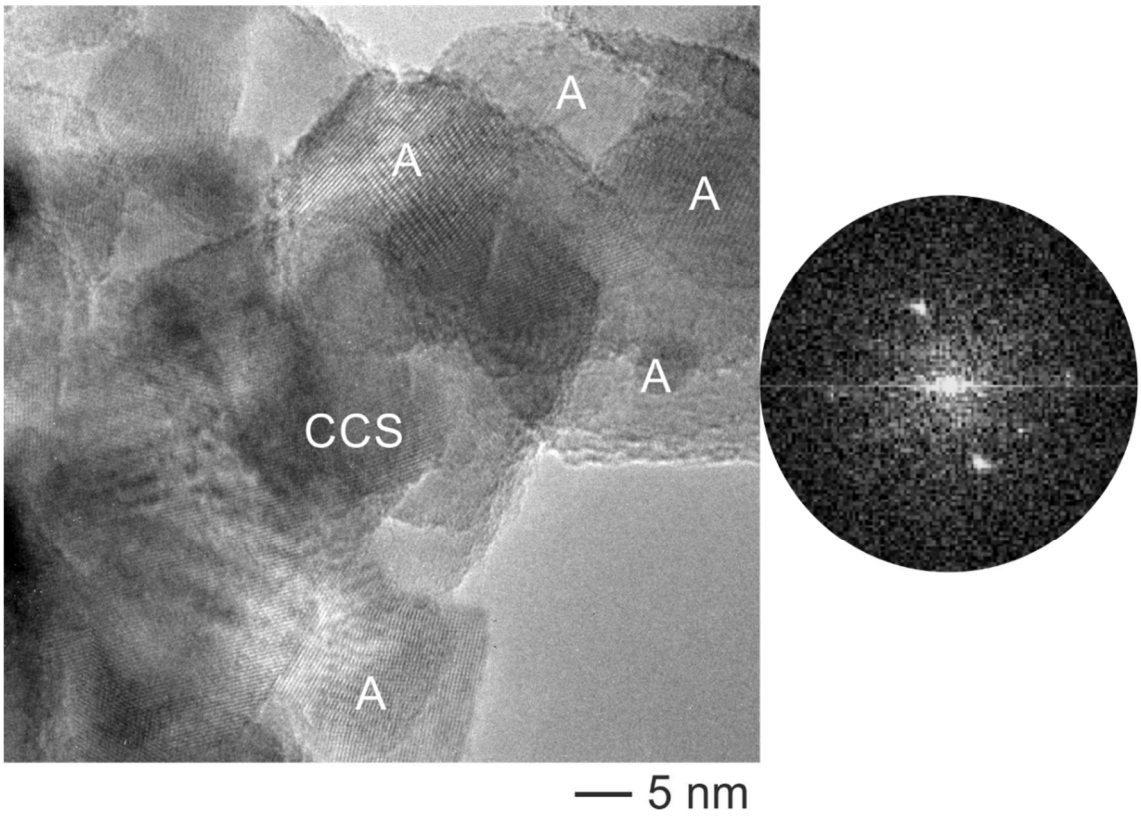

Figure S4: TEM micrograph and FFT of a particle cluster of CCS20. Most particles and their corresponding d-spacings could be matched to anatase (A)[69]; one particle, however, could be attributed to $CuCo_2S_4$ (CCS)[71]. The d-spacings from the FFT show good agreement with literature data; a corresponding zone axis could not be assigned due to sample misalignment and particle thickness.

S6. Rietveld refinements and UV/Vis-spectra of CCS5 and CCS20

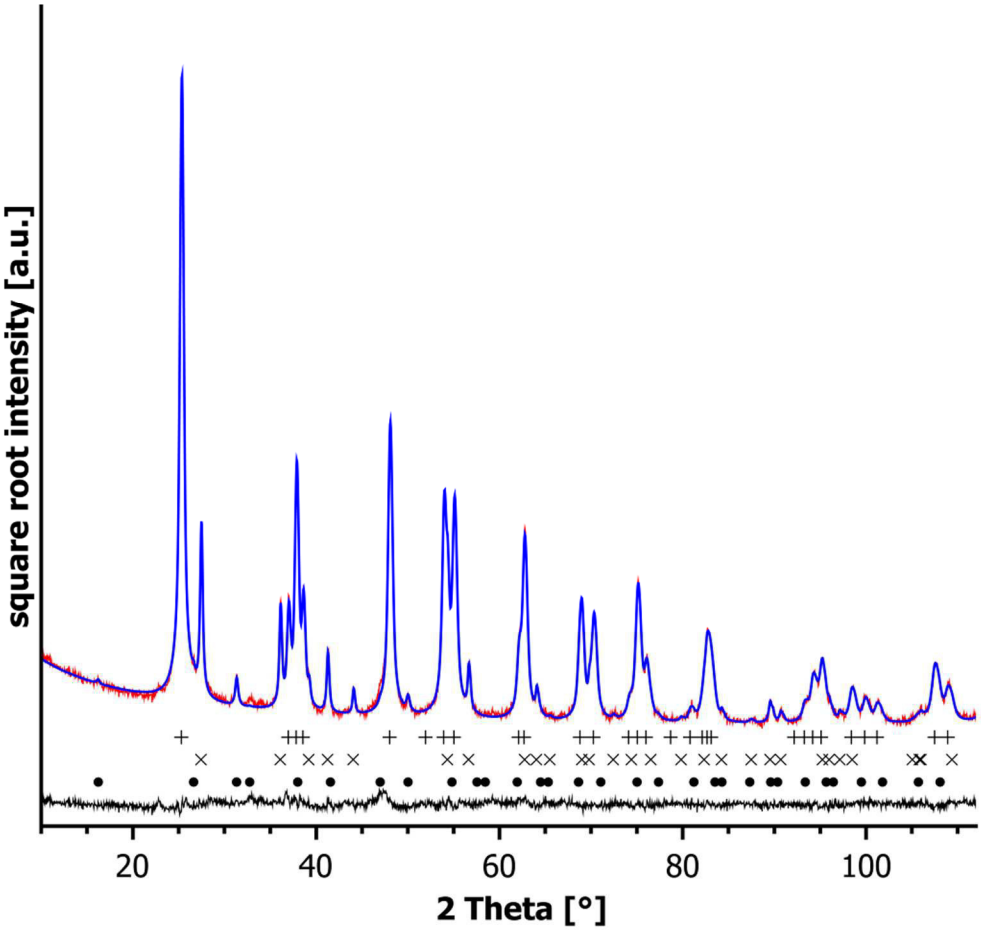

Fig. S5: Rietveld refinement data of CCS5. (Red) measured data, (blue) simulated data and (black) difference curve. Marks correspond reflection postitions of Anatase[2] (+), Rutile[3] (x), $CuCo_2S_4$[4] (●). The difference curve shows that the simulated pattern matches perfectly with the experimental pattern and that there are no additional phases detectable.

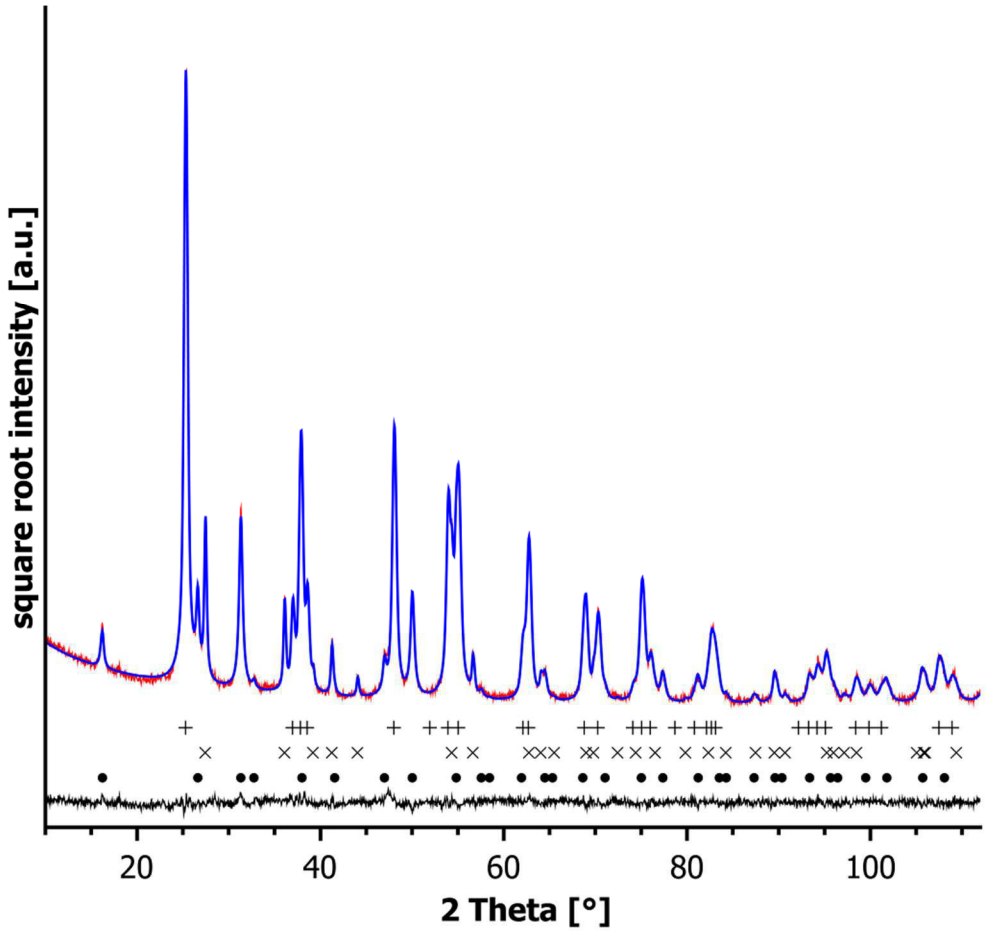

Fig. S6: Rietveld refinement data of CCS20. (Red) measured data, (blue) simulated data and (black) difference curve. Marks correspond reflection postitions of Anatase[2] (+), Rutile[3] (x), $CuCo_2S_4$[4] (●). The difference curve shows that the simulated pattern matches perfectly with the experimental pattern and that there are no additional phases detectable.

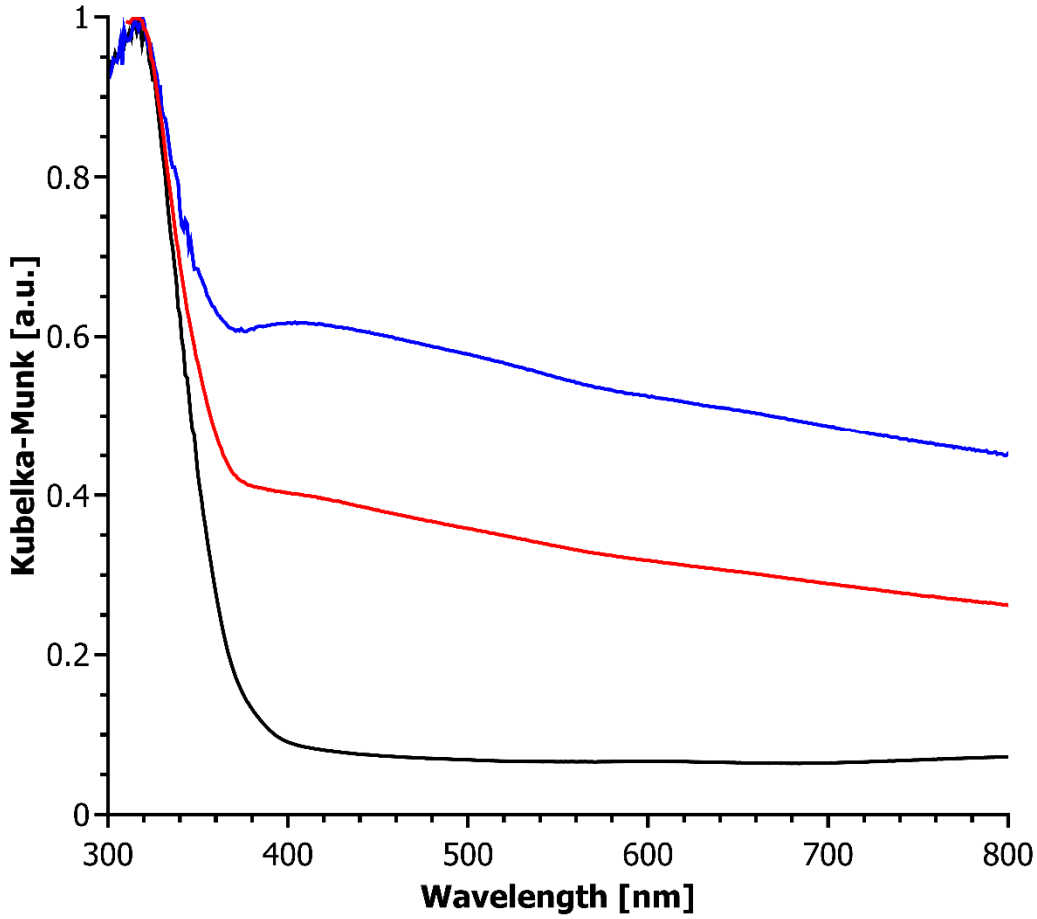

Fig. S7: UV/Vis absorption data of CCS5 (black), CCS10 (Red) and CCS20 (blue).

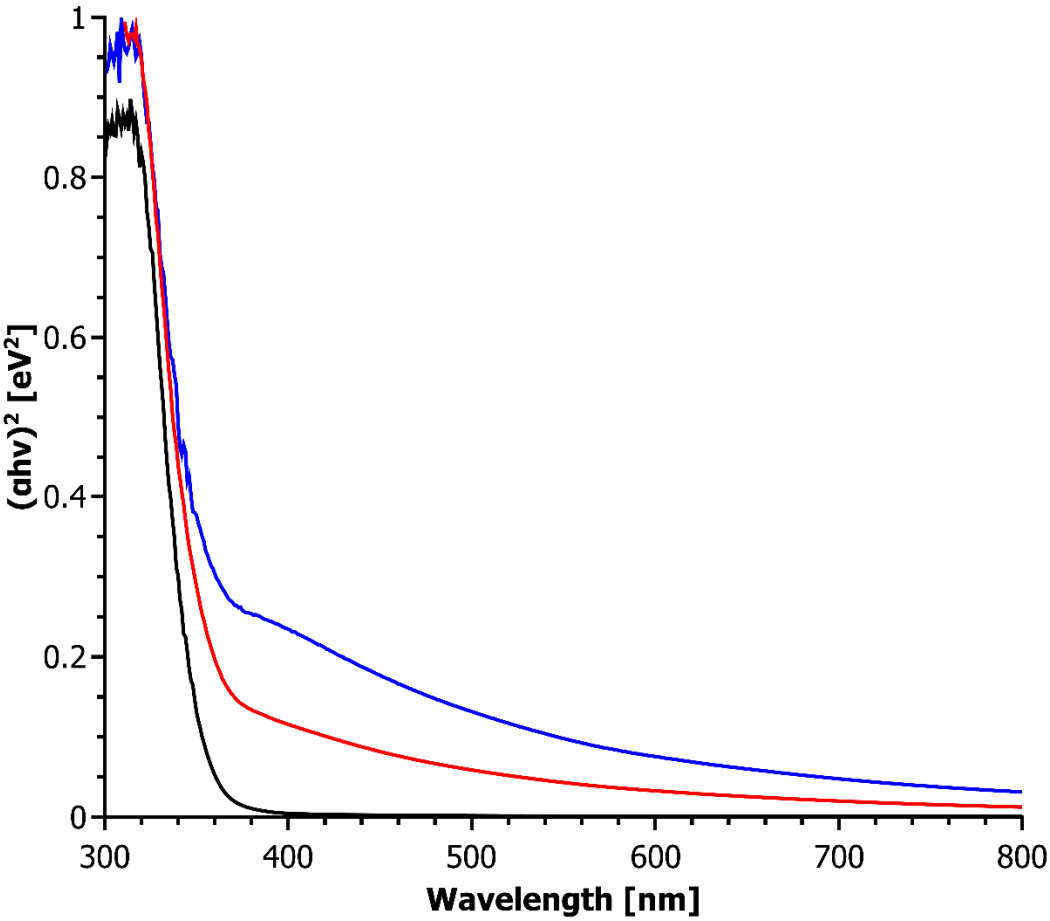

Fig. S8: Tauc plots of CCS5 (black), CCS10 (Red) and CCS20 (blue).

S7. Rietveld refinements of $CuCo_2S_4$ and mechanical mixture of 10 wt-% $CuCo_2S_4$ with P25

EDX-analysis results into a ratio of Cu:Co:S of 1±0.1 : 2±0.1 : 3.8±0.2, which matches very good with the desired element ratios in $CuCo_2S_4$.

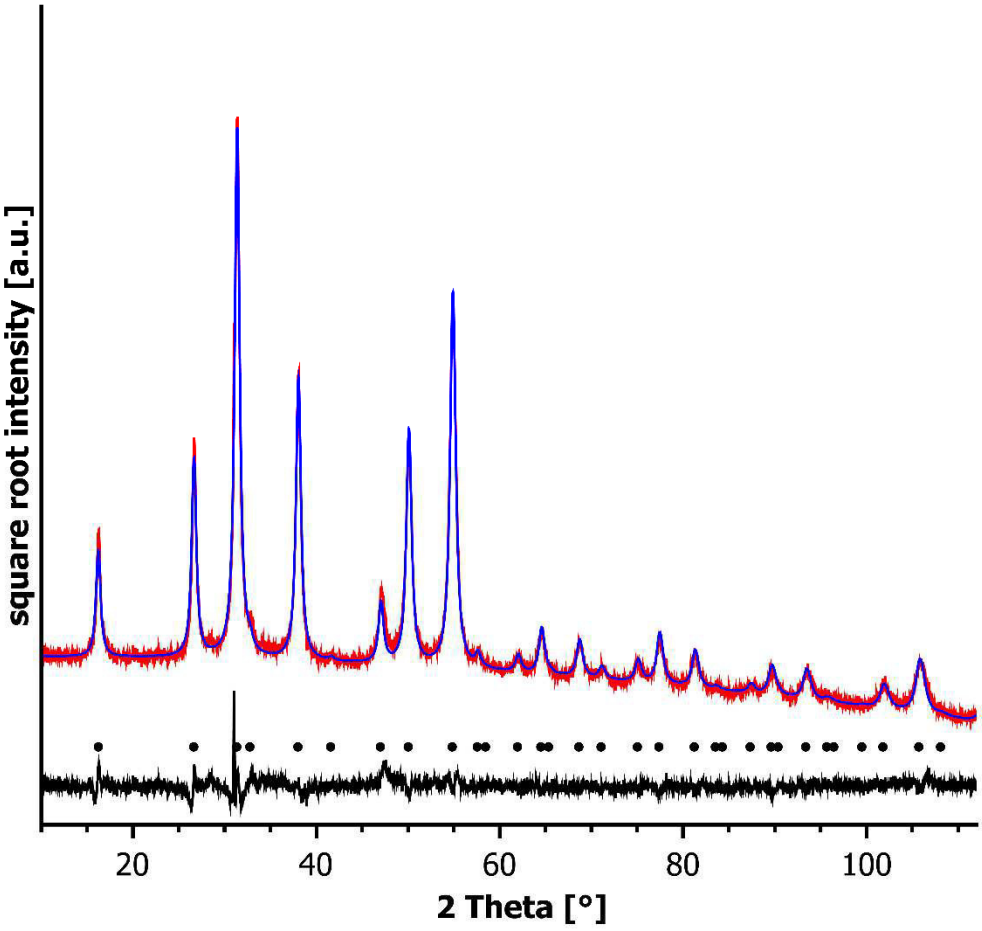

Fig. S9: Rietveld refinement data of synthesized $CuCo_2S_4$. (Red) measured data, (blue) simulated data and (black) difference curve. Marks correspond reflection postitions of $CuCo_2S_4$[4] (✳). The difference curve shows that the simulated pattern matches perfectly to the detected one and that there are no additional phases detectable.

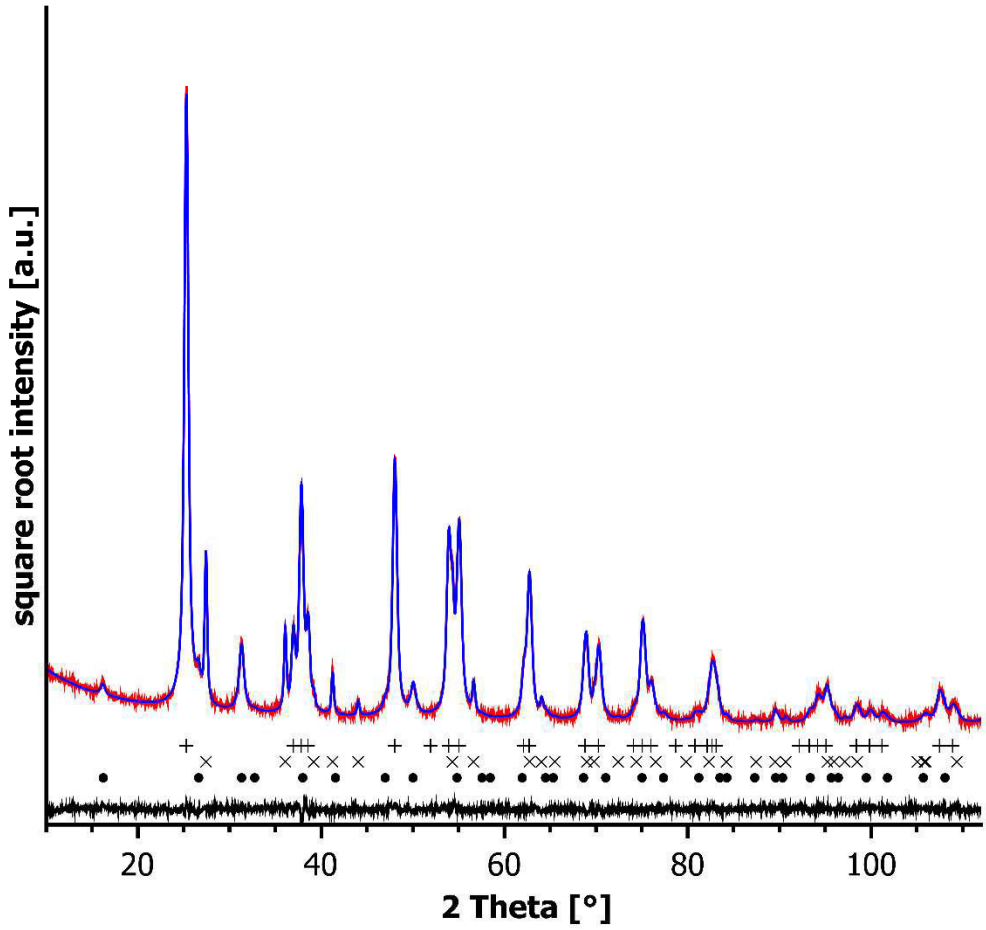

Fig. S10: Rietveld refinement data of a mechanical mixture of 10 wt-% $CuCo_2S_4$ and P25. (Red) measured data, (blue) simulated data and (black) difference curve. Marks correspond reflection postitions of Anatase[2] (+), Rutile[3] (x), $CuCo_2S_4$[4] (✳). The difference curve shows that the simulated pattern matches perfectly to the measured one and that there are no additional phases detectable.

Tab. S4: From Rietveld refinements of XRD data determined parameters for phases observed in synthesized $CuCo_2S_4$ and mechanically mixed $CuCo_2S_4$ and P25.

Parameter	$CuCo_2S_4$	CCS20		
		Anatase	Rutile	$CuCo_2S_4$
Cell parameter [Å]	a = b = c = 9.4689(4)	a = b = 3.78658(3) c = 9.50778(12)	a = b = 4.59499(11) c = 2.95961 (14)	a = b = c = 9.4673(5)
Chalcogen position	x = y = z = 0.26042(9)	x = y = 0 z = 0.20781(7)	x = y = 0.3031(5) z = 0	x = y = z = 0.2611(3)
Space group	*Fd*-3*mZ*	$I4_1/amdS$	$P4_2/mnm$	*Fd*-3*mZ*
R-Bragg	0.264	0.503	0.781	0.730
Weight fraction [%]	100	82.1	10.1	7.8
Volume averaged domain size [nm]	11	21	31	11

S8. Supporting photocatalysis data

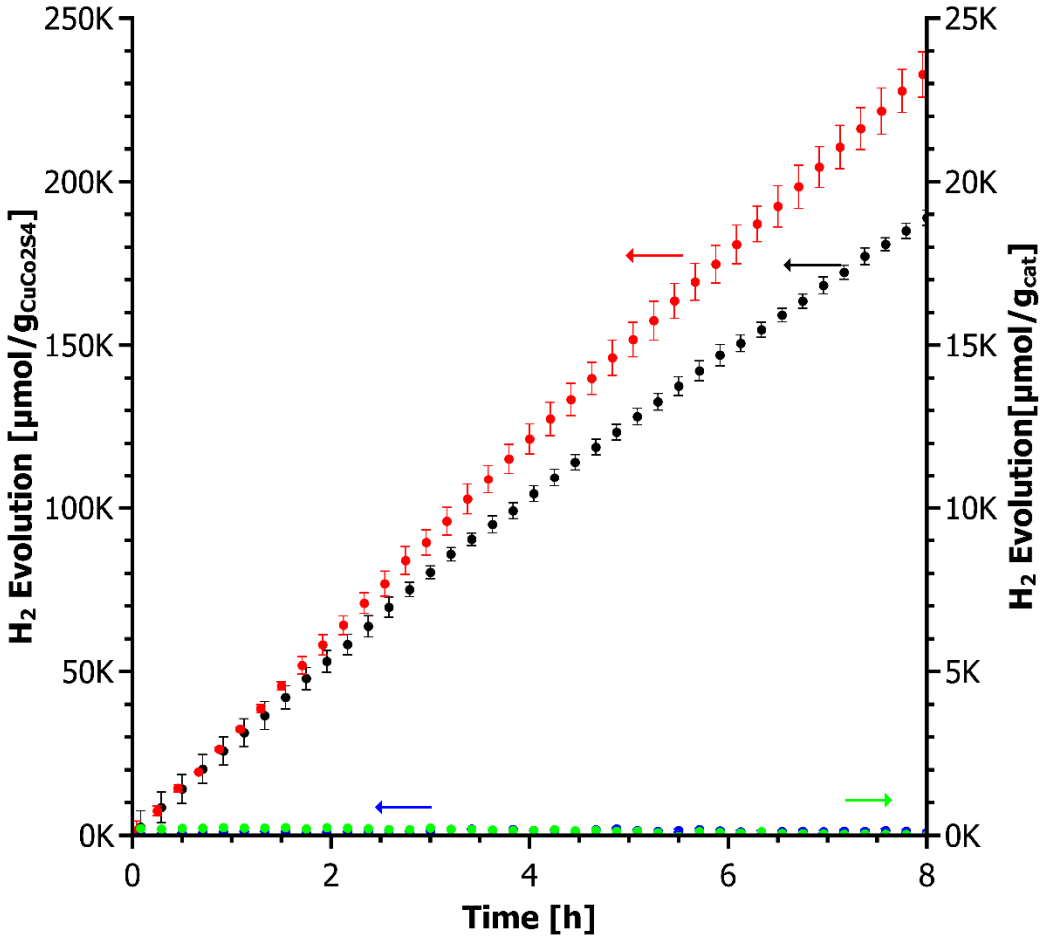

Fig. S11: Hydrogen evolution data of a mechanical mixture of 10 wt-% $CuCo_2S_4$ and P25 (black), CCS10 (red), pure $CuCo_2S_4$ (blue) and pure P25® (green). This demonstrates the synergistic effect of P25® and $CuCo_2S_4$.

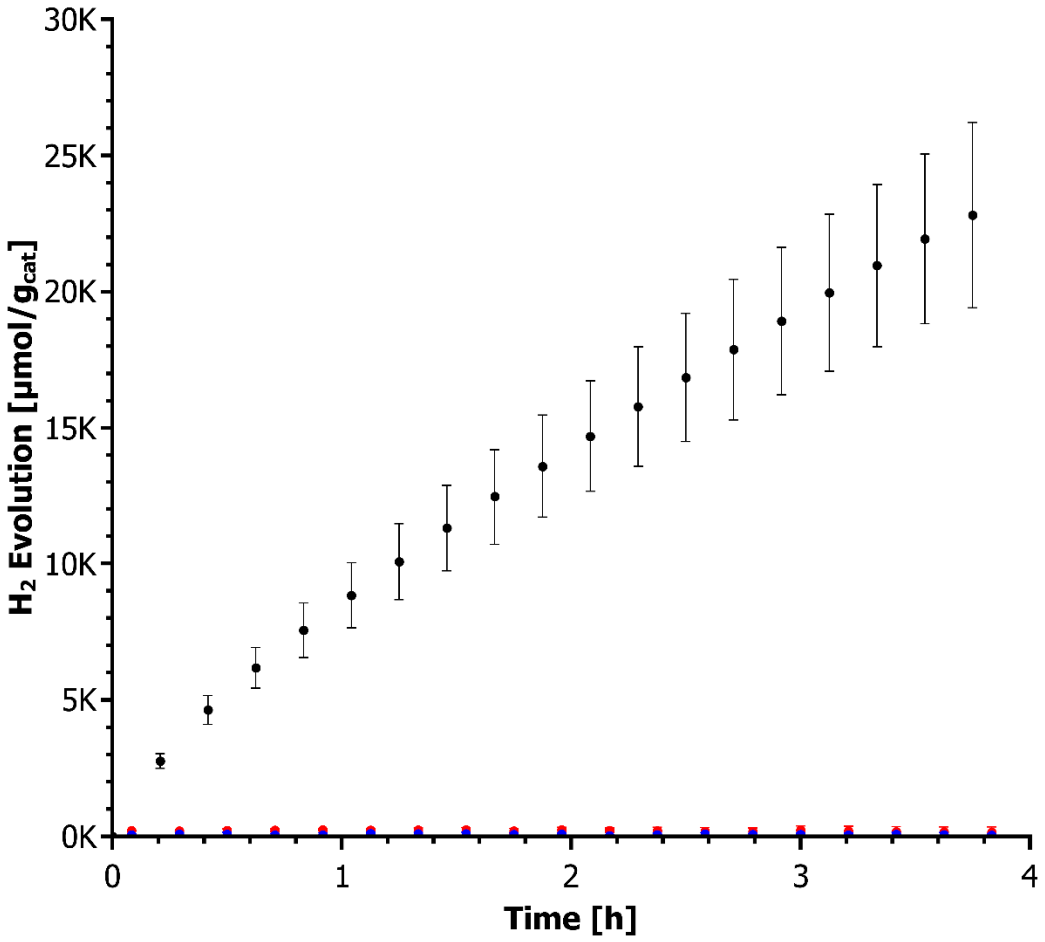

Fig. S12: Hydrogen evolution data of P25@Pd 1wt-%(black), P25 (red) and P25 with added Cu^{II}- andCo^{II}-salt (blue).

S9. Literature

[1] H. W. King, F. D. Manchester, *J. Phys. F: Met. Phys.*, **1978**, *8*, 15–26.
[2] M. Horn, C. F. Schwerdtfeger, E. P. Meagher, *Z. Krist.*, **1972**, *136*, 273–281.
[3] S. C. Abrahams, J. L. Bernstein, *J. Chem. Phys.*, **1971**, *55*, 3206–3211.
[4] D. P. Williamson, N. W. Grimes, *J. Phys. D: Appl. Phys.*, **1974**, *7*, 1–6.

5. Zusammenfassung

Im Rahmen der Doktorarbeit konnte eine Syntheseroute entwickelt werden, um $ZnCr_2O_4$ mit unterschiedlichen Teilchengrößen herzustellen. Dafür hat sich als Precursor $NH_4Zn(CrO_4)_2 \cdot 2NH_3$, in dem das Zn:Cr-Verhältnis dem des Spinells entspricht, als besonders geeignet herausgestellt, da $ZnCr_2O_4$ in hoher Reinheit bei moderaten Temperaturen darstellbar ist. Da für Katalysatoren mit guter Aktivität eine große spezifische Oberfläche oftmals Voraussetzung ist, ist es vorteilhaft, dass die gewählte Syntheseroute zu nanoskaligen Partikeln mit einer spezifischen Oberfläche von bis zu 60 m^2/g führt. In den Röntgenbeugungsdiffraktogrammen der bei niedrigen Temperaturen hergestellten Proben konnte eine große Anzahl an Punktdefekten und {111}-Stapelfehlern nachgewiesen werden. Die optischen Bandlücken betragen 3.4 bis 4.0 eV, was eine photokatalytische Nutzung bei Bestrahlung mit sichtbarem Licht ausschließt. Trotzdem konnte eine äußerst hohe Aktivität bei der Zersetzung von y-Eosin bei Bestrahlung mit sichtbarem Licht nachgewiesen werden. Mit einer detaillierten Untersuchung konnte jedoch nachgewiesen werden, dass diese Aktivität aus Rückständen von Cr^{VI} im Katalysator resultiert. Werden diese Rückstände vor einer Verwendung als Katalysator entfernt, so nimmt die katalytische Aktivität drastisch ab. Zusätzlich kommt es zur Bildung von CrO_4^{2-}-Anionen während der Bestrahlung der Dispersionen. D.h., unter den katalytischen Reaktionsbedingungen tritt Photokorrosion des Katalysators ein. Durch die hohe Giftigkeit von Cr^{VI} muss daher geschlossen werden, dass $ZnCr_2O_4$ ungeeignet für eine Verwendung als umweltfreundlicher Katalysator im wässrigen Medium ist.

Zwei neue Vertreter der Oxothiostannate mit der Zusammensetzung {[Ni(1,4,7,10-Tetraazacyclododecan)]$_6$[$Sn_6S_{12}O_2(OH)_6$]}$\cdot 2(ClO_4) \cdot 19H_2O$ und [Ni(1,4,7,10-Tetraaza-cyclododecan)$(H_2O)_2$]$_4$[$Sn_{10}S_{20}O_4$]$\cdot \sim 13H_2O$ konnten synthetisiert werden. Sie enthalten sowohl oxidische als auch sulfidische Anteile. Da sowohl Zinnoxide als auch Zinnsulfide häufig Anwendung in der Photokatalyse finden, war es von großem Interesse die Verbindung auf ihre photokatalytische Eigenschaften zu untersuchen. Tatsächlich konnte in einem Gemisch aus Acetonitril, Triethylamin, Wasser und dem Sensibilisator [Ru(2,2‘-Bipyridin)$_3$]$(PF_6)_2$ innerhalb von drei Stunden mit beiden VerbindungenWasserstoff generiert werden. Jedoch näherten sich die H_2-Entwicklungen einem Maximum an, was die Interpretation des photokatalytischen Prozesses besonders im Hinblick auf die komplexe Mischung der Reaktanden schwierig macht. Daher kann nicht eindeutig festgestellt werden, ob diese Verbindungen tatsächlich katalytisch aktiv sind oder ob ein Zersetzungsprodukt dafür verantwortlich ist.

Außerordentlich hohe photokatalytische Wasserstoffproduktionen konnten mit einem Nanokomposit aus TiO_2 und $CuCo_2S_4$ mit unterschiedlichen Gewichtsanteilen erreicht werden. In einer einfachen solvothermalen Reaktion konnte $CuCo_2S_4$ auf P25, einer TiO_2-Mischung aus Anatas und Rutil, abgeschieden werden. In Transmissions Elektronen Mikroskop Aufnahmen, Röntgenbeugung und Energiedispersive Röngenfluoreszenzanalyse bestätigen die erfolgreiche Bildung von $CuCo_2S_4$ in der Spinellstruktur. Eine hohe photokatalytische Wasserstoffentwicklungsrate in dem Reaktionsmedium aus Triethanolamin und Wasser wird bei UV-Bestrahlung beobachtet. Die Reaktion kann durch eine Kinetik pseudo nullter Ordnung beschrieben werden mit einer Reaktionskonstante von 1.68 mmol/(g_{cat} h) bei einer $CuCo_2S_4$ Beladung von 10 Gew.-%. Bei einer Bestrahlungsdauer von mehr als 80 h ist eine stetige Abnahme der katalytischen Aktivität zu beobachten. Trotzdem kann geschlossen werden, dass es sich bei dem Nanokomposit um einen sehr aktiven Photokatalysator zur Wasserstoffentwicklung bei Bestrahlung mit UV-Licht handelt. Die Herausforderung besteht darin, das optimale katalytische System zu identifizieren, welches eine bessere Langzeitstabilität aufweist.

6. Ausblick

Um die Forschung im Bereich der Chromite weiter zu führen, sollte überprüft werden, ob die Beobachtungen, die mit Zinkchromit gemacht wurden, auch für andere Chromite zutreffen. Sollte bei allen Chromiten beobachtet werden, dass bei einer Katalyse zur Zersetzung von organischen Substanzen Chromat freigesetzt wird, dann kann diese Verbindungsklasse nicht als Photokatalysatoren für Abwasserklärung in Betracht gezogen werden.

Oxothiostannate haben interessante erste Ergebnisse bei photokatalytischen Untersuchungen gezeigt. Hier bieten sich viele Möglichkeiten zur Fortsetzung der Untersuchungen zur photokatalytischen Aktivität an. Zunächst muss für das gewählte katalytische System geklärt werden, warum die Wasserstoffentwicklung zeitlich limitiert ist. Wenn das jeweilige Oxothiostannat in dem verwendeten Reaktionsmedium nicht stabil ist, wofür qualitative Hinweise gefunden wurden, sollte die Wasserstoffentwicklung in anderen Reaktionsmedien untersucht werden, um die katalytische Aktivität des Materials zu beweisen. Ist ein Katalysesystem gefunden in dem das Material eine dauerhafte Entwicklung aufweist, können Variationen der Zusammensetzung versucht werden, um den Einfluss der verschiedenen Bestandteile auf die katalytische Aktivität zu erfassen.

Mit dem Komposit aus TiO_2 und $CuCo_2S_4$ sollten Untersuchungen mit einem anderen Reaktionsmedium durchgeführt werden, z. B. in einer sauren Lösung, um eine bessere Stabilität des Katalysatormaterials bei gleichzeitig hoher katalytischer Aktivität zur Wasserstoffentwicklung zu erreichen. Zusätzlich könnte TiO_2 dotiert oder durch ein anderes Halbleitermaterial ersetzt werden, um eine katalytische Aktivität bei Bestrahlung mit sichtbarem Licht zu erzielen. Zusätzlich bietet es sich an, $CuCo_2S_4$ durch Dotierung oder Substitution zu modifizieren, um eine erhöhte Aktivität und/oder Stabilität zu gewährleisten. Schlussendlich könnte auch versucht werden, die Bifunktionalität zur simultanen katalytischen Entwicklung von Sauerstoff und Wasserstoff durch die Spaltung von Wasser auf ein Komposit mit $CuCo_2S_4$ als Katalysator zu übertragen.

7. Listen der wissenschaftlichen Beteiligung, Betreuung und Arbeiten

7.1. Publikationen als Erstautor

The Hazardous Origin of Photocatalytic Activity of $ZnCr_2O_4$

Michael Poschmann, Ulrich Schürmann, Wolfgang Bensch und Lorenz Kienle, Zeitschrift für Anorganische und Allgemeine Chemie, 2018, 644: 564-573.
DOI:10.1002/zaac.201800072

$CuCo_2S_4$ deposited on TiO_2 nanoparticles leading to high photocatalytic H_2 evolution

Michael Poschmann, Hendrik Gross, Reza Amin, Torben Dankwort, Lorenz Kienle, Wolfgang Bensch, submitted to Dalton Transactions, RSC Publishing Group.

7.2. Publikationen mit Beteiligung

In diesen Publikationen wurde bei der Untersuchung der photokatalytischen Eigenschaften mitgewirkt.

New Transition Metal Oxo-Thiostannate: Synthesis, Characterization, and Investigation of its Photocatalytic Properties

Assma Benkada, Michael Poschmann, Christian Näther, und Wolfgang Bensch, Zeitschrift für Anorganische und Allgemeine Chemie, 2019, 645, 433-439.

DOI: 10.1002/zaac.201800475

Synthesis and Characterization of a rare Transition Metal Oxo-Thiostannate and Investigation of its Photocatalytic Properties

Assma Benkada, Helge Reinsch, Michael Poschmann, Jan Krahmer, Nicole Pienack,

Wolfgang Bensch, Inorganic Chemistry, 2019, 58, 2354-2362.

DOI: 10.1021/acs.inorgchem.8b02773

7.3. Zusätzliche Journalbeiträge

Inside Cover der Zeitschrift für anorganische und allgemeine Chemie 07/2018

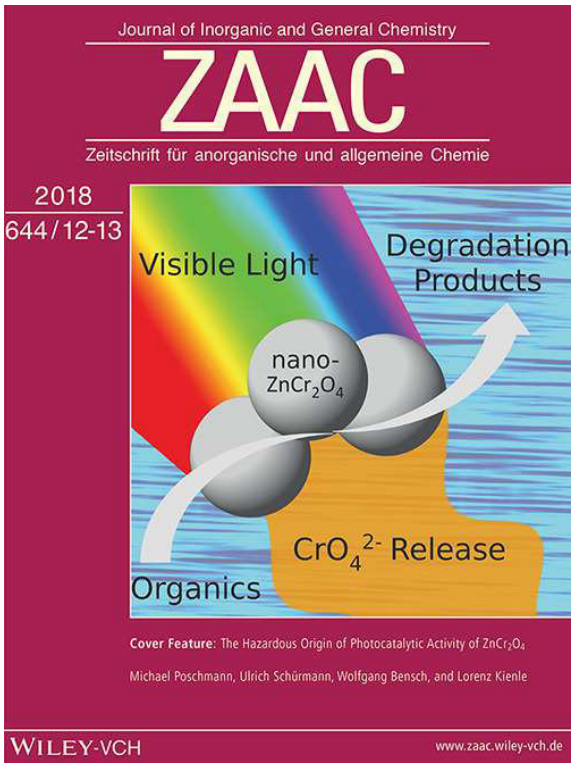

The cover picture shows the visible light irradiation of $ZnCr_2O_4$ nanoparticles which can be used for efficient degradation of organic molecules in waste water into small and harmless degradation products like CO_2, H_2O, etc. Unfortunately, a chromate release is observed generating even more dangerous waste water. This makes nanosized $ZnCr_2O_4$ useless for environmental friendly photo catalysis. Details are discussed in the article by Michael Poschmann, Ulrich Schürmann, Wolfgang Bensch and Lorenz Kienle on page 564 ff.[119]

7.4. Betreute Abschlussarbeiten

Photokatalytische Eigenschaften von Kobalt-Zinkchromiten

Hannah Puntschuh, Bachelorarbeit, CAU Kiel, November 2016.

Substitution von Zink in $ZnCr_2O_4$ und Charakterisierung als potentieller Katalysator zur H_2-Generierung

Jonas Gosch, Bachelorarbeit, CAU Kiel, September 2016.

Photokatalytische Eigenschaften von Zink-Ferriten, Zink-Chromiten, Magnesium-Chromiten und deren Mischphasen

Daniel Sandkuhl, Masterarbeit, CAU Kiel, Mai 2017.

Photokatalytische Wasserstoffproduktion unter Einsatz von auf Zinktitanat basierenden Core-Shell-Partikeln

Valentin Wies, Bachelorarbeit, CAU Kiel, Mai 2018.

7.5. Teilnahme an Workshops

Basics and Applications of the Rietveld Method

Am Max-Planck Institut für Festkörperforschung, Stuttgart, März 2017.

Pair distribution function (PDF) analysis workshop

Am Max-Planck Institut für Festkörperforschung, Stuttgart, Oktober 2018.

8. Eidesstattliche Erklärung

Hiermit versichere ich, Michael Alexander Thomas Poschmann, an Eides statt, dass ich die vorliegende Dissertation, abgesehen von der Beratung durch meinen Doktorvater Prof. Dr. W. Bensch, nach Inhalt und Form selbstständig und nur mit den angegebenen Hilfsmitteln verfasst habe. Weder ganz noch zum Teil wurde diese Arbeit an anderer Stelle im Rahmen eines Prüfungsverfahrens vorgelegt oder zur Veröffentlichung eingereicht. Ich erkläre, dass ich die hier vorliegende Arbeit nach den Grundsätzen guter wissenschaftlicher Arbeit der Deutschen Forschungsgemeinschaft verfasst habe. Außerdem wurde mir bisher kein akademischer Grad entzogen.

Kiel, Datum Michael A. T. Poschmann

9. Lebenslauf

Schulischer und Wissenschaftlicher Werdegang

1994-1996	Grundschule Herten, Nordrhein-Westfalen
1996-2000	Grund- und Orientierungsstufe Surwold, Niedersachsen
2000-2008	Mittelstufe und gymnasiale Oberstufe Papenburg, Niedersachsen
2008-2012	Bachelorstudium 1-Fach Chemie CAU Kiel, Schleswig Holstein Abschlussarbeit: Wasseroxidationskatalyse mit „biomimetischen“ Oxiden
2012-2014	Masterstudium 1-Fach Chemie CAU Kiel, Schleswig Holstein Abschlussarbeit: Synthese von Fe^{III}- und Ca^{II}-substituierten $MgAl_2O_4$-Spinellen und deren photokatalytische Anwendung zur Wasserstoffentwicklung
2014-2019	Wissenschaftlicher Mitarbeiter und Promotionsstudent CAU Kiel, Schleswig Holstein

10. Danksagung

Diese Arbeit wäre ohne die Unterstützung vieler Personen natürlich nicht möglich gewesen.

Besonders Prof. Dr. Wolfgang Bensch möchte ich danken für stetige Unterstützung und dafür, dass er mir die Freiheit gelassen hat dieses Thema nach meinen Wünschen zu bearbeiten.

Sebastian Mangelsen, Philipp Breuninger und Florian Lange möchte ich für die vielen Ratschläge, Denkanstöße und wahnwitzigen Ideen danken, die mich bei kniffligen Problemen auf den richtigen Weg zur Lösung gebracht haben. Ihrer Freundschaft ist auch zu danken, dass ich während der ganzen Zeit nicht dem Wahnsinn verfallen bin.

Bedanken möchte ich mich beim Arbeitskreis Bensch, aber auch den Arbeitskreisen Näther und Kienle für die tatkräftige Unterstützung, die Ausführung zahlreicher Messungen und die freundliche Arbeitsatmosphäre.

Besonderer Dank gilt auch Torsten Bies, Hannah Puntschuh, Jonas Gosch, Daniel Sandkuhl, Ephraim Akpari und Reza Amin, die mit ihren Beiträgen zu meiner Forschung stets passende Puzzleteile geliefert haben.

Mein umfassender Dank gilt natürlich auch meiner Familie und Jana Jacobsen für die herausragende mentale und emotionale Unterstützung bei allen Rückschlägen, Herausforderungen und Erfolgserlebnissen.

Schlussendlich bedanke ich mich auch bei den Bürgern des Landes Schleswig-Holstein und der Bundesrepublik, die mit ihren Steuerzahlungen Grundlagenforschung ermöglichen.

11. Literaturverzeichnis

[1] T. F. Stocker, D. Qin, G.-K. Plattner, M. Tignor, S. K. Allen, J. Boschung, A. Nauels, Y. Xia, V. Bex, P. M. Midgley, *Climate Change 2013: The Physical Science Basis*, **2014**, https://www.ipcc.ch/site/assets/uploads/2018/02/WG1AR5_all_final.pdf, Abgerufen am 30.01.2019.

[2] European Environment Agency, *Persistent Organic Pollutant Emissions*, **2018**, https://www.eea.europa.eu/data-and-maps/indicators/eea32-persistent-organic-pollutant-pop-emissions-1/assessment-9, Abgerufen am 15.01.2019.

[3] A. Joas, E. Müller, Umweltbundesamt Germany, *Dioxine: Daten aus Deutschland*, **2007**, http://www.umweltbundesamt.de/sites/default/files/medien/publikation/long/3328.pdf, Abgerufen am 30.01.2019.

[4] D. Drosihn, P. Icha, G. Kuhs, F. Sandau, J. Pabst, B. Hain, M. Nowakowski, D. Pfeiffer, K. Juhrich, B. Bünger, L. Köder, B. Lünenbürger, D. Osiek, A. Matthey, G. Penn-Bressel, W. Straff, D. Plaß, D. Wintermeyer, R. Wolter, C. Baumgarten, S. Grimm, I. Kirst, J. Frauenstein, M. Langner, R. Beckers, D. Lewandrowski, C. Gibis, J. Weiß, S. Schlömer, *Daten und Fakten zu Braun- und Steinkohlen*, **2017**, https://www.umweltbundesamt.de/publikationen/daten-fakten-zu-braun-steinkohlen, Abgerufen am 30.01.2019.

[5] S. Schwermer, P. Preiss, W. Müller, *Best-Practice-Kostensätze für Luftschadstoffe, Verkehr, strom- und Wärmeerzeugung: Anhang B der „Methodenkonvention 2.0 zur Schätzung von Umweltkosten“*, **2014**, https://www.umweltbundesamt.de/sites/default/files/medien/378/publikationen/uba_methodenkonvention_2.0_-_anhang_b_0.pdf, Abgerufen am 30.01.2019.

[6] X. Zou, Y. Zhang, Noble Metal-free Hydrogen Evolution Catalysts for Water Splitting, *Chem. Soc. Rev.*, **2015**, *44*, 5148–5180.

[7] W. Wang, M. O. Tadé, Z. Shao, Research Progress of Perovskite Materials in Photocatalysis- and Photovoltaics-related Energy conversion and environmental treatment, *Chem. Soc. Rev.*, **2015**, *44*, 5371–5408.

[8] M. Schwarze, D. Stellmach, M. Schröder, K. Kailasam, R. Reske, A. Thomas, R. Schomäcker, Quantification of Photocatalytic Hydrogen Evolution, *Phys. Chem. Chem. Phys.*, **2013**, *15*, 3466–3472.

[9] A. Kudo, Y. Miseki, Heterogeneous Photocatalyst Materials for Water Splitting, *Chem. Soc. Rev.*, **2009**, *38*, 253–278.

[10] World Health Organization, *Polynuclear Aromatic Hydrocarbons in Drinking-water: Background document for development of WHO Guidelines for Drinking-water Quality*, **1998**, https://www.who.int/water_sanitation_health/dwq/chemicals/polyaromahydrocarbons.pdf, Abgerufen am 30.01.2019.

[11] European Commission, *Pollutants in Urban Waste Water and Sewage Sludge: Final Report*, **2001**, http://europa.eu.int/comm/environment/sludge/sludge_polutants.htm.

[12] R. Loos, R. Carvalho, D. C. Antonio, S. Comero, G. Locoro, S. Tavazzi, B. Paracchini, M. Ghiani, T. Lettieri, L. Blaha, B. Jarosova, S. Voorspoels, K. Servaes, P. Haglund, J. Fick, R. H. Lindberg, D.

Schwesig, B. M. Gawlik, EU-wide Monitoring Survey on Emerging Polar Organic Contaminants in Wastewater Treatment Plant Effluents, *Water Res.*, **2013**, *47*, 6475–6487.

[13] A. Bergmann, R. Fohrmann, F.-A. Weber, *Zusammenstellung von Monitoringdaten zu Umweltkonzentrationen von Arzneimitteln*, **2011**, http://www.uba.de/uba-info-medien/4188.html, Abgerufen am 21.01.2019.

[14] B. C. Hodges, E. L. Cates, J.-H. Kim, Challenges and Prospects of Advanced Oxidation Water Treatment Processes using Catalytic Nanomaterials, *Nat. Nanotechnol.*, **2018**, *13*, 642–650.

[15] Bundesregierung 16. Wahlperiode, *Belastung von Abwässern und Klärschlammen mit Arzneimittelwirkstoffen: Zum 20. Tätigkeitsbericht des BfD 2003/2004*, **2007**.

[16] E. Corcoran, C. Nellemann, E. Baker, R. Bos, D. Osborn, H. Savelli, *Sick Water: The Central Role of Wastewater Management in Sustainable Development*, **2010**, https://wedocs.unep.org/bitstream/handle/20.500.11822/9156/Sick%20Water.pdf?sequence=1&isAllowed=y, Abgerufen am 30.01.2019.

[17] P. J. Kershaw, V. Kup, V. Njoroge, *Marine Plasitc Debris and Microplastics: Global lessons and research to inspire action and guide policy change*, **2016**, http://wedocs.unep.org/bitstream/handle/20.500.11822/7720/-Marine_plasctic_debris_and_microplastics_Global_lessons_and_research_to_inspire_action_and_guide_policy_change-2016Marine_Plastic_Debris_and_Micropla.pdf?sequence=3&isAllowed=yAOvVaw1TbiUycdwyexp9N6Ym1fag, Abgerufen am 30.01.2019.

[18] M. Smith, D. C. Love, C. M. Rochman, R. A. Neff, Microplastics in Seafood and the Implications for Human Health, *Curr. Environ Health Rep.*, **2018**, *5*, 375–386.

[19] K. L. Law, R. C. Thompson, Microplastics in the Seas, *Science*, **2014**, *345*, 144–145.

[20] K. Pirkanniemi, M. Sillanpää, Heterogeneous Water Phase Catalysis as an Environmental Application, *Chemosphere*, **2002**, *48*, 1047–1060.

[21] H. Zangeneh, A.A.L. Zinatizadeh, M. Habibi, M. Akia, M. Hasnain Isa, Photocatalytic Oxidation of Organic Dyes and Pollutants in Wastewater using Different Modified Titanium Dioxides, *J. Ind. Eng. Chem.*, **2015**, *26*, 1–36.

[22] K. J. Laidler, A Glossary of Terms used in Chemical Kinetics, Including Reaction Dynamics, *Pure Appl. Chem.*, **1996**, *68*, 149–192.

[23] A. F. Holleman, N. Wiberg, *Lehrbuch der anorganischen Chemie,* 102. Aufl., De Gruyter, Berlin, **2007**.

[24] G. Ertl, Reactions at Surfaces, *Angew. Chem. Int. Ed. Engl.*, **2008**, *47*, 3524–3535.

[25] D. W. Rice, P. Peterson, E. B. Rigby, Phipps, P. B. P., Cappell, R. J., Tremoureux, R., Atmospheric Corrosion of Copper and Silver, *J. Electrochem. Soc.*, **1981**, *128*, 275–284.

[26] D. D. Eley, E. K. Rideal, The Catalysis of the Parahydrogen Conversion by Tungsten, *Proc. R. Soc. Lond. A*, **1941**, *178*, 429–451.

[27] D. D. Eley, E. K. Rideal, Parahydrogen Conversion on Tungsten, *Nature*, **1940**, *146*, 401–402.

[28] C. N. Hinshelwood, Chemical Kinetics in the past few Decades, *Nobel Lecture*, **1956**.

[29] I. Langmuir, The Mechanism of the Catalytic Action of Platinum in the Reactions $2CO+O_2=2CO_2$ and $2H_2+O_2=2H_2O$, *Trans. Faraday Soc.*, **1922**, *17*, 621–654.

[30] P. Mars, D. W. van Krevelen, Oxidations Carried out by Means of Vanadium Oxide Catalysts, *Chem. Eng. Sci.*, **1954**, *3*, 41–59.

[31] N. Serpone, A. V. Emeline, Suggested Terms and Definitions in Photocatalysis and Radiocatalysis, *Int. J. Photoenergy*, **2002**, *4*, 91–131.

[32] K. N. Ferreira, T. M. Iverson, K. Maghlaoui, J. Barber, S. Iwata, Architecture of the Photosynthetic Oxygen-evolving Center, *Science*, **2004**, *303*, 1831–1838.

[33] B. Loll, J. Kern, W. Saenger, A. Zouni, J. Biesiadka, Towards Complete Cofactor Arrangement in the 3.0 A Resolution Structure of Photosystem II, *Nature*, **2005**, *438*, 1040–1044.

[34] J. P. McEvoy, G. W. Brudvig, Water-splitting Chemistry of Photosystem II, *Chem. Rev.*, **2006**, *106*, 4455–4483.

[35] D. G. Nocera, The Artificial Leaf, *Acc. Chem. Res.*, **2012**, *45*, 767–776.

[36] T. Lazarides, T. McCormick, P. Du, G. Luo, B. Lindley, R. Eisenberg, Making Hydrogen from Water using a Homogeneous System without Noble Metals, *J. Am. Chem. Soc.*, **2009**, *131*, 9192–9194.

[37] F. E. Osterloh, Inorganic Nanostructures for Photoelectrochemical and Photocatalytic Water Splitting, *Chem. Soc. Rev.*, **2013**, *42*, 2294–2320.

[38] T. Kawai, T. Sakata, Photocatalytic Hydrogen Production from Liquid Methanol and Water, *J. Chem. Soc., Chem. Commun.*, **1980**.

[39] I. Paramasivam, H. Jha, N. Liu, P. Schmuki, A Review of Photocatalysis using Self-organized TiO_2 Nanotubes and Other Ordered Oxide Nanostructures, *Small*, **2012**, *8*, 3073–3103.

[40] S. Tschierlei, M. Presselt, C. Kuhnt, A. Yartsev, T. Pascher, V. Sundström, M. Karnahl, M. Schwalbe, B. Schäfer, S. Rau, M. Schmitt, B. Dietzek, J. Popp, Photophysics of an Intramolecular Hydrogen-evolving Ru-Pd Photocatalyst, *Chemistry*, **2009**, *15*, 7678–7688.

[41] K. Arifin, E. H. Majlan, W. R. Wan Daud, M. B. Kassim, Bimetallic Complexes in Artificial Photosynthesis for Hydrogen Production, *Int. J. Hydrogen Energ.*, **2012**, *37*, 3066–3087.

[42] R. Marschall, L. Wang, Non-metal Doping of Transition Metal Oxides for Visible-Light Photocatalysis, *Catal. Today*, **2014**, *225*, 111–135.

[43] A. Ibhadon, P. Fitzpatrick, Heterogeneous Photocatalysis, *Catalysts*, **2013**, *3*, 189–218.

[44] Q. H. Wang, K. Kalantar-Zadeh, A. Kis, J. N. Coleman, M. S. Strano, Electronics and Optoelectronics of Two-dimensional Transition Metal Dichalcogenides, *Nat. Nanotechnol.*, **2012**, *7*, 699–712.

[45] A. P. Alivisatos, Perspectives on the Physical Chemistry of Semiconductor Nanocrystals, *J. Phys. Chem.*, **1996**, *100*, 13226–13239.

[46] D. V. Talapin, J.-S. Lee, M. V. Kovalenko, E. V. Shevchenko, Prospects of Colloidal Nanocrystals for Electronic and Optoelectronic Applications, *Chem. Rev.*, **2010**, *110*, 389–458.

[47] J. Smoliner, *Grundlagen der Halbleiterphysik,* 1. Aufl., Springer, **2018**.

[48] R. Gross, A. Marx, *Festkörperphysik,* 2. aktual. Aufl., Oldenbourg, München, **2014**.

[49] Y. Xu, A. Li, T. Yao, C. Ma, X. Zhang, J. H. Shah, H. Han, Strategies for Efficient Charge Separation and Transfer in Artificial Photosynthesis of Solar Fuels, *ChemSusChem*, **2017**, *10*, 4277–4305.

[50] M. A. Butler, D. S. Ginley, Prediction of Flatband Potentials at Semiconductor-Electrolyte Interfaces from Atomic Electronegativities, *J. Electrochem. Soc.*, **1978**, *125*, 228–232.

[51] Y. Xu, M. A.A. Schoonen, The Absolute Energy Positions of Conduction and Valence Bands of Selected Semiconducting Minerals, *Am. Mineral.*, **2000**, *85*, 543–556.

[52] X. Yang, D. Wang, Photocatalysis, *ACS Appl. Energy Mater.*, **2018**, *1*, 6657–6693.

[53] D. S. P. Cardoso, B. Šljukić, D. M. F. Santos, C. A. C. Sequeira, Organic Electrosynthesis, *Org. Process Res. Dev.*, **2017**, *21*, 1213–1226.

[54] K. D. Moeller, T. Wu, B. H. Nguyen, M. C. Daugherty, Paired Electrochemical Reactions and the On-Site Generation of a Chemical Reagent, *Angewandte Chemie (International ed. in English)*, **2019**.

[55] M. Chandra, K. Bhunia, D. Pradhan, Controlled Synthesis of CuS/TiO_2 Heterostructured Nanocomposites for Enhanced Photocatalytic Hydrogen Generation through Water Splitting, *Inorg. Chem.*, **2018**, *57*, 4524–4533.

[56] F. Chen, W. Luo, Y. Mo, H. Yu, B. Cheng, *In situ* Photodeposition of Amorphous CoS_X on the TiO_2 towards Hydrogen Evolution, *Appl. Surf. Sci.*, **2018**, *430*, 448–456.

[57] Q. Xiang, J. Yu, M. Jaroniec, Synergetic Effect of MoS_2 and Graphene as Cocatalysts for Enhanced Photocatalytic H_2 Production Activity of TiO_2 Nanoparticles, *J. Am. Chem. Soc.*, **2012**, *134*, 6575–6578.

[58] H. X. Sang, X. T. Wang, C. C. Fan, F. Wang, Enhanced Photocatalytic H_2 Production from Glycerol Solution over ZnO/ZnS Core/Shell Nanorods prepared by a Low Temperature Route, *Int. J. Hydrogen Energ.*, **2012**, *37*, 1348–1355.

[59] T. Sreethawong, S. Ngamsinlapasathian, Y. Suzuki, S. Yoshikawa, Nanocrystalline Mesoporous Ta_2O_5-based Photocatalysts prepared by Ssurfactant-assisted Templating Sol–gel Process for Photocatalytic H_2 Evolution, *J. Molec. Catal. A: Chem.*, **2005**, *235*, 1–11.

[60] J. Liu, G. Chen, Z. Li, Z. Zhang, Hydrothermal Synthesis and Photocatalytic Properties of $ATaO_3$ and $ANbO_3$ (A=Na and K), *Int. J. Hydrogen Energ.*, **2007**, *32*, 2269–2272.

[61] N. Nuraje, X. Dang, J. Qi, M. A. Allen, Y. Lei, A. M. Belcher, Biotemplated Synthesis of Perovskite Nanomaterials for Solar Energy Conversion, *Adv. Mater.*, **2012**, *24*, 2885–2889.

[62] Q. Li, B. Guo, J. Yu, J. Ran, B. Zhang, H. Yan, J. R. Gong, Highly Efficient Visible-light-driven Photocatalytic Hydrogen Production of CdS-cluster-decorated Graphene Nanosheets, *J. Am. Chem. Soc.*, **2011**, *133*, 10878–10884.

[63] L. Ge, F. Zuo, J. Liu, Q. Ma, C. Wang, D. Sun, L. Bartels, P. Feng, Synthesis and Efficient Visible Light Photocatalytic Hydrogen Evolution of Polymeric g-C_3N_4 Coupled with CdS Quantum Dots, *J. Phys. Chem. C*, **2012**, *116*, 13708–13714.

[64] A. Asghar, A. A. Abdul Raman, W. M. A. Wan Daud, Advanced Oxidation Processes for *In-Situ* Production of Hydrogen Peroxide/Hydroxyl Radical for Textile Wastewater Treatment, *J. Clean. Prod.*, **2015**, *87*, 826–838.

[65] E. Casbeer, V. K. Sharma, X.-Z. Li, Synthesis and Photocatalytic Activity of Ferrites under Visible Light, *Sep. Purif. Technol.*, **2012**, *87*, 1–14.

[66] M. R. Hoffmann, S. T. Martin, W. Choi, D. W. Bahnemann, Environmental Applications of Semiconductor Photocatalysis, *Chem. Rev.*, **1995**, *95*, 69–96.

[67] W.-K. Jo, R. J. Tayade, Recent Developments in Photocatalytic Dye Degradation upon Irradiation with Energy-efficient Light Emitting Diodes, *Chinese J. Catal.*, **2014**, *35*, 1781–1792.

[68] A. Mills, C. Hill, P. K.J. Robertson, Overview of the Current ISO Tests for Photocatalytic Materials, *J. Photoch. Photobio. A*, **2012**, *237*, 7–23.

[69] M. Rochkind, S. Pasternak, Y. Paz, Using Dyes for Evaluating Photocatalytic Properties, *Molecules*, **2015**, *20*, 88–110.

[70] I. K. Konstantinou, T. A. Albanis, TiO_2-assisted Photocatalytic Degradation of Azo Dyes in Aqueous Solution, *Appl. Catal. B-Environ.*, **2004**, *49*, 1–14.

[71] S. Bagheri, A. TermehYousefi, T.-O. Do, Photocatalytic Pathway toward Degradation of Environmental Pharmaceutical Pollutants, *Catal. Sci. Technol.*, **2017**, *7*, 4548–4569.

[72] J. Bandara, U. Klehm, J. Kiwi, Raschig Rings-Fe_2O_3 Composite Photocatalyst Activate in the Degradation of 4-chlorophenol and Orange II under Daylight Irradiation, *Appl. Catal. B-Environ.*, **2007**, *76*, 73–81.

[73] Y. Li, Q. Yang, Z. Wang, G. Wang, B. Zhang, Q. Zhang, D. Yang, Rapid Fabrication of SnO_2 Nanoparticle Photocatalyst, *Inorg. Chem. Front.*, **2018**, *5*, 3005–3014.

[74] H. Fu, T. Xu, S. Zhu, Y. Zhu, Photocorrosion Inhibition and Enhancement of Photocatalytic Activity for ZnO via Hybridization with C_{60}, *Environ. Sci. Technol.*, **2008**, *42*, 8064–8069.

[75] Y. Qiu, M. Yang, H. Fan, Y. Xu, Y. Shao, X. Yang, S. Yang, Synthesis and Characterization of Nitrogen Doped ZnO Tetrapods and Application in Photocatalytic Degradation of Organic Pollutants under Visible Light, *Mater. Lett.*, **2013**, *99*, 105–107.

[76] J.-C. Sin, S.-M. Lam, K.-T. Lee, A. R. Mohamed, Photocatalytic Performance of Novel Samarium-doped Spherical-like ZnO Hierarchical Nanostructures under Visible Light Irradiation for 2,4-dichlorophenol Degradation, *J. Colloid Interface Sci.*, **2013**, *401*, 40–49.

[77] S. Fu, H. Niu, Z. Tao, J. Song, C. Mao, S. Zhang, C. Chen, D. Wang, Low Temperature Synthesis and Photocatalytic Property of Perovskite-type $LaCoO_3$ Hollow Spheres, *J. Alloy Compd.*, **2013**, *576*, 5–12.

[78] S. Thirumalairajan, K. Girija, I. Ganesh, D. Mangalaraj, C. Viswanathan, A. Balamurugan, N. Ponpandian, Controlled Synthesis of Perovskite $LaFeO_3$ Microsphere Composed of Nanoparticles via Self-assembly Process and their Associated Photocatalytic Activity, *Chem. Eng. J.*, **2012**, *209*, 420–428.

[79] W. Yin, W. Wang, L. Zhou, S. Sun, L. Zhang, CTAB-assisted Synthesis of Monoclinic $BiVO_4$ Photocatalyst and its Highly Efficient Degradation of Organic Dye under Visible-light Irradiation, *J. Hazard. Mater.*, **2010**, *173*, 194–199.

[80] K. E. Sickafus, J. M. Wills, N. W. Grimes, Structure of Spinel, *J. Am. Ceram. Soc.*, **1999**, *82*, 3279–3292.

[81] C. Biagioni, M. Pasero, The Systematics of the Spinel-type Minerals, *Am. Mineral.*, **2014**, *99*, 1254–1264.

[82] B. Seidlhofer, N. Pienack, W. Bensch, Synthesis of Inorganic-Organic Hybrid Thiometallate Materials with a Special Focus on Thioantimonates and Thiostannates and in situ X-Ray Scattering Studies of their Formation, *Z. Naturforsch. B*, **2010**, *65*, 937–975.

[83] H. Ahari, G. A. Ozin, R. L. Bedard, S. Petrov, D. Young, Synthesis and Compositional Tuning of the Band Properties of Isostructural TMA-SnS_xSe_{1-x}, *Adv. Mater.*, **1995**, *7*, 370–374.

[84] P. Enzel, G. S. Henderson, G. A. Ozin, R. L. Bedard, Imaging the Surfaces of Nanoporous Semiconductors by Atomic Force Microscopy, *Adv. Mater.*, **1995**, *7*, 64–68.

[85] P. Feng, X. Bu, N. Zheng, The Interface Chemistry between Chalcogenide Clusters and Open Framework Chalcogenides, *Acc. Chem. Res.*, **2005**, *38*, 293–303.

[86] T. Jiang, A. Lough, G. A. Ozin, Very Soft Chemistry, *Adv. Mater.*, **1998**, *10*, 42–46.

[87] W. S. Sheldrick, Network Self-assembly Patterns in Main Group Metal Chalcogenide-based Materials, *J. Chem. Soc., Dalton Trans.*, **2000**.

[88] K. Tsamourtzi, J.-H. Song, T. Bakas, A. J. Freeman, P. N. Trikalitis, M. G. Kanatzidis, Straightforward Route to the Adamantane Clusters $[Sn_4Q_{10}]^{4-}$ (Q = S, Se, Te) and use in the Assembly of Open-framework Chalcogenides $(Me_4N)_2MSn_4Se_{10}$ (M = Mn(II), Fe(II), Co(II), Zn(II)) including the First Telluride Member $(Me_4N)_2MnGe_4Te_{10}$, *Inorg. Chem.*, **2008**, *47*, 11920–11929.

[89] R. M. Braun, R. Hoppe, Über Oxostannate(II). III. $K_2Sn_2O_3$, $Rb_2Sn_2O_3$ und $Cs_2Sn_2O_3$, *Z. Anorg. Allg. Chem.*, **1982**, *485*, 15–22.

[90] B. Nowitzki, R. Hoppe, Über Oxostannate(II) V. $Na_4[SnO_3]$, *Z. Anorg. Allg. Chem.*, **1984**, *515*, 114–126.

[91] H. G. v. Schnering, R. Nesper, H. Pelshenke, Hydroxoverbindungen, *Z. Anorg. Allg. Chem.*, **1983**, *499*, 117–129.

[92] W. Bubenheim, U. Müller, Reaktionen von Zinnchloriden mit Polysulfiden. Die Kristallstrukturen von $(PPh_4)_2[SnCl_2(S_6)_2]$, $(PPh_4)_2[Sn_4Cl_4S_5(S_3)O]$ und $(PPh_4)_2[SnCl_6]$ S_8 $2CH_3CN$, *Z. Anorg. Allg. Chem.*, **1993**, *619*, 779–785.

[93] L. Wu, L. Chen, J. Dai, C. Cui, Z. Fu, X. Wu, The First Octanuclear Tin(IV)–oxosulfide Cluster, *Inorg. Chem. Commun.*, **2001**, *4*, 574–576.

[94] J.-J. Zhang, S.-M. Hu, X.-T. Wu, W.-X. Du, R.-B. Fu, L.-S. Wang, A simple method for the preparation of octanuclear tin (IV) oxosulfide cluster and the conversion of it to decanuclear cluster, *Inorg. Chem. Commun.*, **2003**, *6*, 744–747.

[95] T. Kaib, M. Kapitein, S. Dehnen, Synthesis and Crystal Structure of $[Li_8(H_2O)_{29}]$-$[Sn_{10}O_4S_{20}]\cdot 2H_2O$, *Z. Anorg. Allg. Chem.*, **2011**, *637*, 1683–1686.

[96] W. Schiwy, B. Krebs, $Sn_{10}O_4S_{20}^{8-}$, *Angew. Chem.*, **1975**, *87*, 451–452.

[97] J. B. Parise, Y. Ko, Material Consisting of Two Interwoven 4-Connected Networks, *Chem. Mater.*, **1994**, *6*, 718–720.

[98] Z. Cheng, F. Wang, T. A. Shifa, C. Jiang, Q. Liu, J. He, Efficient Photocatalytic Hydrogen Evolution via Band Alignment Tailoring, *Small*, **2017**, *13*.

[99] C.-F. Fu, R. Zhang, Q. Luo, X. Li, J. Yang, Construction of Direct Z-Scheme Photocatalysts for Overall Water Splitting using Two-dimensional Van der Waals Heterojunctions of Metal Dichalcogenides, *J. Comput. Chem.*, **2018**.

[100] W. Fu, J. Wang, S. Zhou, R. Li, T. Peng, Controllable Fabrication of Regular Hexagon-Shaped SnS_2 Nanoplates and Their Enhanced Visible-Light-Driven H_2 Production Activity, *ACS Appl. Nano Mater.*, **2018**, *1*, 2923–2933.

[101] J. Ge, P. J. Roland, P. Koirala, W. Meng, J. L. Young, R. Petersen, T. G. Deutsch, G. Teeter, R. J. Ellingson, R. W. Collins, Y. Yan, Employing Overlayers To Improve the Performance of Cu_2BaSnS_4 Thin Film based Photoelectrochemical Water Reduction Devices, *Chem. Mater.*, **2017**, *29*, 916–920.

[102] J. Han, S. Li, L. Zhang, W. Zheng, W. Jiang, D. Jia, T3 supertetrahedral cluster $[Mn_4Sn_6S_{20}]^{8-}$, *Inorg. Chem. Commun.*, **2018**, *93*, 73–77.

[103] H. She, H. Zhou, L. Li, Z. Zhao, M. Jiang, J. Huang, L. Wang, Q. Wang, Construction of a Two-Dimensional Composite Derived from TiO_2 and SnS_2 for Enhanced Photocatalytic Reduction of CO_2 into CH_4, *ACS Sustainable Chem. Eng.*, **2018**, *7*, 650–659.

[104] Y. Shim, B. D. Yuhas, S. M. Dyar, A. L. Smeigh, A. P. Douvalis, M. R. Wasielewski, M. G. Kanatzidis, Tunable Biomimetic Chalcogels with Fe_4S_4 Cores and $[Sn_nS_{2n+2}]^{4-}$ (n = 1, 2, 4) Building Blocks for Solar Fuel Catalysis, *J. Am. Chem. Soc.*, **2013**, *135*, 2330–2337.

[105] W. Wang, H. Yang, C. Xue, M. Luo, J. Lin, D. Hu, X. Wang, Z. Lin, T. Wu, The First Observation on Dual Self-Closed and Extended Assembly Modes in Supertetrahedral T3 Cluster Based Open-Framework Chalcogenide, *Cryst. Growth Des.*, **2017**, *17*, 2936–2940.

[106] B. Zhang, J. Li, C.-F. Du, M.-L. Feng, X.-Y. Huang, $(CH_3NH_3)_2Ag_4Sn^{IV}_2Sn^{II}S_8$, *Inorg. Chem.*, **2016**, *55*, 10855–10858.

[107] Y. C. Zhang, Z. N. Du, K. W. Li, M. Zhang, D. D. Dionysiou, High-performance Visible-light-driven SnS_2/SnO_2 Nanocomposite Photocatalyst prepared via *In Situ* Hydrothermal Oxidation of SnS_2 Nanoparticles, *ACS Applied Materials & Interfaces*, **2011**, *3*, 1528–1537.

[108] Z. Zhang, J. Huang, M. Zhang, Q. Yuan, B. Dong, Ultrathin Hexagonal SnS_2 Nanosheets Coupled with g-C_3N_4 Nanosheets as 2D/2D Heterojunction photocatalysts toward high photocatalytic activity, *Appl. Catal. B-Environ.*, **2015**, *163*, 298–305.

[109] Z. Zhang, C. Shao, X. Li, Y. Sun, M. Zhang, J. Mu, P. Zhang, Z. Guo, Y. Liu, Hierarchical Assembly of Ultrathin Hexagonal SnS_2 Nanosheets onto Electrospun TiO_2 Nanofibers, *Nanoscale*, **2013**, *5*, 606–618.

[110] M. Zhong, Z. Yang, Y. Yi, D. Zhang, K. Sun, H. W. Roesky, Y. Yang, Tin Sulfide and Selenide Clusters Soluble in Organic Solvents with the Core Structures of Sn_4S_6 and Sn_4Se_6, *J. Chem. Soc., Dalton Trans.*, **2015**, *44*, 19800–19804.

[111] K. Gelderman, L. Lee, S. W. Donne, Flat-Band Potential of a Semiconductor, *J. Chem. Educ.*, **2007**, *84*, 685–688.

[112] E. A. Kraut, R. W. Grant, J. R. Waldrop, S. P. Kowalczyk, Precise Determination of the Valence-Band Edge in X-Ray Photoemission Spectra, *Phys. Rev. Lett.*, **1980**, *44*, 1620–1623.

[113] N. Barbero, D. Vione, Why Dyes Should Not Be Used to Test the Photocatalytic Activity of Semiconductor Oxides, *Environ. Sci. Technol.*, **2016**, *50*, 2130–2131.

[114] C. G. Hatchard, C. A. Parker, A New Sensitive Chemical Actinometer, *Proc. R. Soc. Lond. A*, **1956**, *235*, 518–536.

[115] C. A. Parker, A New Sensitive Chemical Actinometer, *Proc. R. Soc. Lond. A*, **1953**, *220*, 104–116.

[116] H. J. Kuhn, S. E. Braslavsky, R. Schmidt, Chemical Actinometry, *Pure Appl. Chem.*, **2004**, *76*, 2105–2146.